The Soft X-ray Background towards Ophiuchus

Ludwig-Maximilians-Universität München

Paulo Mendes

München 2010

The Soft X-ray Background towards Ophiuchus

Dissertation

der Fakultät für Physik

der Ludwig-Maximilians-Universität München

zur Erlangung des grades
Doktor der Naturwissenschaften
Dr. rer. nat.

vorgelegt von

Paulo Mendes
aus Maputo, Moçambique

München, March 2010

Erstgutachter: Prof. Dr., Dr. h.c. Gregor E. Morfill
Zweitgutachter: Prof. Dr. Dieter Breitschwerdt

Tag der müdlichen Prufung: 30 July 2010

Citations

Felizes os que ignoram, abençoados os que procuram não ignorar! Tristes os que julgam saber, alegria ao peito de quem procura compreender! Carrega com orgulho às claras as tuas dúvidas, se elas parecem hoje chumbo, serão, Talvez um dia, Talvez nunca, ouro do mais verdadeiro.

Dedication from David Eduardo Roque
Ferragudo, Portugal

" ... in the life of the intelect there is also a law of inertia. Everything continues to move along its old rectilinear path, and every change, every transition to new and modern ways, meets strong resistence".

Felix Klein (1849–1926)

Imagination was given to man to compensate him for what he is not; a sense of humor to console him for what he is.

Francis Bacon (1561–1626)

Acknowledgements

This thesis would never have been completed were it not for the moral and financial support of a great number of persons and institutions.

I would like to gratefully acknowledge the supervision, the support, the advice, the attention to detail, the constructive criticism and encouragement throughout the course of this thesis of Professor Dr. Dieter Breitschwerdt, now at the Technische Universität of Berlin.

Dr. Michael Freyberg, from the Max Planck Institut für extraterrestrische Physik (MPE), guided me through the intricate tracks of the XMM-Newton data, especially, through the complicated detector and sky *background* issues and their possible manifestations. I would like to acknowledge his advice, encouragement, enthusiasm, the football games, and all support given to me. Without his guidance this work would never have found the right path.

I would like to acknowledge all the support given by Professor Günther Hasinger, as the director of the X-ray and γ-ray Group at MPE, during the realization of this project. Many thanks to João Alves, then at the European Southern Observatory, for his enthusiastic support and collaboration. I thank Dr. Frank Harbel, Dr. Vadim Burwitz from MPE and Dr. Craig Gordon from HEASARC Software Development, Astrophysics Science Division, for the technical discussions on the XSPEC package.

Postgraduates of the MPE X-ray Group are thanked for numerous stimulating discussions and for their friendship, in particular to Alina Streblyanska, Daniel Schaudel, Elisa Costantini, Martin Henze, Michael Bauer, Thomas Stadlbauer and Zdenka Misanovic. Special thanks also to the MPE outsiders Alessandro Stenico and Katya Dimova. They have made MPE a very special place over all these years.

To more physically distant friends a word of thanks for their enthusiasm and enlightenment. To Carlos Tiago, David Roque, Emanuel Alexandre, Gisela Oliveira, Gustavo Rodrigues, João Borges, João Emanuel Dias, José Afonso, José Santos, Michael Odenwald, Nuno Moreira, Nuno Peixinho, Nuno Santos and Ricardo Barbosa.

This research was supported by a scholarship from Fundação para a Ciência e a Tecnologia (FCT) - Ministério de Ciência e Tecnologia of Portugal.

To Doris I would like to say thanks for her patience, support and understanding during the realization of this thesis.

Finally, a word of thanks to my parents for all what they have done in their lives to support me and to whom this work is dedicated.

The X-Ray Shadow of the Dark Filament of the Ophiuchus Molecular Cloud

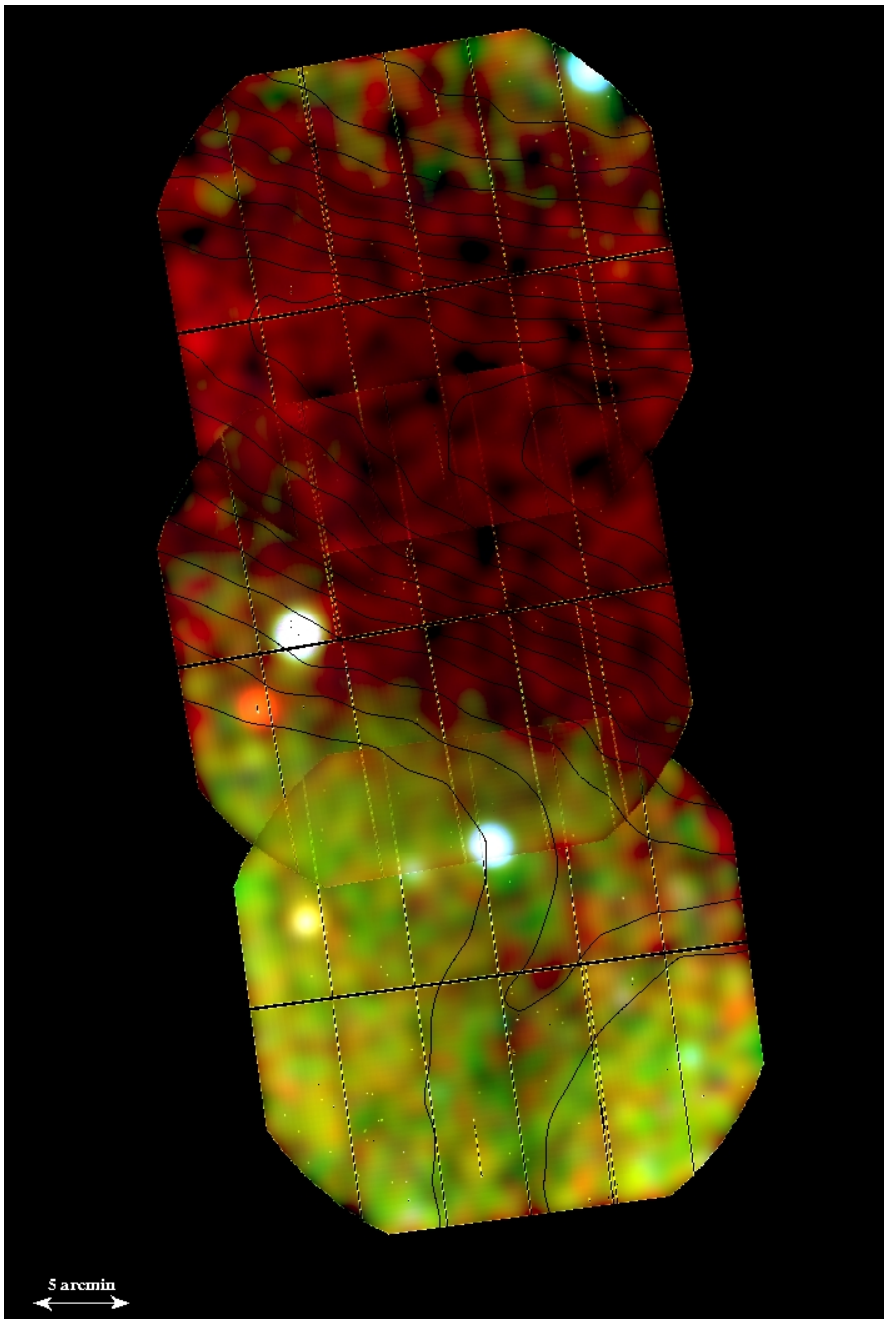

The X-ray Shadow due to the dark filament of the Ophiuchus Molecular Cloud, obtained by ESA's XMM-Newton satellite. Three energy bands were used to create three images. These images were color coded according to the following criteria: 0.3 – 0.5 keV as red, 0.5 – 0.9 keV as green and 0.9 – 2.0 keV as blue. As it can be seen, the dark molecular filament casts a shadow in the soft x-ray background due to the absorption of x-rays by neutral and molecular material present in the filament. The X-ray shadow is compared with the 100 μ IRAS contour map (black lines) due to the dust component of the cloud, which is superimposed to the x-ray mosaic image.

Summary

In this work we present the results of the analysis performed on the soft and diffuse x-ray emission of the so-called Local Hot Bubble (LB), using data collected by the XMM-Newton satellite, in the energy range of $\sim$ 0.2–7.0 keV. The spectacular progress in space science over the last decades has opened new and fundamental research areas, such as X-ray Astrophysics. The launch of space vehicles equipped with scientific observational instruments, the latest state of the art detectors, has revealed a new Universe, a hot and violent Universe. X-ray Astronomy started with the discovery that the corona of the Sun is a source of X-ray photons. Further research revealed that the whole sky is illuminated by a diffuse x-ray radiation. This all-sky X-ray emission is now interpreted as a superposition of different astronomical X-ray components. The first of these astrophysical X-ray sources is the Cosmic X-ray Background (CXB). This component has been resolved into X-ray point sources. It is now widely accepted, that this CXB is due to an extragalactic population of Active Galactic Nuclei (AGN). This extragalactic X-ray component clearly dominates at energies above 1.0 keV and is described by a power-law with a spectral index (Γ) of -1.4 in the energy range of 1.0–10.0 keV. At energies below 1.0 keV the x-ray emission is dominated by a sum of galactic hot thermal plasmas of different origins, with the strongest contribution on the very soft x-ray regime being due to the LB plasma. The present standard model of the LB, based upon the analysis of data obtained by the ROSAT satellite and on "simple" theoretical considerations, describes the LB x-ray emission arising from a plasma with a temperature of $\sim 1.2 \times 10^6$ K, an electron density of 4.5×10^{-3} cm^{-3} and a pressure of $P/k_B \sim 10^4$ cm^{-3} K. This plasma is pervading a cavity largely devoid of H I, with a radius of $\sim$ 100 pc. The Sun is located close to its centre. The paradigm of the LB is based upon the principle that the astrophysical LB plasma is in a collisional ionization equilibrium (CIE) state. The present thesis was designed to study the soft x-ray emission below 1.0 keV due to plasmas present in our Galaxy. In particular, to study the contribution of the LB x-ray emission and to find further observational features which could lead to a conflict with the basic picture of the LB. Some observations point to the existence of such contradictions. For instance, there is observational evidence for the existence of clouds and filaments of neutral H, e.g. the Local Cloud with a pressure of $P/k_B \sim 3 \times 10^3$ cm^{-3} K located within the LB ($P/k_B \sim 10^4$ cm^{-3} K). This huge imbalance in pressure would actually lead to the destruction of such clouds. Another contradiction is found in observations performed by the Diffuse X-ray Spectrometer (DXS), designed to obtain spectra in the energy range of 0.15–0.284 keV, which showed that the observed spectra are

not consistent with those predicted by CIE plasma models. From a theoretical perspective, it has been argued that the assumption of a CIE for interstellar medium (ISM) plasmas has serious flaws. One is the fact, that no astrophysical mechanism capable of permanently maintaining the observed range of temperatures is known. Another is, to neglect that the dynamic and thermal evolution of hot plasmas is coupled. It has been shown that, when the thermal evolution of ISM plasmas is taken into account, a wide range of observations can in principle be unified within the so-called non-equilibrium ionization (NEI) plasmas. In particular, for the LB it was possible to explain the main observations with a plasma having a temperature as low as 4.2×10^4 K and an electron density of 2.4×10^{-2} cm^{-3}. In order to improve the studies of its emission, an x-ray shadow experiment was performed on a dark filament of the OPHIUCHUS MOLECULAR CLOUD at a distance of 125 pc, using the unique capabilities of ESA's XMM-Newton satellite, its high effective area and spectral resolution. Since this molecular filament has column densities ranging from 10^{21} to 10^{22} cm^{-2}, it effectively absorbs most of the soft x-ray background below 1.0 keV, which then allows us to disentangle the x-ray emission originated within the LB boundaries from other galactic hot plasmas. The analysis of the x-ray shadow experiment on the dark filament shows, that the physical parameters for the electron temperature and density (T_e, n_e) of the LB plasma, derived from the spectral fitting using the CIE condition, require a $T_e(LB) = 1.2^{+0.67}_{-0.61} \times 10^6$ K and a $n_e(LB) = 0.017^{+0.025}_{-0.007}$ cm^{-3}. This analysis was complemented with another study of the x-ray diffuse emission in the opposite direction to OPHIUCHUS (in direction to TAURUS). The spectral analysis of the x-ray data in this direction requires a $T_e(LB) = 0.86^{+0.16}_{-0.11} \times 10^6$ K and a $n_e(LB) = 0.016^{+0.005}_{-0.005}$ cm^{-3} for the LB. The derived temperatures are very different in value and, therefore, do not corroborate the standard model of the LB. Not only the temperature values are in conflict, but also the electron densities derived from the present analysis. The values derived for the electron densities using the assumption of CIE, are much higher than these from older studies performed with the ROSAT satellite data. The present results undoubtedly give support for the claim of a revision of the standard model of the LB. The eROSITA mission (MPE) and future X-ray observatories like XEUS (ESA), with high spatial and spectral resolution, will provide high quality data. In particular, they will perform high resolution spectroscopy and consequently allow to resolve spectral emission lines present in the spectrum of galactic and intergalactic plasmas as well as in extragalactic x-ray emission sources. This information is of fundamental importance to distinguish between CIE and NIE plasmas, and therefore, to settle the question of the physical state of the LB plasma. As an example of the capabilities of these missions, we refer, e.g., that the eROSITA CCD detectors will operate in the energy range of 0.2–12 keV, with an energy resolution of 54 eV at 0.277 keV, of 74 eV at 1.5 keV and of 134 eV at 5.9 keV, reaching almost 100 per cent in terms of quantum efficiency in the energy band of 0.3–10 keV. Therefore eROSITA is a very important instrument for future studies on the diffuse soft x-ray emission of our Milky Way Galaxy and as well of the rest of the known Universe.

Zusammenfassung

In dieser Arbeit präsentieren wir die Ergebnisse der Analyse der weichen und diffusen Röntgenemission der sogenannten Lokalen Blase (LB), basierend auf Daten, die im Energiebereich von $\sim$ 0.2–7.0 keV vom XMM-Newton Satelliten gesammelt wurden. Der spektakuläre Fortschritt in der Weltraumwissenschaft der letzten Jahrzehnte hat neue und grundlegende Forschungsgebiete, wie die Röntgen-Astronomie, eröffnet. Das Aussenden von Raumfahrzeugen, ausgestattet mit Beobachtungsinstrumenten auf dem neuesten Stand der Technik, hat uns ein neues Universum offenbart, ein heißes und extremes Universum. Die Röntgen-Astronomie begann mit der Entdeckung, dass die Korona der Sonne eine Quelle von Röntgen-Photonen ist.Weitere Forschung brachte die Erkenntniss, dass der gesamte Himmel von einer diffusen Röntgenhintergrundstrahlung erleuchtet wird. Diese Röntgenhintergrundstrahlung wird nun als eine Überlagerung verschiedener astronomischer Röntgenkomponenten interpretiert. Die erste dieser astrophysischen Röntgenquellen ist der kosmische Röntgenhintergrund (Cosmic X-ray Background, CXB). Diese Komponente wurde in Röntgen-Punktquellen aufgelöst. Heute wird überwiegend angenommen, dass die Ursache des CXB in einer extragalaktischen Population von Aktiven Galaktischen Kernen (Active Galactic Nuclei, AGN) liegt. Diese extragalaktische Komponente dominiert deutlich bei Energien über 1.0 keV. Sie wird durch ein Potenzgesetz mit spektralem Index (Γ) = - 1.4 im Energiebereich von 1.0–10.0 keV beschrieben. Den größten Teil der Röntgenstrahlung unter 1.0 keV bilden Emissionen galaktischer heißer Plasmen unterschiedlichen Ursprungs, wobei der Hauptanteil aus dem weichen Röntgenbereich stammt, der dem LB Plasma zuzuschreiben ist. Das aktuelle Standardmodell der LB, das auf der Analyse von Daten des ROSAT Satelliten und auf "einfachen" theoretischen Überlegungen basiert, beschreibt die LB als ein Plasma mit einer Temperatur von 1.2×10^6 K, einer Elektronendichte von 4.5×10^{-3} cm^{-3} und einem Druck von $P/k_B \sim 10^4$ cm^{-3} K, welches Röntgenstrahlung aussendet. Dieses Plasma erfüllt ein weitgehend staubfreies Raumgebiet mit einem Radius von $\sim$100 pc. Unsere Sonne befindet sich nahe seines Zentrums. Das Paradigma der LB basiert auf dem Prinzip, dass sich das physikalische LB Plasma in einem Stoßionisationsgleichgewicht (Collisional Ionization Equilibrium, CIE) befindet. Das Ziel der vorliegenden Arbeit ist es, die weiche Röntgenstrahlung unterhalb von 1.0 keV zu untersuchen, die durch in unserer Galaxie befindliche Plasmen verursacht wurde. Im Besonderen wollen wir den Anteil der LB Röntgenstrahlung untersuchen und zu den bereits bekannten noch weitere Merkmale finden, die im Widerspruch zu dem Standardmodell der LB stehen könnten. Einige Beobachtungen deuten auf die Existenz solcher Widersprüche hin. Es gibt

zum Beispiel wider Erwarten Hinweise für die Existenz von Wolken und Filamenten aus neutralem Wasserstoff, so zum Beispiel die LOKALE WOLKE, die sich mit einem Druck von $P/k_B \sim 3 \times 10^3$ cm^{-3} K innerhalb der LB ($P/k_B \sim 10^4$ cm^{-3} K) befindet. Dieser hohe Druckunterschied würde eigentlich zu der Zerstörung solcher Wolken führen. Ein weiterer Widerspruch fand sich in Beobachtungen, die mit dem Diffusen Röntgenspektrometer (Diffuse X-ray Spectrometer, DXS) durchgeführt wurden. Es wurde entworfen, um Spektren in dem Energiebereich von 0.15–0.284 keV zu erhalten. Die beobachteten Spektren stimmten nicht mit denen überein, die durch die CIE-Plasma-Modelle vorhergesagt wurden. Vom theoretischen Standpunkt aus wurde argumentiert, dass die Annahme eines CIE für interstellare Medium (ISM) Plasmen ernstzunehmende Schwachstellen hat. Eine davon ist die Tatsache, dass kein astrophysischer Mechanismus bekannt ist, der es ermöglichen würde, die beobachteten Temperaturen dauerhaft zu halten. Eine andere Schwachstelle besteht darin, zu vernachlässigen, dass die dynamische und thermische Entwicklung heißer Plasmen miteinander gekoppelt ist.Es ist erwiesen, dass, sobald die thermische Evolution von ISM Plasmen berücksichtigt wird, eine weite Spanne an Beobachtungen prinzipiell durch die sogenannten Nicht-gleichgewichtsionisations (Non-collisional Ionization Equilibrium, NIE) Plasmen erklärt werden kann. Insbesondere für die LB war es möglich, die wesentlichen Beobachtungen durch ein Plasma mit einer Temperatur von 4.2×10^4 K und einer Elektronendichte von 2.4×10^{-2} cm^{-3} zu erklären. Um die Strahlung der LB genauer zu untersuchen, wurde ein Röntgenschatten-Experiment an einem dunklen Filament der OPHIUCHUS Molekülwolke in einer Entfernung von 125 pc durchgeführt, unterstützt durch die hohe Leistungsfähigkeit des ESA XMM-Newton Satelliten, seiner großen effektiven Fläche und seiner hohen spektralen Auflösung. Da dieses molekular Filament Säulendichten im Bereich von 10^{21} bis 10^{22} cm^{-2} hat, absorbiert es effektiv das meiste der weichen Röntgenhintergrundstrahlung unter 1.0 keV, was uns erlaubt die Röntgenemissionen, die innerhalb der LB Grenzen ihren Ursprung haben, von denen anderer galaktischer heißer Plasmen zu unterscheiden. Die Analyse des Röntgenschatten-Experiments am dunklen Filament zeigt, dass man durch spektrale Modellierung unter Verwendung der CIE-Bedingung für das LB Plasma eine Temperatur $T_e(LB) = 1.2^{+0.67}_{-0.61} \times 10^6$ K und eine Dichte $n_e(LB) = 0.017^{+0.025}_{-0.007}$ cm^{-3} erhält. Diese Analyse wurde durch eine andere Studie der diffusen Röntgenstrahlung, in der OPHIUCHUS entgegengesetzten Richtung (in die Richtung von TAURUS), ergänzt. Die Spektralanalyse der Röntgendaten in diese Richtung ergibt für die LB ein $T_e(LB) = 0.86^{+0.16}_{-0.11} \times 10^6$ K und ein $n_e(LB) = 0.016^{+0.005}_{-0.005}$ cm^{-3}. Die daraus für das Plasma erhaltenen Temperaturwerte unterscheiden sich stark von den in Richtung OPHIUCHUS gewonnenen Werten und bestätigen somit das Standardmodell der LB nicht. Nicht nur die Temperaturwerte stehen im Widerspruch, sondern auch die der Elektronendichten, die aus der vorliegenden Analyse abgeleitet wurden. Die Werte für die Elektronendichten unter Verwendung der Annahme des CIE sind viel höher als die Werte älterer Studien, die anhand von ROSAT Satellitendaten durchgeführt wurden. Die gegenwärtigen Ergebnisse unterstützen unzweifelhaft die Forderung nach einer Revision des Standardmodells der LB. Die eROSITA Mission (MPE) und zukünftige Röntgen-Observatorien wie XEUS (ESA), mit hoher effektiver Fläche und hoher spektraler

Auflösung, werden dafür qualitativ hochwertige Daten liefern. Im Besonderen werden sie hoch auflösende Spektroskopie ermöglichen und dadurch erlauben, spektrale Emissionslinien, vorhanden in Spektra galaktischer und intergalaktischer Plasmen sowie extragalaktischer Röntgenquellen, genauer aufzulösen. Diese Information ist von fundamentaler Wichtigkeit, um zwischen CIE und NIE Plasmen zu unterscheiden und folglich auch, um die Frage des physikalischen Zustands des LB Plasmas endgültig zu klären. Als Beispiel der Leistungsfähigkeit dieser Missionen verweisen wir darauf, dass z.B. die eROSITA CCD Detektoren in einem Energiebereich von 0.2–12 keV operieren werden, mit einer Energieauflösung von 54 eV bei 0.227 keV, mit 74 eV bei 1.5 keV und 134 eV bei 5.9 keV, wobei sie eine annährend hundertprozentige Quanteneffizienz im Energiebereich von 0.3–10 keV erreichen. Damit ist eROSITA ein sehr wichtiges Instrument für zukünftige Untersuchungen der diffusen weichen Röntgenstrahlung unserer Milchstraße und ebenso des restlichen bekannten Universums.

Contents

List of Figures

List of Tables

Chapter 1

The Interstellar Medium

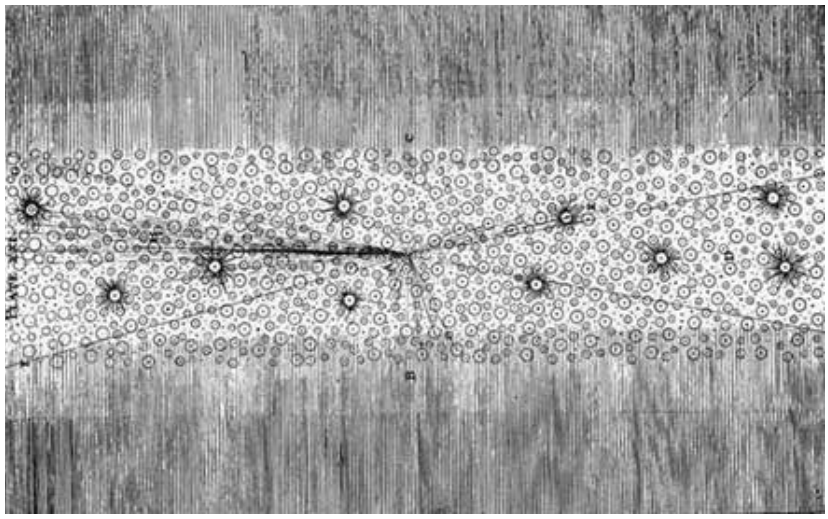

The Englishman Thomas Wright was one of the first to postulate a structure for the Milky Way. In his "An Original Theory or New Hypothesis of the Universe" (1750) Thomas Wright presents the hypothesis that the Milky Way is a spherical thin shell of stars. The apparent structure form would be the result of observing in different directions through the shell of stars. By looking along a tangent plane an observer would see many stars—The Milky Way—and by looking perpendicular to it much less.

" ... the ISM is like the ocean of a galaxy, a fluid confined by gravity to a thin layer, and serving as a reservoir for all of the material in the stars and planets that will ever form, evolve, and disperse."

Bruce G. Elmegreen [1]

In the ancient world a great number of myths flourished to explain the Universe. The ancient Greek civilization, one of many civilizations fascinated by the sky, developed elaborated myths to explain its origin and dynamics. In their mythology it was the milk from Goddess Hera's breast nourishing the Milky Way. It took about two millenia for the human thought to change from a purely mythological vision of the universe to a vision based on reason, with important contributions being given since the 17^{th} century.

The real departure from the magic understanding of the World, and in particular

of the Milky Way, only occurred with the arrival of the 20$^{\text{th}}$ century. During the 20$^{\text{th}}$ century a huge amount of astrophysical data was gathered and a theoretical framework appeared to interpret it. Only then, it was possible to tackle some issues regarding the physical processes taking place in the Milky Way Galaxy—by then, already an island universe—and in a larger extent, in the Universe.

In the modern astrophysical context, the Milky Way Galaxy is a physical system of extreme complexity. A truly understanding of the myriad phenomena taking place in it is of paramount importance, if we desire to know how the Galaxy as a whole works and interacts with its surroundings.

1.1 The Milky Way Galaxy

Over the last decades astronomers have collected substantial information about the Milky Way Galaxy, which has allowed them to elaborate a model of its structure and composition. Without going into great detail, a brief description of the present understanding of our Galaxy's morphology is given.

The Milky Way Galaxy is most easily defined by its optical content. This content is formed by stars.[1] They are found to agglomerate in a disc structure and in globular star clusters surrounding the stellar disc. These latter stellar systems form the so-called stellar halo component.

Different astronomical investigations have revealed that, in fact, the disc structure is composed by stars with different ages, speeds and chemical compositions, see e.g., Carroll and Ostlie [2]. These studies have shown, that these distinct stars are associated with different discs. Three stellar disc structures have been identified: A disc composed of young stars with a vertical scale height of Z $\sim$ 50 pc, where the current star formation occurs, is called the young thin disc. There is another thin disc, but composed by older stars with a vertical scale height of Z $\sim$ 325 pc, called the old thin disc. Finally, there is a disc made of much older stars, reaching a vertical scale height of Z $\sim$ 1.4 kpc (1 kpc $\equiv$ 1000 pc[2]) denominated as the thick disc. These discs form the galactic disc, which is a thin and fast rotating structure, consisting mainly of young and intermediate age stars. The stellar halo component is composed by very old stars and star clusters, a slowly rotating spheroid, gravitating the Milky Way Galaxy disc. Besides the stellar halo spheroid, there are other two spheroid components in the center of the Galaxy. The first is the bulge, primarily made of old stars and with a scale height of Z $\sim$ 2 kpc. The second, within the bulge, is the nucleus. If we ignore the contribution of matter filling the space between the stellar fluid component of the Galaxy, this is the visible content of the galaxy, made of known matter—the baryonic matter.

There is, however, plenty evidence, that some form of matter, of undefined nature, is present in the Galaxy and in other galactic systems. This type of matter only manifests itself by the gravitational pull on normal matter. This is the non-baryonic matter or the dark matter. The first suggestion of unseen matter was

[1] H II regions are also visible in the optical through the emission of Balmer lines.
[2] 1 pc = 3.0857$\times$10^{18} cm

done by Zwicky [3] to explain the stability of the Coma cluster. Later studies on the rotation curves of galaxies showed, that the visible matter was insufficient to explain these rotation curves. An invisible matter was invoked to explain their rotation curves anomaly. Until today all attempts to detect it directly have failed.[3] This "hidden" component is thought to have a spherical distribution around the center of the Galaxy. From the point of view of the Galaxy, the dark matter content is only important for understanding the dynamics and the formation of the Galaxy. Therefore in the present work, there will be no attempt to describe the interaction between the dark matter content and the baryonic content, for such is far beyond the scopes of this work.

The stellar disc content was found to flow through another and tenuous galactic component, the interstellar medium (ISM), made of gas in different physical phases, of dust and of Cosmic Rays (CRs).

The first indication that what we now call the ISM, was, indeed, a medium with matter and not a perfect vacuum, was the discovery of stationary absorption lines of ionized calcium (Ca II) in the spectrum of the spectroscopic binary δ Orion, Hartmann [6]. It only became clear that these lines were of interstellar origin and not of circumstellar origin after the work of Plaskett and Pearce [7]. By the time, with the development of better observational techniques, it became clear that the space between stars was far from being empty. Significant quantities of very tenuous material in homogeneously filled the interstellar space. The interstellar matter was found to exist in the form of gas and dust, mainly due to the way they affect the propagation of light in the interstellar space.

The ISM is the gas reservoir of galaxies, albeit it constitutes only a small fraction of their total mass. A percentage between 15 to 20 per cent of the Galactic disc mass rests in the interstellar medium reservoir. From this mass half is clumped into clouds, which only occupy 1 to 4 per cent of the total interstellar volume. The rest of its mass is distributed over the entire Galaxy, following approximately the distribution of the stellar content.

In order to put the present work into context, there is the need to describe in some detail, the present understanding of the ISM. The next section is a general and qualitative description of the ISM, mostly, from an observational point of view and focused on the hot ISM component. The remaining sections are concerned to give a brief description of several modern concepts of the ISM, viewed from a local to a more global Galactic perspective.

1.2 The observational ISM

From the beginning of last century to the present days, a huge set of observations has revealed, that the diffuse ISM is a very complex physical system. These observations have shown that the ISM is composed by three distinct and intermixed physical

[3]There is a recent claim of an "empirical detection" of dark matter, see Clowe et al. [4]. Others authors, Brownstein and Moffat [5], have seen evidence for a revision of the model used for the gravity.

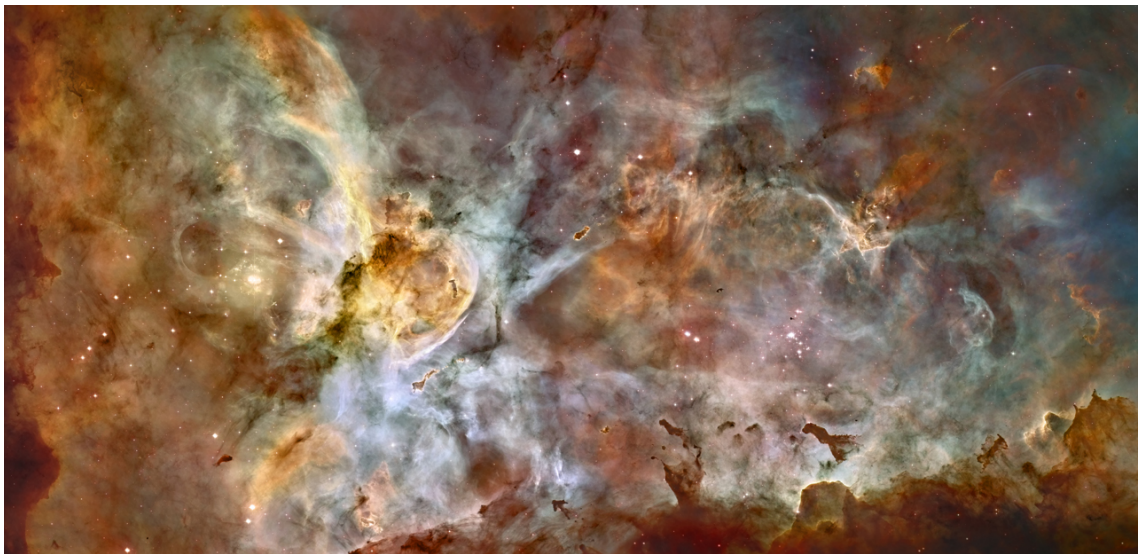

FIGURE 1.1: The Carina Nebula. From this image we can get a glimpse of the complex interaction between the three ISM phases. The different phases coexist simultaneously, with their different boundary regions defined by discontinuities of physical variables, such as temperatures and densities. This color image combines many exposures from Hubble Space Telescope's Advanced Camera for Surveys and NOAO/AURA/NSF Cerro-Tololo Interamerican Observatory's (CTIO) 4m Blanco Telescope and MOSAIC2 camera. Red corresponds to sulfur, green to hydrogen, and blue to oxygen emission. © NASA, ESA, N. Smith (University of California, Berkeley), and the Hubble Heritage Team (STScI/AURA).

phases, reflecting different thermal and ionization structures. Presently, it is known that, the ISM is composed by a multi-phase state, with a cold, a warm and a hot phase component.

In figure 1.1 a region of the Carina Nebula is shown, where the three-phase ISM coexists in a complex and delicate interaction. In this image one can have a glimpse of the myriad phenomena taking place in the ISM, in particular, of the presence of all different gas phases, from the cold dark clouds to the very hot ejected material from the Eta Carina Wolf-Rayet star (WR). The Eta Carina is a highly luminous and unstable star, with more than 100 $M_\odot$, showing ejected hot material with a bipolar form.

The typical values for the temperature and density, observed in our Galaxy, for the ISM phases are summarized in table 1.1. These different values were compiled from different sources. Even if these values differ slightly, they have, however, the same order of magnitude.

1.3 The Cold ISM phase

The first of the three ISM phases is the cold phase. In this phase we find molecular material, mainly in the form of molecular hydrogen (H_2), and neutral material in the form of atomic hydrogen (H I).

TABLE 1.1: Categorization of the Interstellar Medium: Typical values for the temperature and density in the multi-phase galactic ISM. Table adapted from different sources. (1) taken from Dopita and Sutherland [8], (2) taken from Ferrière [9] and (3) from Bland-Hawthorn et al. [10]. Some nomenclature regarding the different ISM phases: Cold Molecular Medium (CMM), Cold Neutral Medium (CNM), Warm Neutral Medium (WNM), Warm Ionized Medium (WIM), Hot Ionized Medium (HIM).

	Designation	T Kelvin (K)	n (cm^{-3})	P/k_B (cm^{-3} K)
Phase I -	CMM			
	H_2[1]	$\sim 10-75$	$\sim 20-2500$	~ 5000
	H_2[2]	$10-20$	10^2-10^6	~ 1000
	H_2[3]	15	200	~ 3000
	CNM			
	H I[1]	>100	$\sim 20-60$	~ 4000
	H I[2]	$50-100$	$20-50$	~ 2600
	H I[3]	120	25	3000
Phase II -	WNM			
	H I[1]	~ 6000	$\sim 0.3-1.0$	~ 3600
	H I[2]	$6000-10000$	$0.2-0.5$	~ 2800
	H I[3]	8000	$0.3^{(*)}$	2400
	WIM			
	H II Regions[1]	$\sim 8000-12000$	$\sim 0.15-1.0$	~ 10000
	H II Regions[2]	~ 8000	$0.2-0.5$	~ 5600
	H II Regions[3]	8000	0.15	~ 2400
Phase III -	HIM			
	H II[1]	$\sim 10^5-10^6$	$\sim 10^{-3}-10^{-2}$	~ 10000
	H II[2]	$\sim 10^6$	$\sim 6.5\ 10^{-3}$	~ 13000
	H II[3]	$\sim 10^6$	$\sim 2.0\ 10^{-3}$	~ 4000

$^{(*)}$Value uncertain by at least a factor of 2.

1.3.1 Molecular gas

This cold material is seen in absorption, but can also be traced by using indirect methods, such as the radio emission of molecules, like carbon monoxide. The typical orders of magnitude for the temperature and density, for the molecular component, are 10 K and 10^3 cm^{-3}, respectively, with a vertical galactic scale height $Z \sim 65$ pc [11]. The range of the observed values for these parameters can be found in table 1.1. Although this component represents a very small fraction of the total volume of the ISM, it represents ~ 30 to 60 per cent of its total mass. In general, this component is found in molecular clouds, bound by their self-gravity, with some of

their dense cores in gravitational collapse, breeding a new generation of stars. Most of the information of this cold component has been inferred from radio observations of the carbon monoxide (CO) molecule, which is a good tracer of the cold material found in the molecular H_2 form.

More recently, ultraviolet absorption line studies of this cold material have gained a new impetus with the launch of the Far Ultraviolet Spectroscopic Explorer (FUSE), in continuation of studies performed with the COPERNICUS satellite. These absorption studies are possible, because the H_2 molecule, in its electronic ground state, has many absorption lines in the ultraviolet (e.g., 900 Å - 1130 Å). In a recent survey [12] to high galactic latitudes, H_2 was detected in most of the lines of sight. The measured H_2 column densities range from $10^{14} - 10^{20}$ molecules cm^{-2}. These molecular material is normally designated by the acronym of CMM, meaning Cold Molecular Medium.

1.3.2 Neutral atomic gas

The second cold component is found in the form of neutral atomic hydrogen (H I), and is seen most readily in absorption. The absorption signature is better studied at the radio wavelength of 21-cm, using the H I velocity line profiles. In particular, the absorption at 21-cm, produced by the cold H I, is compared with the emission of 21-cm background.

This atomic component is extremely inhomogeneous, being concentrated in dense sheets, filaments or shells, occupying 1 to 4 per cent of the total ISM volume. Most of this cold H I is found close to the galactic mid-plane, forming a gaseous disc about 300 pc thick [11], roughly half of the height of the stellar disc of the Milky Way. However, since Lockman [13] it is known, that the H I reaches scale heights of about 1 kpc in the inner regions of the Galaxy, maintaining a constant value until the Sun position, about 8 kpc from the Galactic center, which is known as the Lockman layer. In contrary to the molecular clouds, this material is not gravitationally bound. Neutral cold gas is also found in the halo, with a velocity dispersion of 60 kms^{-1}, and at a scale height of the order of 4.4 kpc [14]. This cold material has typical temperatures T $\simeq$ 100 K and densities of the order of $\sim$ 10 cm^{-3}. Again, table 1.1 shows typical values for this cold H I. To this physical component normally the designation of cold neutral medium (CNM) is attributed.

1.4 The Warm ISM phase

The second phase of the ISM is composed by warm material. In this phase we find warm H I and warm ionized hydrogen (H II).

1.4.1 Warm atomic gas

The warm H I is most easily detected through its 21-cm radio emission. This warm hydrogen occupies a reasonable fraction of the total ISM volume, $\sim$ 30 per cent. A

typical value for the density is $> 1.0\,\mathrm{cm}^{-3}$ and $\mathrm{T} \sim 6000 - 10000\,\mathrm{K}$. This warm H I is found mainly in photodissociation regions. For a review on photodissocation regions see the article from Hollenbach and Tielens [15]. This phase is a major radiative energy sink, since the heating requirements are considerable. This warm material is usually named as the warm neutral medium or simply WNM.

1.4.2 Warm ionized gas

The presence of ionized hydrogen (H II) in the Galaxy has for a long time been associated with the so-called Strömgren spheres [16]. The Strömgren spheres are surrounding photo-ionized regions associated to the intense radiation photon fields from early type OB stars. These early type stars produce tremendous amounts of ultraviolet radiation capable of ionizing the H I atoms, therefore producing the Strömgren spheres. The sizes of the Strömgren spheres are determined by the position at which the rate of recombination equals the rate of photoionization.

For some time this phase was thought to be located on the interfaces between the cold H I clouds and the really hot coronal gas. We now know, that these Strömgren H II regions represent only about 10 per cent of the ionized hydrogen in the Galaxy. In fact, about 90 per cent of this diffuse ionized hydrogen is found in the form of a warm ($\sim$8000 K), low density ($\sim$0.16 cm^{-3}), fully ionized regions, filling about 20 per cent of the ISM volume within a 2 kpc thick layer about the Galactic plane [17, 18]. The idea of the existence of a warm, diffuse and extended layer of H II, surrounding the Galactic disc, was put forward by Hoyle and Ellis [19] to explain some peculiarities on the Galactic synchrotron emission background in the low radio frequencies range. Direct evidence of this phase only came with the discovery of pulsars and with studies of the dispersion measures of the electron density. This warm ionized medium (WIM), also known as the Diffuse Ionized Gas (DIG), is now recognized as a major component of the interstellar medium.

The space average mid-plane density of the WIM, determined by dispersion measurements ($\mathrm{DM} \equiv \int \mathrm{n_e dl}$) toward pulsars, is $\simeq 0.03\,\mathrm{cm}^{-3}$. The column density of H II towards these pulsars is 0.8 - 1.4 $\times$ 10^{20} cm^{-2}. When combined with the mid-plane density, this gives a scale height of $\simeq$ 1 kpc. While in the Galactic mid-plane, the space average density of H II represents less than 5 per cent of that of the H I, the large scale heights of the H II mean that, the total column density of H II may represent between 25 to 50 per cent of that of the H I, implying that at $\sim$ 1.0 kpc the H II may be the predominant gas. Neither the source of ionization, nor the relationship between this gas and other components of the medium (e.g., H I) is really understood. The inferred average ionization rate from the high Galactic latitude H_α background is 5 $\times$ 10^6 H-ionizations s^{-1} per square centimeter [20], which implies an energy input of 10^{-4} erg s^{-1} cm^{-2}. The H II was also observed to be present in a large scale in our own Galaxy [21], now known as the Reynolds layer. The temperature of the Reynolds layer is $\mathrm{T} \sim 6000$ K and it has an average density of $\sim 0.3\,\mathrm{cm}^{-3}$. In terms of volume this represents 15 per cent of the total ISM volume. As for the warm neutral hydrogen, the heating process of the Reynolds layer is considerable of the order of 10^{-24} erg cm^{-3} s^{-1}. However, the nature of the heating source is still uncertain. Observations performed on external galaxies have

shown that there is also a diffuse, extended warm component, occupying filaments, clouds, bubbles and chimneys. This can be seen in H_α and in other optical lines. More recently, the same kind of structures has also been observed in the Milky Way Galaxy [22, 23, 24, 25].

1.5 The Hot ISM phase

The third phase of the ISM is composed by hot gas. The most usual designation for this phase is the hot interstellar medium or HIM. The first direct indication of the presence of a widespread hot gas was given with the discovery of diffuse emission in soft x-rays (< 1 keV), by Bowyer et al. [26]. In 1974 Jenkins & Meloy and York observed with the COPERNICUS satellite absorption lines of O VI [4] (at 1031.93 Å and 1037.62 Å) in many lines of sight, due to a hot interstellar gas. Other absorption lines produced by N V and C IV ions, have also been detected. Inoue et al. [27], Schnopper et al. [28] and, more recently, Sanders et al. [29] have claimed the detection of x-ray emission lines from the interstellar ions of O VII, O VIII and other ions. Another strong confirmation of the presence of hot gas in the halo of the Galaxy came with the launch of the Röntgensatellite [30] (ROSAT) and the observation of x-ray shadows in the soft energy bands, i.e. C band [100 - 300] eV, [31, 32]. The assumed temperature for this phase ranges from 10^5 to 10^6 K. The density of this gas is $< 10^{-2}\mathrm{cm}^{-3}$ with a scale height of $Z \sim 2.4 - 5.0$ kpc [11]. These temperatures are assumed to be maintained by consecutive supernova explosions and by violent stellar winds. Stellar photons, even from OB stars, cannot ionize the gas to such high ionization degrees. For example, to ionize O V into the O VI ion requires a photon with an energy of 113.9 eV ($T \sim 1.32 \times 10^6$ K), an energy that stellar photons do not possess.

Collisional ionization is the physical mechanism assumed to be responsible for ionizing the gas. Since in collisional ionization equilibrium (CIE)[5] 10^6 K gas has a long cooling time, it can occupy a considerable fraction of the total volume of the ISM. In the galactic plane, this ionized gas is relatively confined mostly within giant H II shell regions, supernova remnants and superbubbles — large multi-SN complexes. There, it becomes observable in soft x-rays. The buoyancy effects tend to bring this ionized gas through channels, surrounded by the denser and cooler ISM, in what it is called galactic chimneys.

In the halo and after cooling down, it can be detected in the ultraviolet (UV) by absorption of highly ionized species (e.g., C IV, Si VI, N V and O VI, just to mention the most important) against distant and bright background sources—like early-type O and B stars or quasars. The scale height of O VI above the disc is very high, from 2.3 ± 0.4 kpc [33]. However, a recent analysis on the distribution of O VI in the gaseous Galactic halo has shown, that the scale height of this ion may range from 1.0 and 10.0 kpc [34].

[4] In spectroscopy ionization stages are counted in Roman numerals, starting with I for neutral atoms, II for simply ionized ions, and etc.

[5] See Chapter 2.

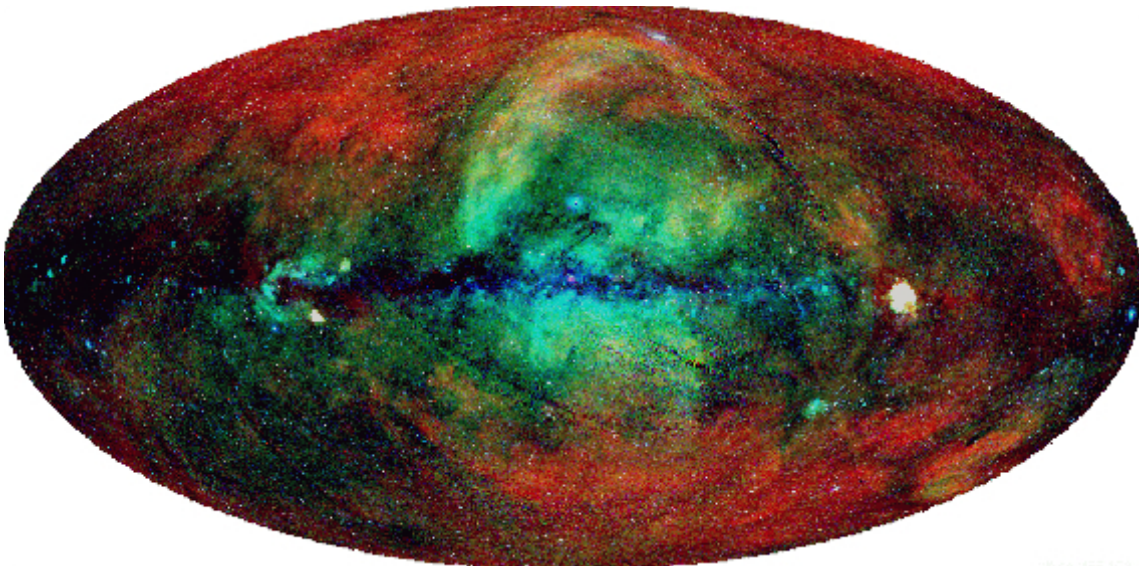

FIGURE 1.2: ROSAT PSPC All-Sky Survey maps completed. The energy range of 0.1-0.4 keV (R1+2) was coded as red, the energy interval of 0.5-0.9 keV (R4+5) as green, and the energy band of 0.9-2.0 keV (R6+7) as blue. © M.J. FREYBERG, R. EGGER (1999), Max-Planck-Instituts für extraterrestrische Physik (MPE).

For ions with low ionization potentials it is still higher, 3.9 ± 1.4 kpc for the N V (77.5 eV), 4.4 ± 0.6 kpc for the C IV (47.9 eV), and 5.1 ± 0.7 kpc for the Si IV (33.5 eV) [33]. The increase of the scale heights of the ion sequence, O VI, N V, C IV and Si IV provides information about the change of ionization state of the gas with distance from the Galactic plane. Several hybrid models were developed to try to explain these observational results. In the model of Shull and Slavin [35] the highly ionized ions at low |Z| are mainly produced by isolated supernova remnants (SNRs), while those at high |Z| are found in radiatively cooling superbubbles that break-up through the disc. In the case of the hybrid model proposed by Ito and Ikeuchi [36], the ionization structure is the result of hot collisional ionized gas due to the Galactic fountain flow in conjunction with photoionization from the extragalactic background.

Bowen et al. [37] using the FUSE satellite in conjunction with the COPERNICUS data found, that in the mid-plane the average density of O VI is 1.7×10^{-8} cm^{-3}. Perpendicular to the plane, Savage et al. [38] found a patchy structure for the O VI ion, with the column density ranging from 0.6×10^{14} to 3×10^{14} cm^{-2}. The large values were mostly observed in the northern sky. The median values observed in the northern and southern skies were 1.8×10^{14} and 1.1×10^{14} cm^{-2}, respectively.

In figure 1.2 the ROSAT All-Sky Survey maps are presented, showing the x-ray emission, which traces the very hot ISM phase component. The x-ray emission associated to ISM gas with temperatures (k_BT) in the range of 0.1 - 0.4 keV, is shown in red. The x-ray emission, color coded in green, traces hot plasma, emitting in the 0.5 - 0.9 keV energy range. The blue color was associated to the x-ray emission in the 0.9 - 2.0 keV energy band.

1.6 Concepts of the ISM

Several concepts of the ISM have been developed to accommodate the available observational data from the last five decades. The first suggestion of the presence of different phases in the ISM was made by Spitzer [39], who postulated the existence of a Galactic hot corona to confine the observed H I clouds at high Galactic latitudes.

The first real advance in understanding the ISM as a physical system with multiple components was done with the work of Field et al. [40]. In their work the ISM is an ensemble of two gas phases, which are in thermal pressure equilibrium with a mean pressure of $p/k_B \approx 1000$ K cm^{-3}. The cold gas phase was assumed to be in cold molecular clouds, with mean densities n ~ 100 cm^{-3} and temperatures of T ~ 10 K, embedded in a diffuse and warm, partially ionized, intercloud medium. The derived density and temperature values for this warm phase were n ~ 0.1 cm^{-3} and T $\sim 10^4$ K, respectively. When this theoretical model for the ISM was proposed by Field et al. [40], it represented a great advance in understanding the ISM, because it could explain all available data. All available observational data had been obtained in the radio—through the 21-cm radio emission line—and at optical wavelengths. However, soon after, a new set of observations showed, that this concept was incomplete.

Measurements of the soft x-ray background (SXB) [41] and the presence of ubiquitous O VI absorption lines [42, 43, 44] required large amounts of hot and low density gas in the disc of the Galaxy. Another observational evidence for the presence of very hot gas in the ISM was the detection of the emission line of Fe XIV from the Cygnus Loop region [45], requiring a temperature of about 2×10^6 K for the gas.

McKee and Ostriker [46], supported by these observations, induced a conceptual change on the ISM paradigm. In their model, the ISM is an inhomogeneous cloudy medium, heated to very high temperatures in local regions by supernova explosions. These explosions evaporate clouds, which will alter the evolution of the supernova remnants. During this process the temperature of the hot gas decreases as it expands, and it gains mass. As the density increases as a result of cloud evaporation, the radiative losses increase with contribution of radiation coming from the conductive interfaces between the clouds and hot gas. The highly ionized O VI ion, observed in absorption, would then arise from these conductive evaporating layers. Finally, this hot gas is able to radiate the supernova energy when the temperature has dropped to a few hundred thousand Kelvin. Conservation of mass and energy determine the density and temperature of the hot medium, with typical values of ~ 0.003 cm^{-3} for density and $\sim 5 \times 10^5$ K for the temperature. The outer layers of the clouds, subjected to intense UV and soft x-ray radiation fields, would then, ionized, provide the warm ($\sim 10^4$ K) and neutral components of the ISM. In this model the ISM is composed by three thermal components, a three phase ISM.

A few years before Cox and Smith [47] had studied the impact of isolated supernovae remnants, with an initial energy of $\sim 4 \times 10^{50}$ ergs, expanding in a homogeneous interstellar medium with an ambient density of n ~ 1.0 cm^{-3}. They found, that during the early expansion of the remnant, a diffuse and heated material would

be formed inside the shell remnant. The temperature associated with this hot gas was found to be of the order of $T \sim 10^6 - 10^8$ K. This model predicted that, the hot gas would radiate hard UV and x-ray photons for a period of $\sim 4 \times 10^6$ years.

Two decades later Slavin and Cox [48] elaborated a different model for the ISM. In this model such disruptive events like supernovae were isolated events, occurring in the warm ISM phase. These catastrophic events did not disrupt the warm medium, as argued by McKee and Ostriker [46], and the O VI, found in absorption line studies, could be explained by the existence of old and invisible remnants. More recently, a huge amount of work has been done by de Avillez and Breitschwerdt [49] and de Avillez and Breitschwerdt [50] to study the production of O VI using numerical magnetohydrodynamics (MHD) simulations, see §§ 1.8.2.

In the following subsections a brief description of the astrophysical mechanisms, responsible for creating the warm and hot phases, as well as for shaping their evolution, is presented.

1.7 Stellar Feedback

The main physical mechanisms of energy input into an ISM are the stellar mass loss, e.g. stellar winds, a rather constant ultraviolet photon field due to O and B stars, jets, and supernova explosions.

All types of stars, in different degrees, contribute to transfer energy into the ISM in the form of stellar winds. But, by far, the most important ones, producing strong winds, and therefore producing a big impact on the ISM, are the early-type O and B stars. These stars have strong winds, which give rise to extended hot bubbles due to the shock between the stellar winds[6] and the surrounding ISM. When this energy is integrated over their main sequence lifetime, this energy output corresponds to 30 per cent of the energy released by a type II supernova. These same stars also produce a huge amount of energetic photons, having their emission peak in the UV domain, injecting a substantial amount of energy on the creation of H II regions. However, by far the most efficient energy and momentum input into the ISM are cataclysmic events, such type I[7] and type II[8] supernovae explosions.

1.7.1 Stellar Photoionization

The early-type OB stars produce UV photons, because their black body emissivity peak intensity is in the UV spectral region, which reflects their high surface tem-

[6]Mechanical wind luminosity of the order of 10^{36} erg is a typical value for the energy output rate of stellar winds, produced by early type stars (OB).

[7]Occurs when the mass deposited in the surface of a white dwarf or neutron star (which is part of a binary system) exceeds the Chandrasekhar limit and begins to burn carbon degenerately, causing an explosion.

[8]Type II supernovae occur when the iron core of a massive star collapses due to gravity. This causes the outer layers to fall inwards, bounce off the core, and explode outwards as a supernova. Type II supernovae are characterized by the lack of hydrogen lines in their spectrum. Type II supernovae are also characterized by the emission of neutrinos (produced by the collapsing core of the star) just before the explosion.

peratures (T $\sim$ 20000 - 50000 K), see e.g. [51, 52]. These UV photons have a big impact on the surrounding medium of the star, because they have energies able to ionize the H I and even the He I atoms. Photons with energies $\geq$ 13.6 electron Volts (eV) (λ $<$ 912 Å) ionize the H I and photons energies $\geq$ 24.6 eV (λ $<$ 504 Å) ionize the He I. These atoms are photoionized by these energetic UV photons, creating the so-called Strömgren sphere around the O or B star, an astrophysical phenomenon that was first investigated by Strömgren [16].

The volume attainable by these photoionization H II systems depends on the distance from the star at which the rate of recombination of H II with electrons, equals the rate of photoionization and the ambient density. The distance of the star, at which this occurs, is given by the Strömgren sphere radius R_S

$$R_S = \left(\frac{3}{4\pi} \frac{S_\star}{\alpha\ n^2} \right)^{1/3} = 64.7 \left(\frac{S_{49}}{n^2} \right)^{1/3} \text{pc} \tag{1.1}$$

where the radiative recombination coefficient $\alpha = 3 \times 10^{-13}$ cm^3 s^{-1}, S_{49} is the number of photons able to ionize the H I in units of 10^{49} photons per second, and n is the ambient density in units of 1 particle per cm^3.

The number of photons, able to ionize the H I or He I, have been investigated by several authors, for instance Panagia [51], Sternberg et al. [52] or more recently by Smith [53]. With this information we can estimate the amount of energy (E) transferred into the ISM around an early-type star. Each of the photons (S_{49}) has an energy of 13.6 eV. Therefore, we can integrate this flux of photons over the star main-sequence lifetime ($\tau_{\rm ms}$), to find, that the total radiated energy is

$$E = 6.86 \times 10^{51}\ S_{49}\ \tau_{\rm ms}\ \text{erg} \tag{1.2}$$

with $\tau_{\rm ms}$ in units of 10^6 years. As an illustrative example, the energy input from a B0 V star is $3.1{\times}10^{51}$ erg, with S_{49}=0.05 [53] and $\tau_{\rm ms}$ = 9 [54]. The radiative feedback of these early-type stars, amounts to 10^{51}-10^{52} erg which is comparable to the kinetic energy of typical SN explosions. The estimated energy deposition of such a star in the Galactic volume[9] is $2.6{\times}10^{-30}$ erg s^{-1} cm^{-3}. Abbott [55] has estimated the total amount of ionizing radiation, due to early type stars, in the Galactic disc to be $\sim$ 1.6×10^{-25} erg s^{-1} cm^{-3}. In another words, the transfer of the photon energy into kinetic energy of the gas is $\lesssim$ 1 percent.

1.7.2 Stellar Winds

For more than thirty years it is known that, when stars are above certain luminosity thresholds they start to have winds, driven by radiation. A recent review on this subject can be found in the article of Kudritzki and Puls [56]. For stars of intermediate and low mass (M $\leq$ 8 M$_\odot$), when they evolve through the post-AGB phase towards the white dwarf final stage, an analogous threshold exists. For this kind of objects, and objects more massive than 0.58 M$_\odot$ or more luminous than $10^{3.6}$L$_\odot$, a

[9]The Galactic volume is assumed to be given by the cylinder of $[\pi(15\ \text{kpc})^2 \times 2 \times 0.1\ \text{kpc}]$.

wind is also present. The terminal velocity of such a wind is a function of the effective temperature of massive stars, with some dependence on the luminosity class. The wind values can range from 3200 km/s for O3 V stars to 160 km/s for A1 Ia stars. Therefore, it is expectable that these stellar winds have a strong impact on the surrounding ISM. The study of the impact of stellar winds in the ISM started with the work of Dyson and de Vries [57]. This work has shown that a bubble, surrounding the star, will be formed.

The structure and evolution of stellar wind-bubbles (SWB) have been investigated —in greater detail—in the classical papers of Castor et al. [58] and Weaver et al. [59], respectively. These authors have obtained analytic and numerical solutions for the initial adiabatic stage, for the intermediate, and for the late stage of strong radiative cooling stellar winds.

The basic assumptions of the stellar wind are a steady outflow and spherical symmetry. In this model, the structure of the bubble is mainly determined by the wind luminosity L_w, which is a function of the star mass loss $\dot{M}$ and the wind velocity v_w. This relation reads,

$$L_w = \frac{1}{2}\dot{M}v_w^2 \tag{1.3}$$

This wind then collides with a homogeneous ISM with a particle density n_0. In the case analysed by Weaver et al. [59], the SWB is produced by an O 7 I type star, with a $\dot{M} = 10^{-6} M_\odot$, where $M_\odot$ means one solar mass, and with a $v_w = 2000$ km s^{-1}, embedded in an ISM with a n_0=1 cm^{-3}. The former values imply a $L_w \simeq 1.3 \times 10^{36}$ erg s^{-1}.

Their analysis has revealed that circa 10^6 years after the initial wind outflow, a multi-layer wind bubble will be formed. This multi-layer bubble structure is composed of four regions. In figure 1.3 the stellar wind bubble structure due to Weaver et al. [59] is depicted.

In an evolved SWB system, the first region (A) is the zone immediately adjacent to the star. In region A the wind expands freely, maintaining a constant temperature, but with decreasing particle density. After 10^6 years the region A has expanded to a radius of 6 pc, where it encounters a shock front R_1 of hot gas, moving in the opposite direction. Region B is composed by gas from the wind, that has been heated by the shock front at R_1, creating a layer with a radius of about 22 pc from hot gas. The prevailing physical conditions of this hot gas are a temperature lying in the interval of $10^{4.7}$ to $\sim 10^7$ K, and a particle density from about 10^{-4} to $\sim 10^{-1}$ cm^{-3}. Region C is a shell of interstellar and heated gas, swept up by the shock wave, where ionized hydrogen H II is found. This region is separated from the ambient and undisturbed ISM by the shock front R_2, and from the hot wind by the discontinuity layer R_{CF}. After one million years, the shock front R_2 has reached a radius of about 27 pc.

The thickness of the "discontinuity" layer R_{CF} depends on physical effects, such as the thermal conductivity and evaporation at the interface between the hot and cold gas. If these effects are taken into account, then an interface layer will be formed. The structure of this interface layer is governed by electron thermal conduction of heat from region B into the region C. Within this interface layer (R_{CF}) at a distance of ~ 2 pc from the shell of warm H II (region C) the gradient temperature varies steeply

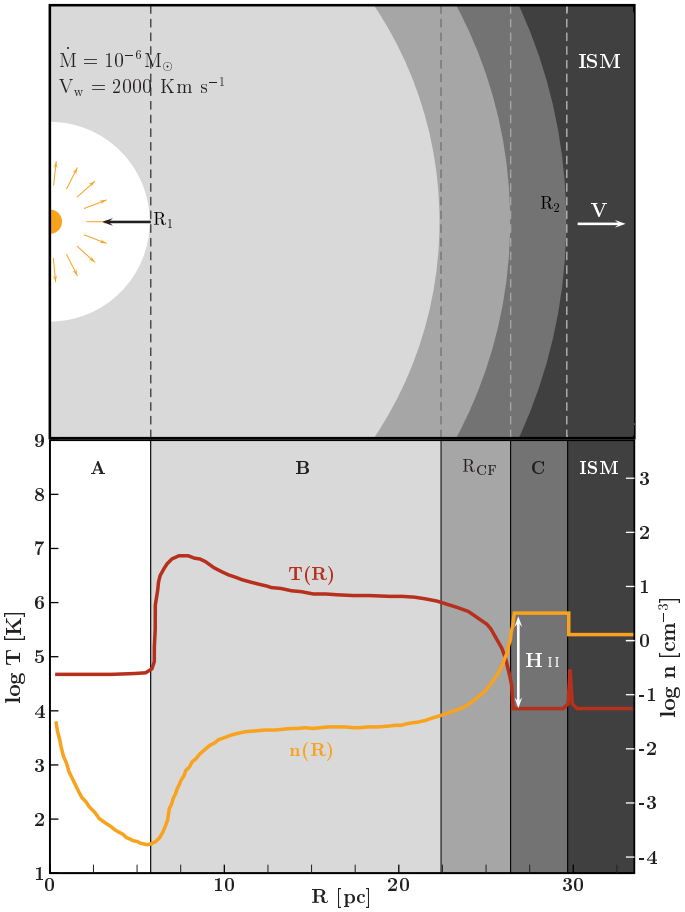

FIGURE 1.3: Stellar Wind Bubble. The two left plots show the calculations performed by Weaver et al. [59] to study a typical stellar wind bubble, produced by a star with a wind luminosity L_w=1.3×10^{36} ergs s^{-1}, and embedded in an ISM with a particle density of n_0=1 cm^{-3}. These plots show the temperature (T) and density (n) profiles for such a wind bubble, after evolving over 10^6 yrs. Four shells are created in a stellar wind bubble. Region A is the zone where the wind expands freely. Region B corresponds to hot gas, heated by the termination shock wave R_1. In between this hot gas region and the H II shell, region C, a conduction front (CF) transports the heat, if the physical effects of conductivity and evaporation are considered.

from $\sim 10^6$ to 10^4 K. In this interface layer, highly ionized species are present. Due to collisional excitation of this ions, about 40 per cent of the conductive heat flux is radiated away in this zone. The remaining 60 percent are employed in evaporating the material of region C. If the effects of thermal conductivity and evaporation are not considered, then this interface layer "collapses" into a contact discontinuity.

The evolution of SWB is composed by three stages. In the first stage, the bubble expands so fast, that radiative losses of the gas are negligible, which allows the system to evolve adiabatically. In the second evolution stage of the SWB system, energy losses in the region C become comparable to the energy input of the stellar wind. The material from this region collapses due to radiative cooling, forming a warm shell. This shell is observable as a ring emission nebula in the optical and radio. In the third and final stage, region B is reduced to a thin layer, and the free expanding stellar wind interacts directly with the swept up interstellar gas in region C.

1.7.3 Supernova explosions

Stars with masses M $\gtrsim 8M_\odot$ inject energy into the ISM through the photoionization processes and through their strong stellar winds, during a relatively long time, as seen in the previous §§ 1.7.1 and §§ 1.7.2. They also inject a tremendous en-

ergy instantaneously, by the end of their evolutionary life, when they collapse and subsequently explode as supernovae.

During a supernova explosion (SNe) a typical energy of 10^{53}erg is released. From this energy only one per cent (10^{51}erg) is transformed into mechanical energy. The energy of 10^{51}erg provides the kinetic energy to form a supernova remnant (SNR), to govern its expansion and to heat the SNR interior. The remaining 99 per cent of the energy of the SNe is radiated away in the form of neutrinos. It was estimated [e.g., 60] that an average energy of 10^{42} erg s^{-1} is released by SNe into the ISM of our Galaxy.

The evolution of a SNR can be divided into four phases [61]. The work from Cowie et al. [60] has been used here, to show the several evolution phases of a SNR, see figure 1.4.

In the initial phase the SNR expands freely–the free expansion (FE) phase–with the expansion rate controlled by the conservation of the kinetic energy. This phase lasts only ∼100 to 1000 years, until the moment, when the mass of the SNR exceeds the ejected mass (M_{ejec}) of the progenitor star. During this phase the radius and velocity of the SNR are described by the following equations,

$$R_{SNR} = V_{SNR}\ t \tag{1.4}$$

$$V_{SNR} \simeq \sqrt{\frac{2E_{kinetic}}{M_{ejec}}} = 10^4\ M_{ejec}^{-1/2} E_{51}^{1/2}\ [\mathrm{km\ s^{-1}}] \tag{1.5}$$

When the amount of circumstellar material, swept-up by the shock front, equals the ejected mass, then the dynamics of the SNR enters a different evolution phase: the Sedov-Taylor phase. At this evolutionary point $M(t)_{SNR}=4/3\pi\rho_0 R_{SNR}^3 \equiv M_{ejec}$, therefore,

$$R_{SNR} = \left(\frac{3\ M_{ejec}}{4\pi\mu\ n_0\ m_H}\right)^{1/3} = 2.13\ \mu^{-1/3}\ n_0^{-1/3}\ M_{ejec}^{1/3}\ [\mathrm{pc}] \tag{1.6}$$

$$t = 208\ \mu^{-1/3}\ n_0^{-1/3}\ M_{ejec}^{5/6}\ E_{51}^{-1/2}\ [\mathrm{yr}] \tag{1.7}$$

where μ is the mean mass per particle, and n_0 is the particle density in units of cm^{-3} of the ambient ISM. E_{51} is the energy of the supernovae in units of 10^{51} erg, and M_{ejec} is ejected material given in solar mass ($M_\odot$) units. A recent investigation of Ellison et al. [62] and references therein, have studied in some detail, the thermal and the non-thermal radiation as well as the particle acceleration in this short phase.

The second phase occurs when the SNR total mass surpasses the ejected material. This phase, known as Sedov phase [63] or Sedov-Taylor phase, lasts for about ≲10000 years. During this period the remnant is bound by the discontinuity front of the shock wave, and the interior gas of the SNR has been heated by the reverse shock. As before, the expansion rate is still controlled by energy conservation, and radiation losses can still be neglected. At this stage, the radius and velocity of the SNR are governed by the following similarity solutions,

$$R_{SNR}(t) \simeq 1.15\ \left(\frac{E_{kinetic} t^2}{\rho_0}\right)^{1/5} = 11.63\ \mu^{-1/5}\ n_0^{-1/5}\ E_{51}^{1/5}\ t_4^{2/5}\ [\mathrm{pc}]$$

$$V_{SNR} = \frac{dR_{SNR}(t)}{dt} = \frac{2}{5}\frac{R_{SNR}(t)}{t} = 455\ \mu^{-1/5}\ n_0^{-1/5}\ E_{51}^{1/5}\ t_4^{-3/5}\ [\mathrm{km\ s^{-1}}] \tag{1.8}$$

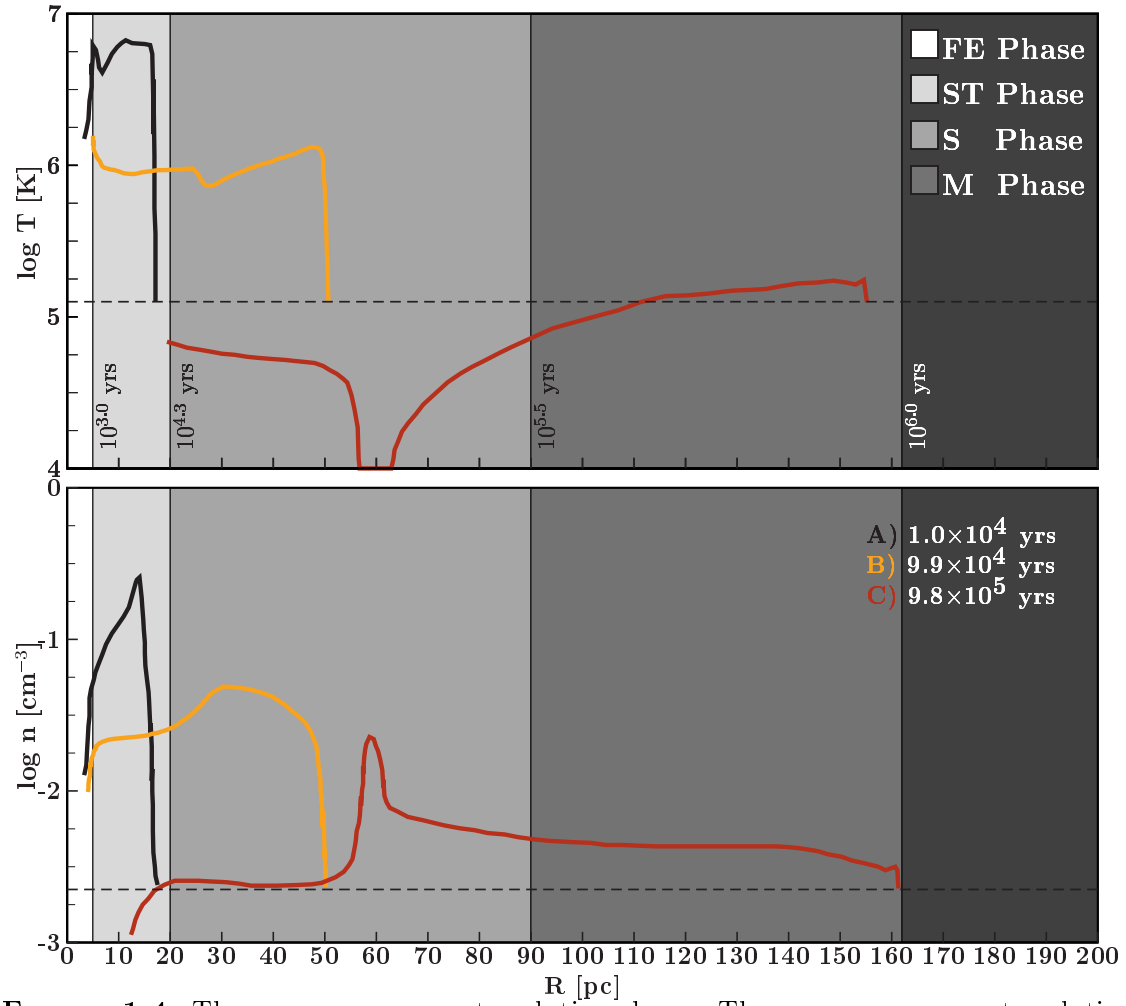

FIGURE 1.4: The supernova remnant evolution phases. The supernova remnant evolution is composed by four phases: the free expansion (FE □) phase, the Sedov-Taylor (ST ■) phase, the snowplow (S ■) phase, and the merging (M ■) phase. In the plot these different phases are represented by different colors, representing the radii and the times at which these transitions occur. The values of the radii and times for these phase transitions were taken from Cowie et al. [60], which follow the definitions given by Woltjer [61]. The typical physical parameters, studied in the evolution of the SNRs, are: the radius, the temperature, the density and the velocity. In these plots only the dependence of the temperature and of the density, as a function of the radius, are presented. As a representative example of a SNR evolution, the numerical model 1 from Cowie et al. [60] was chosen. The evolution of model 1 is depicted at times: 1.0×10^4 yrs (A), 9.9×10^4 yrs (B), and 9.8×10^5 yrs (C). The initial conditions of model 1 are: an energy of $\sim 3.1 \times 10^{50}$ erg, an ambient particle density of 2.4×10^{-3} cm^{-3} and an ambient temperature of 1.4×10^5 K.

where t_4 is the SNR evolution time in units of 10^4 years. The phases which have more relevance to the present work are the snowplow-phase and the merging phase of the SNR. As the remnant expands adiabatically, the temperature of the plasma inside of the SNR decreases due to the expansion process. When the temperature of the plasma reaches a temperature in which radiative cooling becomes an important physical process, then the evolution of the SNR enters a new phase.

The third phase is denominated as the snowplow (S) phase [64]. This stage has a duration of 10000 to 100000 years. At this evolution point the swept-up mass collapses into a thin, dense layer, with the interior of the SNR expanding adiabatically (dW=-PdV). The expansion is driven by momentum conservation and the dynamics of the SNR evolution is now governed by the following expressions:

$$\mathrm{R_{SNR}(t)} = \Big(\frac{147\ \epsilon\ \mathrm{E_{51}(S)\ R^2_{SNR}(S)}}{4\pi\rho_0}\Big)^{1/7}\ \mathrm{t}^{2/7} \tag{1.9}$$

where ϵ is the fraction of internal kinetic energy of the SNe, still available to conduct the SNR evolution at this point. The available internal kinetic energy fraction is normally of the order of $\epsilon \sim 0.2 - 0.3$. $\mathrm{R(S)_{SNR}}$ is the radius at the beginning of the snowplow-phase, and is given by $\mathrm{R(S)_{SNR}} = \mathrm{K\ E_{51}^{0.29}\ n_0^{-0.41}pc}$. Different authors have presented distinct values for the constant K. Cox [64] has derived a value of 25 for K, Chevalier [65] found a value of 19 and Falle [66] obtained a value of 20. The difference in the value of K results from using distinct cooling functions, only. The velocity of the SNR is now given by

$$\mathrm{V_{SNR}} = \frac{2}{7}\frac{\mathrm{R_{SNR}(t)}}{\mathrm{t}} \tag{1.10}$$

The fourth and last phase of the SNR is, when the internal pressure of the gas inside of SNR becomes less than the surrounding ISM pressure. When this happens the SNR merges with the ISM and the SNe energy has been dissipated in the ISM. McKee and Ostriker [46] have estimated the maximum lifetime of a SNR before it merges with the ISM. They found, that the maximum lifetime of a SNR is given by

$$\mathrm{t_{max}} = \ 7 \times 10^6\ \mathrm{E_{51}^{0.32}\ n_0^{0.34}}\ \left(10^{-4}\mathrm{P}\right)^{-0.70}\ \mathrm{years} \tag{1.11}$$

where $\mathrm{P} = \mathrm{P_0/k_B} = \mathrm{n_0 T_0}$ is the pressure of the surrounding ISM. For $\mathrm{E_{51}} = 1$, with an ambient ISM density $\mathrm{n_0} = 1\ \mathrm{cm^{-3}}$ and a temperature of $\mathrm{T_0} = 8000$ K, this would happen after $\mathrm{t_{max}} \sim\ 8.2 \times 10^6$ years. A similar calculation, using the values of model 1 from Cowie et al. [60], gives a $\mathrm{t_{max}} \sim\ 6.7 \times 10^6$ years. At this moment the ISM is enriched with new heavy elements, produced during the explosion of the massive star.

1.8 Concepts of the ISM - Global

The former ideas that have been applied to understand the interaction between stars and the ISM locally and in the galactic disc, have also important physical implications at different galactic scale heights. Several concepts have been developed to explain the presence of the hot gas in the halo of the Milky Way Galaxy. For recent reviews on this issue see the articles of Spitzer [67] and Cox [68].

Following Cox [68], the global galactic model—an idealized and simplified model—of the hot ISM component can be described in three steps. First, the explosion of a supernova ejects a rapidly expanding shell, whose interaction with the surrounding medium creates a hot gas. Second, as the gas expands, it encounters clouds, which

are compressed, heated by conduction, and disrupted or evaporated, creating shells. The presence of physical processes, like conduction and evaporation in the SNRs, leads to the creation of multi-charged ions such as, C IV, O VI, N V and Si IV, which leads to the creation of absorption lines in the far-UV. In the third, and final step, the remnant of heated gas of one or more supernovae can rise to appreciable distances from the galactic plane and may produce a hot galactic corona before if falls back —after cooling— or escapes the Galaxy completely. In reality these different processes interact so much with each other, that any serious model must incorporate them in a self-consistent way.

There are two important characteristic time scales of this process [69, 70]. The first is the time required for the hot uprising gas, to acquire a pressure equilibrium with the ambient medium, which is given by the sound crossing time,

$$\tau_{\rm s} \sim \frac{\rm h}{\rm c_s} \sim 2.8 \times 10^7 \Big(\frac{\rm T}{10^6}\Big)^{1/2} \tag{1.12}$$

where h is the isothermal scale height, and $\rm c_s$ is the sound speed at a given temperature T in K. The second is the time for the hot gas to cool down radiatively, which is given by

$$\tau_{\rm cooling} = \frac{3}{2}\frac{\rm n k_B T}{\Lambda(\rm T)} \approx 2.4 \times 10^8 \Big(\frac{\rm n}{10^{-3}}\Big)^{-1} \Big(\frac{\rm T}{10^6}\Big) \text{ years} \tag{1.13}$$

where Λ(T) is the cooling function for a non-equilibrium plasma [69]. Different approaches have been taken to study the presence of hot gas in the Galactic halo. From these, three models have resulted. In one of these models the hot gas is transported to the halo by Galactic Chimneys, see §§ 1.8.1. In another model, the gas is nourished through a Galactic Fountain, see §§ 1.8.2, and in another by Galactic Winds, see §§ 1.8.3.

1.8.1 Galactic Chimneys

It has long been clear that adjacent explosions of several supernovae, as one might expect to happen on OB star associations, could let the supernovae remnants more easily to break out of the disc and pervade the halo with their hot gas. Such sequence of supernovae would then give rise to the appearance of superbubbles and other structures.

Observational support of such physical systems in the Milky Way Galaxy and in other galaxies exists for quite some time. Studies using the 21-cm radio emission have detected H I shells and supershells [71, 72, 73, 74]. Moreover, x-ray radiation coming from inside the supershells has also been detected. These structures are the boundaries of bubbles and superbubbles. These H I cavities can be formed by two distinct processes. The first are formed by cumulative supernova explosions in OB associations. In this case, massive stars are formed sequentially from giant molecular clouds. These stars produce H II regions and stellar wind bubbles, and eventually, explode as supernovae within previous cavity remnants. This is expected to occur in the spiral arms of the Galaxy where the stellar density is higher. The second possibility is by the collision and merging of neighboring supernova remnants. This

second type of superbubble is expected to occur in the inter-arm regions of the Galaxy.

Ikeuchi [75] and Norman and Ikeuchi [76] have developed models to accommodate the observations and a three-phase ISM. Like in other models, the mechanism for the creation of hot gas is a sequence of supernovae and stellar winds. These events carve a tunnel into the surrounding ISM, creating a chimney and thick walls of neutral material. The density and temperature of the hot gas inside the chimney, are 10^{-3} cm^{-3} and 30 $\times 10^6$ K, respectively. These numerical calculations have shown, that a mass flow rate somewhere in between 0.3 to 3 M$_\odot$ yr^{-1} and an energy input of 10^{40}-10^{42} erg s^{-1} is expected.

In this model the gas flows from the disc at a distance of 1 kpc, being subsequently injected into the upper halo, where complete mixing occurs. According to the model, the gas following through the dense and cold neutral ISM is not severely affected by adiabatic cooling. Because of these combined effects, the resulting vertical temperature profile structure is considerably different from the one of McKee and Ostriker [46]. In their Galactic halo model the vertical temperature decreases faster, due to adiabatic cooling and due to the scale height, at which the injection of hot gas occurs. In case of the chimney model the vertical temperature is hotter, since the gas does not suffer much adiabatic cooling and reaches much higher heights. As a result, high-ionized atomic species are expected to be present at high latitudes in the Galactic halo, in contrast to the McKee and Ostriker [46] model.

The high gas temperature, streaming through the chimneys, should also have a strong signature in the hard x-ray regime. Besides the x-ray emission at energies $\geq$ 1.0 keV, UV absorption studies in direction of the halo should also reveal a population of highly ionized ions, such as O VI, N V, Fe X and Si VI. After achieving a height of several kiloparsecs and after a time of 20 - 30 $\times 10^6$ years, the gas cools down and condenses into clouds. This cool gas then rains back onto the galactic disc, a process that takes further 10 - 20 $\times 10^6$ years. Therefore, the estimated life cycle of the gas is 30 - 50 $\times 10^6$ years, cf. de Avillez and Breitschwerdt [50]: $\tau \sim 200$ Myr.

Another consequence of this model is the number of different sources of neutral material. The cool and neutral material can originate from the SNRs shell filaments, from the fragmentation of the H I chimney wall at $\sim$ 1 kpc, and above 1 kpc from the condensation of the hot gas into clouds. Velocities $|\mathrm{V}| \leq -50$ km s^{-1} are expected from high galactic latitude clouds ($\geq$ 1 kpc), whereas clouds, injected from the galactic disc, have $|\mathrm{V}| \sim -10$ km s^{-1}. In the case in which the material is originated from the fragmentation of the wall of the chimney, intermediate velocities are likely to occur.

In this context three-dimensional numerical calculations were performed by Tomisaka [77]. According to these calculations on a stratified plane medium and with a magnetic field proportional to the square root of the ambient density, breakthrough is expected to happen even when the supernova explosions occur near the mid-plain disc. de Avillez and Berry [78] have also undertaken similar studies upon the evolution of chimneys in the Galactic disc. de Avillez and Mac Low [79] have also performed three-dimensional simulations of individual chimneys, in order to study the newly observed ISM mushrooms, believed to be a Galactic chimney.

1.8.2 The Galactic Fountain

The Galactic fountain originates from widespread supernovae, that warm up the disc gas to temperatures of 10^6 K, which then flows into the halo. In this picture an uprising hot gas moves sub sonically until a distance of Z$\sim$1 kpc. The physical concept of a galactic fountain was first advanced by Shapiro and Field [80] to explain the newly discovered hot galactic gas, observed in absorption by the ubiquitous O VI ion [42, 43], the glowing of the soft x-ray background [81] and the high velocity clouds (HVCs) [82]. This scenario has received considerable refinements and improvements by Bregman [83] and Kahn [84].

In the Galactic fountain model proposed by Kahn [84] the uprising hot gas moves to a scale height of Z $\sim$ 1 kpc, where thermal instabilities promote the formation of clouds. For a gas with a velocity of 130 km s^{-1} this takes 7.5 $\times 10^6$ years, which is of the same order for the gas to cool down, $\tau_{\rm cool} \sim$ 8.3 $\times$ 10^6 years. These clouds, due to their ballistic trajectory, will travel to a maximum distance above the Galactic plane of $Z_{\rm max} \sim 5.5$ kpc, requiring a time less than 50 $\times 10^6$ years. After exhausting their kinetic energy, they fall in a free-fall trajectory onto the galactic disc. This process takes about 80 $\times 10^6$ years, therefore the total mass cycle takes 130 $\times 10^6$ years. The calculated mass rate during this cycle is 5.3 $M_\odot$ yr^{-1}. The associated velocity of such clouds would be of the order of 60 to 100 km s^{-1}. The main assumptions of these models were the height which the hot gas would rise, the expected condensation rate in clouds, which is a function of the temperature and the cooling rate at the base of the fountain; see Breitschwerdt and Komossa [85] for a review.

Dynamical calculations of Houck and Bregman [69] predict, that in order to fit the HVCs velocities, a model for the hot halo with a temperature and density of 3×10^5 K and 10^{-3} cm^{-3}, respectively, is required at the base of the halo. In this scenario the hot gas condenses at a scale height Z $\sim$ 1.5 kpc. The ascending velocity of the gas is 30 km s^{-1}. When its kinetic energy is fully transformed into potential energy, the gas stops its ascending rise, and falls back onto the galactic plane, acquiring an infall velocity of V $\sim$ 100 km s^{-1} near the galactic plane, where the clouds are decelerated by viscosity of the ISM. This model predicts a mass rain of 0.4 $M_\odot$ yr^{-1}.

Meanwhile, substantial numerical work has been done in order to understand the model. Two-dimensional galactic fountain codes have been developed by Rosen et al. [86] and Rosen and Bregman [87]. Even if they were successful in reproducing a three phase ISM, they were neither able to reproduce the vertical structure near the disc, nor the presence of high and intermediate velocity H I clouds. The main reason of this failure may be due to the fact, that modelling in two-dimensions introduces severe constraints to the gas flow modifying the overall structure and phenomena, which would occur in a three-dimensional flow gas.

To overcome these difficulties, three-dimensional and large-scale numerical MHD simulations of galactic fountains have been performed by de Avillez [88] and, more recently, by de Avillez and Breitschwerdt [49, 50], with an impressively high spatial resolution. In their ISM simulations, the evolution of the disc-halo interaction,

driven by supernovae, is followed for a period of 400 Myr and up to 10 kpc from the disc. An essential feature of these simulations is the escape of hot gas into the halo, therefore establishing a galactic fountain flow. An interesting result from these simulations is, that this transport of gas from the disc to the halo occurs even if initially a magnetic field parallel to the disc is present. In their bottom-up model building scheme, there are still important physical processes to be considered, such as non-equilibrium cooling, self-gravity, heat conduction and the effects of cosmic rays.

1.8.3 Galactic Winds

Galactic winds are normally associated to starburst galaxies, i.e., galaxies with a high star formation rate and therefore a high rate of supernova explosions. These SNe give enough mechanical energy and momentum to drive strong galactic winds, see Veilleux et al. [89] for a review.

Since the work of Habe and Ikeuchi [90] it is commonly assumed that in spiral galaxies galactic winds do not play an important role during galactic evolution. This assumption is based on the estimate, that for a galactic wind to occur minimum physical requirements for the parameters $T > 5 \times 10^6$ K and $n = 10^{-3}$ cm^{-3} are necessary. This physical model has been criticized by Breitschwerdt and Komossa [85], who argued that important non-thermal components of the ISM, such as the cosmic rays (CRs), should also be taken into account when modelling galactic winds. It has been shown that there is a net momentum transfer from the CRs to the gas via waves, pushing the gas away from the disc into the halo. Breitschwerdt et al. [91] have been able to demonstrate, that a Galactic wind with a slow mass loss of $\dot{M}_{GW} \sim 0.5\,M_\odot$/yr, given an initial density of $n_i = 10^{-3}$ cm^{-3} and $T_i = 10^6$ K and $P_{C_i} = 10^{-13}$ dyne cm^{-2}, can be formed. In a steady state ISM model, like the one from Cox and Smith [47], the combined pressure of the gas and CRs can drive an outflow to great distances above a height of 1 kpc, when the total pressure surpasses the intergalactic medium. The important role played by CRs lies in their resonant interaction with MHD waves frozen into the plasma and, on the fact of not being subjected to cooling, with the exception of adiabatic energy losses by pdV-work. As a consequence it has been argued by Breitschwerdt and Schmutzler [92, 93], that an outflow of gas with a temperature as low as $T \sim 4 \times 10^4$ K, emitting soft x-rays, due to delayed recombination, could contribute substantially to the diffuse soft x-ray background (SXB).

Galactic winds have also been studied as the result of bubble and superbubbles break-outs, see Koo and McKee [94, 95]. In this model, stellar winds and sequential supernova explosions continuously inject energy into the ISM, generating hot bubbles which expand, sweeping out the ambient medium. During the evolution of these astrophysical outflows, they necessarily interact with different ambient media—different densities and pressures. The main concern of this model [94, 95] is, to study the evolution of bubbles in a medium in which the ambient density has a strong vertical gradient. Due to the vertical high density gradient the bubbles or superbubbles will expand faster in the direction perpendicular to the disc. Then, if

the resulting stellar and supernovae wind is strong, the shell or supershell accelerates and breaks due to Rayleigh-Taylor instabilities. When the shell or supershell structure is broken, the hot gas within it can leak out and produce a shock with the ambient medium. Depending on the wind luminosity strength, two possible flows can result after the bubble break-up. A low wind luminosity creates a jet, and a high wind luminosity will blow directly out the hot gas.

This model has been applied by Koo and McKee [95] to the North Polar Spur (NPS), an H I expanding shell with a hot gas ($\sim 3 \times 10^6$ K), detected as an x-ray emission enhancement. These authors have attributed the existence of the NPS to stellar winds and supernova explosions, acting in concert from the Sco-Cen Association. In order to do so, between 6 to 10 supernovae of 10^{51} erg were necessary.

Chapter 2

The Local Bubble

Painted version of the woodcut, attributed to the French astronomer Nicolas Camille Flammarion (1842-1925), which appeared in the L'atmosphère: météorologie populaire (pag. 163), 1888, which presumably depicts a monk, crossing through the shells of appearance.

"A physical model of the Local Bubble can be tested by its ability to reproduce the spectral features observed in the EUV and soft X-ray."

- Hans Böhringer *in The Local Bubble and Beyond, 1998.*

The first astrophysical object found to radiate x-ray photons was the Sun, during a rocket flight experiment done by Friedman et al. [96]. This discovery lead other experimental groups to develop more sensitive detectors to be flown in rockets, with the purpose of detecting other astrophysical objects in the x-ray regime. In one of such rocket flight experiments an intense and discrete source was discovered in the constellation of Scorpius, which became known as Sco X-1, by Giacconi et al. [97]. During the same rocket flight experiment another remarkable detection was done with the discovery of a cosmic x-ray background (CXB). The discovery of this cosmic background showed a striking isotropy in its intensity, over all the sky, in the 2.0 - 6.0 keV energy band.

The isotropy of this radiation implied a local or very distant origin, since all material in the Galaxy is distributed anisotropically. Moreover, since at these energies the Galaxy is completly transparent above the Galactic plane, the only plausible

origin was an extragalactic source. Soon after, Gould and Burbidge [98] suggested that this x-ray emission could be due to unresolved sources. This exciting discovery lead to the idea that the isotropy of the CXB could be used to study the distribution of interstellar material in the Galaxy, by looking at absorption patterns below 1.0 keV.

The first physical experiment in this energy range was performed by Bowyer et al. [26], who, in fact, observed that the flux at these low energies decreased towards low galactic latitudes. These observational data were then interpreted as being a superposition of two x-ray emission components. One arising from the deep extragalactic space and a second one, having as most likely a Galactic origin. This discovery came to support the idea that a hot interstellar phase may exist in the Milky Way Galaxy. An idea that had been put forward by Spitzer [39], in order to confine the observed high altitude interstellar clouds. Spitzer's proposal was, however, only concerned with a hot corona, surrounding the Galaxy. Soon after, it was realized that the extrapolated x-ray flux of the CXB spectrum above 2.0 keV was insufficient to account for the observed flux at low energies [99], meaning, that an excess of flux at low energies was present.

Almost two decades after Spitzer's proposal, new astrophysical data in the extreme ultraviolet (EUV) domain showed, that a different hot gas from the one sampled by the Bowyer et al. [26] experiment, existed in the ISM. The idea, that many different hot plasmas may coexist in the ISM, was amplified with subsequent observations in the soft x-ray region.

2.1 The Local Bubble Paradigm

Jenkins and Meloy [42], after analysing the spectra in the line of sight to stars, using the COPERNICUS satellite, found broad absorption lines caused by O VI ions in the ISM. The absorption caused by these highly ionized ions could only be explained by the presence of a hot plasma between these stars and the Earth.

In the same year, Williamson et al. [81], also suggested with two dedicated flight rockets to study the soft x-ray diffuse background (SXDB), that the most likely physical mechanism to produce this soft x-ray emission and the O VI absorption lines was a very hot thermal plasma. At the same time the Wisconsin far-ultraviolet spectrometer aboard of the OAO-2 satellite, observed the interstellar absorption of Ly_α towards nearby early-type spectral stars. From this Ly_α survey Savage and Jenkins [100] and Jenkins and Savage [101] were able to demonstrate, that the solar neighborhood was deficient of neutral hydrogen (H I), in particular in the third Galactic quadrant. Furthermore, other highly ionized ions like the N V[1] and the O VI[2] doublets, detectable in the EUV, were observed in the ISM. By measuring the widths of the absorption lines produced by these ions and the degree of ionization, York [43, 44] was able to derive a range of temperatures from 2.8×10^5 to 7.0×10^5 K for the hot phase of the ISM.

[1] 1242.8 Å/1238.8 Å or 9.97 eV/10.0 eV
[2] 1037.6 Å/1031.95 Å or 11.94 eV/12.0 eV

The observations of a hot ISM and low H I were explained within the displacement model proposed by Tanaka and Bleeker [102] and Sanders et al. [103], that the neutral hydrogen that would normally be found, had been blown away by winds and explosions of one or more massive stars acting in concert, forming a low-density bubble where the Solar system is presently located. This H I cavity would then be filled with hot plasma resulting from that star activity. Posterior studies from Frisch and York [104] and Paresce [105] have shown, that this H I cavity is asymmetric in the Galactic plane, where it extends farther in the longitude range of 210°-250° and also in the vertical plane, where it reaches much higher altitudes in the northern hemisphere.

Studies on the SXB conducted by Bloch et al. [106] with the complement of the Wisconsin Survey data [107], showed a surprising constancy between the ratio of the Be-band (nominally 0.078 - 0.111 keV) and B-Band (nominally 0.13 - 0.188 keV) count rates. Since the mean free path [$l = 1/(n\,\sigma)$] of a photon from the Be-band[3] is ≈ 50 pc and a photon from the B-band[4] is ≈ 200 pc, assuming an average density of 0.1 H I cm^{-3} in the midplane, these photons must have the same origin. Moreover, these mean free paths correspond to column densities of H I of $\approx 1.5 \times 10^{19}$ cm^{-2} and $\approx 6.2 \times 10^{19}$ cm^{-2}, implying a local source. These facts, allied to the observation of an anti-correlation between the soft x-rays and the column density of H I, supported the idea of a local interstellar medium (LISM) filled with hot plasma and devoid of neutral material, in alignment with the concept of a displaced LISM [102, 103].

Cox and Reynolds [108] proposed, that the observed soft x-ray background radiation around 1/4 keV would predominantly arise from what they have come to call the Local Hot Bubble (simply LB) which was a leftover of an active supernova remnant. McCammon and Sanders [109], studying the relative intensities of three energy bands, found that the emitting gas had to have a temperature of $\simeq 10^6$ K.

Snowden et al. [110], working within the displacement model, assumed that all the soft x-ray emission observed originated in the LB, therefore, making the task of inferring the physical state of the hot plasma and its geometry easier. The three main assumptions in their model were: (1) an uniform soft x-ray emissivity, (2) which was filling the entire cavity in H I, and (3) a plasma in collisional equilibrium. The observed broad band spectrum - the Be, B and C-bands of the Wisconsin Survey - were fitted with a Raymond & Smith plasma model [111]. To the plasma a temperature of 10^6 K was assigned, leaving the soft x-ray emissivity as a free parameter. The best fit model yielded an electron density of $4.7\times\ 10^{-3}$ cm^{-3}, implying a plasma emissivity in the B-band of 0.48 counts s^{-1} pc^{-1}. The pressure inferred for this plasma was $p/k_B \approx 9000$ cm^{-3} K. Given the fact, that the observed soft x-ray intensity (I_{x-ray}) is equal to the product of the soft x-ray emissivity (ϵ_{x-ray}) by the distance (D), the geometry of the LB could be inferred. From this analysis the LB was found to extend ~ 30 pc in the Galactic plane and ~ 200 pc towards the north Galactic pole (NGP). However, after the launch of the ROSAT satellite [30] a different picture emerged.

The data gathered by the ROSAT PSPC showed, that a significant part of the

[3]Cross Section $\sigma_{0.095\ keV} = 6.49258 \times\ 10^{-20}$ cm^2
[4]Cross Section $\sigma_{0.160\ keV} = 1.59365 \times\ 10^{-20}$ cm^2

1/4 keV flux did not originated in the LB but outside of it. This was realized by studying the shadows, that molecular clouds cast on the soft x-ray background emission. Two shadow experiments were performed, one on the Draco Nebula [31, 32] and the other in the constellation of Ursa Major [112].

In particular, the analysis of the Draco shadow experiment revealed, that roughly 50 per cent of the emission at 1/4 keV originated beyond the Draco nebula. Since this nebula is placed at more than 300 pc from Earth, therefore outside of the LB boundaries, 50 per cent of the 1/4 keV flux was produced outside of the LB, a fact, that was not possible to accommodate anymore within the displacement model.

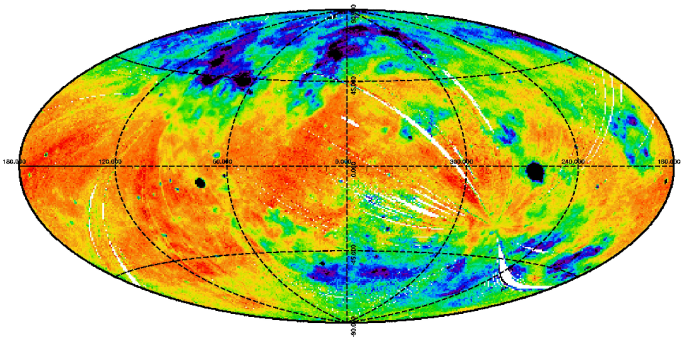

FIGURE 2.1: The ROSAT All Sky Survey 1/4 keV band. The red color corresponds to low count rates, whereas dark blue corresponds to high counts. The map shows the intensity counts/s in units of 10^{-6}. Image from 1/4 keV energy band taken from Snowden et al. [113]. © MPE.

The ROSAT observations also revealed that the 1/4 keV x-ray emission varies over the sky, see figure 2.1 taken from Snowden et al. [113]. The emission of the 1/4 keV band in the northern sky halo, has shown a patchy structure, which sugguests that the observed intensity was the result of the superposition of enhancements, relative to an uniform background emission. Similar studies in the southern hemisphere showed that the 1/4 keV emission is characterized by a gradient towards low latitudes.

Further work on the extent of the LB by Fruscione et al. [114] and Breitschwerdt et al. [115], using the compiled Ly_α absorption line measurements, allowed them to estimate, that the H I cavity in the Galactic plane should have a radius $\sim 60-100$ pc and a vertical extension from the plane $\sim 120-180$ pc.

In the light of the x-ray shadow observations, Snowden et al. [116] re-examined the 1/4 keV ROSAT data obtained during several years in orbit, this time assuming, that this emission was produced by the hot LB, the Galactic halo, and an extragalactic component. The latter two components were subjected to absorption, in particular the halo component, after the discovery of the x-ray shadows. The result of this analysis was a LB with a temperature of $1.17^{+0.15}_{-0.12} \times 10^6$ K, a density of $4.5\times\ 10^{-3}$ cm^{-3}, implying a $p/k_B \approx 10500$ cm^{-3} K and a smaller extension, ranging from 40 pc in the Galactic plane to 130 pc towards the NGP.

The knowledge of the geometry of the LB has been improved, due to sophisticated NaI D line absorption studies towards stars with known distance. In particular, Sfeir et al. [117] have produced a 3D map of the local interstellar medium, using the equivalent widths of the NaI D line doublet at 5890 Å, to trace the cold neutral hydrogen towards lines-of-sight of 143 stars lying within 300 pc of the Sun. More recently, this study has been enlarged by Lallement et al. [118], which show 3D absorption maps of the local distribution of neutral gas towards 1005 sight lines. These

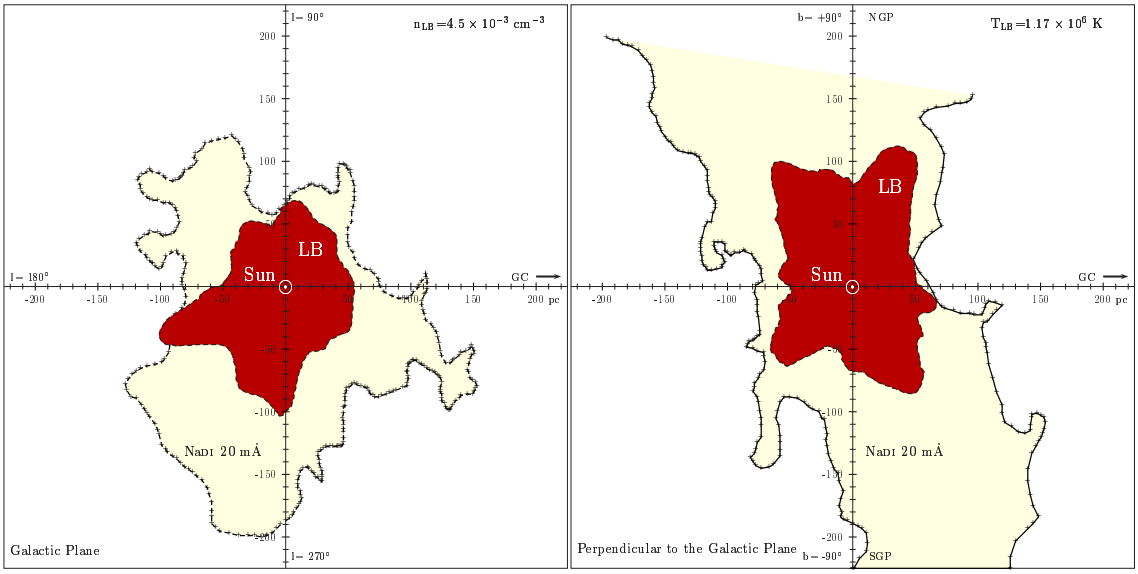

FIGURE 2.2: The LB ISM. In these plots we show the present understanding of the LB soft x-ray emissivity volume, due to Snowden et al. [116] (dark red), complemented with the study of Lallement et al. [118], where the absorption EWs of NaI D were used to infer the local distribution of neutral gas. For producing these plots we have used the EW contour of 20 mÅ (light yellow). An EW of 20 mÅ of the NaID corresponds to a column density of H I of 2.0×10^{19} cm^{-2}. We have simplified the right plot by assuming that the Sun lies in the Galactic plane (GP). However, it is known that the Sun lies at a distance of 34.56±0.56 pc above the GP [119]. The Galactic Center (GC) direction is indicated with an arrow. The North Galactic Pole (NGP) and the South Galactic Pole (SGP) are also shown.

maps show, that the Solar system is approximately in the middle of a deficient H I region.

In figure 2.2 a schematic representation of the present understanding of the local interstellar medium within 200 pc—i.e, the geometric configuration of the LB—is given. The x-ray emissivity contour associated to the hot LB due to Snowden et al. [116], and the neutral H I column density inferred from NaI D studies from Lallement et al. [118], were employed. In the Galactic plane (see the left plot of figure 2.2) the contour line of the NaI D shows an irregular structure with some tunnel-like features. Perpendicular to the Galactic plane (see the right plot of figure 2.2) the NaI D map shows a cone-like form without a defined boundary. The later feature indicates, that the LB may be open in direction of the Galactic poles.

2.2 Theoretical models for the Local Bubble

The success of any theoretical model is measured by its ability to reproduce all available observations and predict new phenomena, which can then be tested by new experiments. Also, when analysing the observational data, precise physical information can be derived for an assumed physical model, and, subsequently, subjected to further tests.

A relative big set of observational data has been obtained, ranging from the EUV to soft x-rays. Some of these observations have revealed the presence of highly ionized species in the ISM. In addition to the presence of these ions, detected in absorption studies to nearby bright stars, there is a strong and extended emission of soft x-rays. Therefore, any physical model of the hot ISM and in particular for the LB must have mechanisms to produce highly ionized ions, EUV, and soft x-ray photons. In alignment to this, much theoretical work has been developed to explain the observed features of the LB.

In modelling interstellar plasmas both atomic processes controlling the ionization structure and the astrophysical events leading to that ionization structure have to be taken into account. This means, that these physical processes are intimately related. Two types of models have been invoked to explain these set of observations. Models in which it is assumed that the plasma is in a steady state, and other ones where it evolves with time. The first ones are called collisional ionization equilibrium (CIE) models, and the second ones non-equilibrium ionization (NEI) models.

For modelling interstellar hot plasmas, two major simplifications are done. Firstly, it is assumed that the plasma is optically thin, and secondly that its density is low. The first assumption implies, that once a photon is emitted, the probability to interact (e.g., to be reabsorbed) is negligible. Therefore, this process is not taken into consideration in the code. Moreover, the condition of being optically thin implies, that the resulting radiation spectrum does not affect the ionization structure further. The second assumption of a plasma with low density implies, that the probability of a collision between two particles is also low. This implies that the excited ions cannot de-excite via collisions but have to decay by radiative processes. The line emission rate is then related with the rate of collisional excitation. These simplifications lead to an "easier" way to handle the physics. These are the coronal models. In ionization equilibrium models several equilibria have to be established. The temperatures of ions and electrons have to reach a thermal equilibrium, they have to thermalize to the same temperature, and the ionization and recombination processes have to come to a balance.

The departure from CIE to NEI plasmas occurs, when the ionization and recombination processes come or do not come to a balance. These two different models produce different ionization structures. In CIE the ionization fraction of ions is a peaked and relatively constrained to small temperature intervals, whereas in NEI plasmas the ions fraction population may exist over a wide range of temperatures. These different ionizing population structures also imply different timescales for the existence of the plasma, the CIE plasma being younger. In the case of NEI plasma there are essentially two exteme categories: an younger or an older plasma. In the case of an *young* NEI plasma, the plasma is in an underionized state, i.e., the ionization structure lags behind the thermal structure, e.g. due to the propagation of a shock wave, which heats the interstellar plasma very fast, like in the model developed by Cox and Anderson [120]. In the second case, an *old* NEI plasma, the plasma was heated up during its previous history to $T \geq 10^6$ K, and then experiences a fast adiabatic expansion. In this case, delayed recombination essentially retains the high ionization stages of the expanding plasma, and the emission spectrum resembles a

CIE plasma, Breitschwerdt and Schmutzler [92, 93]

2.2.1 Collisional Ionization Equilibrium Plasmas

From an historical perspective, the first type of model proposed to explain the available EUV and soft x-ray data, was a model in which the ionization occurs by collisional processes and in equilibrium. This type of models are controlled by collisional ionization equilibrium (CIE) physics. They are also known as coronal plasmas. A detailed discussion of these matters is far beyond the scopes of this work. However, a very short description of the physical conditions, in which the CIE plasma holds, is given. For a more detailed physical description of these models, and for some of their applications see the articles by Böhringer [121], Mewe [122], Kallman and Palmeri [123] and Kaastra [124], respectively.

Collisional ionization occurs, when an electron collides with an ion with a relative kinetic energy greater than the ionization potential of that ion. As a result of this physical process, an amount of energy equal to the ionization potential of the ion is removed from the electron plasma and transfered as kinetic energy to the removed electron. Therefore resulting in a net cooling of the electron plasma. In the coronal approximation it is assumed, that the electrons and ions have reached the thermalisation state, meaning that they have reached the same temperature. It is therefore assumed that a Maxwellian distribution describes their energies.

The collisional ionization process is then balanced by a reverse process of equal magnitude, the recombination of an electron with an ion. This process leads to a radiative process with two main channels. The radiative process occurs, because the electrons are mostly captured in an excited state of the ion. The electron then de-excites via a cascade through permitted radiative transitions into the ground state. It is however possible, that the captured electron excites an inner shell electron. As consequence, the excited ion will decay via a two-step process, called di-electronic recombination. One of the valence electrons radiatively de-excites inducing a cascade of photons similar to radiative recombination. At high enough temperatures the di-electronic recombination dominates over the radiative recombination. Since the hot gas is a tenuous one, the photons produced in these recombination processes will have a low probability to interact with the plasma. Therefore, they leave the plasma without any futher interaction.

Several models, e.g. from Hayakawa [125] and Sanders et al. [103], using the assumption of CIE were developed to explain the LB UV and x-ray emission. The first serious attempt to explain the available EUV and soft x-ray data with the model from Cox and Anderson [120]. In their model a very large supernova blast wave, propagating into the hot low-density component of the interstellar (ISM) medium, was invoked to explain the soft x-ray observations with typical parameters of the gas: a temperature of $\sim 10^6$ K, a $p/k_B \sim 10^4 cm^{-3}$ K and an extent ranging from one to several hundred pc. In this model the bubble had an age of $\sim 10^5$ years.

Innes and Hartquist [126] built a model in which the H I cavity was carved by very old supernova remnants and superbubbles. On their model a superbubble created roughly 4×10^6 yr ago was responsible for injecting $\sim 10^{52}$ erg into the

interstellar medium surrounding the Solar system, which could produce the observed soft x-ray and extreme ultraviolet radiation background.

A decade later Edgar and Cox [127] investigated the possibility, that the Local Bubble had been created either by a single supernova or by a series of supernovae. In this way, they have tried to find the physical parameters that could parametrize hot bubbles with a typical radius of 100 pc and with the average count rates in the B and C bands matching the observed ones. With the right model then they could proceed in exploring the features of this model, such as the x-ray and EUV spectra, the emissivity and O VI column densities. In the models developed by Innes and Hartquist [126] and Edgar and Cox [127] the age of the superbubble is much larger.

However, later it was realized by Breitschwerdt [128], that these CIE models produce a high pressure—an order of magnitude higher—which is in conflict with the presence of local clouds, which require much lower pressure in order to survive[5]. Another difficulty of this kind of model resides on its very foundations, see Breitschwerdt [130]. The assumption, that a three body process occurs in a tenuous and hot optically thin plasma is not likely to happen in real hot and rarefied astrophysical plasmas. Moreover, the assumption, that the ionization rate by inelastic collisions is exactly balanced by recombination processes, requires a third body. Therefore, in this process the temperature of the plasma increases. The other difficulty of these models resides in the assumption, that recombination processes dominate in CIE plasmas. Since radiative recombination is a cooling process, the plasma will eventually depart from equilibrium and enter in a non-equilibrium ionization phase, see Kafatos [131], Shapiro and Moore [132], Schmutzler and Tscharnuter [133].

There are two important time scales which control the evolution of the thermal plasma—the cooling time (t_{cool}) and the recombination time (t_{rec}). t_{cool} is the time that a plasma needs to convert all its internal energy into radiative energy. The typical cooling time for a thermal plasma can be estimated by using the following equation:

$$\begin{aligned} t_{cool} = \frac{3}{2}\frac{nk_BT}{\mathcal{L}} &= \frac{3}{2}\frac{(n_e+n_p)k_BT}{n_en_p\mathbf{\Lambda}} = \frac{3}{2}\frac{n_p\left(\frac{n_e}{n_p}+1\right)k_BT}{n_en_p\mathbf{\Lambda}} = \\ &= 6.57\times10^4\frac{\left(\frac{n_e}{n_p}+1\right)T_6}{n_e\mathbf{\Lambda}_{22}}\ \mathrm{yr} \end{aligned} \tag{2.1}$$

where $\mathcal{L}$ is the interstellar cooling function, $\Lambda_{22} = \Lambda/10^{-22}$ denotes the cooling rate in units of 10^{-22} erg cm^{-3} s^{-1}, and T_6 is the temperature in units of $T/10^6$ K.

The recombination time, defined by

$$t_{rec} = 1/(n_e\ \alpha_{rec}^{total}) \tag{2.2}$$

[5]There are several clouds in the solar neighbourhood. One of the best studied cloud is the local interstellar cloud (LIC). For a recent review on the Local Interstellar Medium see the article from Redfield [129]. The derived temperature and density for the LIC are 6300 K, and 0.33 cm^{-3}, respectively. These values imply a $p/k_B \sim 3200$ K cm^{-3} for the LIC. The pressure imbalance between the LB ($p/k_B \sim 10^4$ K cm^{-3}) and the LIC would make the existence of these clouds not probable.

is the time required for a given ion to recombine with a free electron plasma, in a plasma with electron density n_e and where α_{rec}^{total} is total recombination rate for a given ion at a given temperature. After t_{rec} the ion should not be present anymore in the plasma, or it should have a reduced ionization stage.

These two time scales can be easily calculated. Using the values for the LB from Snowden et al. [116], assuming a $\Lambda = 1.081 \times 10^{-22}$ erg cm^{-3} s^{-1} and $n_e \simeq n_p$, a t_{cool} of 31.6 Myr is obtained. Comparing this value with the time required for the, e.g., O VII to recombine, we find a t_{rec} of 4.8 Myr, with the α_{rec}^{total} of 1.47×10^{-12} cm^3 s^{-1}, a coefficient taken from Nahar [134]. Doing the same exercise for the C VI ion one finds a t_{rec} of 7.2 Myr, using the recombination rates coefficients of Nahar and Pradhan [135].

The cooling time establishes how long a hot plasma can exist in CIE at a given temperature and electron density. The time scale required for a plasma to achieve a CIE state is given by the following expression:

$$\tau_{CIE} = \frac{1}{(\alpha_{coll} + \alpha_{rec}) n_e} \tag{2.3}$$

where α_{coll} and α_{rec} are the collisional ionization and recombination rates. This equation gives an estimate of the time scale necessary for a given ion species to achieve a CIE state. It is normally assumed that the CIE condition for a thermal plasma is achieved, when τ_{CIE} is much smaller than the t_{cool}:

$$\tau_{CIE} << t_{cool} \tag{2.4}$$

There are currently a large number of numerical codes, that calculate the emergent spectrum of hot plasmas in CIE and which are used to fit x-ray spectra from interstellar plasmas. Most cited in the literature are the codes from Raymond and Smith [111], Mewe et al. [136] and Kaastra and Mewe [137].

The so-called Raymond-Smith collisional ionized plasma have been widely used to fit low resolution spectra obtained during missions like ROSAT and others. This plasma code has evolved to the Astrophysical Plasma Emission Code (APEC), which combines a sophisticated code along with the APED database, composed by more than one million transition emission lines [138].

2.2.2 Non-Equilibrium Ionization Plasmas

A completely different approach to model the EUV and the soft x-ray background emission was proposed by Breitschwerdt and Schmutzler [92]. The authors have incorporated the atomic physics code developed by Schmutzler and Tscharnuter [133] into an algorithm where the atomic physics evolves according to the dynamics of the astrophysical system in which the atomic processes take place.

The calculations by Kafatos [131] and the Shapiro and Moore [132] have already shown, that even by starting from an equilibrium condition, non-equilibrium effects occur, leading to a different cooling function for a hot plasma. In their calculations the non-equilibrium effects happen in the temperature range from 3×10^5 to 5×10^5 K.

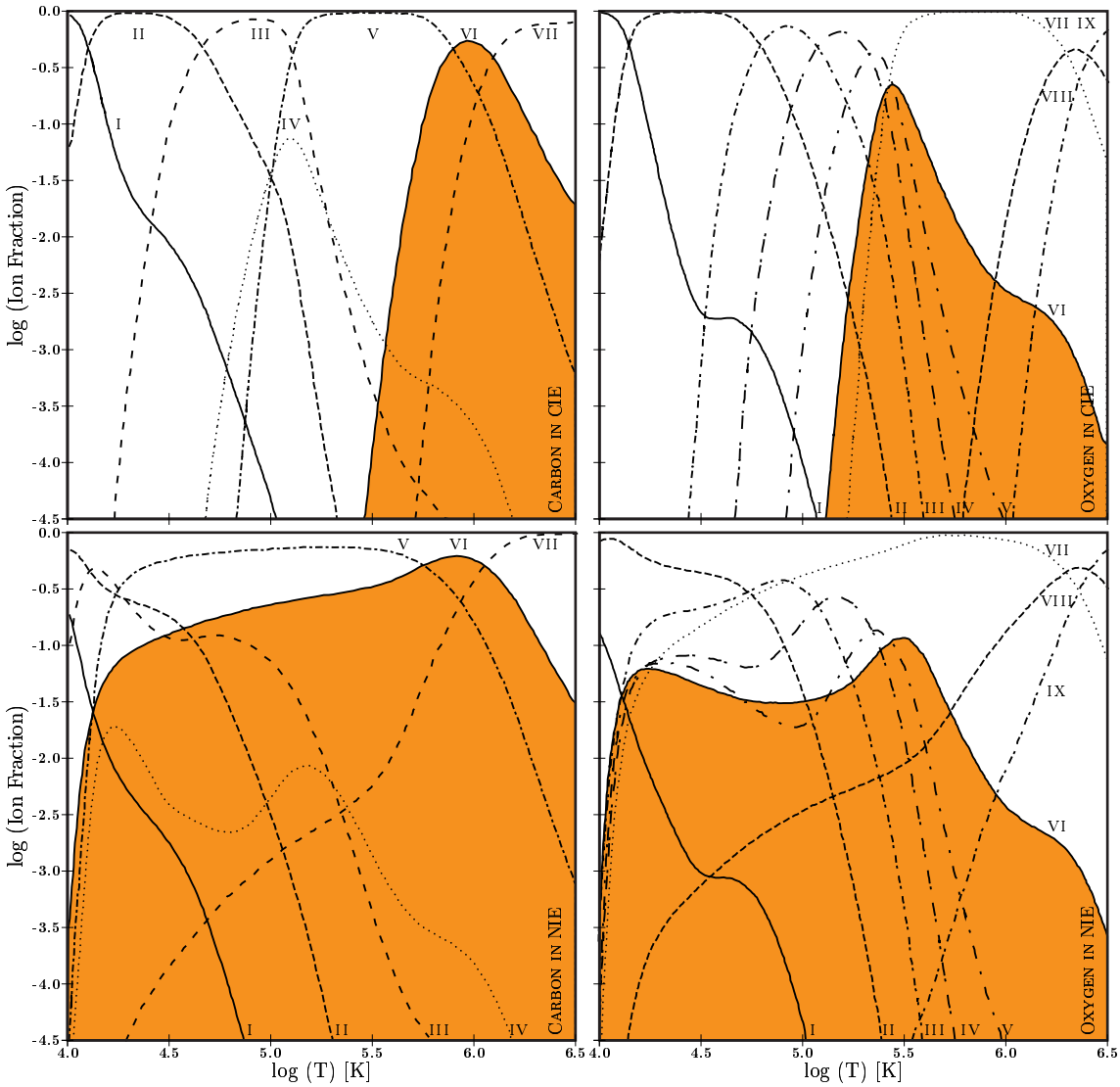

FIGURE 2.3: Ionization fractions of carbon and oxygen. The left top plot shows the carbon ionization fractions assuming a plasma in CIE. The left bottom plot shows the carbon ionization fractions assuming a plasma in a NEI state. On the right top plot the ionization fractions of oxygen in CIE state are shown. The ionization fractions of oxygen in a NEI condition are shown on the bottom right plot. These calculations were performed by Schmutzler and Tscharnuter [133]. The NEI condition allows the presence of an ion over a large range of temperatures.

In this regime, more highly ionized species are found, contributing then with more strong emission lines.

The first real attempt to simultaneously calculate the emission of an astrophysical optically thin plasma and to take into consideration the time-dependent ionization stages due to their thermodynamical history path, was done by Schmutzler and Tscharnuter [133] with the purpose of investigating the emission line regions in Active Galactic Nuclei.

In figure 2.3 the ionization fraction of two important astrophysical ion species

is shown—the ionized carbon and the ionized oxygen— calculated in CIE and NEI, taken from Schmutzler and Tscharnuter [133]. As it can be seen, these two different physical conditions result in two distinct ionization structures. The top plots show the calculations assuming the condition of CIE, and the bottom ones the condition of NEI.

Schmutzler and Tscharnuter [133] had already argued that the CIE assumption for the Galactic halo and hot ISM plasmas with temperatures of 10^5 K [139] and 10^6 K [140], respectively, had a serious flaw. No global astrophysical mechanism, capable of permanently maintaining this wide temperature range is known. Therefore, it was suggested, that we were observing these gases in a point of their thermal history where the gas is out of the CIE condition.

In the Breitschwerdt and Schmutzler [92] elegant model, the dynamical history of the physical system is taken into consideration. This model assumes, that several supernovae explosions occurred in the past, creating a superbubble, in a dense environment.

The most important concept of this model is the assumption, that during a phase of fast adiabatic expansion, the temperature of the plasma decreases very fast, leaving all high ionization stages frozen into the plasma. This happens, because the recombination time is much longer than the cooling time of the plasma. Therefore, a large fraction of the internal energy of the plasma is stored in the highly ionized species, which can subsequently be released by recombination radiation. The dynamics of the plasma also changes the density of the plasma and the ionization structure, which changes the cooling function, and therefore the dynamics of the plasma itself. With this new class of model, Breitschwerdt and Schmutzler [92] derived a much lower temperature $T \approx 4.2 \times 10^4$ K for the LB. From this model they also inferred an emission measure $EM \approx 5.8 \times 10^{-2}$ cm^{-6} pc, to which corresponds an electron density $n_e \approx 2.4 \times 10^{-2}$ cm^{-3} along a line of sight of 100 pc. From the two physical parameters, temperature and electron density, a pressure of $p/k_B = 2nT \approx 2000$ K cm^{-3} is then obtained, which is four times less than the one derived from CIE models. This then makes the very existence of clouds inside the LB medium possible. The estimated age of the LB for this model is about 4×10^6 years. Their model also predicts the loss of some of the hot ISM into a galactic wind.

The emerging spectrum of a LB in a NEI state is characterized by an unusual large contribution from the recombination lines, in such a way that the high energy part of the spectrum is completely dominated by recombination photons. Due to this high energy recombination tail, a NEI plasma with a temperature of 4×10^4 K can mimic the spectrum of $\sim 10^6$ K CIE plasma in shape and in hardness, see figure 2a from Breitschwerdt and Schmutzler [92]. Also, this delayed recombination emission lines leave a strong singnature in the plasma spectrum with a saw-tooth profile in the upper energy part of the spectrum.

In this type of model the existence of ion species like O VI, N V and C IV in the interstellar medium can be easily accommodated within the low temperature plasmas. Because of the highly ionized species and because they did not have enough time to recombine, they are able to exist within a large range of temperatures. This model was very successful in reproducing the observations in the EUV and soft x-ray

regimes.

2.3 The O VI in the Local Bubble

One of the many spectral features that a model has to reproduce is the amount of ions in the LB observed in absorption studies. A recent FUSE absorption survey of O VI (1032 Å) towards 25 white dwarfs within a radius of 225 pc was used to estimate the amount of O VI in the LB or local ISM. This analysis has revealed, that the mean space density of O VI is 2.45×10^{-8} cm^{-3}, with a corresponding averaged column density of $\sim 7 \times 10^{12}$ cm^{-2}, integrated over a path line of 100 pc. The maximum measurement of the column density due to O VI in this survey was $1.7{\times}10^{13}$ cm^{-2}.

The study of O VI absorption has also received considerable attention from a more theoretical side, because the O VI column density [N(O VI)] is a sensitive tracer of the age of an evolved bubble. Recent hydrodynamic simulations carried out by Breitschwerdt and de Avillez [141] in a 3D Galactic ISM, have been designed to study the evolution of the column density of O VI in the ISM, with a special focus on the contribution of the LB and Loop I bubbles.

The quantity of O VI generated in these simulations was investigated over many lines of sight, centred on the solar circle and crossing the Loop I. These calculations were performed, assuming a plasma in CIE and with solar abundances [142]. The averaged N(O VI) was calculated along these lines of sight over a period of 0.4 Myr, starting at 14.3 Myr. The averaged N(O VI) as function of distance and time is shown in their figure 3 (top). From this figure, we see that at a distance of 40 pc the averaged N(O VI) decreases from $40{\times}10^{12}$ to $0.3{\times}10^{12}$cm^{-2} in less than half a million years.

2.4 How to study the soft x-ray emission from the LB

In this section we will discuss how to study the soft x-ray emission from the LB. In the x-ray regime the ideal way to do studies on the nature of the LB plasma physical state, or in general on other Galactic hot plasmas, is to perform x-ray shadow experiments. The existence of ISM x-ray shadows requires the presence of ISM material in between the emission x-ray source and an observer. For the LB the ideal case is to study the x-ray shadows produced by clouds of neutral and molecular material inside of the LB boundaries.

The figure 2.4 has a dual purpose: first to show the ISM photoelectric absorption cross-section (σ), and second, to show the associated mean free path (m.f.p.) of a photon in that medium. The top panel of figure 2.4 shows the effective absorption σ per hydrogen atom for the ISM, using the analytic fit coefficients from Morrison and McCammon [143]. Assuming a particle density of 1.0 cm^{-3}, we can compute the m.f.p. for each photon in the energy band of 0.1 to 10.0 keV. Given that the m.f.p. is inversely proportional to σ, the photons with the highest σ will travel shorter distances in the ISM. This effect is shown in the bottom panel of figure 2.4. The

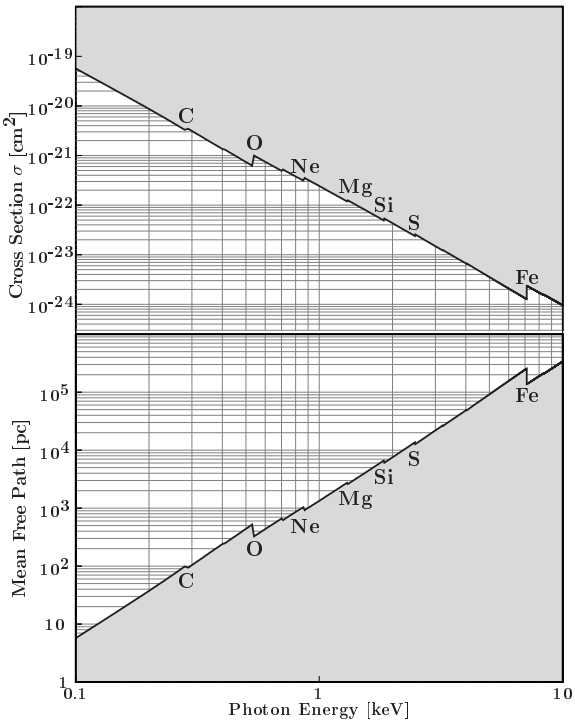

Figure 2.4: The ISM Photoelectric Absorption. The presence of material in the ISM has as a consequence the absorption of radiation, inducing a reduction of the radiation intensity of a given source. The probability of interaction between a given photon of energy E and some particle is given by the cross section σ of the particle. On the top plot the interstellar photoelectric absorption cross sections, calculated by Morrison and McCammon [143], as a function of energy, are depicted. These cross sections were then used to calculate the mean free path of photons, assuming an average particle density $n_0 = 1.0$ cm^{-3}, bottom plot.

most abundant atomic species are also presented in each of the panels.

The LB emission is thought to be produced in a cavity, devoid of H I, filled with a $\sim 10^6$ K hot thin plasma and having an average radius of 100 pc. Early all-sky surveys, like the Wisconsin Survey performed by McCammon et al. [107], had shown a remarkable constancy between the count ratio of the B and Be bands. Given the fact, that a photon of the Be-band has a σ about 4 times higher than a photon of the B-band, the constant count ratio implied the same physical origin for these different photons.

If the effect of the absorption σ is combined with the average particle density (n) along a given line of sight ($l = \int ds$), then the optical depth of the medium is obtained, $\tau = \sigma$ N, where N is the column density along that particular line of sight. The physical parameter τ allows us to calculate whether a given medium is optically thin or thick for a given photon. As an illustrative example: for a photon of 1.0 keV in a medium with an associated column density of 10^{22} cm^{-2} and with $\sigma = 2.422 \times 10^{-22}$ cm^2 [143], we obtain τ of 2.422. This value means, that the radiation at 1.0 keV, emerging from this medium was reduced to about 9 per cent of its original value, since $I/I_0 = e^{-\tau}$, therefore, producing an x-ray shadow for photons with an energy of 1.0 keV. The absorption increases as the photon energy is decreased.

In figure 2.5 a simulation of an astrophysical x-ray shadow is presented. For generating this simulated x-ray shadow, the following astrophysical model was assumed. An unabsorbed thermal plasma, representing the LB, is shown in orange color. To this plasma a temperature of 8.1×10^5 K was assigned. The model is also composed by two other x-ray emission components, but absorbed by a given column density. The first of the former two components is a thermal plasma, representing a Galactic hot halo plasma, with a temperature of 1.5×10^6 K and shown in red

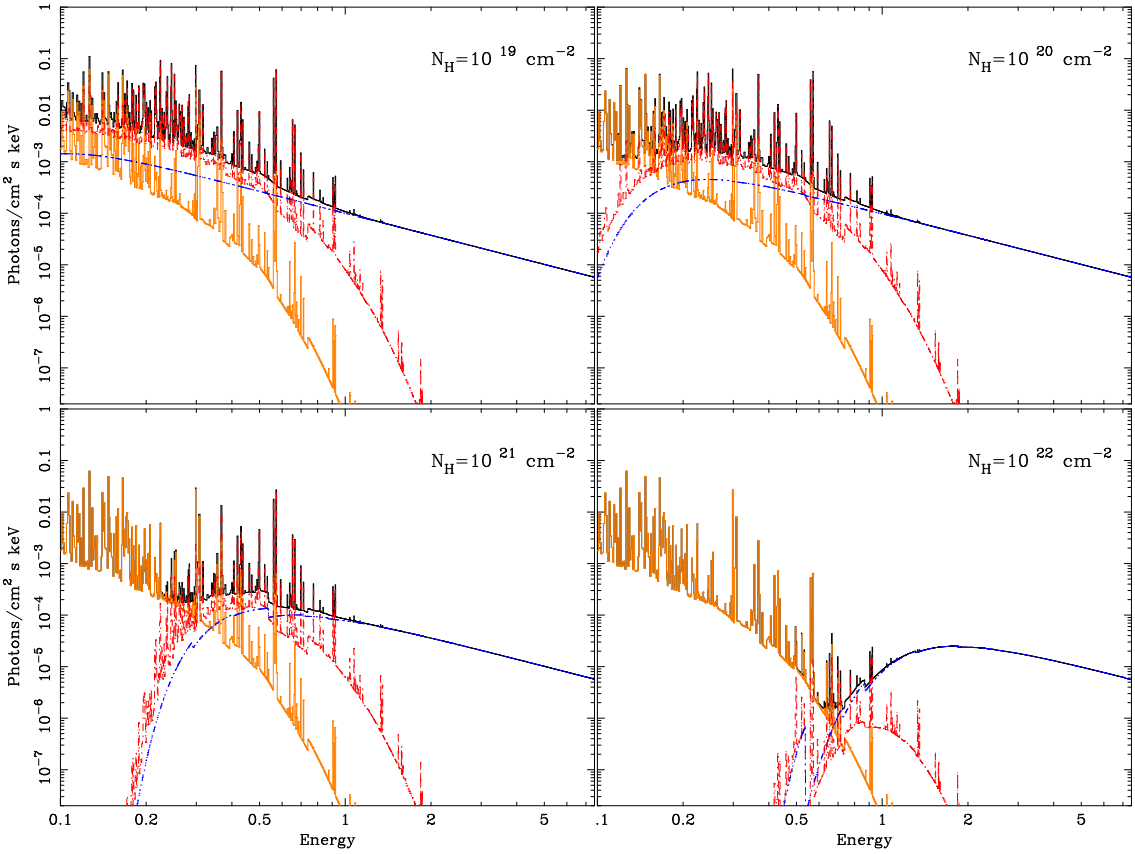

FIGURE 2.5: An ideal x-ray shadow experiment on the CXB. In this figure the effect of an x-ray shadow experiment, due to a molecular cloud in an ideal astrophysical situation is presented. The astrophysical model consists of two thermal plasmas and an extragalactic x-ray component. The first plasma of the model is the LB (orange), and the second plasma corresponds to a distant halo plasma (red). A temperature of 8.1×10^5 K and 1.5×10^6 K was attributed to the LB and halo plasmas, respectively. The power-law representing the extragalactic contribution is shown in blue. The total spectrum is shown as a solid black line (when visible). The halo and extragalactic x-ray emissions are subjected to absorption of intervening material of different column densities (N_H). The N_H of 10^{19} to 10^{20} cm^{-2} represents the Galactic N_H (an off-cloud situation), and the N_H of 10^{21} to 10^{22} cm^{-2} represents the column density of two regions associated to an ideal interstellar molecular cloud (an on-cloud situation). The x-ray absorption effect, due to intervening neutral material, in particular of the molecular cloud, produces an x-ray shadow in the ISM, permitting to disentangle the soft x-ray emission of the LB from the background. The photon energy is given in units of keV.

color. The second is the contribution of the CXB, represented by a power-law, with a spectral index of $\Gamma = -1.4$, and shown as the blue line. The total spectrum is shown in black (when visible).

The two absorbed x-ray components are then subjected to different column densities (N_H). Column densities ranging from 10^{19} to 10^{20} cm^{-2} represent typical values for the Galactic N_H and correspond to a non-shadow or off-cloud situation. As it can be seen in the two top plots, the LB emission is strongly contaminated by the the halo emission. If the N_H is increased to values of 10^{21} cm^{-2}, the very soft x-ray

photons, from the halo and extragalactic components start to be strongly absorbed. Increasing the N_H to 10^{22} cm^{-2}, all photons with energies $\lesssim 1.0$ keV are severely absorbed by the intervening material. These two situations correspond to an on-cloud observation, where an x-ray shadow is produced by a molecular interstellar cloud with a N_H gradient.

This is the ideal physical situation to study the emerging x-ray emission produced by the LB. Therefore, we need to study the x-ray emission towards interstellar molecular clouds with high N_H, which are inside of the LB or close to its boundaries, in order to be able to disentangle its contribution from other Galactic x-ray emissions.

2.5 Challenges to the Local Bubble Paradigm

In recent years it has been argued by Lallement [144, 145], that most of the EUV and x-ray emission, normally attributed to the LB model, may not be from the LB, but from the solar wind charge exchange (SWCE) mechanism.

The importance of the SWCE mechanism in the astrophysical context was first realized by Lisse et al. [146], who observed x-ray and extreme ultraviolet emission from the comet C/Hyakutake 1996 B2 during the ROSAT mission. The physical mechanism, put forward by these authors to explain the observed radiation, relies on the interaction between the neutral material of the comet and solar wind ions. It was assumed, that highly charged ions present in the solar wind, like the C VI, O VII, N VI, and Si X, capture electrons from the cometary neutrals. The captured electrons then de-excite radiating EUV and x-ray photons associated to these atomic transitions. In appendix A.1 (A.2), the x-ray emission lines that contribute to the soft x-ray emission, when the SWCE is present, are given. The five most important lines are the C V K_α, the N VI K_α, the O VII K_α, the O VIII Ly_α and the Ne IX K_α.

In the subsequent year the theoretical treatment was worked out by Cravens [147]. Since then, the SWCE is also a well established astrophysical phenomenon.

The presence of this astrophysical effect in the heliosphere can not be anymore ignored, even if the exact "quiescent" level of this contribution is not known. Another important fact about the soft x-ray emission due to SWCE is, that this contribution is a physical phenomenon variable in time. An effect, that might have been seen already during the ROSAT era by Freyberg [148] found a correlation between the solar wind parameter Dst and the occurence of long-term enhancements (LTEs) [113].

This same effect has been detected in several XMM-Newton observations. The most impressive one corresponds to an observation of the Hubble Deep Field North (HDFN) by Snowden et al. [149].

2.6 The LB as a local laboratory

The physical interpretation of distant astrophysical systems may depend heavily on the knowledge of our own local system. Therefore, a very good understanding of the Local Bubble, the Milky Way Galaxy, is extremely important, if we wish to properly

understand these distant systems.

Chapter 3

Data Reduction & Spectra Extraction

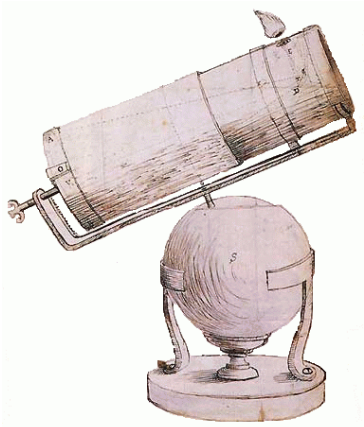

The telescope from Sir Isaac Newton. This figure is an original† drawing of Newton's self made reflector telescope. A different design to Newton's optical reflector has to be used in X-ray astronomy. The x-rays, that impinge normal to a surface, are largely absorbed, rather than reflected. Normal incidence mirrors, like in a Newtonian telescope, are then not adequat for x-ray photons. For x-ray telescopes a new design has to be developed in order to force high-energy photons to be reflected and then focused (grazing incidence). This is only achieved, when the x-ray photons have small incident angles to the surface. This is made possible by the use of parabolic and hyperbolic mirrors which then focus the x-ray photons. To improve the reflectivity of these mirrors they are, normally, covered by reflecting materials such as gold and nickel, for which the critical reflection angle at 1 keV is about 1 degree. The European Space Agency (ESA) has made a tribute to the English physicist Sir Isaac Newton by naming the X-ray Multi-Mirror (XMM) space telescope as XMM-Newton. †Source www.antiquetelescopes.org

3.1 Introduction

The X-ray Multi-Mirror (XMM-Newton) space telescope is a Cornerstone mission of the Horizon 2000 science programme from the European Space Agency (ESA). It was launched on December the 10^{th}, 1999, by an Ariane-v rocket, into a 48^{h} highly eccentric orbit, in order that its instruments could work outside the radiation belts surrounding the Earth. The XMM-Newton is presently the x-ray satellite with the combined highest sensitivity and spectral resolution operating mission. It has a slightly lower spatial resolution, when compared with the Chandra x-ray mission.

The XMM-Newton satellite is composed mainly by two payload modules, see Jansen et al. [150]. The first module consists of three x-ray telescopes, a parallel-mounted optical/UV telescope and two star trackers. Each of the three x-ray telescopes are composed by 58 Wolter I parabolic and hyperbolic mirrors shells, see Aschenbach et al. [151]. This combination of mirrors allows a reduction of the focal length of the telescopes to 7.5 meters, permitting at the same time the minimization of astigmatism. The XMM mirrors have an excellent angular resolution with a resolving power (Full Width at Half Maximum–FWHM) of ~ 6 arcseconds and a half energy width (HEW) of its point-spread function of ~ 15 arcsec. The total effective area of the three x-ray mirrors decreases from 1475 cm^2, 580 cm^2, to 130 cm^2 at 1.5, 9 and 12 keV, respectively.

The mirrors focus the x-ray photons onto a set of focal instruments, like the European Photon Imaging Cameras (EPIC) – the EPIC-MOS and EPIC-pn cameras – and the Reflection Grating Spectrometer (RGS), see den Herder et al. [152]. Besides the three x-ray mirrors there is an Optical/UV Monitor (OM), see Mason et al. [153].

The EPIC-MOS cameras, see Turner et al. [154], are composed by 7 identical and front illuminated CCDs. Each CCD is made of 600x600 pixels, and each pixel has a physical size of 40 μm (1.1 arcseconds), forming a field of view (FOV) of about 10.9 by 10.9 arcmin. Therefore, the combined FOV of each of the two MOS cameras is 30 arcmin. The read out time of these cameras is 1.5 ms, being sensitive to photons in the energy range of 0.15-12 keV, with an energy resolution of ~ 70 eV.

The EPIC-pn camera is made by a single monolithic silicon wafer with 12 integrated back illuminated pn-CCD chips, see Strüder et al. [155]. The pn camera is divided into four quadrants of three CCD elements. Each CCD chip is made of 64x200 pixels, and each pixel has a physical size of 150 μm (4.1 arcseconds) with a FOV of 13.6 by 4.4 arcmin. The total FOV of the EPIC-pn camera is also about 30 arcmin. The EPIC-pn camera can be operated in 6 modes. The read out time for EPIC-pn camera depends on the scientific window mode being used. For instance, in the extended full frame window mode the read out time is ~ 200 ms, while in the burst window mode the integration time is only 0.007 ms. The bandpass energy is similar to the MOS cameras, from 0.15 to 15 keV with a spectral energy resolution of ~ 80 eV. At 1.0 keV the total MOS sensivity is ~ 60 per cent of the EPIC-pn camera[1]. At 0.5 keV the total MOS sensivity decreases to ~ 40 per cent of the one of the EPIC-pn. The simulated sensivity of the EPIC-pn for an extended and unabsorbed source, with a $k_BT = 0.3$ keV ($\sim 3.5 \times 10^6$ K), using a Mekal thermal plasma, is about $\sim 6 \times 10^{-12}$ erg s^{-1} cm^{-3} in the energy band of 0.1 to 2.4 keV, with a total integration time[2] of 10×10^3 s (10^3 s $\equiv$ 1.0 ks). With an integration time of 100 ks a sensivity of $\sim 10^{-13}$ erg s^{-1} cm^{-3} is reached.

The x-ray photons are not the only photons to which the EPIC detectors are sensitive. They are sensitive to infrared (IR), optical (Op) and ultraviolet (UV) quanta. To avoid a high degree of contamination, due to these low energy radiation photons, there exists a set of three filters. The THIN filter is made of 1600 Å of

[1] From the XMM User's Handbook. Issue 1.1.

[2] See figure 26 from the XMM User's Handbook. Issue 1.1.

polyamide film, with 400 Å of aluminium evaporated onto one side. The MEDIUM filter is made by the same material, but in this case the thickness of deposited aluminium is 800 Å. The third filter is the THICK filter. This is made of 3300 Å thick Polypropylene with 1100 Å of aluminium, in conjunction with a deposited layer of aluminium with 450 Å.

3.2 Data Reduction

The general process of data reduction and spectra extraction in particular, for studying soft x-ray emission of Galactic diffuse sources, is delicate.

The environment in which the spacecraft is embedded is a harsh one. This means, that the system spacecraft-detector is continuously subjected to a bombardment of cosmic particles, which induces the formation of extra electronic signals that would not be present in normal conditions, during a scientific observation. These electronic signals, of different physical origins, contaminate the astrophysical data differently. To avoid their presence in the astrophysical data, the raw data has to be cleaned from these physical effects. Otherwise, their presence on the final data set would imply, that the "physical" results derived from it would not be meaningful.

There is a further complication. Contrary to the analysis of spectra from point sources, where we do have a proper instrumental background spectrum to be subtracted from the total spectrum, this is not the case for extended Galactic x-ray sources. For this case a different approach must be taken.

3.2.1 Cosmic-rays

Cosmic-rays induce the formation of fluorescent x-ray emission lines during their passage through the detectors. In the case of the XMM-Newton observatory, when they interact with the EPIC-pn and EPIC-mos cameras, they excite the material out of which they are made. These internal fluorescent emission lines are the end product of the interaction of cosmic-rays with the EPIC cameras. They are present in any EPIC spectrum and they are the result of the decay of excited electrons on the EPIC-pn and EPIC-mos cameras.

The most prominent features in the EPIC-pn camera are the Al K_α line at 1.487 keV, the Ni K_α at 7.5 keV and the Cu K_α lines at 8.048 and 8.6 keV. For a detailed analysis of the spatial, spectral and temporal behaviour of this internal detector emission, see Freyberg et al. [156]. For the EPIC-mos camera, besides the Al K_α, there is a strong fluorescent x-ray emission line of Si K_α at 1.7 keV, and weaker ones of Cr K_α at 5.5 keV, Mn K_α at 5.89, Fe K_α and Au L (emission lines), see Lumb [157] and Lumb et al. [158]. In addition to these bound-bound transitions from the detector, there is also a continuous bremsstrahlung emission produced by the cosmic rays.

3.2.2 Instrumental artifacts

In this category three possible types of data contamination can occur. They are the bad pixels, bad columns and out-of-time events.

Bad pixels correspond to CCD pixels which exhibit a signal above a given threshold in most of the read out frames. Most of these bad pixels are blanked out before the telemetry of on-board electronics. However, this does not mean that all bad pixels are properly flagged during this process, because they can be in some transient state, and therefore elusive, to the on-board software. Bad pixels can be recognized as bright pixels in an image. At low energies they are the result of a leakage of charge during the integration CCD frame accumulation time. These small signals are indistinguishable from a signal generated by a real x-ray photon.

There are other additional features peculiar to each camera [158]. In the case of the EPIC-pn camera, they are blocks of bright pixels, typically 4 pixels in extent, along the read out direction. Their presence varies from observation to observation and they are an artefact of the CCD offset bias level calculation at the start of each observation. When calculating the precise local zero signal level, the average values for each pixel are determinated from about 100 read outs. However, this zero level signals can change over time due to cosmic rays and due to highly ionizing events, causing an electronic baseline drop.

At an energy of $\lesssim$ 240 eV it is possible to find streaks at the edge and near the middle of the CCD array. Some of these features can be explained by the same occurrences of electronic baseline drop. They can also be the result of charge transfer loss during the read out, causing the creation of a false event.

The EPIC CCDs for simultaneous x-ray imaging and spectroscopic applications must be operated in a way, that only one x-ray photon hits the detector pixel without an overlap in time and position of another photon.

For the EPIC-pn CCDs a complete read out cycle takes, in the full frame (FF) window mode, 73.3 ms for a single CCD. From this time, 4.6 ms are required for the read out process itself, while the remaining 68.7 ms are used for scientific integration time. In the case of the extended Full-Frame (eFF) window mode, the complete read out cycle is 199.2 ms, and from this, 4.6 ms are needed for the read out itself. Therefore, in this case, the integration time is 194.6 ms.

These numbers mean, that during the IMAGING mode a percentage of x-ray photons hits the CCD, creating the so-called out-of-time (OOT) events. In the eFF window operating mode a total of 2.3% photons will be read out during this process. For the FF window mode a total of 6.3% events will happen during the read out phase. More details on the EPIC-pn camera can be found in Strüder et al. [155] and references therein.

During the read out process, the charges are shifted along the Y direction, which leads to the loss of the Y positional information. Therefore, during this read out process the information of the X coordinate, of this photon, is known, while the information of the Y coordinate is lost producing the OOT events.

3.2.3 Minimum Ionizing Particles

The minimum ionizing particles, or MIPs, are another possible source of contamination. In the EPIC-pn camera the MIPs have been used to monitor the high background space environment [159, 156]. The MIPs are due to high energy particles, such as α particles, protons, etc, that penetrate the detector, creating electron-hole pairs. The charge deposited in each detector pixel is very high - the mean charge deposition in both EPIC cameras is greater than 10 keV per particle. These events typically cross multiple pixels, and as such can be rejected by the event analyzer in the EPIC-pn and EPIC-mos cameras aboard of XMM-Newton satellite.

Since these events cross several pixels, they are easily identified as a non x-ray photon and should therefore be rejected. In the case of the EPIC-mos cameras the expected rejection efficiency is of the order of $\sim$ 99% [160]. For the EPIC-pn camera this information is not available. This issue will be discussed in more detail in section 3.4, when a second closed filter observation is used for the purposes of producing an instrumental background spectrum. Another component, made by secondary gammas and excited electrons is expected to take place due to the particle interactions in the surroundings of the spacecraft [160].

3.2.4 Soft Proton Flares

A physical phenomenon which considerably affects the XMM-Newton and the Chandra X-ray performance, are the soft proton flares (SPFs). The origin of these proton flares is still a matter of debate. The standard interpretation is, that these soft protons have a solar origin. It is common in the literature to find the designation of soft solar protons. However, measurements of the XMM-Newton indicate, that these events are likely to be related with magnetospheric reconnection, during which the soft protons are accelerated to keV energies [157].

Even if they seem to be an unpredictable phenomenon, they occur more frequently further away from the apogee[3][157]. They have typically energies of the order of a few 100 keV. This type of contamination by SPFs, affects 40 to 50 per cent of the dedicated user observing time. Unfortunately, this seems to be an unpredictable physical process occuring in the environment of the satellite, which means that all observations are suitable to be affected by it.

3.3 Cleaning and Filtering the Raw Data

An algorithm was developed, using the XMM-Newton Data Science Analysis Software[4] (SAS), to clean the EPIC-pn event files from bad pixels, bad columns and from periods of soft proton flares. In addition, all detected point sources in the field

[3]The point in the orbit of a satellite which is furthest away from the focus of the orbit of the satellite. For the XMM-Newton the apogee is 114000 km and the perigee is 7000 km. The XMM-Newton has a 48 hour period and has an 40° inclination orbit.

[4]For further details on the XMM-Newton Data SAS tasks, consult the documentation available on-line at http://xmm.vilspa.esa.es/sas/7.0.0/doc/packages.All.htm

of view were also removed, since we were only interested in studying the extended diffuse Galactic x-ray emissions.

In the first stage of the algorithm the procedure of removing the bad columns and bad pixels is implemented. This step is done with the **evselect** task and by using the filter expression: (FLAG == 0). With this flag, not only bad columns, bad pixels and cosmic rays are removed, but all events at the edge of a CCD and at the edge to a bad pixel. If no care is taken, the charge associated to these bad pixels might be lost into nearby pixels, producing, e.g., a wrong spectrum.

After filtering the data for such detector noise, a count rate or a light curve in a given energy band is created by the SAS **evselect** task, in order to be used to clean the data from periods affected by soft proton flares (SPFs). For producing the count rate light curves, the standard time bin size of 40 seconds was used. These light curves are then transformed into a histogram to investigate the distribution of counts for that particular observation. Since the data is still contaminated with SPFs, this means that our histogram will be composed by the diffuse x-ray emission, x-ray sources and SPFs. As a random process, the SPFs counts will distort the expected Poisson count distribution for constant sources, specifically for extended diffuse x-ray sources. Galactic x-ray emission of plasmas are constant astrophysical processes, at least during the observation time. These histograms are then used to define a domain of count rates in which the data is assumed not to be contaminated by SPFs. These count rates are further used to define good time intervals.

A good time interval (GTI) is then created with the SAS **tabgtigen** task for further cleaning the raw data from SPFs periods. At this stage the event file should be clean from bad pixels, bad columns and from SPFs periods. For pre-caution, however, the event file is always checked again for some possible un-removed bad pixels or bad columns. The event file is then filtered using the GTI file. Products, such as images and spectra are now possible to be produced. Simultaneously, the data is filtered, using the filter keyword (PATTERN ≤ 4). This less severe constrain on the pattern keyword has been allowed only for source detection purposes. For spectra extraction the keyword PATTERN was set to zero, which means, that only events flagged as single were taken, when extracting spectra.

At this stage, five images in the energy bands of 0.25-0.5 keV, 0.5-2.0 keV, 2.0-4.5 keV, 4.5-7.5 keV and 7.5-12.0 keV are produced for source detection with the SAS **edetect_chain** task. The detected point sources are then removed, using the **fselect** task of the FUTILS sub-package from the FTOOLS[5] package provided by the NASA High Energy Astrophysics Science Archive Research Center (HEASARC). The use of some tasks from FTOOLS—instead of SAS tasks— was necessary, because during the development of most part of this thesis, it was not possible to remove point sources and extract spectra from extended sources from the remaining detector area without problems. More specifically, problems would have appeared by using the **arfgen** task. Negative or unacceptable positive values would have been obtained for the bad pixel and chip gap fraction parameter. This meant, that a different solution had to be found. To work around this problem, an algorithm

[5] http://heasarc.gsfc.nasa.gov/lheasoft/ftools/

was constructed, in order to remove the point sources without the use of the SAS **evselect** or the SAS **region** tasks. Now, these technical problems seem to have been solved since the middle of the year of 2006.

The algorithm was implemented in FORTRAN 90. As input information, the source counts and the source background counts calculated by the SAS **edetect_chain** task were used. These information is stored in the emllist.fits file. With the use of a point spread function (PSF), the radius at which the level of the source counts equals a given fraction of the source background counts could be estimated and used to define a cut out radius. The cut out radius is calculated, assuming that the PSF on-axis describes all sources, even the ones off-axis. The PSF dependences, such as energy, off-axis angle and others, were not considered, since we were mainly interested in finding a maximum radius, at which the source counts equals a defined fraction of the source background counts. The drawback of this assumption is the reduction of the available detector area for spectra extraction. The fraction value of the source background counts used, was always less than 10 per cent of the source background counts. Whenever necessary, this parameter was lowered, in order to insure that the cut out radius was large enough to contain the source and the spikes, if present. Having reached this stage, the detected point sources were removed from the original raw data file after cleaning and filtering the event file with the SAS **evselect** task, having as filter expression: (PI in [200:7000])&&(PATTERN == 0)&&(FLAG == 0).

The new clean and filtered event file was then used to produce new products, such as a new GTI file with a different time bin size. This new GTI file was then used to produce count rate light curves, having the same time bin size as the newly GTI file in specific energy bands. The energy bands are the 0.5-0.75 keV, 0.75-2.0 keV and 2.0-8.0 keV, which allow us to study the diffuse soft x-ray emission variability during the observation. This is particular important to detect possible x-ray emission due to solar wind charge exchange (SWCE) [149]. In the energy band of 2.0-8.0 keV the dominant emission is due to the Cosmic X-ray Background,[6] which is constant. For the energy band case of 0.5-0.75 keV, the emission is of galactic, intergalactic or more "local" origin. The galactic and intergalactic x-ray emission in the observing time scale is constant. Therefore, if, after removing the detected point sources, variability is detected in this band, it means, that there is a local contribution most likely, due to the emission of the O VII, O VIII and Fe XVII ions present in the solar wind. If, indeed, there is variability, then one should observe a deviation of the count rate on this soft band, in the 0.5-0.75 keV versus 2.0-8.0 keV scattergram. The next step of the algorithm is the extraction of spectra.

3.4 Spectra Extraction

The spectra extraction is performed, using the SAS **evselect** task. At this stage the event file has been cleaned and filtered in the space phase of energy, time and

[6]The Cosmic X-ray Background is believed to be mainly produced by an unresolved cosmic population of Active Galactic Nuclei (AGNs).

in the photon events quality. In terms of the photon energy, we have only made use of photons with energy lying in the interval of 0.2 keV to 7.5 keV. The main reasons to restrict the photon energies to the former interval, is the poor calibration below 0.2 keV and the presence of instrumental lines above 7.5 keV. However, during the spectral fit procedure, the energy interval was constrained to the interval of 0.25 keV to 7.5 keV. The reason to start the x-ray spectral fit at 0.25 keV and not at 0.2 keV is related to the fact, that the APEC plasma code has a lack of emission lines below 0.25 keV. Therefore, x-ray data below 0.25 keV were not included during the fit.

The event file has also been filtered with a GTI file, in order to remove periods affected by soft proton flares (SPFs). The photon quality is ensured by using the keyword (PATTERN==0) in the filter expression. This means, that spectra will only be composed by single-pixel x-ray photons. If we would allow photons with a (PATTERN $>$ 0), then the spectrum would also be composed by photons, which hit the boundary of the pixel. When the photon hits a region near the boundaries, part of the deposited charge is lost to a nearby pixel and two "photons" will be read out, faking a different spectrum. Also, in order to avoid problems resulting from extracting spectra from regions of the detector affected by the out-of-time events, due to bright x-ray sources, the associated out-of-time columns and nearby ones were removed. By doing so, we ensure that our spectrum is as little as possible contaminated by OOT spectra of bright sources.

The analysis of an astrophysical spectrum requires the existence of a proper instrumental background spectrum for subtraction purposes. For the case of spectral analysis of point sources it is sufficient to use some near region to the source on the CCD, to obtain a background spectrum. This simple technique will subtract from the spectrum all spectral features associated to the detector. In principle, with this procedure, not only all spectral detector features are removed, but also the astrophysical background spectrum is removed from the source spectrum.

The technique described above is not applicable, when analyzing the spectrum of diffuse x-ray sources, which fill all field of view of the detector. And in particular, when we are interested in studying the astrophysical "background" itself. The astrophysical background is composed by several components of local, galactic, intergalactic and cosmic origin. The local emission contribution can be composed by some small percentage of x-ray emission due to solar wind charge exchange (SWCE). The galactic contribution, which is not isotropic in nature, is due to the Local Bubble (LB), the hot interstellar gas and due to the hot galactic halo. The intergalactic component is believed to be due to the hot baryons, while the cosmic component is the result of all contributions on an unresolved population of AGNs. Therefore, our spectrum is made by these contributions, which must be taken into consideration when modelling the spectrum. However, the main difficulty does not arrive, in principle, from these astrophysical components themselves, but from the instrumental background, in conjunction with short observation times.

To study these several of x-ray astrophysical backgrounds, a new method had to be developed to deal with the instrumental background. The adopted approach is to consider, that a representative instrumental background spectrum can be obtained from a closed filter EPIC-pn XMM-Newton observation. There is, however,

a number of requirements to follow when using this approach.

In the first place, the same filtering criterion as used for the science observation must be applied for the closed observation. Extremely important is the removal of the exact detector regions of the closed observations, as the ones corresponding to the extraction sources and OOT events.

Secondly, we must verify that our observation with the filter wheel in the closed position had the same operating mode as the science observation. This means, that, if the science observation used, for instance, the Extended-Full-Frame (eFF) mode, then the proper closed observation must have the same eFF mode. The consequence of not using a closed observation with the same operating mode means, that the OOT events contribution will be different with a subsequent contamination of the data, for instance.

The third requirement to follow is, to verify that both, science and closed observations, have the same detector operating settings.

The fourth and until now undetected problem, to deal with, is the radiation background level during each of the observations - science and closed. As mentioned in the beginning of this chapter, the environment in which the spacecraft is embedded is a harsh one. This means, that the XMM-Newton satellite is subjected to a multitude of types of radiation: cosmic rays, soft protons, ionizing particles and others.

During the study of the x-ray sky background spectra obtained by the EPIC-pn camera, it was realized, that the parameters derived for the power-law, representing the CXB, had different values from the ones obtained on other analyses to the CXB by Gendreau et al. [161] and Lumb et al. [158].

The difference between these derived values was found to be the result of the subtraction of the sky spectrum from an "improper" detector background spectrum. The conflict between these different analyses was resolved after realizing, that, most likely, not all MIP events had been properly detected/removed on-board of the XMM-Newton space observatory.

Since the launch of the XMM-Newton satellite, the environment radiation level has been monitorized using the collected data from the number of maximum ionizing particles (MIPs) [159, 156]. If the event amplitude, which is read out for a pixel, exceeds a given threshold (3000 adu $\sim$ 15 keV), then not only the column, in which this pixel is located, but also the left and right columns are rejected by the on-board software for the Full-Frame (FF), for the Extended-Full-Frame (eFF) and for Large-Window (LW) modes. The number of rejected columns is written as "Discard Line Counter" (NDISCLIN) to the PNAUX2 extension into the auxiliary file (...AUX.FIT). The observed number of rejected columns, which basically gives the number of columns in each quadrant of the EPIC-pn camera, where a MIP is detected, were used to derive a numerical value, that could be used as a correction factor for the excess of deposited charge on the EPIC-pn camera. This issue will be developed further in § 3.6 when discussing the method, used to calculate the average number of rejected columns, and where it is explained how to correct it.

The next step of the algorithm is the extraction of spectra for scientific analysis with the SAS **evselect** task. This is done by selecting the interesting regions in the

EPIC-pn field of view in detector coordinates (DETX,DETY). The exact regions in detector coordinates of the closed observation are used to extract a proper instrumental background spectrum. By doing so, we avoid the introduction of problems that would appear, when using distinct detector regions for the instrumental background spectra relative to the scientific ones. The objective of this procedure is to reduce possible effects arising from the detector spatial behaviour, see Freyberg et al. [156].

The three final steps of the algorithm consist on the creation of a redistribution matrix file (RMF) with the SAS **rmfgen** task and the creation of an ancillary response file (ARF), with the SAS **arfgen** task for each individual spectrum. The SAS **rmfgen** task generates the appropriate responses of the instrument as a function of energy and PI channel for the extracted spectra, while the SAS **arfgen** task is used to calculate the proper effective area, filter transmission and quantum efficiency for each spectrum. These spectra are then binned and corrected with the suitable detector background spectra with the response of the instrument and with the ancillary response using the HEASARC FTOOLS **grppha**[7] task.

We could then proceed for spectral analysis with the X-Ray Spectral Fitting Package[8] (XSPEC). However, before that, an investigation of the spectral signature of soft proton flares was conducted.

In the EPIC-mos cameras there is a substantial active CCD area outside the nominal field of view, and defined by the optical blocking filter, that is normally used to obtain the instrumental background spectrum. In general, it is assumed that this zone is representative of the true EPIC-mos cameras internal background, because it is not expected that the soft protons and sky photons are focused by the x-ray mirrors to this region of the detectors.

3.5 The Spectral Signature of the Soft Proton Flares

An investigation on the spectral signature of the soft proton flares (SPFs) is mandatory, because no study has been performed to investigate the consequences of the presence of soft protons in the data. In particular, it is important to investigate, if there are x-ray emission lines associated to the spectrum of the soft protons. To performe this analysis, a set of XMM-Newton observations affected by SPFs was used. This set of observations is shown in table 3.1.

The spectrum, obtained during periods contanimated by SPFs, is composed by the astrophysical spectrum plus the spectrum due to the SPFs. Therefore, for revealing the signature of SPFs, a spectrum composed only by the astrophysical signal, the cleaned period, had to be used for background subtraction purposes.

What was done to perform such a study was, to clean the raw data of these observations from bad pixels and bad columns, and to remove the area of the detector not covered by the the x-ray telescope. Basically, we follow the algorithm,

[7] http://heasarc.nasa.gov/docs/software/ftools/heasarc.html

[8] The documentation of this x-ray spectral fitting package can be found at the HEASARC website http://heasarc.nasa.gov/docs/xanadu/xspec/

TABLE 3.1: The XMM-Newton observations used to study the spectral signature of the soft proton flares.

REV[a] #	OBSERVATION ID	FILTER	OBSERVATION DATE	EPOSURE TIME [ks]	GALACTIC LONGITUDE	GALACTIC LATITUDE	TARGET NAME
0131	0110660101	MEDIUM	2000-08-26T07:03:54	17	159.18°	−34.46°	MBM 12 A
0213	0110660301	THIN	2001-02-05T16:00:09	26	159.31°	−34.55°	MBM 12 B
0230	0086360301	MEDIUM	2001-03-11T13:29:45	71	168.74°	−15.48°	V410 Tau A
0230	0086360401	MEDIUM	2001-03-12T10:20:21	41	168.74°	−15.48°	V410 Tau B
0271	0111550401	THIN	2001-05-18T09:38:04	92	125.90°	+54.86°	HDFN*
0321	0112480101	THIN	2001-09-09T13:12:03	16	355.50°	+14.58°	Oph 1
0321	0112480201	THIN	2001-09-09T19:41:34	14	355.26°	+14.39°	Oph 2
0401	0109880101	THIN	2002-02-15T16:57:16	122	182.48°	−28.27°	Abel 478
0405	0112480301	THIN	2002-02-24T13:46:56	14	355.05°	+14.26°	Oph 3

(a) XMM-Newton revolution number. * The Hubble Deep Field North target.

described in section 3.3, but only for the EPIC-pn data. After removing the sources, we have created three GTI files—when possible—reflecting different observation periods. With these GTI files spectra were extracted from 10 regions of the detector. The first nine regions have a radius of 5.83(3) arcmin, having an off-set, relative to each other, in order to cover all the field of view of the detector. This was done in order to investigate possible variations over the detector area. The tenth region has a radius of 12.5 arcmin, and basically covers all detector CCDs. The exact center positions of these regions, given in detector coordinates, are shown in table 3.2.

After the extraction of point sources, a new count rate light curve was produced. This light curve is then transformed into a histogram, which is used to define appropriate count rate intervals. With the use of these intervals, new GTI files are created. These GTI files are then used to extract spectra from these different periods, reflecting the contamination or not by SPFs. The first GTI file is used to produce spectra with the generic designation of Spectrum1i.pha, with i running from 01 to 10, see table 3.2.

TABLE 3.2: The spectra extraction regions in detector coordinates used for the study of the spectral signature of soft proton flares.

REGION NUMBER i	DETX	DETY	RADIUS	REGION NUMBER i	DETX	DETY	RADIUS
01	+4956.5	+6672.5	7000	06	+4956.5	−767.5	7000
02	−1843.5	+6672.5	7000	07	+4956.5	−9000.5	7000
03	−9363.5	+6672.5	7000	08	−1843.5	−9000.5	7000
04	−9363.5	−767.5	7000	09	−9363.5	−9000.5	7000
05	−1843.5	−767.5	7000	10	−2243.5	−1167.5	15000

The spectra with the generic designation of Spectrum2i.pha are obtained with the second GTI file, while the Spectrum3i.pha spectra were created with the third GTI file. In the following discussion the cited errors are given with a 90% confidence level. The spectral index shown here corresponds to the ones from region number 10. The results for the other regions can be found in the tables of appendix B.1.

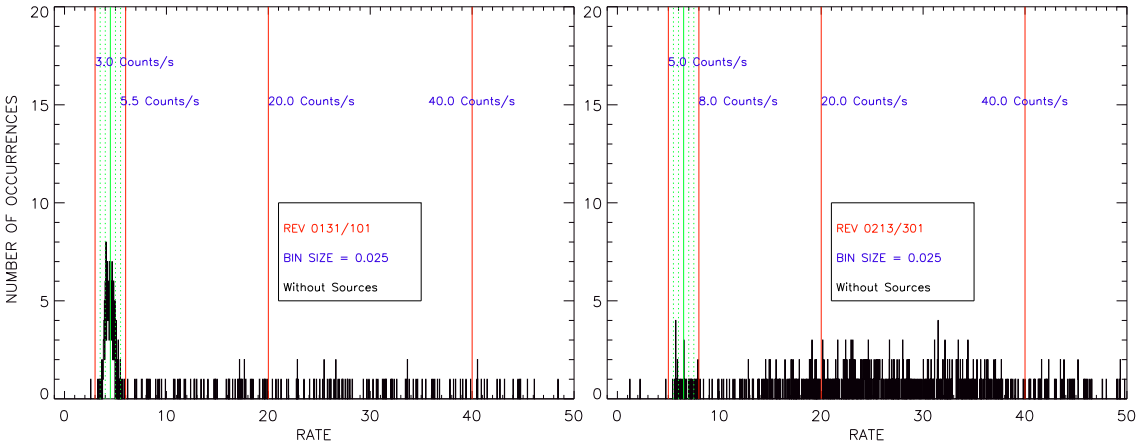

FIGURE 3.1: MBM 12: The count rate histograms of MBM 12 A (left) and MBM 12 B (right) observations. Count rates above 50 were omitted from the plot and count rates above 40 were not considered for this analysis.

3.5.1 The spectral signature of SPFs, during two MBM 12 XMM-Newton observations

These scientific observations were assigned to study the diffuse x-ray emission towards the MBM 12 molecular cloud. In particular, to use the x-ray shadow produced by the molecular cloud to study the LB emission and the galactic hot halo emission. Two XMM-Newton observations, with a slight positional off-set, were used to study the high background due to SPFs about six months apart. The observation with the ID 0110660101, from revolution 0131, will be designated from now on simply as MBM 12 A and the observation 0110660301, from revolution 0213, as MBM 12 B. The XMM-Newton MBM 12 A observation was performed as part of the Guaranteed Time program on August the 26th, 2000, with a total duration of 17 ks. This XMM-Newton EPIC-pn observation was performed, using the window Full-Frame (FF) mode, and with the filter wheel in the MEDIUM position. The second observation MBM 12 B was done within the Guaranteed Time program on February the 5th, 2001, with a total integration time of 26 ks. In this case the XMM-Newton EPIC-pn observation was performed with the filter wheel in the THIN position and with the FF mode.

In figure 3.1 are shown the two corresponding histograms produced with the count rate light curves. In observation MBM 12 A three count rate intervals, defined as 3.0 - 5.5, 5.5 - 20.0 and 20.0 - 40.0 counts/s, were created. They correspond to spectrum1i.pha, spectrum2i.pha and spectrum3i.pha, respectively. In the case of observation MBM 12 B, the intervals defined were 3.0 - 8.0, 8.0 - 20.0 and 20.0 - 40.0 counts/s. As it can be seen, both observations are contaminated by SPFs. In particular observation MBM 12 B, where only a short period is not irremediably lost, see table 3.3.

The higher count rate for the good period (spectrum1i.pha) in observation MBM 12 B is the result of observing off-cloud. Therefore, obtaining more photons from the background of MBM 12 molecular cloud.

TABLE 3.3: The MBM 12 SPFs periods. The periods were defined using different count rates. For each period a set of 10 spectra was produced, with the index i, running from 01 until 10, see table 3.2. This study was done in observations MBM 12 A and MBM 12 B.

PERIOD	COUNT RATE	SPECTRA DESIGNATION	USED TIME MBM 12 A	USED TIME MBM 12 B
1	3.0/5.0 - 5.5/8.0	Spectrum1i.pha	8.4 ks	1.4 ks
2	5.5/8.0 - 20.0	Spectrum2i.pha	2.5 ks	4.4 ks
3	20.0 - 40.0	Spectrum3i.pha	2.7 ks	14.6 ks

In order to study the SPF's spectral signature we have performed a spectral fit, using as background spectra the spectra obtained during the good periods. These spectra are well fitted with an unfolded power-law to the response of the detector. In XSPEC this is implemented as power-law/b. In the appendix table B.2 the results of these fits are presented. For that, the SPFs from period two and spectra from period one were used as background. The results of these two observations have revealed that the spectral index was 0.60 ± 0.03 and 0.65 ± 0.04, for MBM 12 A and MBM 12 B, respectively. The spectral index is represented by Γ and the normalization by Nor in the appendix tables. The plots from these fits for regions number 10 are shown in figure 3.2.

The same was done for period three. As a background we have used the spectra from period one. Again, an unfolded power-law fitted the spectra very well. The results of these fits are presented in the appendix table B.3 for both, MBM 12 A and MBM 12 B observations. In this case, and for the detector region number 10, the spectral indices, derived from the spectral fits were 0.60 ± 0.02 and 0.64 ± 0.01 for MBM 12 A and MBM 12 B, respectively. The plots from these fits, for region number 10, are shown in figure 3.3.

Finally, we have compared the SPFs from periods 3 and 2. In this case we have used the spectra from period 2 as the background spectra. As before, these spectra are well fitted with an unfolded power-law. In appendix table B.4 the results from these fits are shown for all detector regions. Approximately, the same spectral indices were found. The spectral index obtained for region number 10 were 0.60 ± 0.03 and 0.62 ± 0.02 for MBM 12 A and MBM 12 B, respectively. The plots from the fits from region number 10 are shown in figure 3.4.

3.5.2 The spectral signature of the SPFs during two observations of the V 410 T-Tauri star

The scientific purpose of these observations was the study of the x-ray emission from the T-Tauri star V410. These two observations were chosen, in order to study the SPFs in two consecutive observations and in exactly the same direction of the sky. To simplify the writing we will designate from now on the XMM-Newton observations, see table 3.1, with IDs 0086360301 and 0086360401 from revolution 0230 by V 410 A and V 410 B, respectively. The V 410 A and V 410 B observations were performed as Guaranteed Time on March the 11^{th} and 12^{th} of 2001 with an integration time

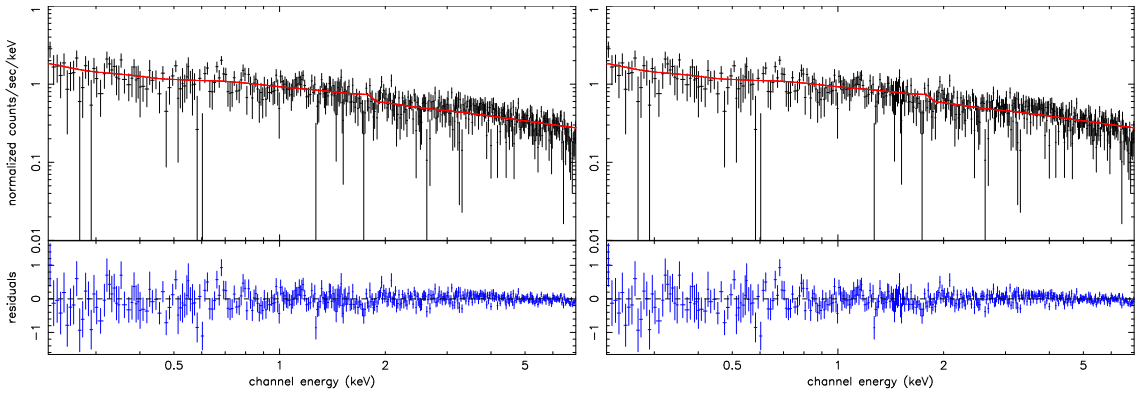

FIGURE 3.2: MBM 12. The left plot shows the spectral signature of the soft protons from period 2, using period 1 as background from region number 10, from the MBM 12 A observation. On the right plot the equivalent spectrum of the soft protons from period 2 is shown, with period 1 as background of region number 10 from the MBM 12 B observation. Both spectra are well fitted by an unfolded power-law.

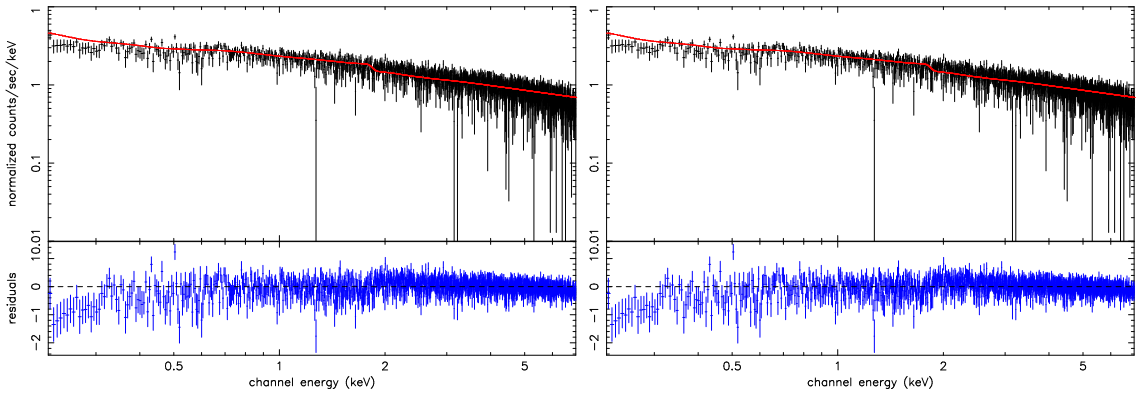

FIGURE 3.3: MBM 12. The left plot shows the spectral signature of the soft protons from period 3, using period 1 as background from region number 10 from the MBM 12 A observation. On the right plot the equivalent spectrum of the soft protons from period 3 is shown, with period 1 as background of region number 10 from the MBM 12 B observation.

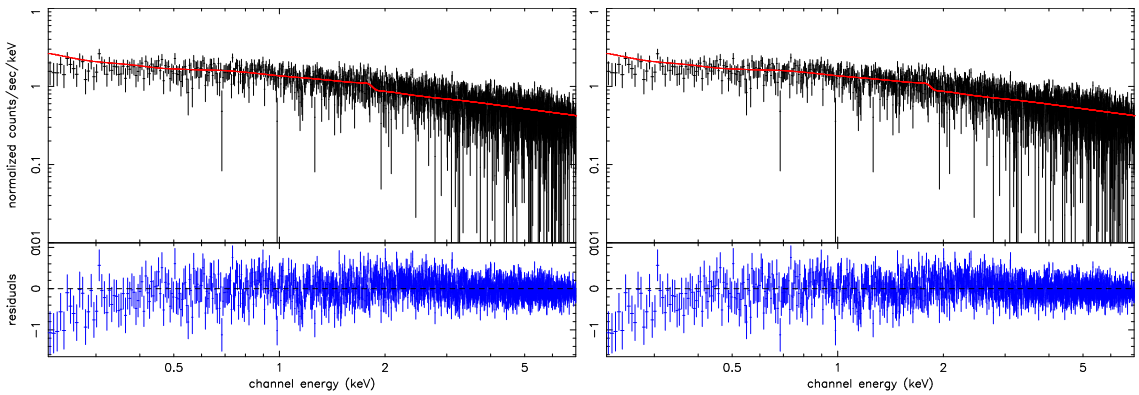

FIGURE 3.4: MBM 12. The left plot shows the spectral signature of the soft protons from period 3, using period 2 as background from region number 10 from the MBM 12 A observation. On the right plot the equivalent spectrum of the soft protons from period 3 is shown, with period 1 as background of region number 10 from the MBM 12 B observation, for observation MBM 12 A.

TABLE 3.4: The V410 Tau SPFs periods. The periods were defined using equal count rates. For each period a set of 10 spectra was produced, with the index i running from 01 until 10, see table 3.2. This study was done in observations V 410 A and V 410 B.

PERIOD	COUNT RATE	SPECTRA DESIGNATION	USED TIME V 410 A	USED TIME V 410 B
1	4.5 - 7.0	Spectrum1i.pha	23.6 ks	12.6 ks
2	7.0 - 20.0	Spectrum2i.pha	21.4 ks	12.1 ks
3	20.0 - 40.0	Spectrum3i.pha	10.4 ks	2.9 ks

of 71 and 41 ks, respectively. The EPIC-pn camera was operated in both cases in the FF mode, with the filter wheel in the MEDIUM position.

In figure 3.5 we show the histograms of the count rate for these two observations only from 0 to 40 counts/s. This interval was then divided in three subintervals,

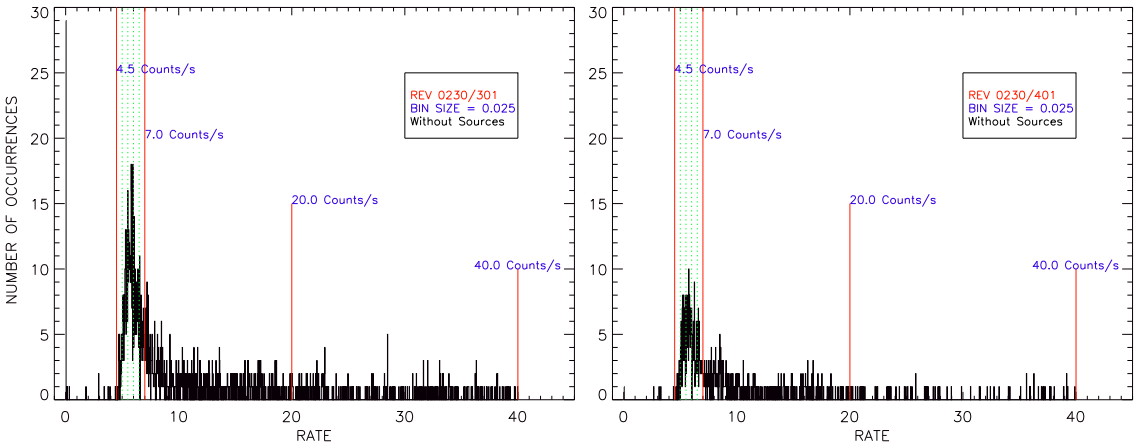

FIGURE 3.5: V410 Tau. The count rate histograms for observations V 410 A (left) and V 410 B (right) of revolution 0230. The count rate is only shown in the interval from 0 to 40. Count rates above 40 were omitted from the plot and from the present analysis.

where spectra were extracted for 10 regions. For these two observations we used the intervals from 4.5 to 7.0, from 7.0 to 20.0 and from 20.0 to 40.0 counts. In table 3.4 we show the relevant information of the count rate and the exposure times for each observation.

As discussed in the subsection 3.5.1 we have first studied the spectral signature of the SPFs from period 2, using background spectra obtained from period 1, from the uncontaminated period. The spectra were well fitted with an unfolded power-law. The complete results of such fits are shown in the appendix table B.5. The spectral fit for region number 10 gives a spectral index of 0.76 ± 0.04 and 0.64 ± 0.02, for V 410 A and V 410 B, respectively. The plots of these two fits are shown in figure 3.6.

The same was performed for period 3. For that, we have fitted the spectra with an unfolded power-law and used as background spectra the spectra from period 1. The results are presented in the appendix table B.6. In this case the spectral fits have revealed a spectral index of 0.69 ± 0.04 and 0.59 ± 0.02, for V 410 A and V 410 B, respectively. The plots from these fits, for the detector region number 10, are shown

in figure 3.7.

We have also performed a spectral fitting between the spectra from period 3 and 2. As done before, we have fitted the spectra with an unfolded power-law, using the spectra from period 2 as the background spectra. Again, the total results from this fits are shown in the appendix table B.7. The spectral indices, derived from these analyses on region number 10 were 0.67 ± 0.04 and 0.57 ± 0.03, for V 410 A and V 410 B, respectively. Figure 3.8 shows the two corresponding plots from these two spectral fits. As it can be seen, there seems to be a different population of soft protons occurring during these two observations, due to their different spectral indices.

3.5.3 The spectral signature of the SPFs during one of the Hubble Deep Field North observations

This particular observation was chosen, because during this observation solar wind charge exchange (SWCE) was detected [149]. It is important to verify, if some x-ray emission due to this physical mechanism could be present in periods of SPFs. If present, then one should expect emission features at low energies, between 0.2 to 1.0 keV. We have denominated the XMM-Newton observation with ID 0111550401 from revolution 0271 simply as HDFN.

The EPIC-pn camera was operated in the FF mode, using the filter wheel in the THIN position. This XMM-Newton observation executed on May the 18^{th}, 2001, was part of the Guaranteed Time.

As described in the previous subsections, a count rate light curve is produced for this particular observation. This light curve is then transformed in a histogram as shown in figure 3.9. The light curve is then divided into three different count rate intervals, namely 5.0 - 8.0, 8.0 - 20.0 and 20.0 - 40.0. The first interval corresponds to period 1, the second interval to period 2, and finally, the third interval to period 3, see table 3.5 for more details. After extracting the spectra for each of these periods, we have fitted the spectra with an unfolded power-law, like done for the other previous observations.

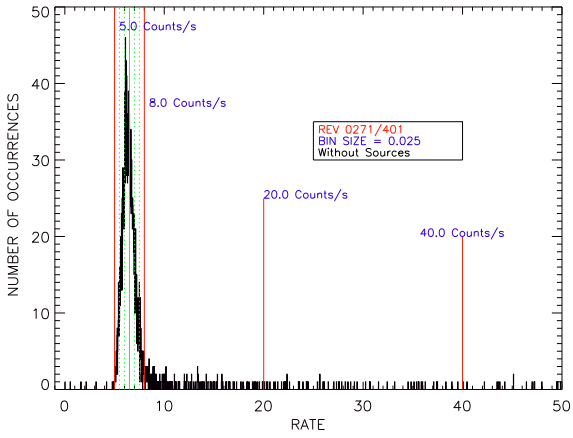

FIGURE 3.9: HDFN histogram. The count rate histograms for observation HDFN. The count rate is only shown in the interval from 0 to 50. Count rates above 50 were omitted from the plot and above 40 not included in the analysis.

The spectra from period 2 were fitted, using as background spectra the spectra from period 1. The results of these fits for each detector region are shown in the appendix table B.8. The spectral index derived from the fit was 0.72 ± 0.03 for the detector region number 10. The corresponding plot for region number 10 is shown in figure 3.10a.

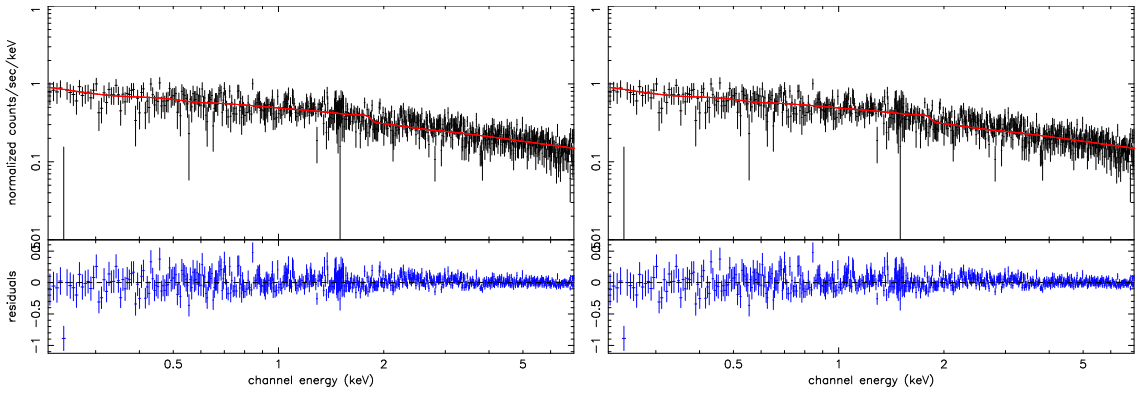

FIGURE 3.6: V410 Tau. The left plot shows the spectral signature of the soft protons from period 2, using period 1 as background from region number 10 of observation V 410 A. On the right plot the equivalent spectrum of the soft protons from period 2 is shown, using period 1 as background from region number 10, from observation V 410 B.

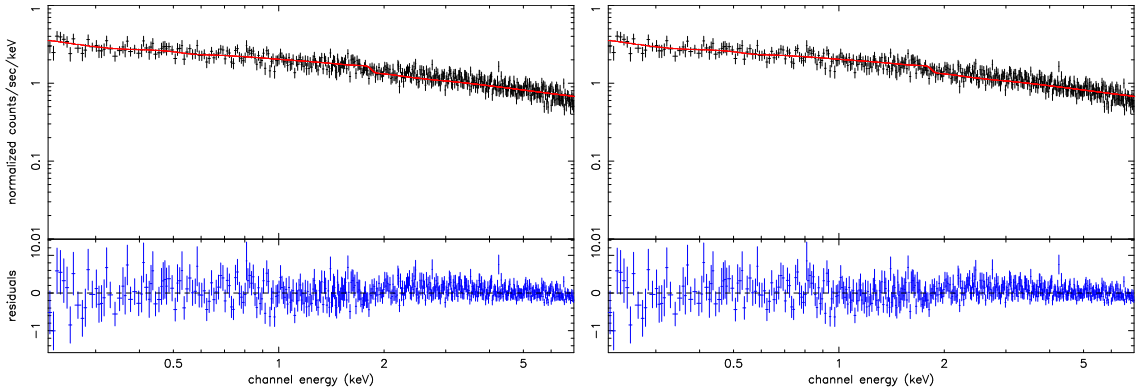

FIGURE 3.7: V410 Tau. The left plot shows the spectral signature of the soft protons from period 3, using period 1 as background from region number 10 of observation V 410 A. On the right plot the equivalent spectrum of the soft protons from period 3 is shown, using period 1 as background from region number 10, from observation V 410 B.

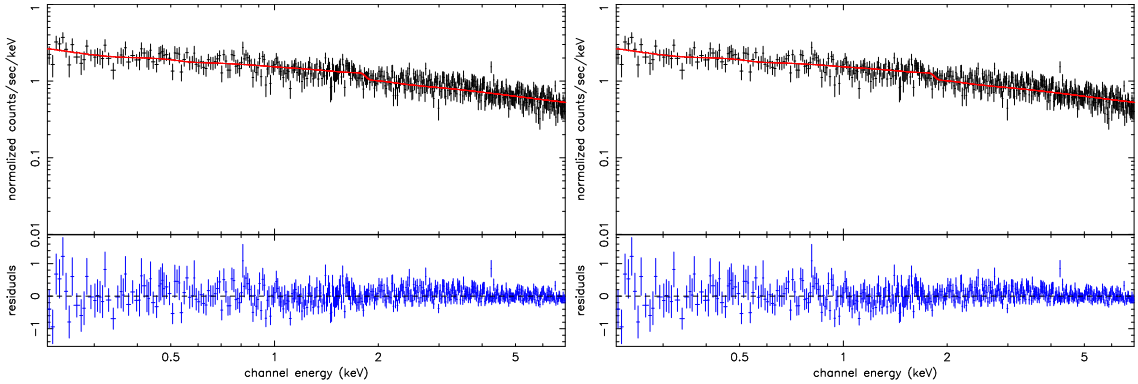

FIGURE 3.8: V410 Tau. The left plot shows the spectral signature of the soft protons from period 3, using period 2 as background from region number 10 of observation V 410 A. On the right plot the equivalent spectrum of the soft protons from period 3 is shown, using period 2 as background from region number 10, from observation V 410 B.

TABLE 3.5: The HDFN SPFs periods. The periods were defined using equal count rates. For each period a set of 10 spectra was produced, with the index i running from 01 until 10, see table 3.2. This study was done in observations HDFN.

PERIOD	COUNT RATE	SPECTRA DESIGNATION Rev 0271/0401	USED TIME
1	5.0 - 8.0	Spectrum1i.pha	70.9 ks
2	8.0 - 20.0	Spectrum2i.pha	6.8 ks
3	20.0 - 40.0	Spectrum3i.pha	2.3 ks

Also the spectra from the third period were fitted, using as background the spectra from period 1. The same procedure was applied, and the spectra were then fitted with an unfolded power-law. The results of this analysis are presented in the appendix table B.9. The plot from the fit of region number 10 is shown in figure 3.10b. The spectral index derived for this period was 0.65 ± 0.02, again for the detector region number 10.

In a similar way the spectrum corresponding to period 3 was fitted, using as background spectrum the one of period 2. In table B.10 the results of such fits are given. In this case a spectral index of 0.63 ± 0.03 was obtained. In figure 3.10c the plot of the fit for region number 10 is presented.

3.5.4 The spectral signature of the SPFs during the observations of Ophiuchus.

A similar analysis was also performed for our XMM-Newton observations, dedicated to study the x-ray shadow due to the Ophiuchus molecular filament. This study was only carried out for two of the three observations. The observations analyzed were Oph 1 and Oph 3. Observation Oph 2 was a very clean one and therefore not considered for this analysis. Observations Oph 1 and Oph 3 were performed as part of the Guaranteed Time program on September the 9^{th} 2001 and Oph 3 on February the 24^{th}, 2002, about six months apart. The Oph 1 and Oph 3 XMM-Newton observations had a total integration time of 16 and 14 ks. In both cases the EPIC-pn camera was operated in the eFF window mode, with the filter wheel in the THIN position.

After removing the detected point sources, a light curve for the count rate was produced for these two observations. The light curves were then transformed into histograms. These histograms are shown in figure 3.11.

Two intervals 4.0 - 7.0 and 7.0 - 32.0 for observation Oph 1 and 6.0 - 8.5 and 8.5 - 24.0 for Oph 3 were then defined, see table 3.6. These intervals were used to create GTI files which were then used to extract spectra for these two periods.

The spectra were fitted with an unfolded power-law. For the background spectra, the spectra from period 1 were used. The total results of such fits are shown in the appendix table B.11. The analysis to the SPFs for these observations reveal a spectral index of 0.90 ± 0.04 and 0.58 ± 0.07 for Oph 1 and Oph 3, respectively. The

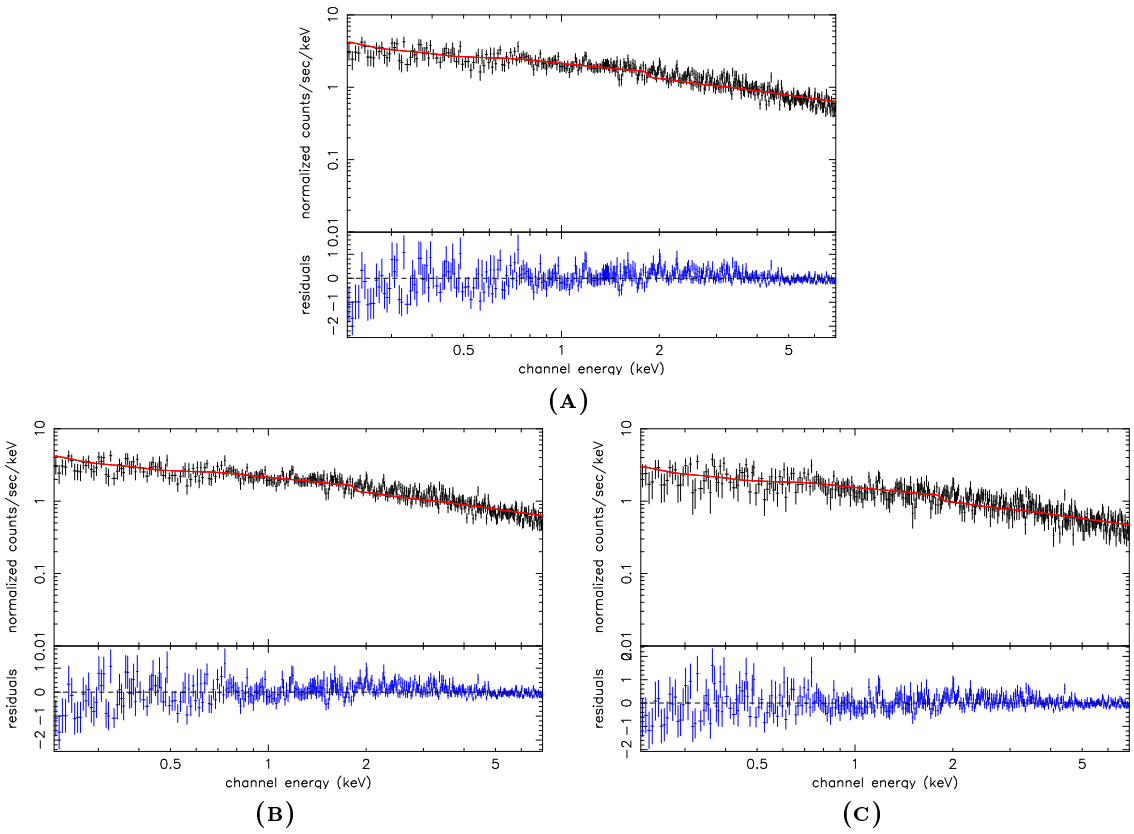

FIGURE 3.10: HDFN. Spectral fit plots of the soft proton flares. Figure 3.10a is the spectral fit of the soft proton flares in period 2, using period 1 as background. Figure 3.10b is the equivalent spectral fit of the soft proton flares in period 3, using the period 1 as background. Finally, figure 3.10c is the corresponding spectral fit of the soft proton flares in period 3, with the period 2 as background.

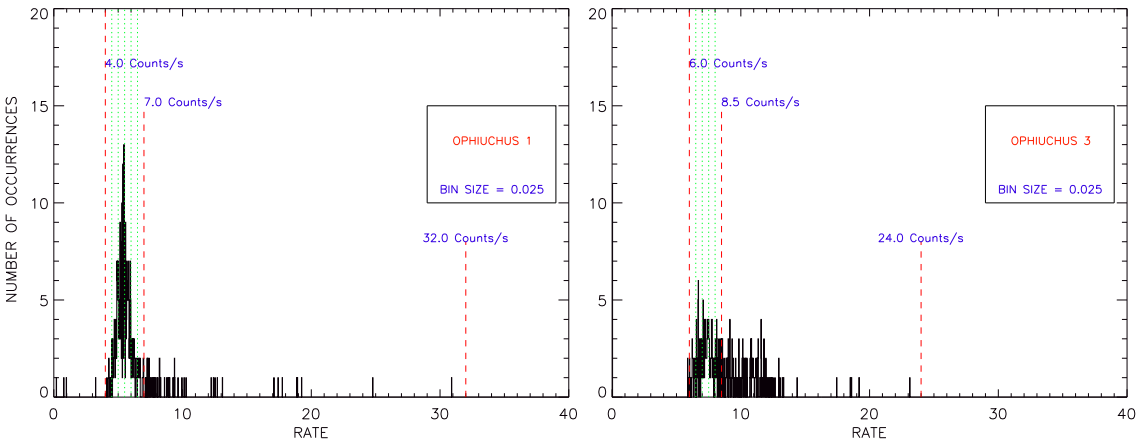

FIGURE 3.11: Ophiuchus histograms. The count rate histograms for observation Oph I (left) and observation Oph III (right) of revolutions 0321 and 0405, respectively . The count rate is only shown in the interval from 0 to 40. Count rates above 40 were omitted from the plot and not considered for this analysis.

TABLE 3.6: The Ophiuchus SPFs periods. The periods were defined, using different count rates. For each period a set of 10 spectra was produced, with the index i running from 01 until 10, see table 3.2. This study was done in observations Oph 1 and Oph 3.

PERIOD	COUNT RATE	SPECTRA DESIGNATION Oph 1 and Oph 3	USED TIME
1	4.0/6.0 - 7.0/8.5	Spectrum1i.pha	13.5/7.3 ks
2	7.0/8.5 - 32.0/24.0	Spectrum2i.pha	2.1/6.1 ks

plots from the fits from region number 10 are shown in figure 3.12.

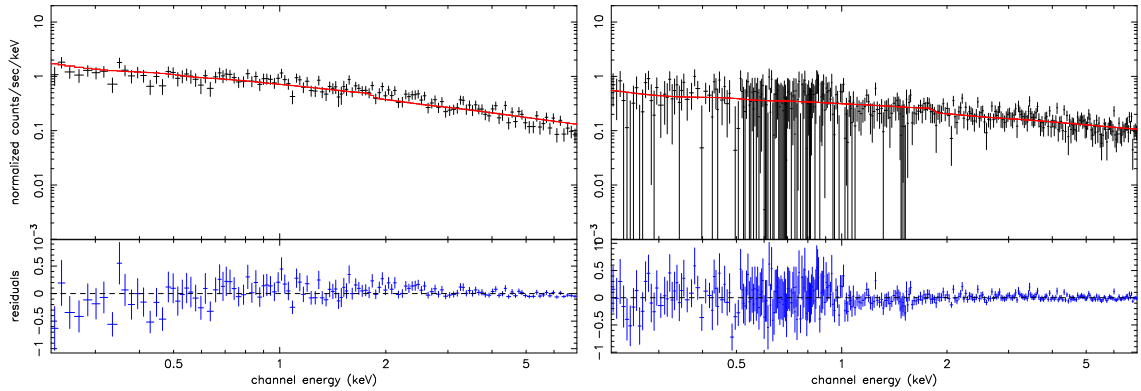

FIGURE 3.12: Ophiuchus. The plot shows the spectral signature of the soft protons from period 2, using period 1 as background from region number 10 of observation Oph 1 (left). On the right plot the equivalent spectrum of period 2 is shown, using period 1 for observation Oph 3.

3.5.5 The spectral signature of SPFs during the XMM-Newton observation of the Abell 478 galaxy cluster

The Abell 478 galaxy cluster target [162] was also investigated, because it had long exposure times and it is an extended x-ray source.

This observation was performed as part of the Guaranteed Time program on February the 15th, 2002, with a total duration of 122 ks. The XMM-Newton EPIC-pn observation was performed, using the window extended-Full-Frame (eFF) mode, with the filter wheel in the THIN position. The count rate light curve was produced in the energy range of 0.2 to 8.0 keV, with a time bin size of 40 s, and then transformed into a histogram as shown in figure 3.13. With the help of this histogram three intervals of the count rates were chosen. They are the interval of 13.5 to

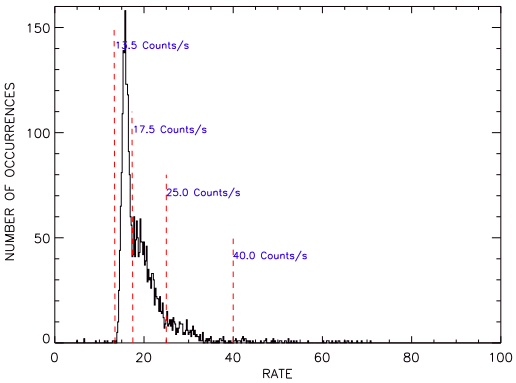

FIGURE 3.13: Abell 478 Cluster Histogram. Count rates above 100 were omitted from the plot and above 40 not considered for this analysis. Three intervals were used to do this analysis.

17.5 counts, the interval of 17.5 to 25.0 and the interval of 25.0 to 40.0 counts per second, all presented in table 3.7.

These analyse have shown a spectral index of 0.68 ± 0.02, 0.62 ± 0.01 and 0.58 ± 0.02. The global results from this observation are given in the appendix tables B.12, B.13 and B.14, respectively.

TABLE 3.7: The Abell 478 cluster SPFs periods. The periods were defined using different count rates. For each period a set of 10 spectra was produced, with the index i running from 01 until 10, see table 3.2.

PERIOD	COUNT RATE	SPECTRA DESIGNATION Abell 478 cluster	USED TIME
1	13.5 - 17.5	Spectrum1i.pha	59.3 ks
2	17.5 - 25.0	Spectrum2i.pha	48.6 ks
3	25.0 - 40.0	Spectrum3i.pha	11.5 ks

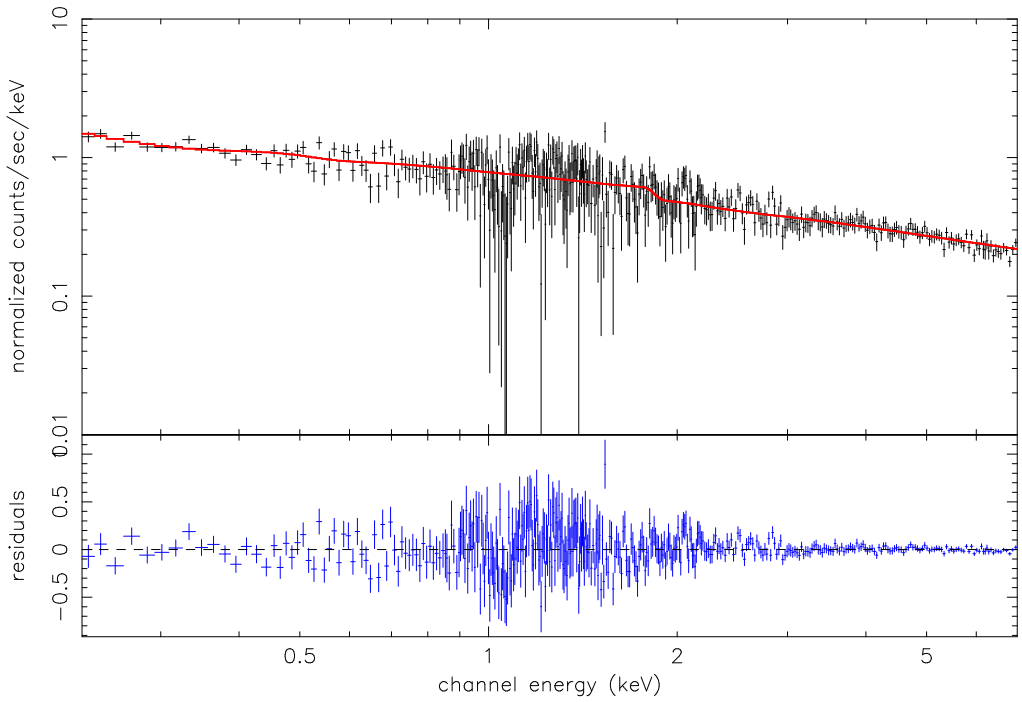

FIGURE 3.14: The plot shows the spectral signature of the soft protons from period 2 from region number 10 for the observation of the Abell 478 Cluster.

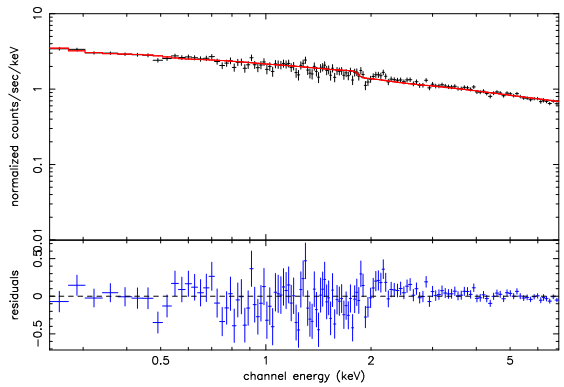

FIGURE 3.15: The plot shows the spectral signature of the soft protons from period 3, using period 1 as background from region number 10 for the observation of the Abell 478 Cluster.

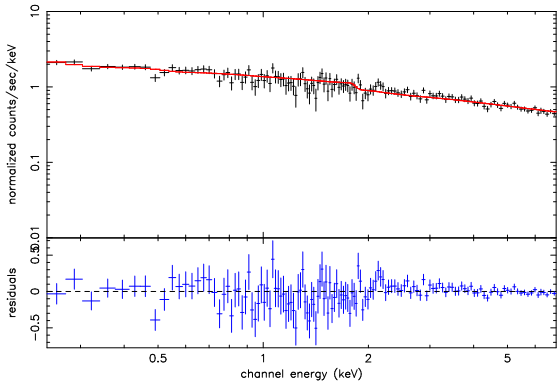

FIGURE 3.16: The plot shows the spectral signature of the soft protons from period 3, using period 2 as background from region number 10 for the observation of the Abell 478 Cluster.

This analysis shows, that the only contribution of these SPF events to the global x-ray spectra is with a continuum signal. Their spectra do not show any kind of emission lines, and they are well described by a power-law. Also, these analyse do not reveal any significant variation across the EPIC-pn camera.

3.6 MIPs Again

In this section a description of the procedure, developed to correct the contamination of MIPs, will be summarized.

As mentioned, in section 3.2.3, the MIPs were found to affect the astrophysical data in an unexpected way. In particular, when analyzing the x-ray spectra of some XMM-Newton observations in the same sky region, the normalization of the extragalactic power-law was found to vary 2 to $\sim$ 2.5 times. Besides showing variability within this small sky region, their values were also lower than one should expect from other studies of the extragalactic component. The deviation of the expected extragalactic power-law normalization was first realized when studying the extragalactic component in direction of the Hyades star cluster, lying at a distance of $\sim$ 46 pc [163]. In fact, there where already some suspicions regarding the XMM-Newton Ophiuchus observations. This is, why an analysis of the extragalactic component in the opposite sky direction to the Ophiuchus observations was initiated. In table 3.8 the main properties of the XMM-Newton observations used in this study are resumed.

In figure 3.17 the spectra from the four XMM-Newton Hyades observations (in black) as well as the two closed EPIC-pn observations (in red) are superimposed to infer the internal detector background spectra. In two of these observations, namely on Hyades A and Hyades B, there are some indications of a different internal background. For, when we compare the Cu K x-ray fluorescence emission lines

TABLE 3.8: The main properties of the Hyades XMM-Newton observations. The values presented in this table correspond to the ones of the EPIC-pn camera.

REV #	OBSERVAT. ID	FILTER	OBSERVAT. DATE	TIME [ks]	GALACTIC LONGITUDE	GALACTIC LATITUDE	TARGET NAME
0049	0094810301	THIN	2000-03-16T00:12:12	10	179.7830°	−20.5840°	HYADES X
0059	0122320701	CLOSED	2000-04-05T07:06:39	52	279.9951°	−19.8089°	CLOSED A
0135	0101440501	THICK	2000-09-03T03:08:43	43	180.2301°	−21.9713°	HYADES A
0138	0109060301	MEDIUM	2000-09-10T10:18:12	55	178.8850°	−20.0110°	HYADES B
0321	0112480101	THIN	2001-09-09T13:12:03	16	355.50°	+14.58°	OPH 1
0321	0112480201	THIN	2001-09-09T19:41:34	14	355.26°	+14.39°	OPH 2
0355	0106660401	CLOSED	2001-11-16T17:31:31	30	39.262°	−52.957°	CLOSED
0405	0112480301	THIN	2002-02-24T13:46:56	14	355.05°	+14.26°	OPH 3
0410	0101441501	MEDIUM	2002-03-06T06:44:07	47	180.5870°	−23.5390°	HYADES C
0462	0134521601	CLOSED	2000-04-05T07:06:39	23	275.3203°	−33.0685°	CLOSED B

(at $\sim$ 1600 adu[9]), a discrepancy on its intensity is evident. Also, the closed EPIC-pn observations show that the Al K x-ray fluorescence emission lines (at $\sim$ 300 adu) have the same intensity as the Hyades XMM-Newton observations. This should not be the case, since the spectrum from an astrophysical observation is composed by the astrophysical spectrum plus the internal detector background spectrum. Therefore, the intensity of the Al K emission line of the detector background should be smaller than the global spectrum. The spectra are shown in adu units instead of the customary energy channels, given in units of keV. The data reduction and spectra extraction for these observations follow the recipe described in previous sections.

The information, stored in the fields F1330 (quadrant 0), F1375 (quadrant 1), F1420 (quadrant 2), and F1465 (quadrant 3), from the main periodic housekeeping file (PMH), were used to calculate the average value of rejected columns (RC) due to MIPs. The PMH files are first filtered, using the same GTI files as the one used for spectra extraction, because we are only interested in knowing what was the number of discarded columns during the good time period. The default time bin size of the PNX00000PMH files, during the process of data recording, is 8.0 s. In order to perform a consistent analysis it is necessary to rebin this interval time size into the same time bin size as the GTI file. In the present analysis this meant to rebin the time bin size of the PNX00000PMH files into 40.0 s. After the rebinning process these files were filtered with the appropriate GTI files, as used to produce products such like images and spectra. After binning the rejected columns, the average number of rejected columns is calculated. This procedure is applied in both, science and closed observations.

The ideal case would be to have the same average number of rejected columns in both observations. Therefore, since we should have approximately the same PMH value for both, scientific and closed observations, one can use the ratio be-

[9]Analog to Digital Units (adu). Engineering units used to describe the quantization of the charge per pixel in the CCD detector. To convert from adu units to eV units we must multiply the adu units by 5.

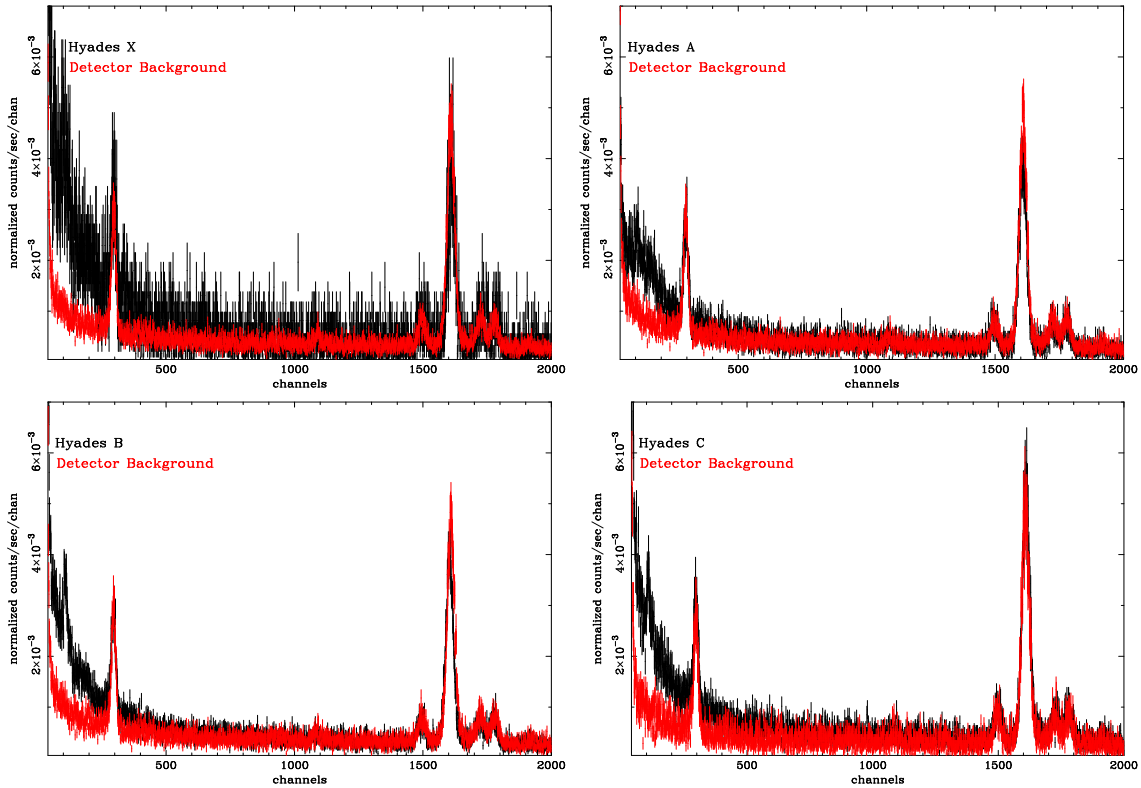

FIGURE 3.17: The spectra from the Hyades XMM-Newton observations. In each of these plots the x-ray sky spectrum (black) and the proper detector background spectrum (red) are shown. The detector background spectrum for subtraction purposes in the Hyades A and B show higher fluorescence x-ray emission lines when compared with the scientific observations. This is an indication of a possible contamination, since the signal of the sky emission plus the detector background should be higher than the signal from the detector itself.

tween these two values to artificially correct this physical effect. This correction is implemented, for instance, by changing the EXPOSURE keyword from the detector background spectrum by the ratio $RC_{background}/RC_{observation}$. This procedure artificially increases/decreases the number of counts from the detector background spectrum, allowing a compensation of this effect. For a deep analysis on this theme, see Freyberg [2003],[10] Freyberg et al. [164] and Freyberg [2005].[11] A more profound analysis on the non-linear read out behaviour of the eFF mode is under way and will be presented elsewhere.

In figures 3.18, 3.19 and 3.20, the binned and filtered number of RCs from quadrant 0 (F1331), from the PNX00000PMH files are shown. These figures correspond to the Hyades and to the closed XMM-Newton observations. In the figure 3.24 the same is presented, but for the Ophiuchus dark filament observations. Figures 3.21, 3.22 and 3.23 show the rejected number of columns versus the filtered count rate for each of the three Hyades and corresponding closed observations.

In table 3.9 the average number of rejected columns due to MIPs for the analysed

[10] http://www.src.le.ac.uk/projects/xmm/technical/index.html?0903#cal
[11] http://www.src.le.ac.uk/projects/xmm/technical/index.html?0205#cal

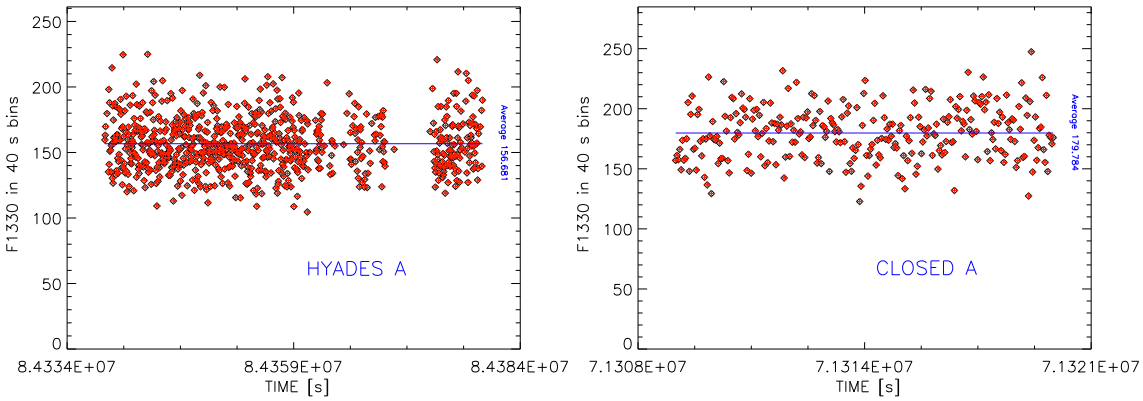

Figure 3.18: PMH (F1330) plots from quadrant 0 from the Hyades A and from the closed A observations.

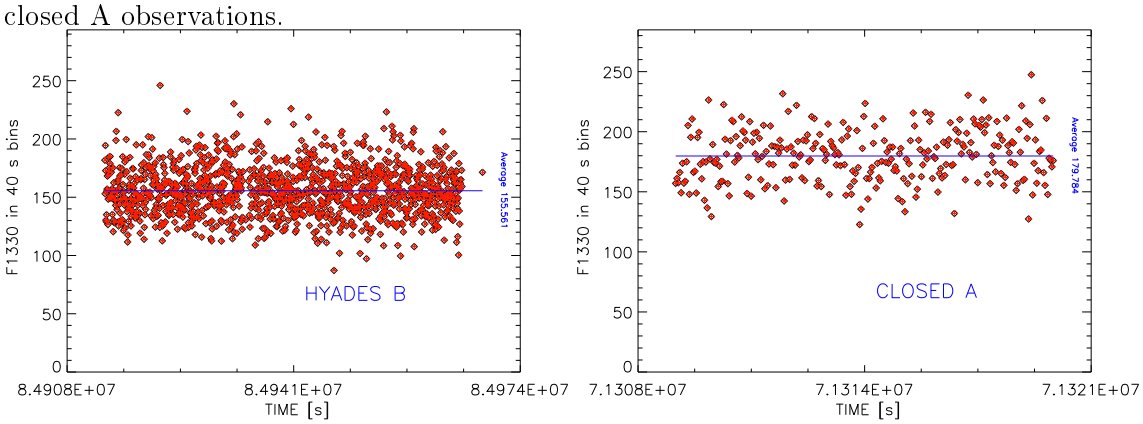

Figure 3.19: PMH (F1330) plots from quadrant 0 from the Hyades B and from the closed A observations.

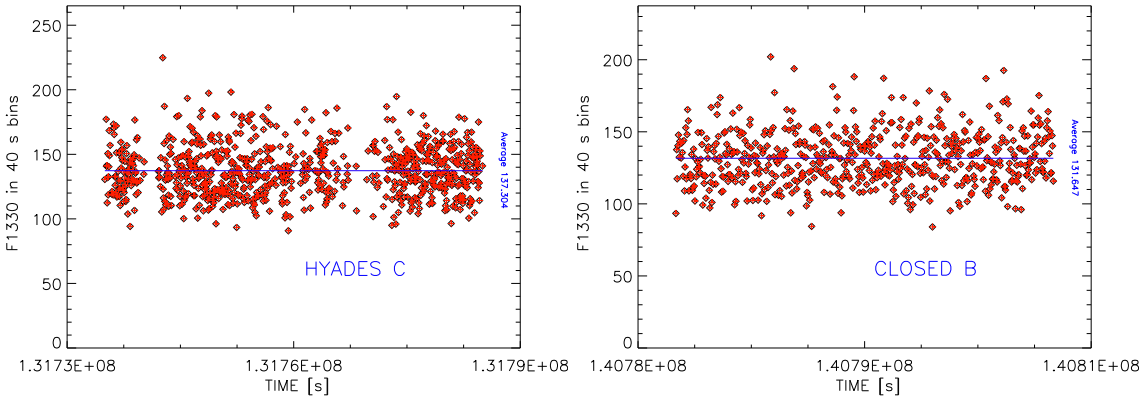

Figure 3.20: PMH (F1330) plots from quadrant 0 from the Hyades C and from the closed B observations.

XMM-Newton observations are given.

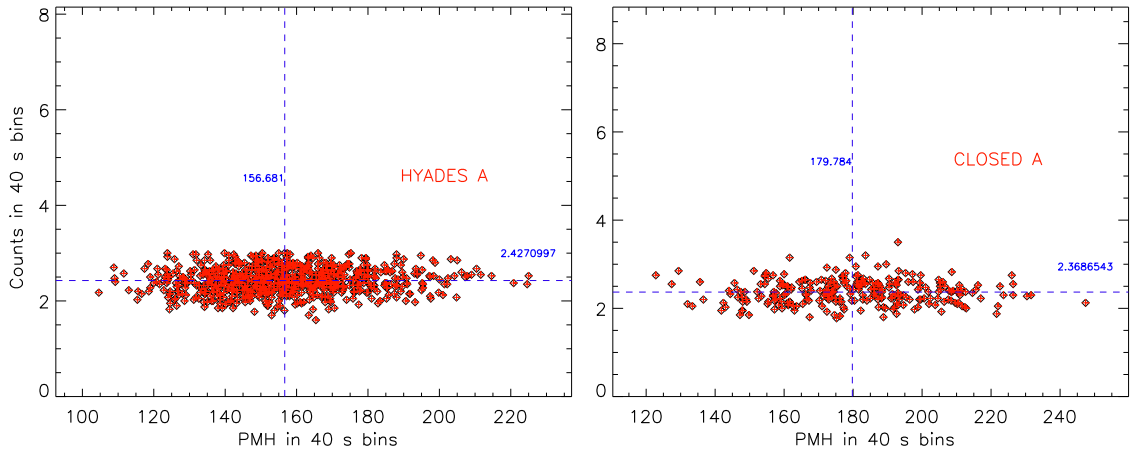

FIGURE 3.21: PMH (F1330) versus count rate plots from quadrant 0 from the Hyades A and from the closed A observations.

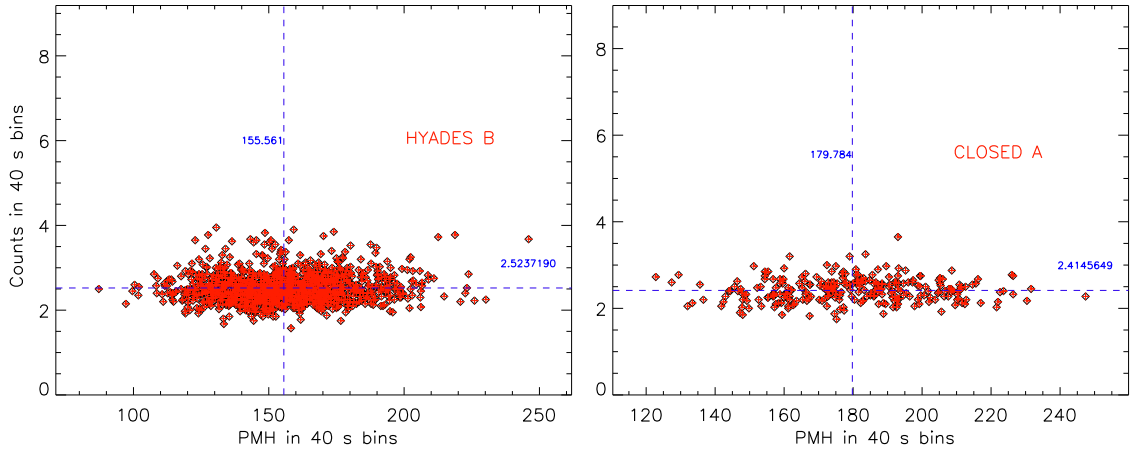

FIGURE 3.22: PMH (F1330) versus count rate plots from quadrant 0 from the Hyades B and from the closed A observations.

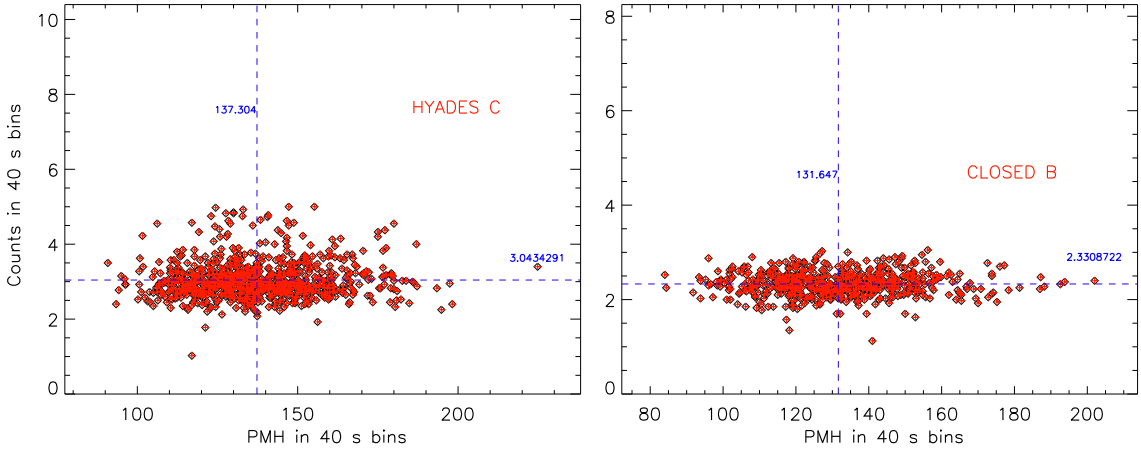

FIGURE 3.23: PMH (F1330) versus count rate plots from quadrant 0 from the Hyades C and from the closed B observations.

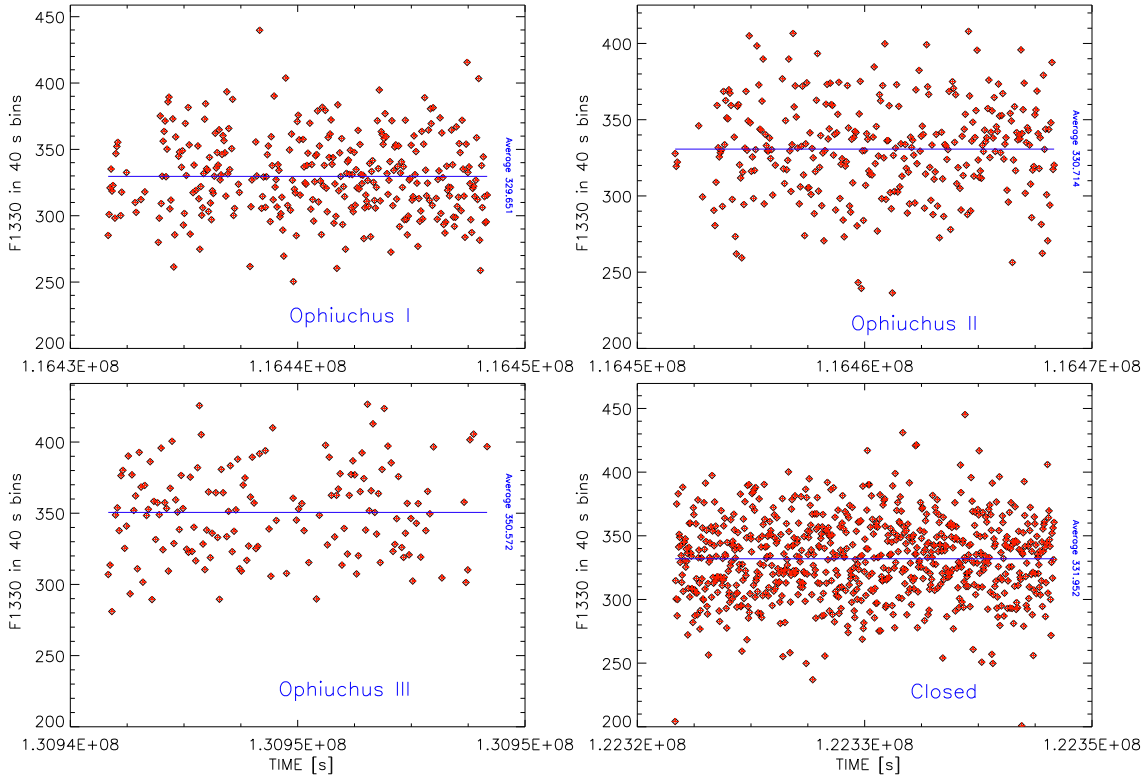

Figure 3.24: MIPs in the XMM-Newton Ophiuchus Observations. Plots, showing the number of rejected columns due to MIPs, during the good time interval. The plots shown correspond to the rejected columns of Quadrant 0.

Table 3.9: The Periodic Main Housekeeping (PMH) files from the EPIC-pn XMM-Newton observations. Column (1) shows the revolution number (Rev) of the observations, while in column (2) and (3) the ID and extension file name are presented. In the table columns (4) to (7) show the average number of rejected columns for each quadrant, within the GTIs.

Rev	ID	File	EPIC-pn Quadrant			
#		Extension	0	1	2	3
(1)	(2)	(3)	(4)	(5)	(6)	(7)
0049	0094810301	PNX00000PMH	n.avai.	n.avai.	n.avai.	n.avai.
0059	0122320701	PNX00000PMH	179.784	182.024	183.151	181.555
0135	0101440501	PNX00000PMH	156.681	157.209	157.557	156.783
0059	0122320701	PNX00000PMH	179.784	182.024	183.151	181.555
0138	0109060301	PNX00000PMH	155.561	154.781	155.778	156.123
0321	0112480101	PNX00000PMH	329.651	329.872	326.561	330.409
0321	0112480201	PNX00000PMH	330.714	331.317	323.977	329.204
0355	0106660401	PNX00000PMH	331.952	333.368	329.692	334.250
0405	0109880101	PNX00000PMH	350.572	345.676	343.526	346.897
0410	0101441501	PNX00000PMH	137.304	136.677	137.203	138.169
0462	0134521601	PNX00000PMH	131.647	129.833	129.897	130.684

n.avai. $\equiv$ Not available at the time of this analysis.

Chapter 4

The Ophiuchus Dark Filament

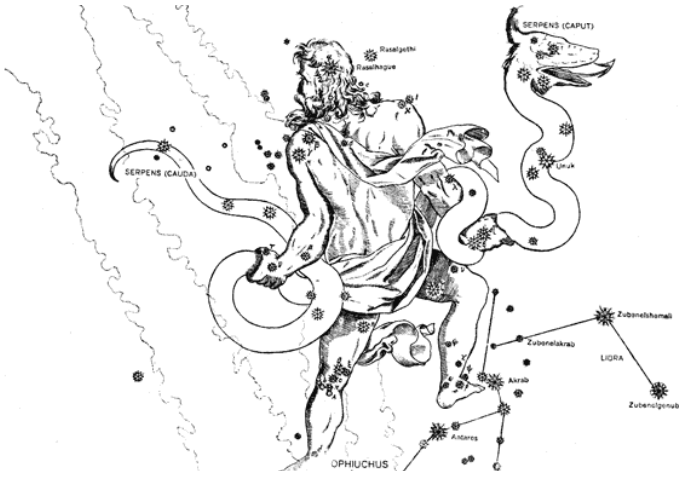

The constellation of Ophiuchus. A drawing from the German lawyer Johann Bayer (1572–1625) taken from his celestial atlas Uranometria, Augsburg, 1603. This is considered to be the first celestial atlas due to the accurate indication of star's position and brightness. Source Astronomy Education Review.

4.1 Introduction

In chapter 2, § 2.4 we have seen that the best way to disentangle the LB soft x-ray emission from other Galactic x-ray emissions is, to perform x-ray shadow experiments, using nearby interstellar molecular clouds. As discussed there, the soft x-ray emission that is produced in the background of a cloud of neutral and molecular material, will be strongly attenuated, e.g., due to the photo-electric absorption of electrons.

The main requisites to perform such studies is the use of interstellar molecular clouds, with high column densities of H I and H_2, which are close, preferentially inside or on the boundaries of the LB. For that reason, the Ophiuchus molecular cloud was used to perform an x-ray shadow experiment.

The Ophiuchus clouds are delimited by the Galactic coordinates l = 345° to 10°and b= −10° to +20°. In figure 4.1 a column density map of the Ophiuchus

molecular complex is presented. The accepted distance to this system of molecular clouds has varied over time, according to the sensitivity of astronomical techniques. For instance, Bertiau [165] has located the ρ Oph dense cloud at a distance of 160 pc. This distance has been adopted by several authors such as Imanishi et al. [166] and Luhman and Rieke [167], who used distances of 165 pc and 160 pc, respectively. In the following disscusion we adopte the distance to the molecular cloud to be 125±25 pc, derived by de Geus et al. [168]. This value is in good agreement with more recent works. Knude and Høg [169], combining the data from the HIPPARCOS parallaxes and the TYCHO B - V colors, have inferred a distance of 120 pc to the Ophiuchus molecular complex. More recently, Sujatha et al. [170] have used the diffuse far-ultraviolet (FUV) radiation from the VOYAGER observations to infer a minimum distance of 100 pc and a maximum of 125 pc to the Ophiuchus molecular cloud complex.

This molecular complex has been intensely studied, due to its proximity and to the ongoing star formation process [see 171]. In particular, the densest clouds, such as the ρ Oph, has been the mostly studied cloud of this molecular system. The CO survey, performed by de Geus et al. [172], has shown, that the system has a total mass of $\sim 10^4$ $M_\odot$. The average density of H I has been estimated to be $\sim 2\times10^3$ cm^{-3} [173]. In the densest regions, many Young Stellar Objects (YSO) have been identified. For instance, in a survey with the J, H and K infrared bands a total of 332 YSOs have been detected in ρ Oph [174]. In other clouds YSOs are also present, but in smaller number. Stellar objects, that are in the formation process, produce copiously x-rays. Since, in the densest regions of the molecular complex we find a high number of such objects, all that regions had to be avoided when performing soft x-ray emission studies. Otherwise, it would have impaired this kind of analysis, because a big percentage from the field of view would have to be masked or removed. This would then imply a reduction on the available collecting area, so important in diffuse emission studies. Moreover, the use of the densest regions on such studies would have as consequence the contamination of our x-ray data with the x-ray emission from YSOs. To prevent these complications, a dark filament region of the molecular complex without star formation, but still with high column densities, was chosen to do an x-ray shadow experiment.

As already alluded in chapter 2, in § 2.1, the ROSAT shadows experiments on the Draco Nebula and on the Ursa Major have made clear, that about 50 per cent of the flux in the 0.25 keV band is not originating within the LB.

The XMM-Newton satellite, due to his high effective area over a wide range of energies, allied to high sensitivity, spatial resolution (comparable to some ground-based optical and infrared telescopes) and spectral resolution, has been chosen to perform three pointings on the dark filament of the Ophiuchus molecular complex. In chapter 3, table 3.1, the Galactic coordinates of these three XMM-Newton observations have been presented. These three pointings on dark filament were aimed to the on-cloud regions, where the soft x-ray emission background is efficiently blocked, and aimed to more off-cloud, where the soft compoment of the x-ray emission background is not so severely absorbed.

In the following § we present a large scale image of the Ophiuchus molecular

complex and a zoom image, where the three XMM-Newtom pointings were taken from.

4.2 The Ophiuchus neutral and molecular material region

The hydrogen column density map from Dickey and Lockman [175] and the CO map from Dame et al. [176] are important tools, when one desires to estimate the amount of neutral and molecular hydrogen in a given direction in the Galaxy. However, they have a poor spatial resolution, when performing detailed spatial studies as the one presented here. In the present analysis we have adopted to use the extinction maps produced by Lombardi and Alves [177], Ridge et al. [178]. They have used the intrinsic colors of stars in the near-infrared to produced an extinction A_v map of the Ophiuchus region.

This new extinction map has two main advantages regarding the former two. Not only the column densities are better estimated, also the map has a higher spatial resolution in the Ophiuchus region, see figure 4.1. A conversion factor of 2.0×10^{21} mag^{-1} cm^{-2} was used to transform the A_v map into a column density map (Alves 2005, personal communication). The inside box image of figure 4.1 shows a close look of the Ophiuchus molecular cloud, where the XMM-Newton observations were taken. The different colors correspond to regions of the dark filament with distinct column densities. The white color corresponds to high column densities, whereas the blue color corresponds to low column densities. In the dark filament, in the regions of interest for this work, the column density ranges from 5.0×10^{20} cm^{-2} to 1.6×10^{22} cm^{-2}. In table 4.1 we present the minimum and maximum values for the total column density, from the 27 subregions investigated in the three XMM-Newton observations. In columns (1), (2) and (3) is shown the XMM-Newton observation number, the organization set name and the corresponding number region, respectively. In columns (4) and (5) the sky positions coordinates. Finally, in column (6), the measured column density gradient within each subregion is presented.

4.3 The Ophiuchus dark filament X-ray shadow

Galactic ISM X-ray shadows were first observed with the ROSAT satellite by Snowden et al. [32] and Burrows and Mendenhall [31]. These two observations have releaved a shadow in the so-called 1/4 keV energy band against the soft x-ray background, produced by the interstellar Draco cloud lying at a distance between 327 and 861 pc [179].This shadow is the result of the absorption produced by the neutral and molecular material present in the cloud, which effectively blocks the on-cloud 1/4 keV background photons.

The same shadow effect produced by ISM clouds can be observed with more energetic x-ray photons, if the column densities associated to the clouds are higher. This is precisely the case of the Ophiuchus dark filament, see figure 4.2. We have produced a mosaic image of the three pointings to the dark filament of the Ophiuchus molecular cloud. For each pointing images in the 0.3 - 0.5, 0.7 - 0.9 and 0.9 - 2.0 keV

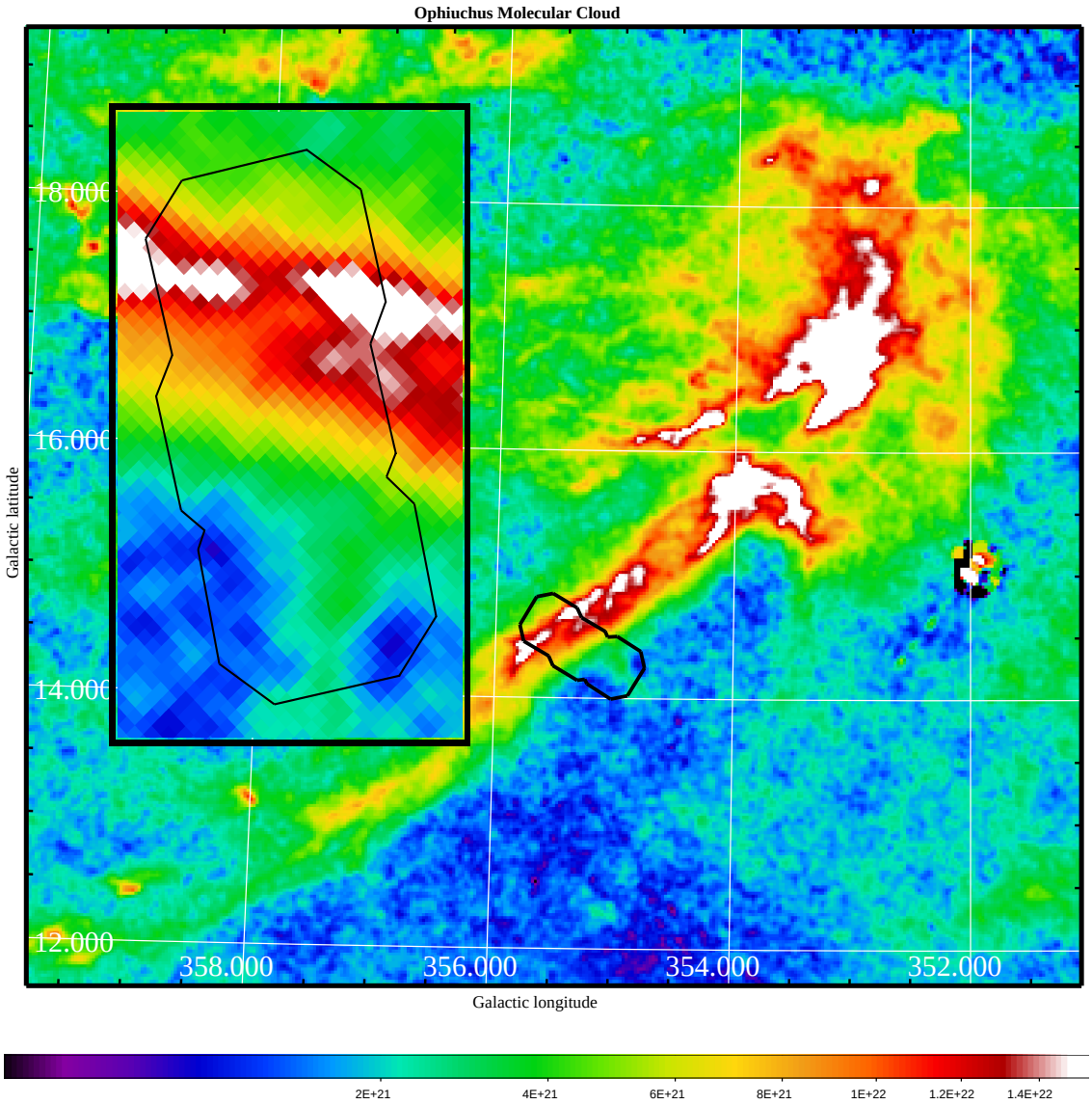

FIGURE 4.1: The Ophiuchus molecular cloud column density map. Lombardi and Alves [177], Ridge et al. [178] have used the intrinsic colors of stars in the near-infrared to produce an extinction map of the Ophiuchus region. This map was then transformed in a column density map, using a conversion factor of 2.0×10^{21} mag^{-1} cm^{-2}. This map has the advantage of a higher spatial resolution and a better estimate of the column densities required to perform high spatial resolution studies of soft x-ray diffuse emission. A square root scale was used to generate the distribution of colors, starting at 1.0×10^{20} (blue) until 1.6×10^{22} cm^{-2} (white). A sketch from the field of views of the XMM-Newton EPIC-pn camera is also shown by the black lines. In the top left part of the image, a zoom to the column density map is made for a better visualization of the column density gradient on the three XMM-Newton pointings.

energy bands were created, adaptively smoothed and merged, in order to create a color image. During the smoothing process a gaussian of five pixels width was used. Each energy band was color coded as follows: 0.3 - 0.5 keV as red, 0.7 - 0.9 keV as

TABLE 4.1: Extraction region positions from the XMM-Newton Ophiuchus Observations. Each XMM-Newton Ophiuchus observation was divided in nine sets, from A to I, to obtain spectra for analysis, given in column (2). In columns (4) and (5), the center of these sky regions are presented. In column (6) the minimum and maximum values of the total column density for each particular region is shown. The column densities were obtained from the extinction (A_V) map of Lombardi and Alves [177], Ridge et al. [178].

Ophiuchus Observation (1)	Set (2)	Region # (3)	R.A. J2000 (4)	Dec J2000 (5)	N_H Gradient 10^{22} cm^{-2} (6)
I	G	1	16:40:36.00	−23:58:03.2	0.36 - 0.98
I	H	2	16:41:00.52	−23:59:04.1	0.46 - 1.40
I	I	3	16:41:27.61	−24:00:07.8	0.49 - 1.69
I	D	4	16:41:22.50	−24:06:54.3	0.99 - 1.78
I	E	5	16:40:55.39	−24:05:50.5	0.64 - 1.62
I	F	6	16:40:30.85	−24:04:49.6	0.61 - 1.87
I	A	7	16:40:25.92	−24:10:57.5	1.07 - 1.98
I	B	8	16:40:50.95	−24:12:01.7	1.05 - 1.33
I	C	9	16:41:17.85	−24:12:59.1	0.81 - 1.62
II	G	10	16:40:36.06	−24:16:12.6	0.93 - 1.50
II	H	11	16:41:00.88	−24:17:09.7	0.69 - 1.25
II	I	12	16:41:27.78	−24:18:09.6	0.52 - 1.04
II	D	13	16:41:22.92	−24:24:50.6	0.27 - 0.81
II	E	14	16:40:55.10	−24:23:46.0	0.33 - 1.09
II	F	15	16:40:30.99	−24:22:53.2	0.55 - 1.46
II	A	16	16:40:26.11	−24:28:57.2	0.29 - 0.77
II	B	17	16:40:50.63	−24:30:01.9	0.24 - 0.68
II	C	18	16:41:17.92	−24:31:01.9	0.09 - 0.50
III	A	19	16:41:09.37	−24:36:44.9	0.05 - 0.30
III	B	20	16:40:44.50	−24:36:00.3	0.17 - 0.36
III	C	21	16:40:17.52	−24:35:08.9	0.26 - 0.55
III	D	22	16:40:13.74	−24:41:16.9	0.20 - 0.39
III	E	23	16:40:40.98	−24:42:02.3	0.14 - 0.38
III	F	24	16:41:05.64	−24:42:53.0	0.09 - 0.22
III	G	25	16:41:01.89	−24:49:42.6	0.09 - 0.24
III	H	26	16:40:36.98	−24:48:54.7	0.14 - 0.37
III	I	27	16:40:09.72	−24:48:06.4	0.06 - 0.39

green and 0.9 - 2.0 keV as blue.

This image is then compared with an optical counterpart. The optical color image was created by using three Digital Sky Survey (DSS) plates, with their intensities scaled differently, in order to enhance the Ophiuchus dark filament. To this image a sketch from the three XMM-Newton EPIC-pn fields of view was added. The image on the right of figure 4.2 shows an x-ray shadow cast on the ISM due to the Ophiuchus dark filament, which exactly follows the optical counterpart and, as well, the 100μ IRAS dust contour map, not shown in this figure. The brightest x-ray sources were also marked with letters, from A to F, with a corresponding circle for better visualization. In the appendix C some information, regarding these bright x-ray sources, is given.

Before proceeding to the discussion of the x-ray data fit procedure, in § 4.11, it is necessecary to have a physical model to which the x-ray data can be "folded". For that, we need to have a reasonable astrophysical model, representing the different x-ray emission contributions in the line of sight crossing the Ophiuchus dark filament. To begin with, this implies to have a reasonable knowledge of the environment to which the Ophiuchus complex belongs. This leads us to the Upper-Scorpius OB star

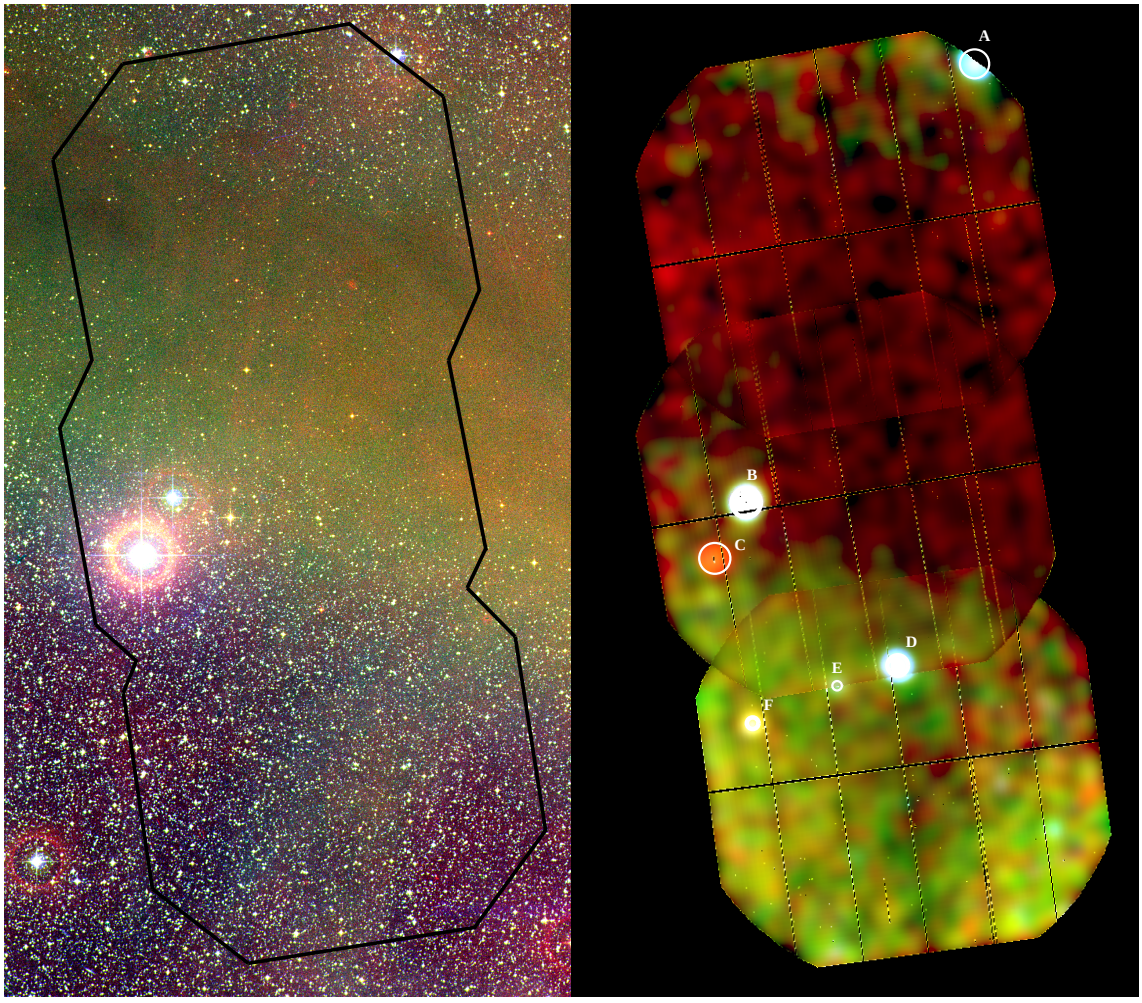

FIGURE 4.2: Left figure: Composite image from three Digital Sky Survey (DSS) plates to which a sketch of the XMM-Newton EPIC-pn field of view (black thick) is superimposed. Right figure: Soft x-ray shadow of the dark filament from Ophiuchus Molecular Cloud obtained by the XMM-Newton satellite. Three energy bands were used to create three images. These images were coded according to the following criteria 0.3 - 0.5 keV red, 0.5 - 0.9 keV green and 0.9 - 2.0 keV blue. As it can be seen, the dark molecular filament casts a shadow in the soft x-ray background, due to absorption of neutral and molecular material present in the filament. The red image was square root scaled from 2.0×10^{-6} to 2.1×10^{-5}, and the green image from 8.0×10^{-6} to 4.0×10^{-5}. In the blue image case, a squared scale was used from 1.7×10^{-7} to 2.5×10^{-5} intensity units. The six most bright x-ray sources are also marked from A to F.

association.

4.4 The Upper-Scorpius OB association and the Ophiuchus molecular cloud

The Ophiuchus molecular complex is embedded in a very complex system. In the following sections a simple description of the interaction of this system with the

molecular cloud is drawn. The Ophiuchus molecular cloud complex was chosen to perform studies on the soft x-ray emission, because it is close to the Solar system (125±25 pc, de Geus et al. [168]) and has high column densities (10^{21}-10^{22}cm^{-2}), which effectively block the soft x-ray emission produced on the background of the molecular cloud. Therefore, XMM-Newton observations were done in one of the dark filaments of the cloud, in order to disentangle the soft x-ray emission foreground, thought to be mainly due to the LB.

This molecular and neutral material complex is located in the youngest of the Scorpius-Centaurus (Sco-Cen) OB association, the Upper-Scorpius subgroup, which lies at a distance of 145 pc, see table 4.2, where the main properties of the three subgroups of Sco-Cen OB association are resumed.

Since the Ophiuchus molecular cloud is located in an OB association and in a relatively young one, it means that one should expect some complex interaction between the OB star members and the Ophiuchus clouds. In the energy range, in which we are mostly interested, this interaction is done by energetic UV photons, stellar winds and, finally, in the form of supernova remnants.

Castor et al. [58], Weaver et al. [59] and McCray and Kafatos [74], see § 1.7 in chaper 1, have calculated the effects of such physical phenomena on the ambient interstellar medium of early-type stars. They found, that large bubbles will be formed around such massive stars, which in due time will merge together to form even bigger bubbles —the so-called superbubbles surrounding OB associations. One physical consequence of such physical activity is the formation of huge H I shells. In the Upper-Scorpius OB subgroup there is at least one such structure. This H I shell (H I shell 1 in figure 4.4) is centered at the galactic coordinates l= 346°±2° and b= +21°±2°, see table 4.3. This H I shell has a radius of 40±4 pc, lies at a distance of 160±20 pc from the Solar system and the measured velocity of the shell is 10±2 kms^{-1} [180]. A general schematic view of the sky is shown in figure 4.4.

Assuming that such a shell can be explained by the model of McCray and Kafatos [74], we would derive an age of the order of $\sim 2.4 \times 10^6$ years, which is half of the age of the Upper-Scorpius OB association, see table 4.2. If one would boldly assume a unique supernova explosion for the cause of such a H I shell, then with an ambient density of 0.003 cm^{-3} (Egger [182], the central density of Loop I superbubble). With an energy of 10^{51} erg we would obtain then an age of 12×10^3 years. The latter assumption, if true, would mean, that a significant contribution of x-ray synchrotron emission, with probably some thermal x-ray emission as well, would be present in our line of sight, due to this middle age supernova remnant.

Plotting the position of the H I shell 1 and of the Ophiuchus molecular complex, like shown in figure 4.4 (a), one sees immediately that the Ophiuchus clouds may have been subjected or are being subjected to a shock wave, from which the most obvious physical evidence is the apparent surface of the H I shell.

In fact, such an hypothesis was already advanced by Vrba [183] to explain the filamentary structure of the Ophiuchus clouds, as the result of a passage of a shock wave by the ρ Oph dark cloud. This hypothesis has been re-enforced later by de Geus [184]. More recently, Moreira and Yun [185] have also suggested, that the velocity gradients observed in the Lupus globular filament GF 17 and GF 20 are

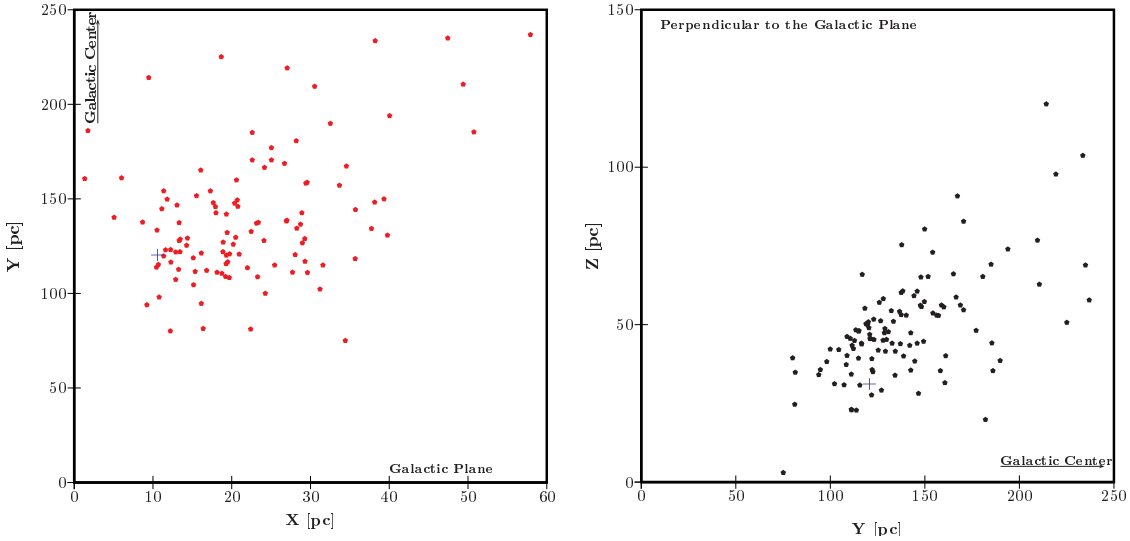

FIGURE 4.3: Projection of stars of the fourth quadrant with b> 0° from the Upper-Scorpius OB association, taken from de Zeeuw et al. [181]. Therefore only 115 stars were used to produce this plot. The blue "+" marks the position of our "Ophiuchus" observations.

also the result of the interaction of expanding H I shells from the Upper-Scorpius and from the Upper-Centaurus-Lupus.

Apparently, this is not the only structure observed in the Upper-Scorpius region. Indeed, Combi et al. [186] (and references therein) have confirmed the existence of a radio structure having an egg-like shape, centered around l, b $\sim$ (353°, +13°), see the blue dashed egg-like structure on figure 4.4. These authors have interpreted this radio structure as the result of the interaction of a shock wave due to one or more supernova explosions in the Upper-Scorpius OB association, $54{\times}10^3$ years ago. Jonas [187] has suggested that this structure is the superposition of two different supernova remnants, being the lower part of the egg-like radio structure, due to the G356.9+8.5 supernova remnant candidate, marked by a black dashed circle inside of the egg-like structure, see figure 4.4. The G356.9+8.5 supernova remnant candidate has been associated to the pulsar PSR J1654-2707. However, given the inferred distance to this pulsar of 3.97 kpc, this would imply, that the apparent diameter of such supernova remnant would translate into a rather large linear diameter of 660 pc for the shell [187]. Such a middle age SNR, suggested by Combi et al. [186], would have certainly other signatures, like x-ray emission of different natures, e.g. x-ray synchrotron emission.

In the literature several SNRs have been observed to radiate x-ray synchrotron emission. The SN 1006 and the Crab, which are young supernova remnants, show synchrotron emission in the form of a power law with a spectral index (Γ) of 3 and 2.1, respectevely [188]. The same synchrotron x-ray emission was observed on the northwest shell of the millenarian SNR RX J1713.7-3946 by Koyama et al. [189], again with Γ of 2.5. Also in the edge of the SRN IC 443, synchrotron emission was detected with a spectral index of 2.3, in addition to a thermal component of $\sim$0.8 keV (9.3×10^6 K) [190]. Gulliford [191] has initially estimate the age of SRN

TABLE 4.2: Scorpius-Centaurus OB Association - Main properties taken from A HIPPARCOS Census of the Nearby OB Associations [181]. Upper-Scorpius (US), Upper-Centaurus-Lupus (UCL), and Lower-Centaurus-Crux (LCC).

SCORPIUS-CENTAURUS OB ASSOCIATIONS					
SUBGROUP	GALACTIC LONGITUDE	GALACTIC LATITUDE	D [pc]	AGE [Myr]	B, A STARS (stars total)
US	351.5°	+20.0°	145	5	49, 34 (120)
UCL	327.5°	+12.5°	140	13	66, 68 (221)
LCC	298.5°	+05.5°	118	10	42, 55 (180)

IC 443 to be 13×10^3 years, however this value was raised to 30×10^3 years, based on theoretical grounds by Chevalier [54] and confirmed by Olbert et al. [192]. In the case of SRN IC 443, the physical mechanism, advanced to explain this synchrotron emission, relies on the interaction of accelerated electrons, when the supernova shock impacts on dense clouds [190].

Although it is well sited within the Upper-Scorpius OB association, the Ophiuchus cloud complex may still be devoid of wind erosion from the OB star members. However, it is likely to be under the radiative influence of such stars.

4.5 The Sco-Cen OB association and Loop I

The Upper-Scorpius OB star association, where the Ophiuchus molecular cloud complex is located, is one of three subgroups of OB stars, forming the so-called Scorpius-Centaurus (Sco-Cen) OB association. This association is composed by the Upper-Scorpius, the Upper-Centaurus-Lupus, and the Lower-Centaurus-Crux associations, see table 4.2. There is observational evidence that the correlated stellar activity of these OB stars have created the Loop I superbubble.

The superbubble of Loop I was first detected as a radio loop, centered at l = 329.0°±1.5°, b = 17.5°±3.0°, having an apparent radius of 58.0°±4.0° by Berkhuijsen et al. [193]. Several observations indicate, that Loop I results from the interaction of a shock wave with the surrounding ISM, resulting from the stellar activity in the Sco-Cen OB association. Another indication of the interaction of a shock wave with the ISM is the existence of an expanding shell of neutral material surrounding the radio structure of Loop I with a radius of $\sim 68°$ and a velocity of 19 km/s [194].

Egger [195] and Egger and Aschenbach [196] have been able to model Loop I as a superbubble produced by collective stellar winds and several consecutive supernova explosions (SNe) in the Sco-Cen association. It has also been shown by Egger and Aschenbach [196], that an interaction between the superbubble of Loop I and the LB is taking place, see figure 4.4 (a). This is most easily seen by an annular ring of neutral material and a corresponding x-ray shadow, Egger and Aschenbach [196]. In figure 4.4 (a) several astrophysical observational results are depicted. The annular ring of neutral material is shown as a gray ring. This image is centered

TABLE 4.3: Neutral Hydrogen Shells with centers in the Sco-Cen OB associations.

HYDROGEN SHELLS	GALACTIC LONGITUDE	GALACTIC LATITUDE	D [pc]	RADIUS [pc]	v [kms^{-1}]
$1^{(a)}$	347°	+21°	160±22	40±4	10.0±2
$2^{(a)}$	320°	+10°	140±20	110±10	10.0±2
$3^{(b)}$	313°	+28°	∼160	∼153	15.3

(a) Crawford [180] (b) Génova et al. [197]

in the superbubble of Loop I. The blue rectangular boxes in the figure represent the three OB association subgroups, forming the Sco-Cen OB association. The sky region associated to the Ophiuchus molecular cloud is delimited by a red box. The red cross shows the three XMM-Newton observation positions, and the star symbol markes the position of the τ Sco B0 V star. Superimposed are also shown the three H I shells, which were associated to the stellar activity in the Sco-Cen association, see table 4.3. The egg-shape structure is associated to radio emission, detected by Combi et al. [186]. The filled orange circle represents the superbubble of Loop I.

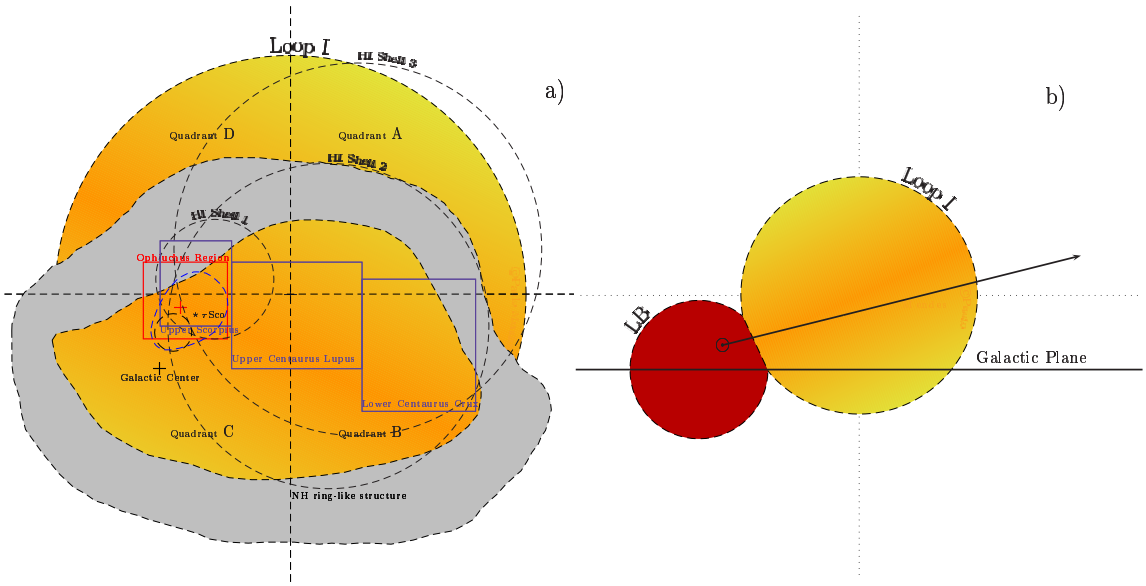

FIGURE 4.4: Schematic view of Loop I. In figure (a) the global view in direction of Loop I is depicted. The picture is centered in Loop I superbubble, and has a radius of 128 pc. The annular ring of neutral material, due to the interaction of the LB and Loop I bubbles, is shown in a gray color. The three dashed circles represent the H I shell discussed in the text, see table 4.3. The blue boxes show the three subgroups of OB stars, forming the Sco-Cen OB association. The red box delimits the Ophiuchus molecular cloud region, the red cross shows the XMM-Newton observations position, while the star symbol represents the position of the τ Sco star. Also shown is an egg-like shape radio structure, involving the XMM-Newton observations. The annular ring of H I was divided in four quadrants to further investigate the column density of H I in each quadrant. Figure (b) is a side view of an idealized interaction between the two bubbles.

In figure 4.4 (b) is shown an idealized sketch of the interaction between the LB (in red color) and Loop I (in orange color).

Egger and Aschenbach [196], using data compiled by Fruscione et al. [114], have

derived, that the column density towards stars projected onto the ring has a sharp discontinuity at a distance of $\sim$ 70 pc. From less than 10^{20} cm^{-2} the column density jumps to 7.0×10^{20} cm^{-2}. Therefore, one should expect values for the column density of the neutral wall between the former two values, because the Ophiuchus molecular complex lies inside of the ring. However, since the distance of the stars were pre-HIPPARCOS we have re-analyzed the column density versus the distance to these stars, using the modern parallaxes obtained by the HIPPARCOS satellite. We have also enlarged the sample of stars by adding the stars from the Welsh et al. [198] and Sfeir et al. [117] catalogues, see figure 4.5.

The projected stars were divided in four regions, according to their sky positions. Each region representing a different sky quadrant, having as reference point the center of Loop I. Quadrant A was defined as the region with Galactic coordinates l,b (>329°,>17.5°), quadrant B defined as l,b (>329°,<17.5°), quadrant C as the sky region with l,b (<329°,<17.5°) and, finally, quadrant D as l,b (<329°, >17.5°).

With the new distances, the discontinuity appears to occur at $\sim$ 40 pc. The "+" signs on figure 4.5 show the stars used by Egger and Aschenbach [196] with the modern distances from the HIPPARCOS satellite. This new result implies, that the LB extension in this direction is smaller than previously assumed.

In the past Egger and Aschenbach [196] have modelled the Loop I as a super-bubble, having a radius R_S of 158 pc and lying at a distance of $\sim$ 170 pc, with the center located in the Upper-Centaurus-Lupus OB subgroup. However, the modern distance to this OB star subgroup, derived by de Zeeuw et al. [181], is 140 pc. This new result in conjuction with the $R_S \sim 160$ pc derived by Egger and Aschenbach [196] would imply, that the Solar system could be sited inside of Loop I. Otherwise we could not observe the H I wall towards Loop I. Assuming, that the superbubble of Loop I is spherically symmetric, that an interaction between Loop I and the LB takes place at $\sim$ 40 pc, most easily seen as a NH ring-like shape [196], and with the center lying at a distance of 140 pc, we crudely estimate a radius of 128 pc for Loop I. This radius is about 19 per cent smaller than the one previously estimated by Egger and Aschenbach [196]. From the previous geometrical considerations we also derive an inclination angle for the interaction plane between the LB and Loop I of 32°. Using the projected column density of a simulation of two colliding bubbles, reported on [115, 182], an angle of 30° was found for this inclination angle. The ellipticity of the NH ring-like shape and the offset of its center from the center of Loop I shows, that the Solar system has an offset regarding the line passing through the center of the ring-like shape and the center of Loop I. There is also futher evidence, that this NH ring-like shape is tilted, for when we divide the projected stars in the ring into four quandrants, we see that the interaction in each quadrant occurs at different distances, see figure 4.5. As a consequence of these new considerations, the Ophiuchus molecular complex is more deeply embedded in the Loop I supperbubble than assumed before.

Since the Ophiuchus molecular cloud is more deeply embedded in the Loop I than previously assumed, our second model component had to be split into two components. One, representing the unabsorbed emission from Loop I, and another representing the absorbed x-ray emission from Loop I.

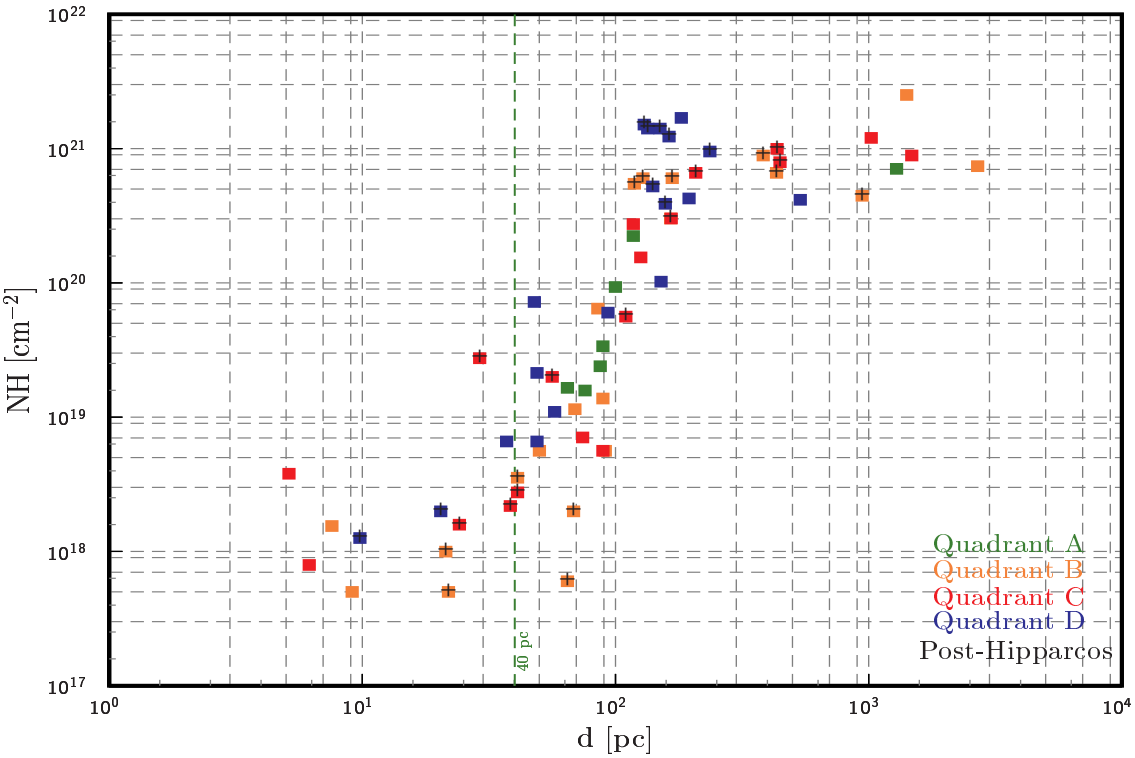

FIGURE 4.5: The neutral column density (NH) of stars with their projected sky position onto the NH ring, due to the interaction of the LB and the Loop I superbubble. Besides correcting the distances of the stars, used by Egger and Aschenbach [196], we also added new stars from the Welsh et al. [198] and Sfeir et al. [117] catalogues. The interaction, resulting in a neutral hydrogen wall, occurs at a distance of $\sim$ 40 pc. The distance, at which this wall was previously thought to occur, was at a distance of $\sim$ 70 pc. It is also possible to see, that the interaction of this ring is slightly bended, because, when we consider the stars in each ring quadrant the column densities increase faster in quadrant D (blue squares). The plusses show the stars used previously by Egger and Aschenbach [196], corrected with the modern HIPPARCOS satellite distances.

As described in § 4.4, the Ophiuchus cloud seems to have been subjected to a shock wave. However, this may not be the only one. Other shock waves, associated with H I shells 2 and 3, may also have interacted or are still interacting with the Ophiuchus cloud, see figure 4.4 and table 4.3.

4.6 Solar Wind Charge Exchange

As briefly discussed in chapter 2, section 2.5, the physical mechanism of charge exchange between ions from the solar wind and neutral material has been pointed out as the mechanism responsible for the soft x-ray emission, normally explained within the LB paradigm, see Lallement [144, 145]. Therefore, the possibility of solar wind charge exchange (SWCE), being the mechanism responsible for some fraction of the total soft x-ray emission, was investigated.

The presence of this astrophysical effect in the local interstellar medium (LISM)

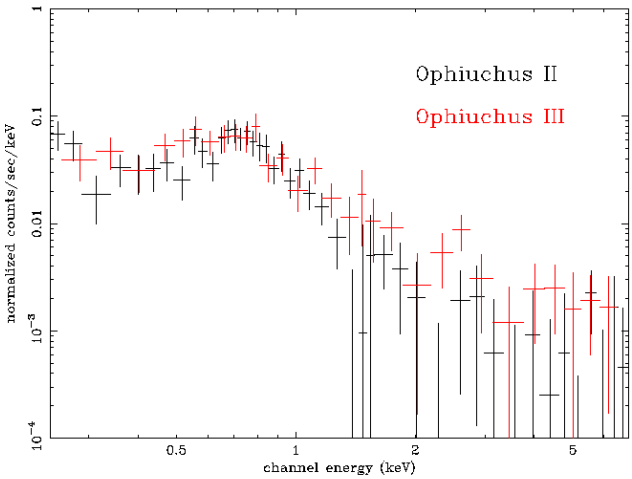

FIGURE 4.6: Ophiuchus Spectra analysis on SWCE. The plot shows the two spectra obtained six months apart from the same regions of the dark filament in the Ophiuchus molecular cloud. Given the statistics, no significant variation of intensity is observed. The spectrum of the second observation, named Ophiuchus II, is plotted in black while the spectrum obtained during the third observation, named Ophiuchus III, is plotted in red. The background spectrum usued for detector subtraction in Ophiuchus III observation was also corrected using the PMH ratio.

can not be ignored, even if the exact "quiescent" level of this contribution is not known. Another important fact about the soft x-ray emission, due to SWCE, is, that this contribution is a physical phenomenon variable in time. An effect that may have been seen already during the ROSAT era by Freyberg [148], and dubbed as long-term enhancements (LTE) [113]. We have investigated a possible variability on the three dark filament Ophiuchus XMM-Newton observations. They were then compared with another XMM-Newton observation, where SWCE was detected by Snowden et al. [149].

This was done in two ways. First by studying the spectra of the same sky region, which were observed about six months apart, and second, by analysing for each observation the count rate in two energy bands.

Since the third observation named Oph III was performed about six months apart and since it partly covers the same sky region as Oph II, we have selected the same region of the cloud, with the highest possible column density, in order to investigate the possibility of seasonal SWCE emission variability in a time scale of six months.

The region of the cloud corresponds to a circle, centered at the position $\alpha = 16^{\mathrm{h}}40^{\mathrm{m}}20^{\mathrm{s}}$ and $\delta = -24^{\mathrm{d}}32^{\mathrm{m}}00^{\mathrm{s}}$, with a radius of 3 arcmin. The same data reduction procedure, as described in section 3, was applied to these spectra. In figure 4.6 the spectra are shown. As it can be seen, no significant variation in the intensity of the spectra is observed.

Recently, the same astrophysical phenomenon was detected in one of the XMM-Newton observations in the Hubble Deep Field North (HDFN) by Snowden et al. [149]. The same SWCE effect has been detected in other XMM-Newton observations, e.g. in the observation with ID 0109060101, performed during revolution 0139. Another way to investigate a possible contamination, due to SWCE, is, to study the count rate in some energy interval where this phenonemon can be observed. We have chosen the interval 0.5 - 0.75 keV since, and if present, the SWCE will contribute

in this range due to O VII, O VIII and Fe XVII ions. We then compare these rate with the rate in a given energy interval, where the SWCE does not contribute, e.g. in the 2.0 - 8.0 keV interval, where the x-ray photons are due to the Cosmic X-ray Background.

Count rates of the three Ophiuchus observations and of the HDFN observation (revolution 0271, ID 0111550401) were created, using only the data from the EPIC-pn detector. The procedure for creating this count rates consists on the following: First, light curves are produced for each observation after cleaning the event files from bad pixels, bad columns (FLAG==0) and after removing all detected point sources. The point sources have to be removed, because their emission can be variable and produce a similar effect mimicking a SWCE situation. Therefore, it is important to be sure, that there is no x-ray emission contribution from the sources in the field of view. Snowden et al. [149] have not removed the point sources in their analysis. The rate light curves were produced, having 200 s for the three Ophiuchus observations, and 1150 s for the HDFN one. The high time bin for the HDFN observation was chosen, in order to better distinguish the two emission regimes. Otherwise, a continuous count rate from ~ 0.2 to ~ 0.7 counts/s in the 0.5 - 0.75 keV band would be the relevant result.

The second step consists on the creation of appropriate good time intervals (GTI's) for each observation.

The third step, the production of count rates is done by selecting the events obeying the filtering criterion of (PATTERN==0), using the corresponding GTI file, selecting the x-ray photons in the energy bands of 0.5 - 0.75 keV and 2.0 - 8.0 keV, and using the same time bins as before. In figure 4.7 we show the scattergrams of the eight count rates. The scattergrams a), b), c) show the count rates for the first, second, and third observation, dedicated to the Ophiuchus molecular cloud, d) shows the count rate from the HDFN observation. The scattergrams a) and b) correspond to the XMM-Newton on-cloud pointings, where the highest hydrogen column densities are observed. The scattergram c) corresponds to the off-cloud and, therefore, is highly contaminated by the Loop I superbubble and halo emission.

Given the GTIs for these three observations, one cannot infer what is, if there is any, a quiescent x-ray emission level, due to SWCE. However, one may confidently assume, that during these three observations no significant variation of x-ray emission due to SWCE occured. Any strong x-ray emission variation in the 0.5 - 0.75 keV band should then be followed by a distribution of this count rate over a constant count rate in the 2.0 - 8.0 keV band. An effect that is not convincingly seen in any of the scattergrams a), b) and c). The scattergram d) is the equivalent for the HDFN observation. As it can be seen in this scattergram and as reported by Snowden et al. [149], two different x-ray emission regimes occur during this observation. The dashed lines in the scattergrams represent the rate averages for the total GTI. It is interresting to note, that the level, corresponding to the x-ray emission in the 0.5 - 0.75 keV band of the low count rate regime in the HDFN observation, is not significantly higher than the ones from the first and second observations to the Ophiuchus molecular cloud, respectively a) and b) plots. This points to the conclusion, that a series of dedicated observations towards nearby molecular clouds

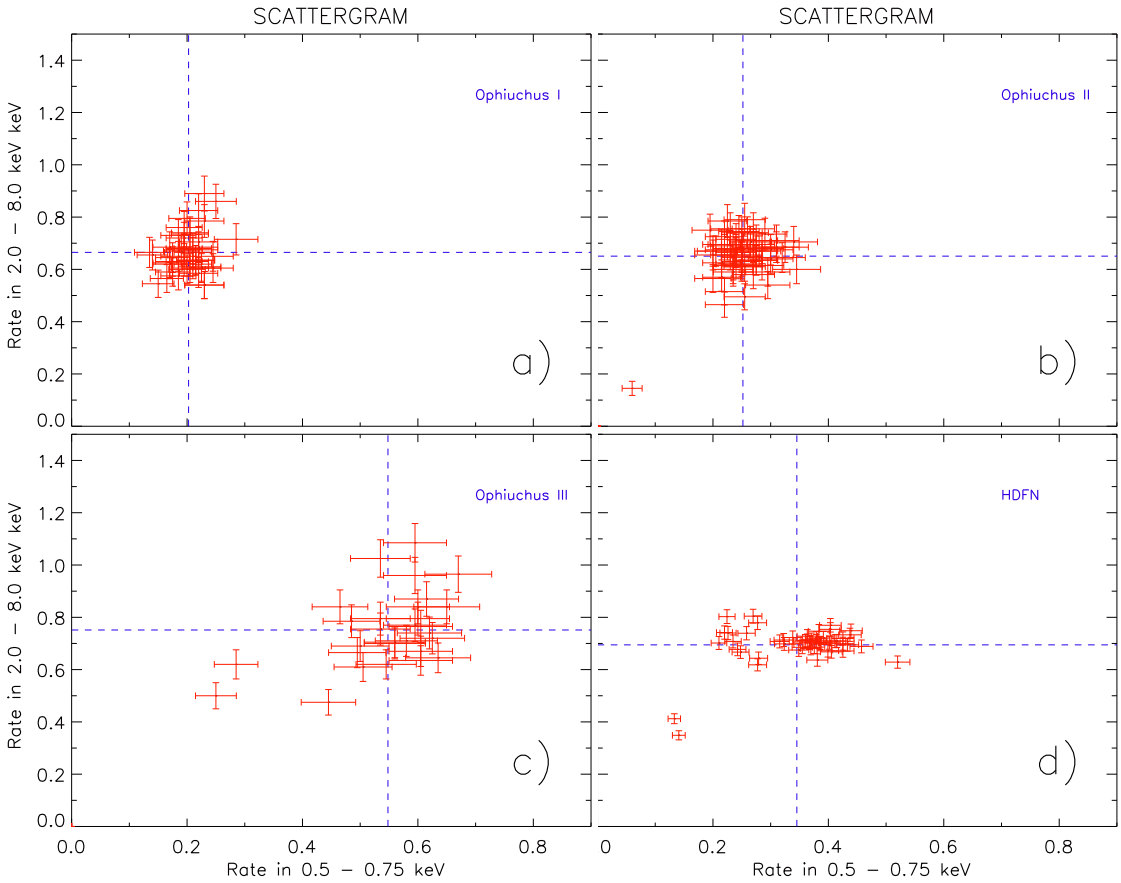

FIGURE 4.7: SWCE analysis scattergrams. The four scattergrams show the count rates in the 0.5 - 0.75 keV and 2.0 - 8.0 keV bands for four different observations. The first three scattergrams correspond to the dedicated Ophiuchus shadow experiment (Ophiuchus I, II, III, respectively scattergram a), b) and c)). The fourth scattergram d) corresponds to one of the dedicated XMM-Newton Hubble Deep Field North (HDFN) observations. These scattergrams were produced to investigate possible Solar Wind Charge Exchange (SWCE) contamination of the Ophiuchus shadow experiment data, and to compare with an observation, known to be contaminated by SWCE [149]. The dashed lines in each scattergram show the average count rate values for the total GTI. The scattergram d) shows convincingly two distinct soft x-ray emission regimes.

may be the best method to study a quiescent x-ray emission level due to SWCE.

4.7 The local Galactic ISM

The knowledge of the immediate or local Galactic ISM has gained a great momentum over the last decade with a series of different astronomical observations.

The low density H I cavity, in which the Solar system is embedded, has been intensively investigated by studying the absorption equivalent widths of the interstellar NaI D doublet at 5890 Å towards nearby stars. The equivalent widths (EWs) of NaI D have been used to trace the local Galactic distribution of neutral hydrogen.

Welsh et al. [198] have initiated the work of compiling a database of previous

measurements of sodium EWs from the literature, to which they added a new sample of NaI D EWs measurements. This continued with the work of Sfeir et al. [117], which added a new sample of 143 EWs measurements and corrected the distance to stars, previously analysed with the new distance measurements from the HIPPARCOS satellite. Vergely et al. [199] have used the former work to derive a three dimensional (3D) density distribution of NaI and H I in the Solar neighbourhood. Presently, the most complete work in this field was presented by Lallement et al. [118], who have created a more detailed 3D map of interstellar neutral material surrounding the LB, using a total of 1005 EWs measurements towards stars within a radius of 360 pc from the Sun.

In figure 4.8, the 20 mÅ EW contour level of NaI D is plotted in the galactic plane and perdendicular to it. This contour level is shown as the cross lines. The EW of 20 mÅ corresponds approximately to a H I column density of 2.0×10^{19} cm^{-2}. Lallement et al. [118] have also presented a 50 mÅ EW contour level of neutral material, to which corresponds a H I column density of $> 1.0 \times 10^{20}$ cm^{-2}. The transition from the column density of $< 2.0 \times 10^{19}$ cm^{-2} to more than 1.0×10^{20} cm^{-2} occurs typically within $\sim$ 30 pc, and has been associated by these authors to the LB boundary.

The discovery that only 50 per cent of the 1/4 keV band flux is originating in the surroundings of the Solar system had dramatic consequences for the knowledge of the x-ray emissivity volume associated to this emission. Another step forward on the knowledge of the local Galactic ISM was given around the end of the ROSAT mission with the release of the all-sky survey data. From the analysis of this data, and after adding a new model component to accomodate the contribution of the galactic hot halo, Snowden et al. [116] derived the volume, associated to the LB soft x-ray emissivity. The derived temperature for the LB was $1.17^{+0.14}_{-0.13} \times 10^6$ K and the electron density n_e of 4.5×10^{-3} cm^{-3}. In figure 4.8 the emissivity volume of the LB derived by Snowden et al. [116] has been superimposed on the 20 mÅ contour level. As it can be seen, the soft x-ray emissivity in these two planes are completely confined by the 20 mÅ contour level. In the previous § 4.5 we have seen, that the radius of the Loop I is 128 pc. This information has been used to complement the plots from figure 4.8 with the extension of Loop I. The representation of Loop I in these two plots corresponds to the intersection with the two Galatic planes. Therefore, the radii of these circles have 121 and 108 pc in the Galactic plane (GP) and perpendicular to the Galactic plane (PGP), respectively. The plots were also enriched by projecting the position of the Ophiuchus molecular cloud complex on them.

These plots allow us to depict already two x-ray emissivity contributions in direction of Ophiuchus, the LB and Loop I emission. The position of the Ophiuchus molecular complex is also shown, and it was assumed that the distance to the system of molecular clouds is 125±25 pc [168].

The astrophysical model of the local Galactic ISM should have, necessarily, the LB x-ray emission component, and the Loop I emission component. Since, the XMM-Newton line of sight crosses the Ophiuchus dark filament, the Loop I emission should be separated in two sub components. One, not absorbed by the dark filament,

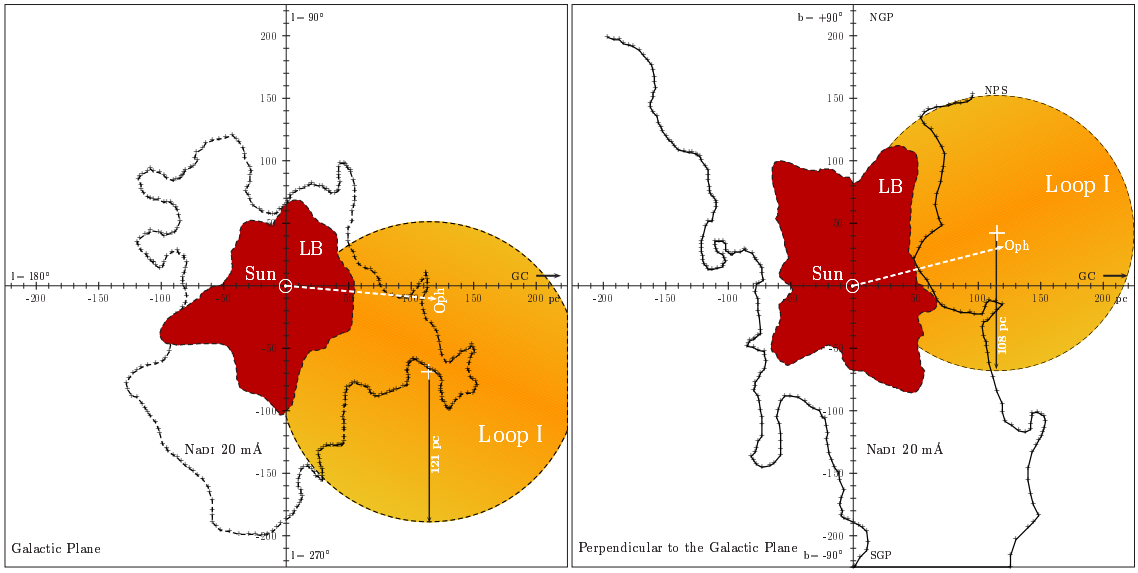

FIGURE 4.8: The local Galactic ISM. In these plots we show the present understanding of the LB soft x-ray emissivity volume, due to Snowden et al. [116], complemented with the study of Lallement et al. [118], where the absorption EWs of NaID were used to infer the local distribution of neutral gas. For producing these plots, we have used the EW contour of 20 mÅ. We have also added a schematic representation of Loop I, assuming a radius of 128 pc. On the Galactic plane (GP) and perpendicular to the Galactic plane (PGP), we have plotted the intersections between Loop I and these two planes. Therefore, the radii of these circles have 121 and 108 pc for the GP and PGP, respectively. We also plot the projection of the Ophiuchus position onto these two planes. We have simplified the left plot, by assuming, that the Sun lies in the GP. However, it is known that the Sun lies at a distance of 34.56±0.56 pc above the GP [119]. The Galactic Center (GC) direction is indicated with an arrow. The North Galactic Pole (NGP) and the South Galactic Pole (SGP) are also shown in both sketches.

and another, subjected to the effect of absorption, due to the molecular filament. However, the second Loop I contribution, the absorbed one, was not possible to resolve from other Galactic and more distant components. For that reason, the second Loop I contribution was not included in the final fitting model. This means, that this emission was included in the model of the Galactic hot halo component.

4.8 The Milky Way Galaxy's hot Halo

The existence of a hot Galactic halo has been postulated more than 50 years ago by Spitzer [39], in order to confine the observed H I clouds at high Galactic latitudes. Astrophysical studies, done in the seventies and later on, have shown that a widespread hot plasma is pervading the Galactic ISM. Several highly ionized species, like the O VI ion, have been detected in absorption towards stars at different Galactic latitudes, sampling a gas supposed to be in a CIE state, with a temperature of more than 2×10^5 K. For instance the abundance of the O VI ion, in CIE, has a peak at 2.8×10^5 K.

Studies of more high-energy photons (0.25 keV $\sim 2.9\times10^6$ K) have also revealed the presence of a hot gas [26, 107] in the neighbourhood of the Sun, with low density and temperatures $\geq 10^6$ K. X-ray shadow observations, performed with the ROSAT satellite to high Galactic latitudes, have made clear, that half of this emission has a different origin [32, 31], i.e. the hot halo of the Galaxy.

In the light of these discoveries and subsequent work, it is natural to add one or more new model components, representing the different gases that XMM-Newton may be sampling. In particular, since the line of sight of the XMM-Newton x-ray shadow experiment towards Ophiuhus, is in direction of the Galactic center (GC), it is not unrealistic to expect hot gas streaming from the GC and from the boiling stellar activity around the GC.

The x-ray spectra, obtained on 625 ks Chandra observations of the GC [200], required two hot plasmas to reproduce the data. A cooler plasma with $k_BT \approx 0.8$ keV ($\sim 9.3\times10^6$ K) and a hotter one with a $k_BT \approx 8$ keV ($\sim 93.0\times10^6$ K) were necessary. The softer plasma is probably heated by supernovae, along with a small contribution from the winds of massive Wolf-Rayet (W-R) and O stars. It was calculated, that a wind of 10^{-3} $M_\odot$ yr^{-1} [201] is driven out of the central star cluster. According with Muno et al. [202] a $k_BT \approx 8$ keV plasma would be too hot to be bound to the Galactic center and therefore would form a slow wind or fountain of plasma. The energy required to sustain such a freely expanding plasma within the inner 20 pc of the Galaxy, is 10^{40} erg s^{-1}. This would correspond to the entire kinetic energy of one supernova every 3000 years. Such value is unreasonably high.

The physical origin of the hotter component is still a mystery. Several hypotheses have been put forward to explain this harder contribution. The favored hypothesis suggests, that this x-ray emission has, as most likely, origin in unresolved cataclysmic variables. Based on the analysis of Chandra data, [202] have argued, that cataclysmic variables are 10 times too few to be able to reproduce the observed emission. However, Revnivtsev et al. [203], Sazonov et al. [204] have claimed to be able to reproduce the GC x-ray emission in the 3-20 keV energy band as the result of weak x-ray sources, mostly cataclysmic variables and coronally active binaries.

Non-thermal x-ray features with knot-like morphologies were recently discovered by analysing the energy band of 3.42 to 6.30 keV of Chandra data by Senda et al. [205]. The spectral analysis of these structures showed, that they are well reproduced by a single power-law, with photon indices of 1-2. Interestingly, three of these knot-like x-ray features are aligned, which was suggested to be the result of ejected material from Sgr A^* in the recent past.

In figure 4.9 we present the morphology of the Milky Way Galaxy, based on the sketch from Matteucci [206]. This sketch allows us a visualization of the XMM-Newton observations lines of sight through our Galaxy. As it can be depicted, the sight line crosses the plane perpendicular to the GC at a scale height (Z) of about 2 kpc, assuming that the distance to the GC is 8.0 kpc.

These sight lines cross several Galactic spiral-arm and inter-arm regions, where different types of superbubble structures are expected to be formed. To be more precise, and according to the work of Taylor and Cordes [207] and McClure-Griffiths et al. [208], the three XMM-Newton observations cross at least three spiral-arm and

three inter-arm regions until the CC. In the arms SNRs are expected to form a bunch of bubbles, because this is, where early OB association stars are formed. Whereas, in the inter-arm regions O and B stars are formed isolated.

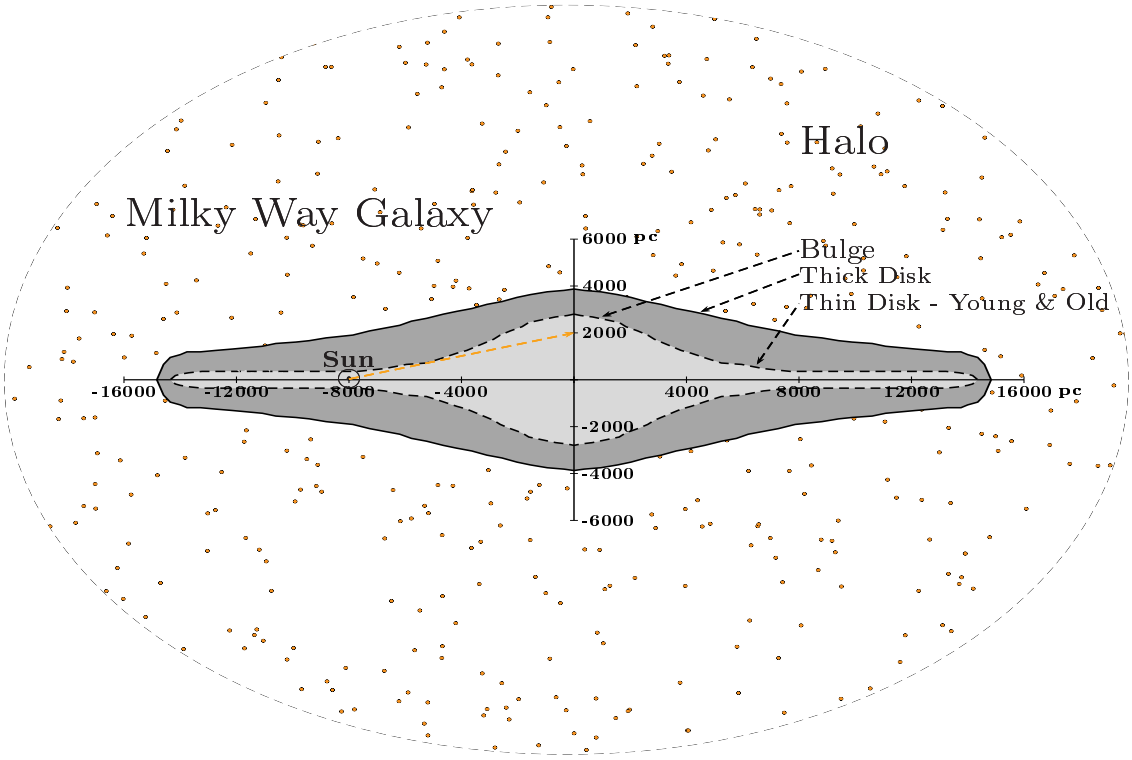

FIGURE 4.9: Schematic view of the stellar morphology of the Milky Way Galaxy. The schematic representation of the Milky Way is based on the sketch from Matteucci [206], see references therein. In this plot the traditional distance value to the Galactic Center (GC) of 8.0 kpc was assumed. However, recent research has lowered this value to 7.62±0.32 kpc [209]. The line of sight of the three XMM-Newton observations is also depicted, as an arrow dashed (orange) line. As it can be seen, at a distance of 8.0 kpc these observations are sampling gas at a scale height of 2 kpc above the GC. The points in the figure represent random globular clusters.

To the previous model two more Galactic components were added. They intent to represent a cooler and a hotter galactic plasma, which are expected to be present in this line of sight.

4.9 The extragalactic X-ray Background continuum

The discovery of the Cosmic X-ray Background (CXB) by Giacconi et al. [97] showed the existence of a diffuse x-ray emission of approximately constant intensity in all sky directions. All-sky surveys performed after the Uhuru and Ariel V satellites revealed a high degree of isotropy. X-ray data from another x-ray mission, the HEAO-1 mission showed, that this data could be reproduced, assuming a plasma with a temperature $k_BT \approx 40$ keV ($\sim 464\times10^6$ K) [210] emitting bremsstrahlung

radiation in the 3.0-50.0 keV energy band. This lead to the idea, that a pervading hot intergalactic medium was the source of this radiation.

The deep pointed observations from the Einstein satellite showed, that 25 per cent of the x-ray emission, in the energy band of 1-3 keV, could be resolved into point sources. These sources where identified as Actice Galactic Nuclei (AGN) objects by Giacconi et al. [211], which had been found to be strong x-ray emitters [212]. Deeper surveys had to wait until the launch of x-ray missions with more sensivity and high angular resolution Wolter type telescopes, like the one aboard the ROSAT satellite.

Sensitive surveys were performed in the energy band of 0.5-2.0 keV by Hasinger et al. [213, 214], which have allowed them to resolve 75 per cent of the x-ray flux in this energy band into discrete sources. Brandt and Hasinger [215] have reviewed the present understanding of the origin of this CXB.

These results in conjunction with the fact, that no distortion of the cosmic microwave background (CMB) was observed, due to a strong Compton effect of a 40 keV hot plasma, lead the astronomers to abandon the hypothesis of a widespread intergalactic plasma with a temperature of $\sim 464{\times}10^6$ K.

Since its discovery the CXB was studied intensively through its spectrum. A major step forward in modelling and deriving some properties, using the 3-10 keV energy range, was done by Gendreau et al. [161] with the ASCA satellite data. This analysis showed, that a single power-law with spectral index (Γ) of 1.4 could reproduce the x-ray data even down to 1 keV. Below 1 keV the extra flux was attributed mainly to the hot ISM surrounding the Solar system and other Galactic emissions. The extrapolated intensity at 1 keV of this power-law was found to be 9.6 keV s^{-1} cm^{-2} sr^{-1} keV^{-1}.

From the above discussion one sees, that our model must incorporate another component representing the extragalactic x-ray contribution. This component is very well described by a single power-law. For our spectral analysis we have used recent measurements, obtained with the XMM-Newton by Lumb et al. [158]. Identical values were found for the spectral index $\Gamma{=}1.42 \pm 0.03$, and for the extrapolated intensity at 1.0 keV, a value of 11.1 photons cm^{-2} sr^{-1} keV^{-1} was obtained from their analysis. Therefore, the power-law model component used in this work is expressed as follows,

$$\mathrm{I_{PW}(E)} = 11.1\ \mathrm{E}^{-\Gamma} \times\ \Omega \text{ photons cm}^{-2}\ \mathrm{s}^{-1}\ \mathrm{keV}^{-1} \tag{4.1}$$

where E is the energy of the photons in units of keV, and Ω is the solid angle in units of steradians (sr).

4.10 The X-ray Background Emission Model towards Ophiuchus

Having presented in the previous sections, the several x-ray emissions along the XMM-Newton lines of sight, we can now formulate explicitly the model to be used in the spectral fitting procedure. The model is as follows,

$$\mathrm{I} = \mathrm{I_{LB}} + \mathrm{e}^{-\sigma \mathrm{N_H(Wall)}} \Big[\mathrm{I_{Loop\ 1}} + \mathrm{e}^{-\sigma \mathrm{N_H(Oph)}} \Big(\mathrm{I_{Halo\ 1}} + \mathrm{I_{Halo\ 2}} + \mathrm{I_{PW}(E)} \Big) \Big]. \tag{4.2}$$

The observed spectra are then fitted with the above model, where I means the total intensity, measured by the observer. I_{LB} is the LB contribution, N_H(Wall) is the column density of H I, due to the interaction between the LB and Loop I, $I_{Loop\ I}$ is the Loop I emissivity, N_H(Oph) is the column density, due to the Ophiuchus dark filament, $I_{Halo\ 1}$ and $I_{Halo\ 2}$ are the two hot halo components, respectively, and finally, I_{PW} is the extragalactic power-law component.

In this model, the column density associated with the local interstellar cloud (LIC), in which the Sun is embedded, was not considered important. Redfield and Linsky [216] constructed a three-dimensional (3D) model of the LIC,[1] based on measurements of the Hubble Space Telescope (HST), the Extreme Ultraviolet Explorer (EUVE), and ground-based Ca II spectra. They have calculate that the column density associated to this cloud has a minimum of 1.5×10^{18} and a maximum of 2.1×10^{18} cm^{-2}. This means, that the x-ray emissions of the model are not attenuated by column densities of $\sim 10^{18}$ cm^{-2}, due to the LIC, in contrast to the ultraviolet emission counterpart. Therefore, neither of these model components were subjected to the LIC absorption.

The N_H(Wall) interstellar absorption was fixed to the value of 2.9×10^{20}cm^{-2}, which is the H I column density towards the τ Sco star [217] at a distance of 132^{+15}_{-13} pc from the Solar system and $\lesssim$11 pc from the Ophiuchus molecular complex.

4.11 X-ray spectral fit of the XMM-Newton Ophiuchus dark filament data

After extracting the spectra from twenty seven regions out of the three XMM-Newton observations, we proceeded for spectral fitting. The spectral fitting is done with the X-ray Spectral Fitting Package[2] (XSPEC) version 11.3.0.

The twenty-seven spectra were first binned, in order to have a minimum of 40 counts in each energy bin. This is done by using the **grppha** task from the HEASARC sub-package of the FTOOLS[3] package, provided by the NASA High Energy Astrophysics Science Archive Research Center (HEASARC).

The minimization, or the fitting procedure, consists in estimating unknown parameters of a given model function M($\mathbf{x}$) of one or more variable parameters, minimizing the difference between M($\mathbf{x}$) and the experimental data, using some statistic function. In other words, given a function M($\mathbf{x}$), the general problem is to find the value of the variable $\mathbf{x}$ for which the function M($\mathbf{x}$) takes its smallest value.

For fitting the spectra, the χ^2-statistics function was used, which assumes, that all the spectral channels are Gaussian distributed and that the estimate for the variance is uncorrelated with the observed counts. The χ^2 is given by

$$\chi^2(\alpha) = \sum_{i=1}^{n} \frac{M(\mathbf{x}, \alpha) - e_i}{\sigma_i^2} \tag{4.3}$$

[1]The 3D structure of the LIC can be found at http://cobalt.as.utexas.edu/∼sredfield/

[2]The documentation of this x-ray spectral fitting package can be found at the HEASARC website http://heasarc.nasa.gov/docs/xanadu/xspec/

[3]http://heasarc.gsfc.nasa.gov/lheasoft/ftools/

where, $\mathbf{x}$ is the vector representing the number of variable parameters, α the number of free variable parameters, e_i the observed data and σ_i^2 the associated error to each e_i. Also, since our data have few counts, a different weighting was used to better estimate the variance. The standard weigthing was then changed to the **Churazov** weight [218], as suggested in the XSPEC manual. Churazov weighting estimates the weight for a given channel by averaging the counts in surrounding channels, when the spectrum has low counts.

The XSPEC package is composed by a relative big set of astrophysical codes to re-produce x-ray emission. Of particular concern to the present work are the interstellar thermal plasmas. Several plasma codes have been developed over the years, thermal plasmas such as: the Raymond & Smith, the Meka (Mewe, Gronenschild and Kaastra 1992), the Mekal (Mewe, Kaastra and Liedahl 1995) plasmas and their derivative, where the abundances are allowed to vary. The Raymond & Smith thermal plasma has been recently revised with the inclusion of more than million lines. The new Raymond & Smith plasma, now termed as Astrophysical Plasma Emission Code (**APEC**) [138], was used to fit the XMM-Newton x-ray data.

For calculating the x-ray emissivity spectrum of any CIE plasma, dominated by emission lines, it requires a table of atomic abundances, reflecting the element adundances in the ISM. The abundance table is not only important to calculate the plasma emission, but it is also important for the photoelectric absorption models. During the fit procedure, the elements abundance table of Wilms et al. [219], see the appendix table C.3, instead of the abundance table of Anders and Grevesse [142], was used. This is, because the absorption features on x-ray spectra from BL Lac objects—a class of Active Galactic Nuclei (AGN)—due to the ISM, are more consistent with the Wilms et al. [219] abundances, see e.g. Haberl et al. [and references therein, 220].

The Tübigen-Boulder absorption model (**TBabs**), which takes into account the cross-sections for x-ray absorption due to the gas-phase, grain-phase and molecular-phase in the ISM, was used to calculate the H column density of the dark filament, instead of the traditional photoelectric absorption (**wabs**) model. The photoelectric absorption cross-sections used, were the ones due to Balucinska-Church and McCammon [221] and implemented in XSPEC with the command **bcmc**. To fit the extragalactic component, of the CXB, a simple photon power-law was used. This contribution is implemented in the XSPEC by the **powerlaw** model.

The XSPEC **fit** command was then used to find the best fit model parameters of the current data, to minimize the χ^2. The default XSPEC minimization method, and the one used, is a modified Levenberg-Marquardt code based on the CURFIT routine from Bevington and Robinson [222].

The twenty-seven spectra were organized in sets of three elements, from A to I, see table 4.1, with the criterion of having been extracted from the same EPIC-pn detector positions. This means, that each set had a spectrum from the first pointing (i), a spectrum from the second pointing (j), and one from the third XMM-Newton pointing (k). Each set of three spectra was then fitted simultaneously by insuring, that during the fit, the plasma temperature for each spectrum model component $T_{(i,j,k)}$ had the same value, and by establishing a relation between their emission

TABLE 4.4: The Ophiuchus Dark Filament column densities. The column densities observed in each of the 27 regions studied, and the column densities derived from the x-ray spectral fits. In columns (3) and (4) the minimum and maximum column densities for that particular region are given. In column (5) the observed average column density in that region is given, while in column (6) we give the best column density fit value. The column density values are given in units of 10^{22} cm^{-2}.

	REGIONS	NH MIN	NH MAX	NH AVERAGE	NH FIT
(1)	(2)	(3)	(4)	(5)	(6)
Set A	7	1.07	1.98	1.36	1.40
	16	0.29	0.77	0.48	0.48
	19	0.06	0.30	0.17	0.19
Set B	8	1.05	1.33	1.18	1.45
	17	0.24	0.68	0.41	0.36
	20	0.17	0.36	0.26	0.18
Set C	9	0.81	1.62	1.08	0.90
	18	0.09	0.50	0.25	0.27
	21	0.26	0.55	0.26	0.36
Set D	4	1.00	1.78	1.36	1.45
	13	0.27	0.81	0.53	0.58
	22	0.20	0.39	0.31	0.33
Set E	5	0.64	1.62	1.12	1.39
	14	0.33	1.09	0.68	0.80
	23	0.14	0.38	0.26	0.29
Set F	6	0.61	1.87	1.18	1.47
	15	0.55	1.46	0.94	1.15
	24	0.09	0.22	0.15	0.17
Set G	1	0.36	0.98	0.62	0.57
	10	0.93	1.50	1.23	1.51
	25	0.09	0.24	0.17	0.20
Set H	2	0.46	1.40	0.79	0.75
	11	0.69	1.25	0.99	1.25
	26	0.14	0.37	0.24	0.26
Set I	3	0.49	1.70	1.00	1.08
	12	0.52	1.04	0.82	0.92
	27	0.06	0.39	0.22	0.17

measures. The relation is given by the product of EM_i and the ratio of their solid angle, $EM_{j,k} = EM_i\ (\Omega_{j,k}/\Omega_i)$. The assumption behind this procedure is, that in scales, smaller than a degree, the temperatures are the same and also their EMs.

We have attempted for each simultaneous fit to calculate the 90 per cent confidence levels for eleven interesting parameters, implying a $\chi^2 = \chi^2_{\rm min} + \Delta\chi^2$, with $\Delta\chi^2 = 17.3$. However, given the low photon statistics for such a complex model, which reflected in the incapacity to constrain all these eleven physical parameters, we have abandoned this approach in favor of a different one.

The new approach consisted in freezing the halo plasmas temperature and normalization ($K_{\rm plasmas} \propto$ EMs) to their best fit values. Also, since the hydrogen column densities, derived from the fits for the Ophiuchus dark filament, had similar values as the ones obtained from the extinction map, we have also fixed them to their best values, reducing the number of interesting parameters to four. The column densities, associated to the Ophiuchus filament, obtained from the extinction map, and the corresponding values derived from the spectral fits, are presented in table 4.4.

This reduction of the number of model space parameters implies also a reduction of the $\Delta\chi^2$, used for calculating the 90 per cent confidence levels. Therefore, for four

interesting parameters, the LB and Loop I temperatures and their EMs, the $\Delta\chi^2$ to be used is 7.8. With this approach it was possible to constrain the four model parameters, in particular the LB, the main subject of the present study and the first of all contributing sources to the CXB.

After minimizing the χ^2 function, estimates of the associated errors for the best fit model parameters are calculated. The estimates of the errors are calculated in XSPEC with the **error** command. The simultaneous joint confidence levels are calculated, using the XSPEC **steppar** command. In the appendix table D.1 a list of the $\Delta\chi^2$ values, used for calculating the joint confidence contours as a function of the number of free parameters, are given.

The x-ray spectra, obtained with the XMM-Newton towards the Ophiuchus dark filament, as well as the fit results to the model, are presented in figures 4.10, 4.11, 4.12, 4.13 and 4.14, respectively. In each of these figures we plot the set of x-ray spectra from the three different regions, the theoretical model derived from the XSPEC fit procedure and the residuals of that model to the data. The data points are shown as crosses and the theoretical model as solid lines. The contribution due to the LB is also shown in these plots.

The results, obtained from the x-ray spectral fits, are resumed in table 4.5. In the first two columns of this table the set and region numbers are given. The following two columns, number 3 and 4, correspond to the LB temperature and EM, respectively. Columns 5 and 6 are the temperature and EM from the Loop I superbubble. The columns 7 and 9 show the temperatures of the two Halo components, while 8 and 10 show the EMs of these model components. Finally, in column number 11 the reduced χ^2 of the fit is presented. In figure 4.15 the main results given in table 4.5 are depicted.

The corresponding confidence levels, obtained from the best fit for each data set, are presented in the appendix D on figures D.1, D.2, D.3, D.4, D.5, D.6, D.7, D.8 and D.9. In each of these figures four contour plots are shown. The top-left plot shows the confidence levels from the LB temperature and EM. In the top-rigth plot the confidence levels of the LB versus Loop I temperatures are depicted. On the bottom-left plot the correlation confidence levels from the LB temperature versus Loop I EM are shown. In the bottom-right plot the contour levels from the Loop I temperature and EM are presented.

We have assumed that the $\frac{n_H}{n_e}$ is 1.0, which means, that we are considering a plasma composed only of hydrogen. The former assumption implies, that the calculated EMs and electron densities (n_e) are the minimum possible values. If instead a value of 0.813, for a fully ionized gas with 10 per cent of helium, would be assumed for $\frac{n_H}{n_e}$, then this would imply, that the EM would increase by about 20 per cent. The reason relies on the fact that when calculating the EM, one uses the normalization factor K_{plasma}, derived from the x-ray spectra fits, which are proportional to $n_H n_e$. Since $EM \equiv n_H n_e D \propto K_{plasma}$ and $n_H = 0.813\ n_e$, this means that $n_e{}^2 D \propto K_{plasma}/0.813$. In other words, the $n_e{}^2 D$ is inversely proportional to the relative number of H to electrons.

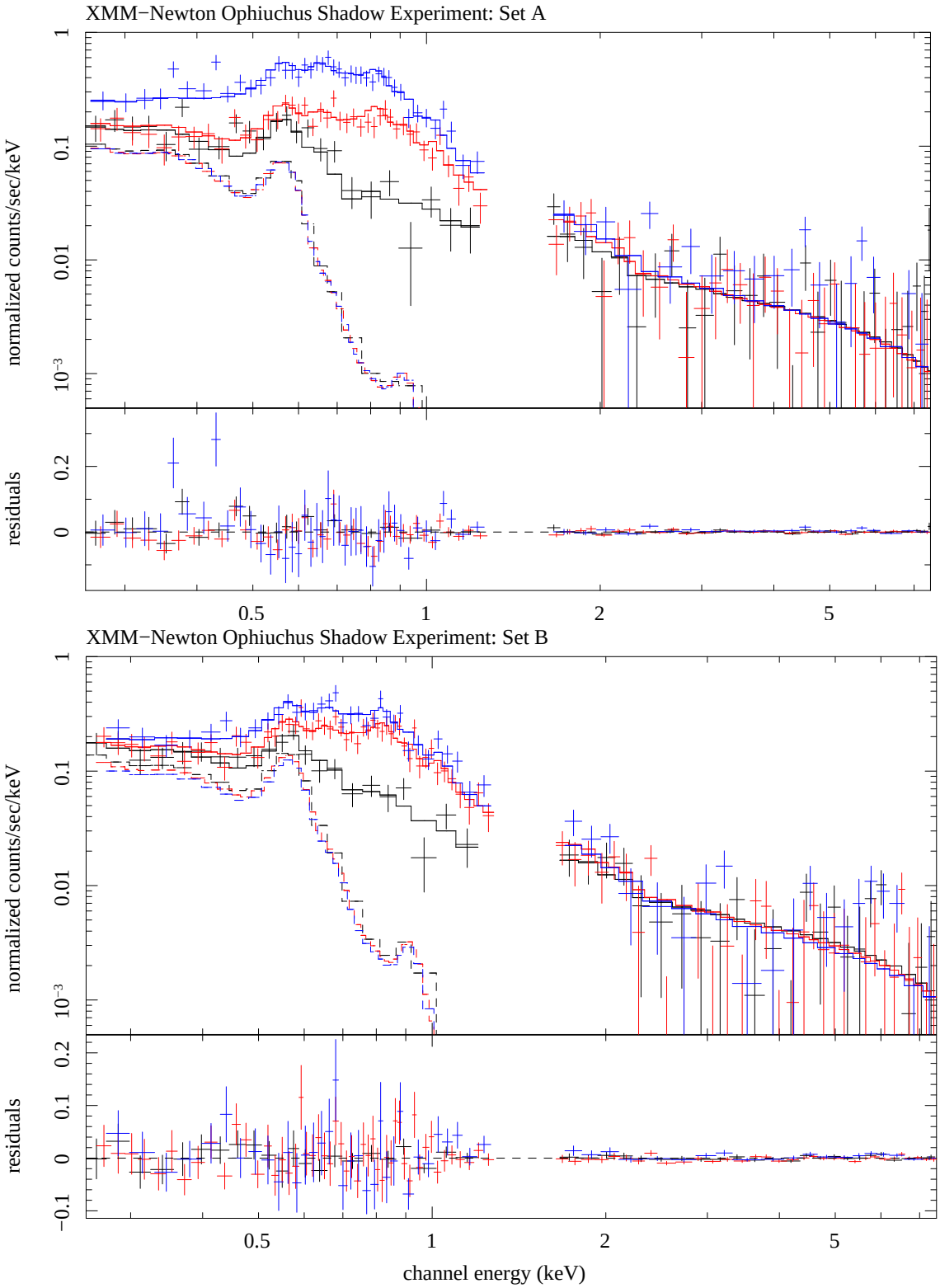

FIGURE 4.10: X-ray spectral fits from the Ophiuchus x-ray shadow experiment. In the plots above we show the resulting simultaneous fits from the x-ray data to the adopted model. The LB component was also added to show its contribution to the general spectrum. In black are shown the data, the model and the LB component of the first XMM-Newton Ophiuchus pointing. The second and third pointings are shown in red and blue colors. Each of this plots corresponds to spectra of set A (top) and of set B (bottom).

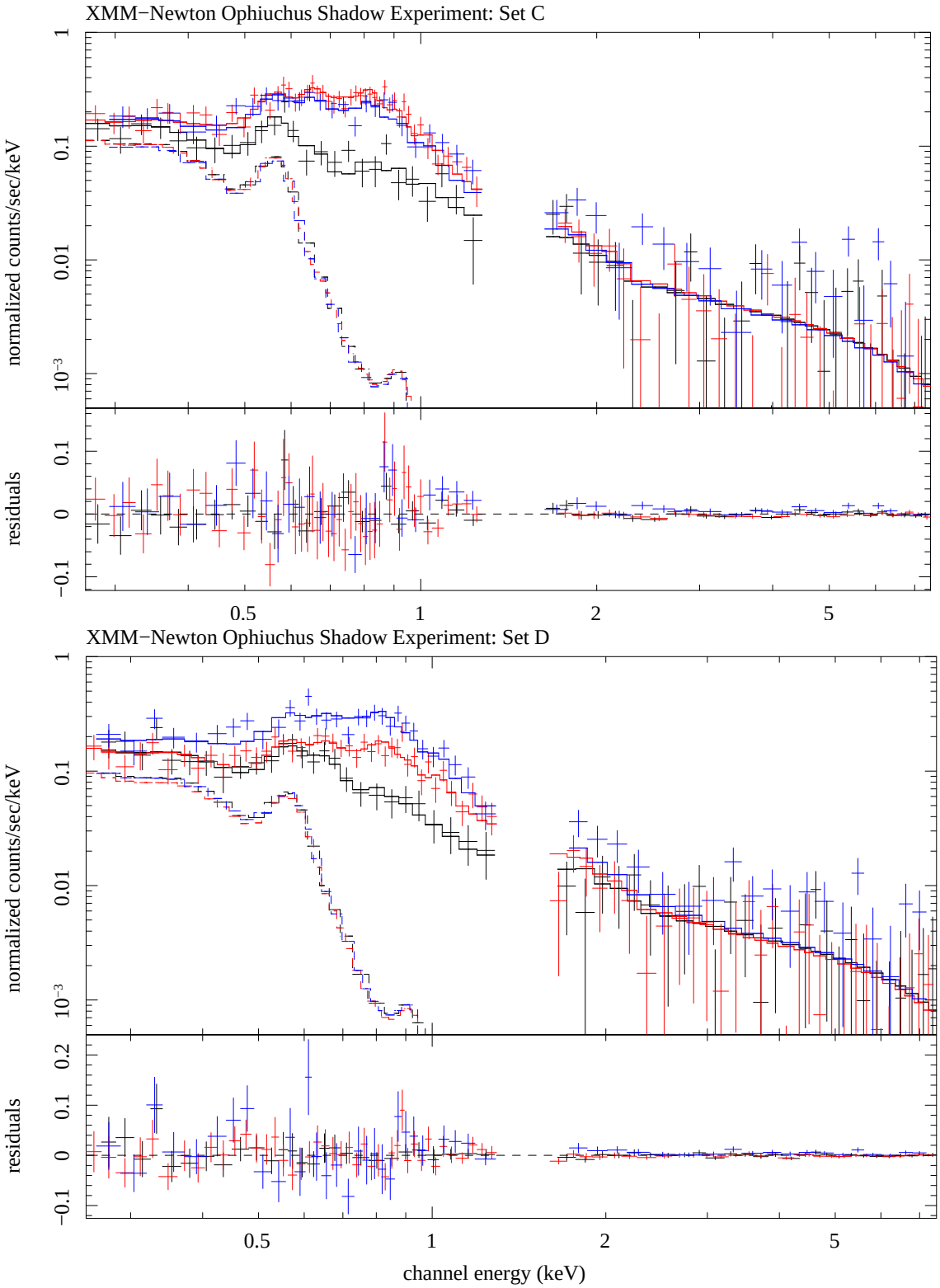

FIGURE 4.11: X-ray spectral fits from the Ophiuchus x-ray shadow experiment. In the plots above we show the resulting simultaneous fits from the x-ray data to the adopted model. The LB component was also added to show its contribution to the general spectrum. In black are shown the data, the model and the LB component of the first XMM-Newton Ophiuchus pointing. The second and third pointings are shown in red and blue colors. Each of this plots corresponds to spectra of set C (top) and of set D (bottom).

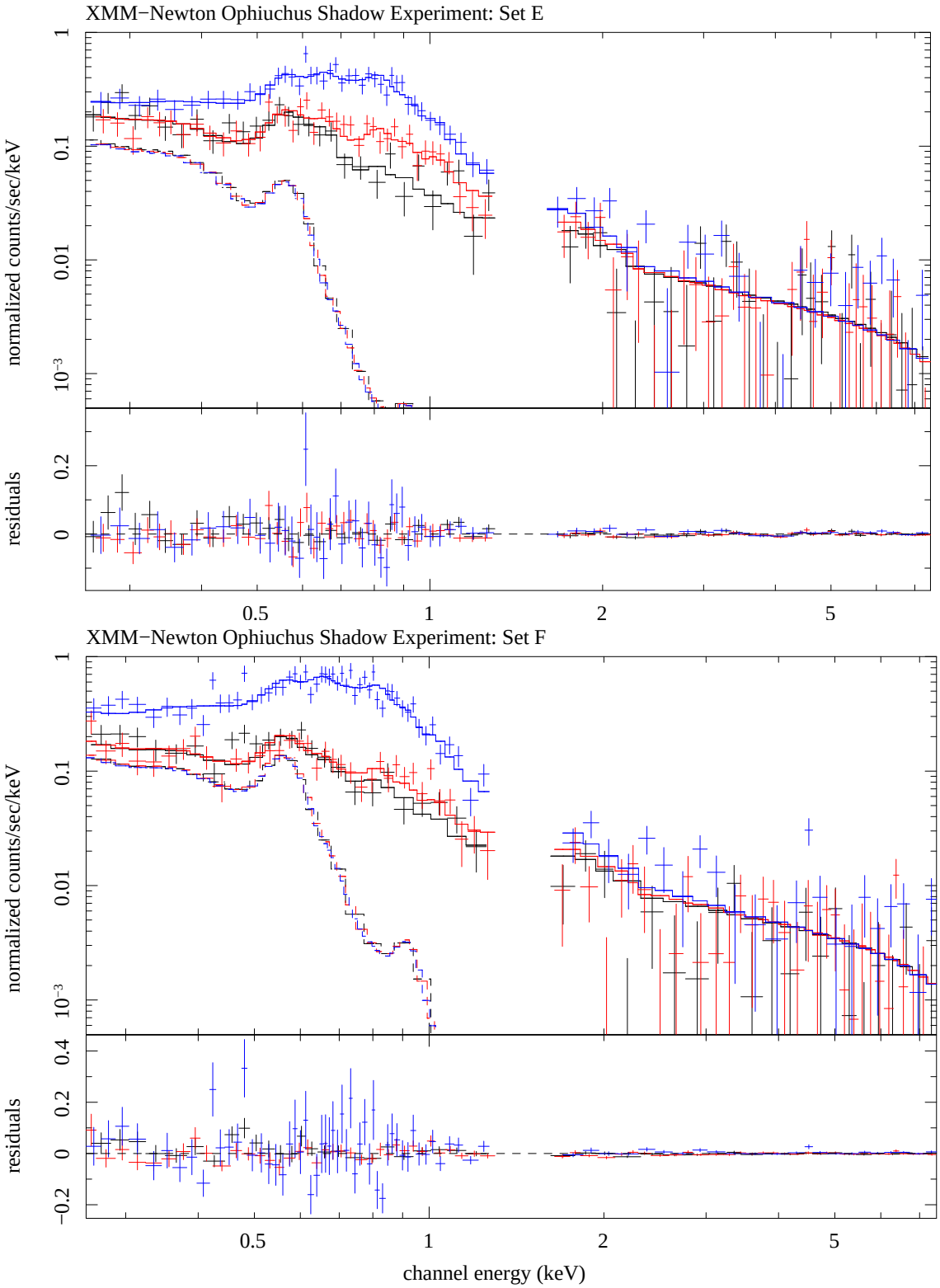

FIGURE 4.12: X-ray spectral fits from the Ophiuchus x-ray shadow experiment. In the plots above we show the resulting simultaneous fits from the x-ray data to the adopted model. The LB component was also added to show its contribution to the general spectrum. In black are shown the data, the model and the LB component of the first XMM-Newton Ophiuchus pointing. The second and third pointings are shown in red and blue colors. Each of this plots corresponds to spectra from set E (top) and from set F (bottom).

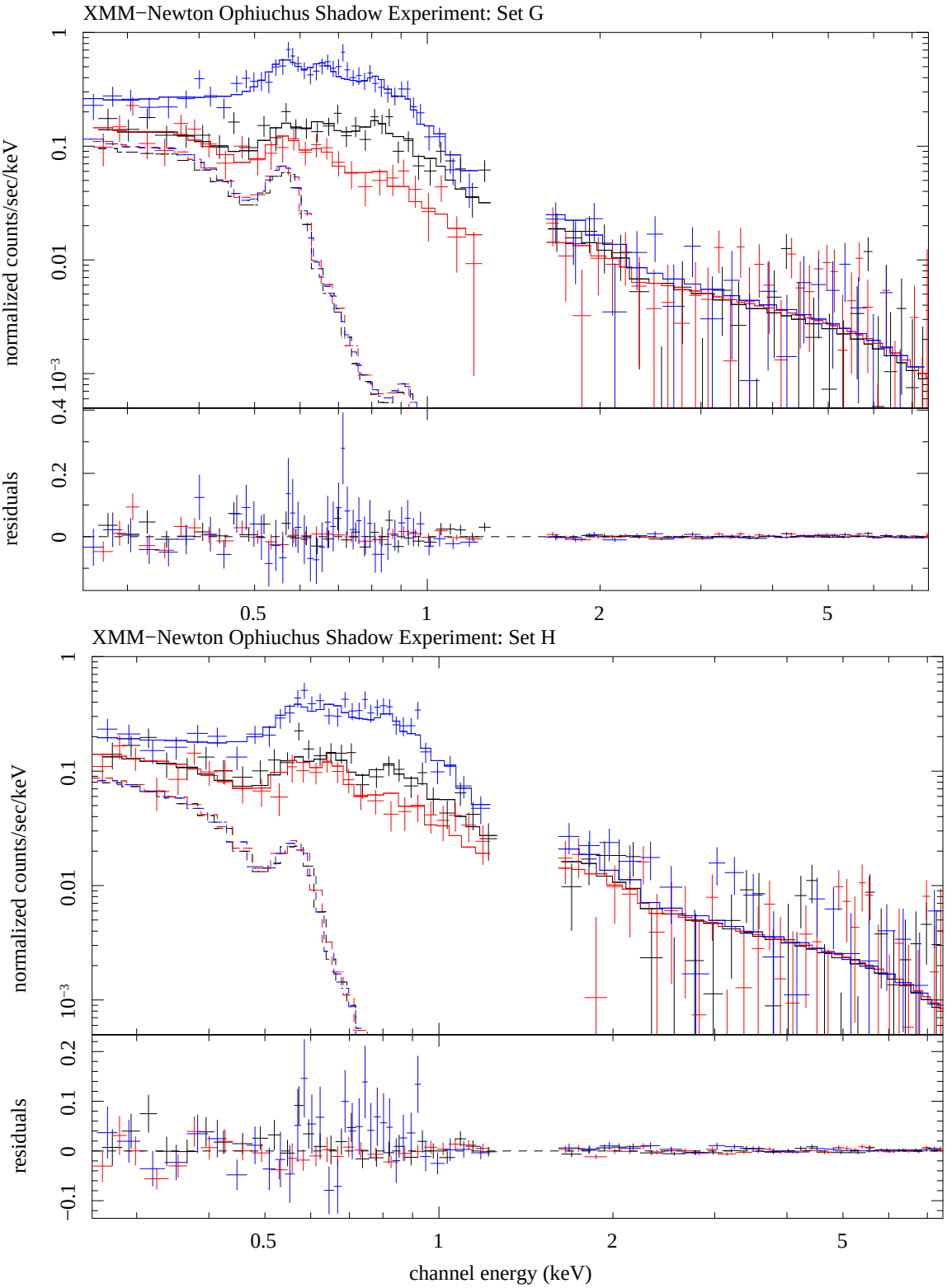

FIGURE 4.13: X-ray spectral fits from the Ophiuchus x-ray shadow experiment. In the plots above we show the resulting simultaneous fits from the x-ray data to the adopted model. The LB component was also added to show its contribution to the general spectrum. In black are shown the data, the model and the LB component of the first XMM-Newton Ophiuchus pointing. The second and third pointings are shown in red and blue colors. Each of this plots corresponds spectra from set G (top) and from set H (bottom).

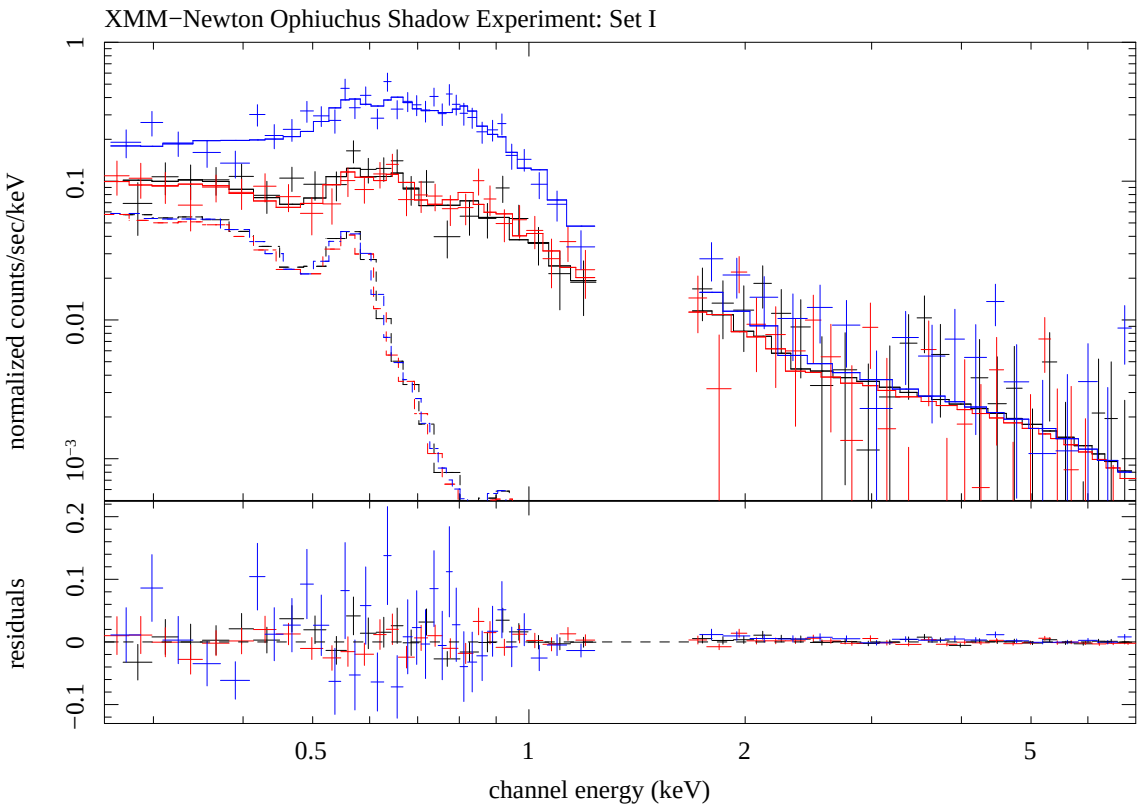

FIGURE 4.14: X-ray spectral fits from the Ophiuchus x-ray shadow experiment. In the plot above we show the resulting simultaneous fits from the x-ray data to the adopted model. The LB component was also added to show its contribution to the general spectrum. In black are shown the data, the model and the LB component of the first XMM-Newton Ophiuchus pointing. The second and third pointings are shown in red and blue colors. Each of this plots corresponds to spectra from set I.

TABLE 4.5: Results from the spatial and spectral analysis of the x-ray shadow experiment to the dark filament of Ophiuchus molecular complex. The errors shown are within the 90% confidence level for 4 interesting parameters, implying $\chi^2 = \chi^2_{\rm min} + \Delta\chi^2$, with $\Delta\chi^2 = 7.8$. The plasma temperatures are given in units of $\mathbf{10}^6$ Kelvin and the emission measures (EMs) in units of $\mathbf{cm}^{-6}$ $\mathbf{pc}$. The EMs are related by the following expression: $\mathrm{EM_{j,k}} = \mathrm{EM_i}\ (\Omega_{\rm j,k}/\Omega_{\rm i})$, see the text for more details.

		LB		LOOP I		HALO 1		HALO 2		
	Regions	Temperature	EM	Temperature	EM	Temperature	EM	Temperature	EM	$\chi^2_{\rm red}$
(1)	(2)	(3)	(4)	(5)	(6)	(7)	(8)	(9)	(10)	(11)
Set A	7	$1.22^{+0.36}_{-0.52}$	$0.009^{+0.024}_{-0.004}$	$2.50^{+1.12}_{-0.50}$	$0.004^{+0.003}_{-0.003}$	1.62	0.035	3.94	0.041	1.16
	16									
	19									
Set B	8	$1.45^{+0.38}_{-0.43}$	$0.009^{+0.002}_{-0.003}$	$3.36^{+1.93}_{-0.76}$	$0.004^{+0.003}_{-0.002}$	1.62	0.036	4.16	0.035	1.04
	17									
	20									
Set C	9	$1.17^{+0.22}_{-0.24}$	$0.014^{+0.010}_{-0.005}$	$2.40^{+1.01}_{-0.58}$	$0.005^{+0.003}_{-0.002}$	1.65	0.034	3.69	0.052	1.23
	18									
	21									
Set D	4	$1.20^{+0.34}_{-0.46}$	$0.011^{+0.023}_{-0.004}$	$3.06^{+0.65}_{-0.43}$	$0.008^{+0.003}_{-0.002}$	1.55	0.062	4.46	0.040	0.85
	13									
	22									
Set E	5	$1.06^{+0.51}_{-0.41}$	$0.011^{+0.038}_{-0.005}$	$2.66^{+0.83}_{-0.36}$	$0.007^{+0.002}_{-0.003}$	1.00	0.282	3.91	0.048	1.09
	14									
	23									
Set F	6	$1.46^{+0.41}_{-0.39}$	$0.008^{+0.002}_{-0.003}$	$3.54^{+1.37}_{-0.69}$	$0.004^{+0.002}_{-0.002}$	1.03	0.136	3.68	0.047	1.31
	15									
	24									
Set G	1	$1.11^{+0.28}_{-0.29}$	$0.012^{+0.014}_{-0.005}$	$3.44^{+1.00}_{-0.60}$	$0.004^{+0.002}_{-0.002}$	1.56	0.060	3.59	0.045	1.00
	10									
	25									
Set H	2	$0.90^{+0.49}_{-0.31}$	$0.017^{+0.053}_{-0.011}$	$2.94^{+0.58}_{-0.32}$	$0.007^{+0.002}_{-0.002}$	1.58	0.065	3.83	0.042	1.13
	11									
	26									
Set I	3	$1.20^{+0.53}_{-0.56}$	$0.009^{+0.046}_{-0.005}$	$3.10^{+1.06}_{-2.70}$	$0.008^{+0.003}_{-0.002}$	1.52	0.051	3.99	0.045	1.06
	12									
	27									
	Average	$1.20^{+0.67}_{-0.61}$	$0.011^{+0.059}_{-0.007}$	$3.00^{+2.29}_{-2.60}$	$0.006^{+0.005}_{-0.005}$	1.50	0.085	3.90	0.044	

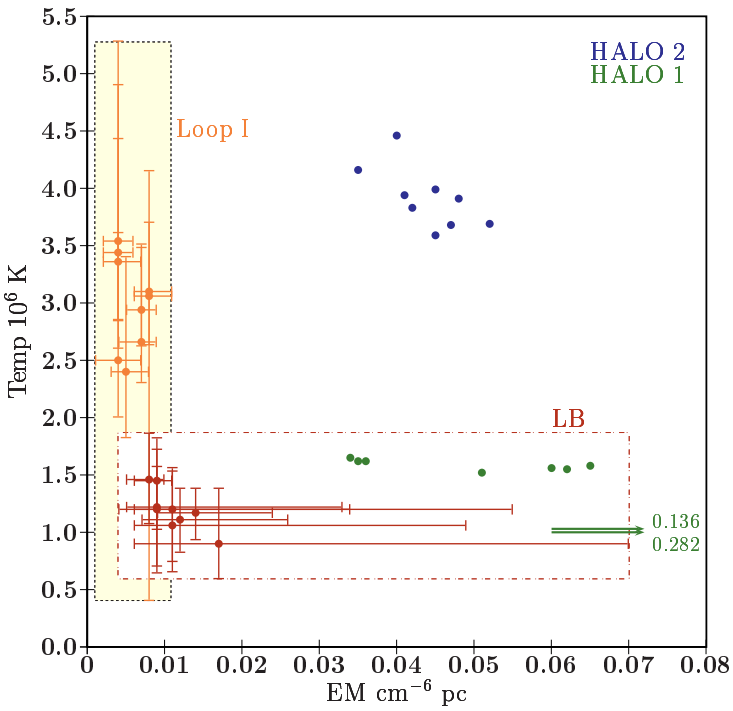

FIGURE 4.15: The main results from the x-ray shadow experiment to the Ophiuchus dark filament. In this plot the derived physical parameters of the temperature and the EM, for the four thermal plasmas, are resumed. The LB and Loop I are represented by the dark red and orange colors, respectively. The two halo components are represented with the green (cooler) and blue (hotter) colors. The two green arrows show two points of the cold Halo in which the EMs are higher than the adopted x-axis range. The respective values are indicated in the front of the arrows.

4.12 The electron densities and thermal pressures from the LB and Loop I

From the physical parameters of EMs and temperatures, derived from the x-ray spectral fits and presented in table 4.5 , the electron densities (n_e) and pressures, respectively, for the LB and Loop I, can be computed. These computed values are given in table 4.6.

This analysis shows, that the global properties, namely, the pressures and electron densities for the LB and Loop I, derived from the work of Egger [195], based on the ROSAT PSPC data by Breitschwerdt et al. [223], are significantly different, especially for the physical parameters of the LB. In case of Loop I, we are only studying a line of sight of 85 pc through it, therefore, significant differences for its electron density and pressure are expected. However, in our model we have assumed, that the Loop I component is entirely in the foreground of the cloud, which could bring the Loop I pressure to lower values, since EM$\propto$D.

Another XMM-Newton observation, using the EPIC-mos detector, has also revealed a much higher LB electron density of $0.013(L/100\ pc)^{-1/2}\ cm^{-3}$ [224], where L is the radius of the LB, normally assumed to be 100 pc. In a recent SUZAKU observation, an n_e of $0.014\ cm^{-3}$ for the LB, was also deduced from an x-ray shadow observation [225].

Interestingly, the pressure derived from this analysis shows, that the LB pressure is about 4 times higher than the one obtained from Snowden et al. [116] (p/k_B 10500 versus 39800 cm^{-3} K).

TABLE 4.6: The LB and Loop I electron densities and pressures. For calculating the electron densities of these two components, an extension of 40 pc and 85 pc was assumed for the LB and Loop I, respectively.

Set	LB		Loop I	
	n_e cm^{-3}	$p/2k_B$ 10^4 cm^{-3} K	n_e cm^{-3}	$p/2k_B$ 10^4 cm^{-3} K
A	$0.015^{+0.014}_{-0.004}$	$1.83^{+0.20}_{-0.10}$	$0.007^{+0.002}_{-0.003}$	$1.75^{+0.05}_{-0.30}$
B	$0.015^{+0.002}_{-0.003}$	$2.18^{+0.44}_{-0.03}$	$0.007^{+0.002}_{-0.002}$	$2.35^{+0.01}_{-0.29}$
C	$0.019^{+0.006}_{-0.004}$	$2.22^{+0.11}_{-0.13}$	$0.008^{+0.002}_{-0.002}$	$1.92^{+0.10}_{-0.13}$
D	$0.017^{+0.013}_{-0.004}$	$2.04^{+0.17}_{-0.04}$	$0.009^{+0.001}_{-0.002}$	$2.75^{+0.13}_{-0.16}$
E	$0.017^{+0.019}_{-0.004}$	$1.80^{+0.53}_{-0.23}$	$0.009^{+0.001}_{-0.002}$	$2.39^{+0.05}_{-0.09}$
F	$0.014^{+0.002}_{-0.002}$	$2.04^{+0.32}_{-0.20}$	$0.007^{+0.002}_{-0.002}$	$2.48^{+0.02}_{-0.09}$
G	$0.017^{+0.008}_{-0.004}$	$1.89^{+0.18}_{-0.08}$	$0.007^{+0.001}_{-0.001}$	$2.41^{+0.14}_{-0.25}$
H	$0.021^{+0.021}_{-0.008}$	$1.89^{+0.59}_{-0.09}$	$0.009^{+0.001}_{-0.002}$	$2.65^{+0.02}_{-0.18}$
I	$0.015^{+0.022}_{-0.005}$	$1.80^{+0.55}_{-0.07}$	$0.010^{+0.002}_{-0.002}$	$3.10^{+0.20}_{-2.60}$
Average	$0.017^{+0.025}_{-0.007}$	$1.97^{+0.65}_{-0.40}$	$0.008^{+0.004}_{-0.004}$	$2.42^{+0.88}_{-1.92}$

4.12.1 The Ophiuchus dark filament distance

A rough estimate of the distance to the Ophiuchus dark filament can be calculated, since the derived pressures of the LB and Loop I are of same order. This means that,

$$n_e(LB)T(LB) \sim n_e(LI)T(LI), \tag{4.4}$$

and using the fact that

$$n_e(LI) = \sqrt{\frac{EM(LI)}{d(LI)}}, \tag{4.5}$$

the following relation is obtained,

$$d(LI) \simeq n_e^{-2}(LB)\ EM(LI)\ \left[\frac{T(LI)}{T(LB)}\right]^2 pc \tag{4.6}$$

So, the distance to the Ophiuchus dark filament is approximately given by the expression

$$d(Ophiuchus) \simeq d(LB) + d(LI), \tag{4.7}$$

where d(LB) is the LB extension in direction to the Ophiuchus cloud, which in the light of the re-analysis of the column density of the H I wall between LB and Loop I, is about 40 pc. It should be noted that, the identical pressure assumption is likely to be incorrect. Since in Loop I there are still SNe, whereas in the LB there are no more OB stars.

TABLE 4.7: Estimate of the distance to the Ophiuchus dark filament. Assuming an ideal equilibrium state between LB and Loop I pressures, a minimum or maximum distance to the cloud is estimated. For that, only the best fit values were used.

Set	n_e(LB) [cm^{-3}]	EM(LI) [cm^{-6} pc]	T(LB) 10^6K	T(LI) 10^6K	d (Oph) [pc]
A	$0.015^{+0.014}_{-0.004}$	0.004	$1.22^{+0.36}_{-0.52}$	$2.50^{+1.12}_{-0.50}$	> 118.6
B	$0.015^{+0.002}_{-0.003}$	0.004	$1.45^{+0.38}_{-0.43}$	$3.36^{+1.93}_{-0.76}$	< 141.8
C	$0.019^{+0.006}_{-0.004}$	0.005	$1.17^{+0.22}_{-0.24}$	$2.40^{+1.01}_{-0.58}$	> 96.3
D	$0.017^{+0.013}_{-0.004}$	0.008	$1.20^{+0.34}_{-0.46}$	$3.06^{+0.65}_{-0.43}$	< 210.5
E	$0.017^{+0.019}_{-0.004}$	0.007	$1.06^{+0.51}_{-0.41}$	$2.66^{+0.83}_{-0.36}$	< 183.0
F	$0.014^{+0.002}_{-0.002}$	0.004	$1.46^{+0.41}_{-0.39}$	$3.54^{+1.37}_{-0.69}$	< 174.6
G	$0.017^{+0.008}_{-0.004}$	0.004	$1.11^{+0.28}_{-0.29}$	$3.44^{+1.00}_{-0.60}$	< 187.1
H	$0.021^{+0.021}_{-0.008}$	0.007	$0.90^{+0.49}_{-0.31}$	$2.94^{+0.58}_{-0.32}$	< 211.8
I	$0.015^{+0.022}_{-0.005}$	0.008	$1.20^{+0.53}_{-0.56}$	$3.10^{+1.06}_{-2.70}$	< 270.3

4.13 The O VI and O VII column densities

We can use the set of results presented in table 4.5 to further investigate what would be the expected values of physical observables, such as the column densities of ions like the O VI and O VII, their thermal speeds and their equivalent widths (EWs) for the four model thermal plasmas. These derived values can, therefore, be compared with available studies or, in the near future, with further studies conducted with the reflection grating spectrometer (RGS) on-board of the XMM-Newton satellite, towards galactic sources which line of sight cross the LB and Loop I. If discrepancies are then observed between high resolution absorption studies and the expected absorption, associated to a LB plasma in CIE, then, this would also indicate that the CIE condition might not be the correct one.

In a recent FUSE survey, conducted by Oegerle et al. [226] towards white dwarfs within a radius of 225 pc of the Sun, an upper limit of 1.7×10^{13}cm^{-2} for the O VI column density N(O VI) was found. The contribution of the LB to the N(O VI) was estimated to be $\sim 7 \times 10^{12}$cm^{-2}, given a mean space density of 2.4×10^{-8}cm^{-3}, assuming a line of sight of 100 pc for the LB.

We start by investigating what would be the expected contribution of O VI in this line of sight from the LB and Loop I. For that, we have assumed the LB extension in this direction to be 40 pc, and the path through Loop I until the Ophiuchus complex to be 85 pc. The column density of a given ion can be estimated, using the following expression,

$$N_{ion} = \frac{n_H}{n_e}\, n_e\, X\left(\frac{atom}{H}\right)\, \delta_{atom}\, f_{ion}(T) \int_0^d ds \qquad (4.8)$$

where the value $\frac{n_H}{n_e}$ is 1.0, in agreement with § 4.11, n_e is the electron density, $X\left(\frac{atom}{H}\right)$ is the fractional abundance of the atom species relative to hydrogen, δ_{atom} is the deplection of the atom into dust grains, $f_{ion}(T)$ is the ionization fraction for that particular ion at a given temperature, and s is the line of sight in consideration.

The former expression can be rewritten as,

$$N_{ion} = A \, \frac{n_H}{n_e} \, X \left(\frac{atom}{H} \right) \, \delta_{atom} \, f_{ion}(T) \, \sqrt{EM \, d} \, cm^{-2} \tag{4.9}$$

where $A = 3.0857 \times 10^{18}$, EM is the emission measure given in units of cm^{-6} pc and the extension of the plasma in this line of sight d is given in units of pc. To calculate this quantity we have used the ionization fractions of the O VI and O VII, taken from Sutherland and Dopita [227], see their table 5. Also, since we have used the abundances table of Wilms et al. [219], the relative abundance of O to H, X(O/H), is set to 4.90×10^{-4}. The depletion value was set to 1.0, following Sofia and Meyer [228, 229].

Table 4.8: The OVI and OVII column densities. In this table we present the expected values for the following physical quantities: The N(O VI) for the LB and Loop I in columns 2 and 4, respectively. In columns 3, 5, 9 and 11 the expected thermal velocity dispersions for these different components of the oxygen ion. Columns 6, 7, 8, and 10 the N(O VII) for the LB, Loop I, Halo 1 and Halo 2, respectively. For calculating the column densities of O VII of the halo components, a line of sight of 8 kpc was assumed.

	LB		Loop I		LB	Loop I	Halo 1		Halo 2	
Set	N(O VI) 10^{12} cm^{-2}	v_{th} km/s	N(O VI) 10^{12} cm^{-2}	v_{th} km/s	N(O VII) 10^{14} cm^{-2}	N(O VII) 10^{14} cm^{-2}	N(O VII) 10^{16} cm^{-2}	v_{th} km/s	N(O VII) 10^{14} cm^{-2}	v_{th} km/s
(1)	(2)	(3)	(4)	(5)	(6)	(7)	(8)	(9)	(10)	(11)
A	$3.2^{+6.6}_{-0.3}$	$35.4^{+5.0}_{-8.5}$	$1.3^{+0.5}_{-1.1}$	$50.8^{+10.3}_{-5.4}$	$8.6^{+8.6}_{-3.2}$	$2.6^{+2.2}_{-2.4}$	1.7	41	10.3	64
B	$2.9^{+0.6}_{-0.6}$	$38.6^{+4.8}_{-3.8}$	$0.3^{+0.6}_{-0.3}$	$58.8^{+15.0}_{-7.0}$	$7.2^{+2.6}_{-3.2}$	$0.6^{+1.7}_{-0.6}$	1.7	41	5.2	66
C	$4.0^{+1.0}_{-0.2}$	$34.7^{+3.1}_{-3.8}$	$1.5^{+1.0}_{-1.2}$	$49.7^{+9.6}_{-6.4}$	$10.7^{+4.2}_{-2.6}$	$2.9^{+2.4}_{-3.9}$	1.7	41	11.6	62
D	$3.5^{+4.1}_{-0.3}$	$35.2^{+3.3}_{-7.6}$	$0.8^{+0.5}_{-0.5}$	$56.2^{+5.6}_{-4.1}$	$9.5^{+8.0}_{-3.6}$	$1.5^{+1.3}_{-1.1}$	2.7	40	5.5	68
E	$3.8^{+7.1}_{-0.6}$	$33.0^{+7.2}_{-7.4}$	$1.2^{+0.5}_{-0.8}$	$52.4^{+7.6}_{-3.7}$	$9.8^{+11.1}_{-3.9}$	$2.3^{+1.6}_{-1.7}$	7.0	32	11.1	64
F	$2.7^{+0.6}_{-0.6}$	$38.8^{+5.1}_{-5.6}$	$0.3^{+0.2}_{-0.3}$	$60.4^{+10.7}_{-6.2}$	$6.8^{+2.5}_{-3.1}$	$0.6^{+0.7}_{-0.5}$	4.9	33	10.0	62
G	$4.0^{+1.8}_{-0.5}$	$33.8^{+4.0}_{-4.7}$	$0.3^{+0.2}_{-0.3}$	$59.6^{+8.0}_{-5.5}$	$10.2^{+5.1}_{-3.1}$	$0.6^{+0.7}_{-0.5}$	2.4	40	10.9	61
H	$5.5^{+15.0}_{-1.3}$	$30.4^{+7.4}_{-5.7}$	$0.7^{+0.5}_{-0.3}$	$55.0^{+5.3}_{-3.1}$	$12.3^{+12.5}_{-5.7}$	$1.4^{+1.2}_{-0.7}$	2.7	40	10.4	63
I	$3.2^{+6.6}_{-0.6}$	$35.2^{+7.0}_{-9.5}$	$0.8^{+87.1}_{-0.7}$	$56.5^{+9.0}_{-36.2}$	$8.6^{+13.6}_{-4.5}$	$1.5^{+11.9}_{-1.3}$	2.4	40	5.9	64
Average	$3.6^{+16.9}_{-1.3}$	$35.0^{+8.9}_{-10.3}$	$0.8^{+87.1}_{-0.8}$	$55.5^{+18.3}_{-35.2}$	$9.3^{+15.5}_{-5.6}$	$1.6^{+11.8}_{-1.6}$	3.0	39	9.0	64

From column (1) of table 4.8 we see, that the LB N(O VI), within the assumed conditions, derived from this analysis is lower than the inferred N(O VI) for the LB from Oegerle et al. [226]. However, if we look at the average O VI space density in this direction, we obtain an average value of $2.9^{+13.7}_{-1.0} \times 10^{-8}$ cm^{-3}, about 17 per cent more than the value obtained by Oegerle et al. [226]. Further, it must be emphasized that this value is the minimum possible value, due to the assumption of a plasma composed by H. Using the average O VI space density of 2.9×10^{-8} cm^{-3} and assuming the radius of the LB to be 100 pc, we find a column density of 9×10^{12}cm^{-2}, a value that is $\sim$ 20 per cent more than the maximum N(O VI) contribution of the LB derived by Oegerle et al. [226]. If instead, a path length of 100 pc would have been used to calculate the N(O VI), a value of $\sim 6 \times 10^{12}$cm^{-2} is obtained, and a space density of 1.9×10^{-8} cm^{-3} is subsequently derived from the former value. This value is $\sim$ 20 per cent lower than the one obtained in the FUSE survey.

In a similar fashion, the column densities of the O VII ions associated to the four model plasmas were also estimated. In table 4.8, the derived values are presented. Manifestly, the HALO 1 component can be seen as the main Galactic reservoir of this ion species. It represents $\sim$ 94 per cent of the total in this line of sight.

To find the contribution of the column density of the O VII (λ 21.602 Å), we would have to correct that value with the oscillator strength (f_{osc}) of 0.696 [230]. Applying this correction to the values of column (8), in table 4.8, and finding the averaged value of these best fit values, we find a value of 2.1×10^{16} cm^{-2} for the column density of O VII (λ 21.602 Å) of the HALO 1 model component.

In recent years, there has been an accumulating observational evidence for x-ray absorption features, which have been interpreted as the result of absorption of large amounts of intergalactic "warm-hot" gas at different redshifts (z). At z $\sim$ 0 the detected oxygen absorption lines in the x-ray spectra from AGNs, see e.g. Fang et al. [231], Nicastro et al. [232], Fang et al. [233], Rasmussen et al. [234], have prompted some discussion, if these highly ionized x-ray absorptions are produced in the Galactic ISM, in the halo of the Milky Way Galaxy, in the Local Group or in the intergalactic medium. For instance, Wang et al. [235] have reported column densities for O VII (λ 21.602 Å) of $1.9^{+1.3}_{-0.7} \times 10^{16}$ cm^{-2}, for a gas with a temperature of $1.3^{+0.5}_{-0.6} \times 10^{6}$ K towards the LMC X-3, a high mass X-ray Binary in the Large Magellanic Cloud (LMC).

The most probable plasma speed for the four model components can also be calculated for the O atom. This is given by the thermal velocity dispersion ($v_{th} = (2k_bT/m_i)^{1/2}$, where m_i is the ion mass). These velocities are given in columns 3, 5, 9 and 11, for the LB, Loop I, the HALO 1 and HALO 2, respectively.

The O VI column density is a sensitive tracer of the age of an evolved bubble. The evolution of the column density of O VI in the local ISM has been recently studied, with a special focus on the contribution of the LB and Loop I bubbles, by Breitschwerdt and de Avillez [141]. High resolution hydrodynamic simulations have been performed in a 3D Galactic ISM. These simulations have allowed a detailed study upon the evolution of these two systems, taking into account a previous realistic background ISM medium—after 200 Myr of a global dynamical equilibrium within the Galactic Fountain scheme—and proper initial mass functions (IMF) of

TABLE 4.9: Equivalent widths (EW) expected to be present in the four Galactic plasma components: the LB, Loop I, Halo 1 and Halo 2. The values shown take in to consideration the x-ray absorption due to the O VII K_β (18.627 Å) and O VII K_α (21.602 Å) ions. The values shown are given in units of mÅ. For more details see the text. In the last column only the values associated to the best fit values are given.

Set	LB EW	LOOP I EW	HALO 1 EW	HALO 2 EW	TOTAL EW
A	$2.9^{+2.8}_{-1.1}$	$0.9^{+0.7}_{-0.9}$	57	3.4	64.2
B	$2.4^{+0.9}_{-1.1}$	$0.2^{+0.6}_{-0.2}$	58	1.7	62.3
C	$3.6^{+1.4}_{-0.9}$	$1.0^{+1.3}_{-0.8}$	56	3.9	64.5
D	$3.2^{+2.6}_{-1.2}$	$0.5^{+0.5}_{-0.4}$	89	1.8	94.5
E	$3.3^{+3.7}_{-1.3}$	$0.8^{+0.5}_{-0.6}$	234	3.7	241.8
F	$2.3^{+0.8}_{-1.1}$	$0.2^{+0.2}_{-0.2}$	162	3.7	168.2
G	$3.4^{+1.7}_{-1.0}$	$0.2^{+0.2}_{-0.2}$	88	3.6	95.2
H	$4.1^{+4.2}_{-1.9}$	$0.5^{+0.4}_{-0.3}$	91	3.4	99.0
I	$2.9^{+4.5}_{-1.5}$	$0.5^{+4.0}_{-0.5}$	81	2.0	86.4
Average	$3.1^{+5.2}_{-1.9}$	$0.5^{+1.8}_{-0.5}$	103	3.0	108.5

stars, which have generate these two bubbles. The LB and Loop I bubbles were carved by 19 and 39 supernovae explosions (SNe), respectively.

From the column densities of the O VII, one can estimate the equivalent widths (EWs) of the absorptions of O VII (18.627 Å) and O VII (21.602 Å) that should be expected, given the results of table 4.8. The EW can be calculated using the following expression,

$$\mathrm{EW} \;=\; \int \tau_\lambda \, \mathrm{d}\lambda =$$

where τ_λ is the optical depth at a given wavelength (λ),

$$\begin{aligned} &= \frac{\pi e^2}{m_e c^2} \, f_{osc} \, N(ion) \lambda^2 [cm] = \\ &= 8.86 \times 10^{-21} \, f_{osc} \, N(ion) \, \lambda^2 \;\; [Å] \end{aligned} \tag{4.10}$$

where f_{osc} is the oscillator strength, N(ion) is the column density of the ion and λ the wavelength of the atomic transition. This translates for the case of O VII (21.602 Å) in,

$$\mathrm{EW}_1 \;=\; 2.88 \times 10^{-18} \, N(ion) \;\; [Å] \tag{4.11}$$

and for the O VII (18.627 Å) case into,

$$\mathrm{EW}_2 \;=\; 4.49 \times 10^{-19} \, N(ion) \;\; [Å] \tag{4.12}$$

Summing up these two contributions yields,

$$\begin{aligned} \mathrm{EW} &= \mathrm{EW}_1 + \mathrm{EW}_2 = \\ &= 3.33 \times 10^{-18} \, N(ion) \;\; [Å] \end{aligned} \tag{4.13}$$

using the oscillator strengths of $f_{osc}(\lambda\ 18.627\ \text{Å})=0.146$ and $f_{osc}(\lambda\ 21.602\ \text{Å})=0.696$ taken from Verner et al. [230].

In table 4.9 the EWs for the nine sets for each model plama component are given. As already anticipated, the HALO 1 can be responsable for a huge absorption in the EUV and X-ray background radiation fields. Taken the average values from table 4.9, the HALO 1 represents ~ 95 per cent of the total absorption of the O VII ion. Using the the O VII K_α (21.602 Å) ion to investigate the absorption by this component, one sees, that in this line of sight, this ion can induce an absorption with an EW of ~ 72 mÅ (103 mÅ $\times$ 0.696). Comparing this last value with the one obtained from the columnn density of $1.9^{+1.3}_{-0.7} \times 10^{16}$ cm^{-2}, and reported by Wang et al. [235], we get $54.7^{+54.7}_{-20.1}$ mÅ. This value is about 25 per cent less than the result derived from our model.

4.14 Discussion

This study clearly shows, that the standard paradigm of the LB is not observed. The temperature derived from this analysis is similar to the one of Snowden et al. [116]. However, this might be the result of the low spectrum statistics. Moreover, the electron density derived from these spectral fits show, that the average value of the LB electron density is about 4 times higher than the Snowden et al. [116]. Higher electron densities were also derived by several independent authors, see Henley et al. [224] and Smith et al. [225]. Also, the pressure associated to this plasma is too high to allow the presence of clouds—which are known to exist in the LISM—inside of the LB.

Chapter 5

The Hyades & Taurus Observations

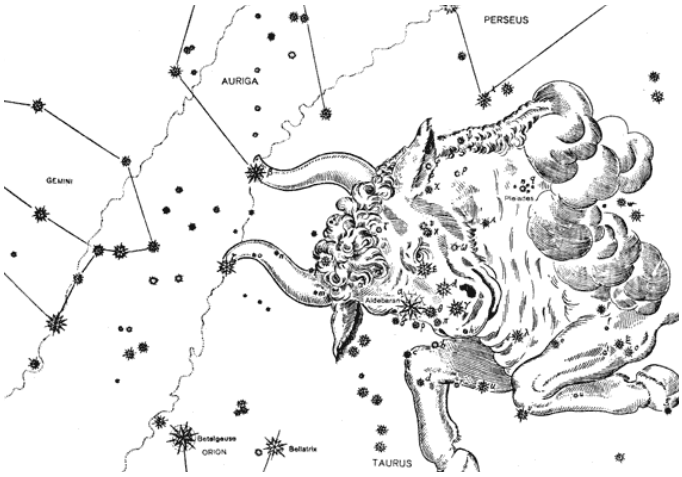

The constellation of Taurus. A drawing from the German lawyer Johann Bayer (1572–1625) taken from his celestial atlas Uranometria, Augsburg, 1603. This is considered to be the first celestial atlas due to the accurate indication of star positions and brightness. Source Astronomy Education Review.

5.1 Introduction

An investigation on the nature of the x-ray emission towards the Galactic anticenter, or more precisely, towards the anti-Ophiuchus sky position, is performed in this chapter. This allows us to do a comparative study on the Galactic x-ray emission in both opposite directions.

The sky region selected was the field of the Hyades open cluster. The star cluster of the Hyades can be defined by the rectangle with the Galactic coordinates of l = 156° — 190° and b = −15° — −28°. This open cluster has been studied by Perryman et al. [163], who derived a cluster distance of 46.34±0.27 pc, with the trigonometric parallaxes from the Hipparcos satellite. These authors have also estimated the age of this star cluster using the He abundance in combination with the theoretical isochrones, to be 625 ± 50 Myr.

The main properties of the analysed XMM-Newton observations are given in table 5.1. The last column, designated as Field, gives the name used for each

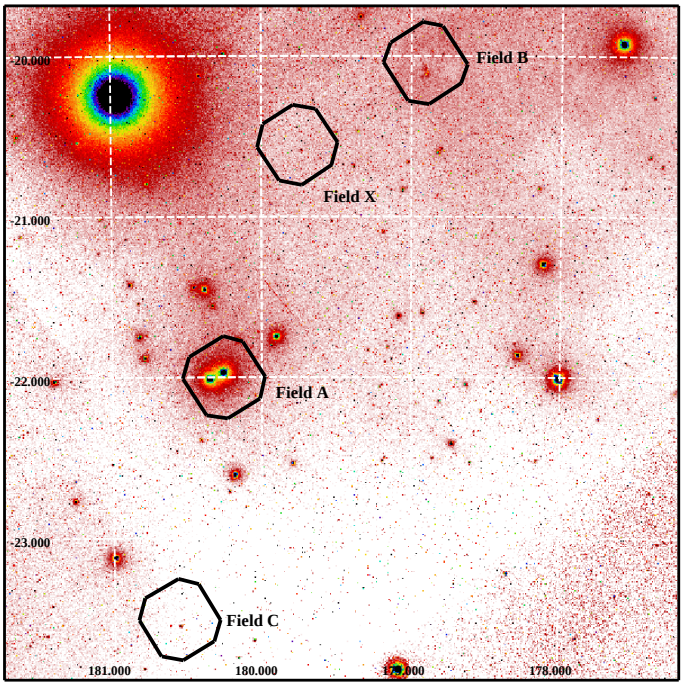

FIGURE 5.1: The XMM-Newton observations in the Hyades Field. The Digitized Sky Survey (DSS) image, having the Hyades star cluster in the field of view. The DSS image has a field of view 5°×5°. Superimposed to the image are also the four XMM-Newton pointings. Only fields A, B and C were used to analyse the soft x-ray emission towards the Hyades field. The color intensity was scaled, using a square scale from 1670 (white) to 10900 (black) in the image units. The very bright object is the Aldebaran star, a star of spectral type K5 III at a distance of 20 pc from the Solar system.

observation throughout this chapter. In figure 5.1 an optical image, obtained from the Digitized Sky Survey (DSS) is used to give a global perspective of the sky and, as well, to show the sky positions of the four XMM-Newton observations employed in this investigation.

TABLE 5.1: The main XMM-Newton Observations in the Hyades field.

Rev #	Observation ID	Filter	Observation Date	Exposure Time [ks]	Galactic Longitude	Galactic Latitude	Field
0049	0094810301	Thin1	2000-03-16T00:12:12	27	179.7830	−20.5840	X
0135	0101440501	Thick	2000-09-03T15:36:03	43	180.2301	−21.9713	A
0138	0109060301	Medium	2000-09-10T10:18:12	58	178.8850	−20.0111	B
0410	0101440501	Medium	2002-03-05T06:17:47	49	180.5870	−23.5390	C

5.2 The Hyades & Taurus XMM-Newton observations

Initially, four XMM-Newton observations in this general direction were chosen to perform this analysis. The XMM-Newton observation, designated by X, was not included in this final analysis, because at the time of this analysis, there was a set of missing files in the observation data files (ODF), files that were not produced at the European Space Astronomy Centre (ESAC)[1] due to time constraints[2]. The lack of such files did not allow a precise analysis of the spectrum for this observation. Moreover, and as an example of the missing information, the EPIC-pn camera mode

[1] xmm.vilspa.esa.es

[2] The missing ODF files were recently produced at ESAC.

was not known, therefore not allowing a proper correction of the high energy background level, when subtracting the internal detector background. A simple analysis of this observation, however, has revealed the presence of one unidentified emission line at 1.7 keV [236].

The XMM-Newton observation, designated by A, was performed to study the x-ray emission from the 77 Tau star by Franciosini et al. [237], a star of spectral K0 IIIb at a distance of $48.4^{+2.1}_{-1.9}$ pc [238], belonging to a double system.

The second analysed XMM-Newton observation, named B, corresponds to an observation of the L1551 dark molecular cloud [239], performed by Favata et al. [240], to study the young stellar population. The L1551 molecular cloud is one of the nearest, and therefore most studied regions of low-mass star formation. It is part of the Taurus-Auriga molecular cloud complex and the distance to its leading edge has been measured to be 140±10 pc by Kenyon et al. [241]. It shows the usual signs of recent star formation: pre-main-sequence stars [242], Herbig-Haro objects [243], reflection nebulosity and some sources show molecular outflows [244, 245, 246]. The stellar population in L1551 has been previously surveyed, using several methods: x-ray mapping (Carkner et al. [247]); optical and near-IR mapping (e.g., Briceño et al. [242]); optical spectra ([248]) and Hα surveys (e.g., [249]).

The XMM-Newton observation C was performed to study the x-ray emission from the variable object V* V895 Tau, a star of spectral type G1 V at a distance of $44.9^{+3.3}_{-2.8}$ pc. For more details see Franciosini et al. [237].

5.3 Solar Wind Charge Exchange variability

An analysis upon the solar wind charge exchange (SWCE) variability was also executed for these observations, in a similar form as for the Ophiuchus x-ray shadow experiment and HDFN observations.

The method to investigate the SWCE variability was described in chapter 4, § 4.6. Briefly, this analysis consists of the creation of scattergrams using two count rates in proper energy bands, and to investigate, if in the energy band, suitable to be affected by SWCE, there is a different count rate during the observation. For this analysis the count rates were produced with a time bin size of 100.0 s.

In figure 5.2 the SWCE scattergrams are given for observations A, B and C. No SWCE variability is seen in these three scattergrams. The averaged values agree quite well with each other. This is an indication that the three XMM-Newton observations were not affected by SWCE, expect for, and if any, a quiescent level.

5.4 The Hyades and Taurus L1551 cloud soft x-ray background

As performed for the Ophiuchus x-ray shadow observations, it is necessary to investigate the LISM in the general direction of the Hyades star cluster. For that the x-ray volume emissivity, derived from the study of the 1/4 keV ROSAT map by Snowden et al. [116], is used. Also, the column density of neutral material, inferred

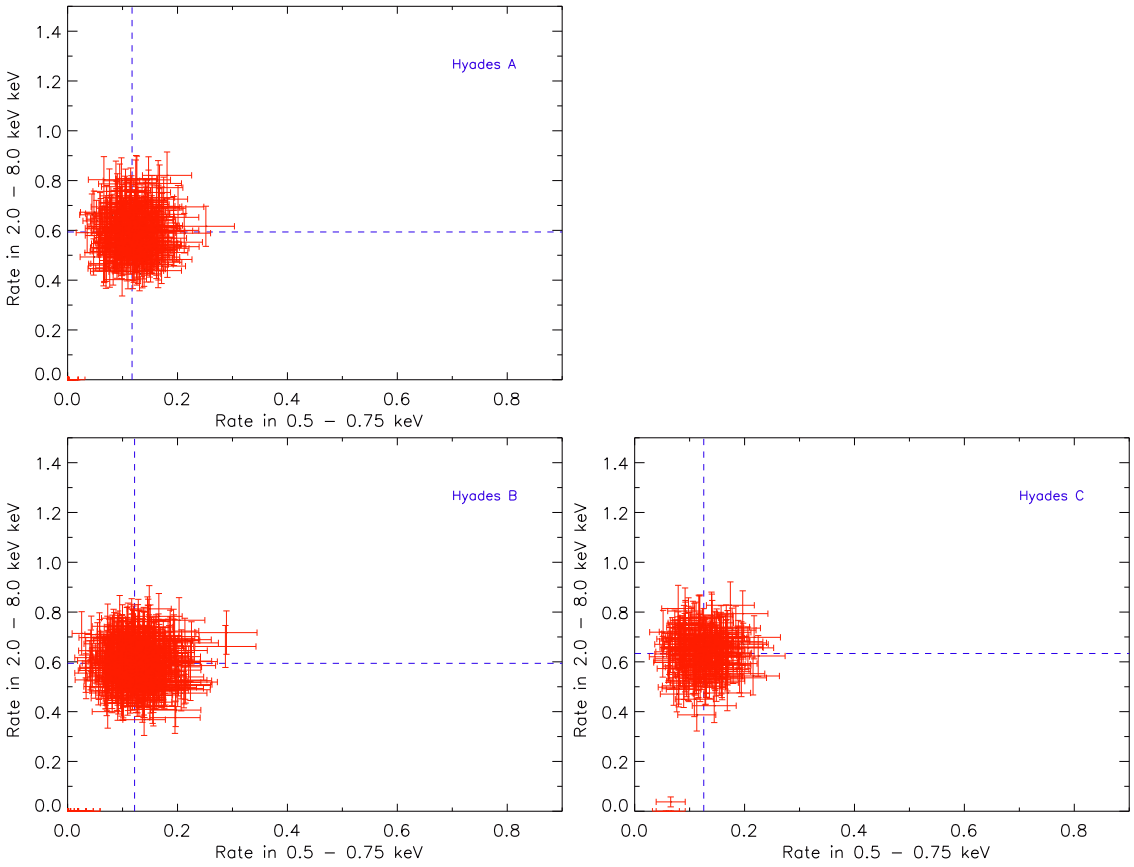

FIGURE 5.2: SWCE Scattergrams. In the above plots the count rates in the 0.5 - 0.75 and 2.0 - 8.0 keV energy bands from the Hyades A, B, and C XMM-Newton observations are presented. This analysis was performed to study the variability of the count rate in the 0.5 - 0.75 keV band. The presence of variability in this energy band would indicate the presence of SWCE x-ray emission. In these observations no variability was detected.

from NaI D absorption studies by Lallement et al. [118], is used. This information is used to depict the LISM as shown in figure 5.3. These images permit us to estimate what is the extension of the LB and, at the same time, the distance at which the column density reaches the value of 2.0×10^{19} cm^{-2}.

Redfield and Linsky [250] have shown, that the column density due to the local interstellar cloud (LIC) and the Hyades cloud component, if present in this region, ranges from $1.45{\times}10^{18}$ cm^{-2} to $1.56{\times}10^{18}$ cm^{-2}. These column densities do not affect the x-ray photons in the interval from 0.25 to 7.0 keV, and therefore were not included in the model.

The Galactic column density, in these three different directions can be estimated by using the online N_H calculator[3]. The values of the column density of H I in these three points are $1.7{\times}10^{21}$ cm^{-2}, $1.9{\times}10^{21}$ cm^{-2} and $1.7{\times}10^{21}$ cm^{-2} for fields A, B and C, respectively.

[3]http://heasarc.nasa.gov/cgi-bin/Tools/w3nh/w3nh.pl

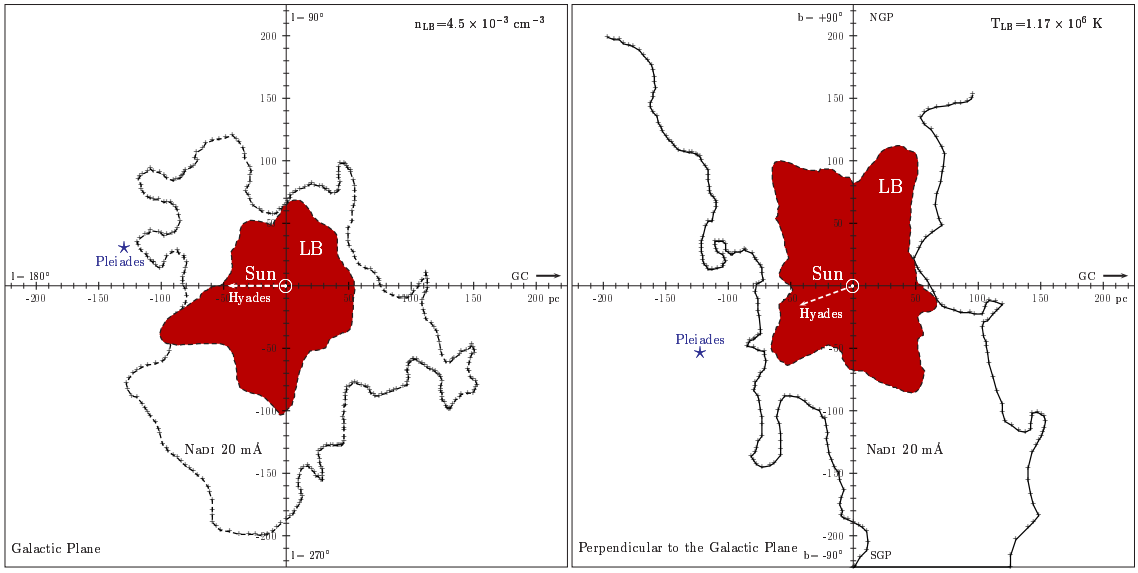

FIGURE 5.3: The local Galactic ISM. This figure is similar to figure 4.8. The only difference regarding figure 4.8 is the superposition of the location of the Hyades star cluster, and the projection of the Pleiades in these two planes.

The large-scale extinction map of the Galactic anticenter, created by Froebrich et al. [251], using the colour excess from the 2MASS, can also be used for independently estimating this quantity in each of these directions. After applying a conversion factor of $2{\times}10^{21}$ A_V mag^{-1} cm^{-2}, we find a column density of $2.54{\times}10^{21}$ cm^{-2}, $8.45{\times}10^{21}$ cm^{-2}, and $2.15{\times}10^{21}$ cm^{-2} for field A, B and C, respectively. Another way to investigate the column density of H I in this sky region is, by studying the column density towards stars with known distances.

The stars belonging to the catalogue of Lallement et al. [118] have also been used to analyse the column densities towards stars lying in the general direction of these XMM-Newton observations. For that, the distance versus column density was used to analyse the column density in this Galactic direction, see figure 5.4. A search centred at the Galactic coordinates of l,b =180°,-20° with a radius of 15° in the former catalogue was performed. No star within a radius of 5° was found. Six stars where found within an annulus ring of 5° to 10°. These stars are shown in figure 5.4 as filled red circles. A larger number of stars, lying within an annulus ring of 10° and 15° was found. These are shown as open green-circles. Another search, using the SIMBAD database, this time centered in each of the these observations and using a radius of 1°, found more ten stars, shown as blue squares. The basic information from the stars employed to make this plot are given in the appendix E.1, in table E.1. The information regarding the column density towards the Hyades stars, was taken from Redfield and Linsky [250], and also included in figure 5.4. This plot shows the presence of a strong column density gradient of H I, somewhere in between the Hyades star cluster and stars at a distance of 100 pc.

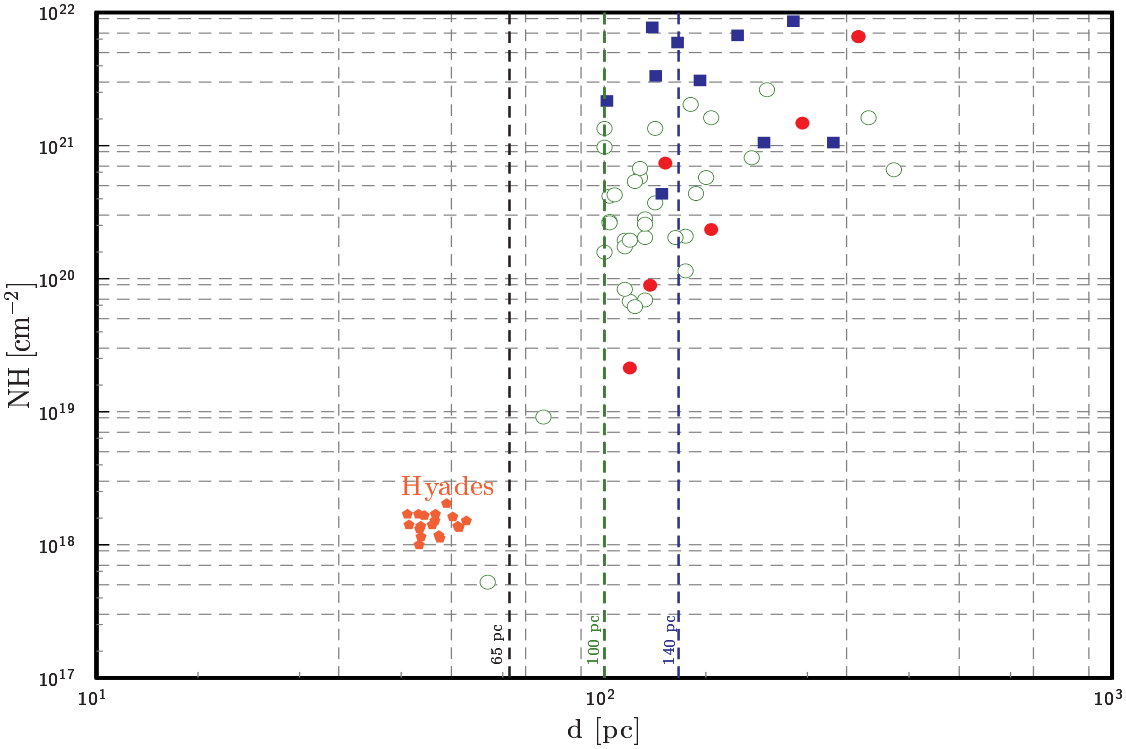

FIGURE 5.4: The column densities towards stars in the Hyades and Taurus fields. For creating this plot, the catalogue from Lallement et al. [118] was used. A search on the former catalogue was done, in order to find stars centered at the galactic coordinates of l,b =180°,-20° and within a radius of 15°. No stars from this catalogue were found within a radius of 5°. Within an annulus of an inner radius of 5° to an outer radius of 10°, a total of 6 stars was found (red filled circles). The open circles represent stars from the former catalogue, within an annulus of 10° to 15°. In blue it is shown another search done in SIMBAD, centered in each of the three XMM-Newton observations with a radius of 1°. Clearly, there is a strong discontinuity seen at about 100 pc. The information regarding the distance and column density of the Hyades open cluster (red pentagons) was taken from Redfield and Linsky [250].

5.4.1 The x-ray spectra

The process of x-ray spectra extraction from these XMM-Newton observations follows the recipe described in chapter 3, § 3.4. In summary, the event files are cleaned from instrumental artifacts, bad pixels, bad columns and OOT events. In particular during these observations, the EPIC-pn camera was operated in the Full Frame Window mode. In this operating mode the OOT events amount to 6.2 per cent of the total events, and, allied to the fact of being relatively crowded fields, it is, therefore, important to properly remove the OOT events. During this process the detected x-ray sources are also removed from the event files, after which spectra are extracted. The clean GTI files have 27 ks, 45 ks and 29 ks for fields A, B and C, respectively. The x-ray spectral fit was performed, using the standard XSPEC package, version 11.3.2ag.

In this general galactic direction there are some strong features of radio continuum, such as Loop II and Loop V, and H I shells, which are thought to be the left over of supernova remnants. Given all the incertanties associated to their geometric properties, it may be possible that the line of sight of the Hyades XMM-Newton observations cross one of these structures. In particular, Loop II with the galactic coordinates centre at l=100° and b=-32.5°, and with an angular diameter of 91° [252]. In a recent study performed by Borka [253] a distance of 97 ± 18 pc and a diameter of 141 ± 22 pc was determined for Loop II.

We have investigated two simple x-ray emission models, composed of three thermal plasmas and an extragalactic component. The only difference between these two models is the change of the position of one of the galactic "halo" plasma regarding the H I wall in this direction. In this way we can investigate the possibility of extra x-ray emission not associated to the LB and not absorbed.

5.4.2 The First Model

The model used to fit these spectra is composed by an unabsorbed thermal plasma, representing the LB by two absorbed thermal halo plasmas of different temperatures, and by an extragalactic x-ray cosmic component. The model can be written as follows,

$$I = I_{LB} + e^{-\tau N_H}[I_{Halo\ I} + I_{Halo\ II} + AE^{\Gamma}] \tag{5.1}$$

The fit procedure consists in simultaneously fitting the three spectra. In the model, the same LB temperature was assumed for the three spectra. This means, that during the fit, the LB model component has been forced to assume the same temperature. However, the EMs were allowed to vary freely. The column density, associated to the intervening ISM material, was also allowed to vary. The model has two halo components representing a cold and a hotter halo plasma. The cold halo model component was forced to have the same temperature in the three spectra and was fixed to the best fit value. Also their EMs were frozen to their best fit values. The temperature of the hot halo component was allowed to vary. Since, this model component had similar temperature values for spectra from fields B and C, they were also assumed to be the same in the fit. The EMs of this model component were also let free during the minimization procedure. The extragalactic component was fixed to the expected values [158] after applying the correction for the high radiation level to the spectra from the closed observations. After finding the best fit model, the column densities were frozen to their best fit values. The reduced χ^2_{red} of the best fit model was 1.06. The results from the fit are shown in table 5.2. The errors given in table 5.2 were calculated in order to have a 90 per cent confidence level, assuming six free model parameters, implying a $\Delta\chi^2$ of 10.640.

In figure 5.5 the plot resulting from the best fit model is shown. The LB contribution is also presented. The contour plots associated to these results are presented in the appendix F.

TABLE 5.2: Hyades spectral fit results 1. The errors shown are within the 90% confidence level for six interesting parameters, implying $\chi^2 = \chi^2_{\rm min} + \Delta\chi^2$, with $\Delta\chi^2 = 10.640$. The plasma temperatures are given in units of 10^6 Kelvin and the emission measures (EM) in units of cm^{-6} pc. The Galactic column densities (NH) are given in units of 10^{21} cm^{-2}. The $\chi^2_{\rm red}$ from this simultaneous fit is 1.06.

	LB			Halo I		Halo II	
Field	Temperature	EM	NH	Temperature	EM	Temperature	EM
A	$0.86^{+0.16}_{-0.11}$	$0.016^{+0.011}_{-0.007}$	2.7	0.75	0.84	$3.53^{+0.52}_{-0.38}$	$0.010^{+0.002}_{-0.002}$
B		$0.018^{+0.012}_{-0.008}$	3.4		1.27	$2.77^{+0.27}_{-0.25}$	$0.009^{+0.002}_{-0.001}$
C		$0.015^{+0.010}_{-0.007}$	2.5		0.74		$0.006^{+0.002}_{-0.001}$

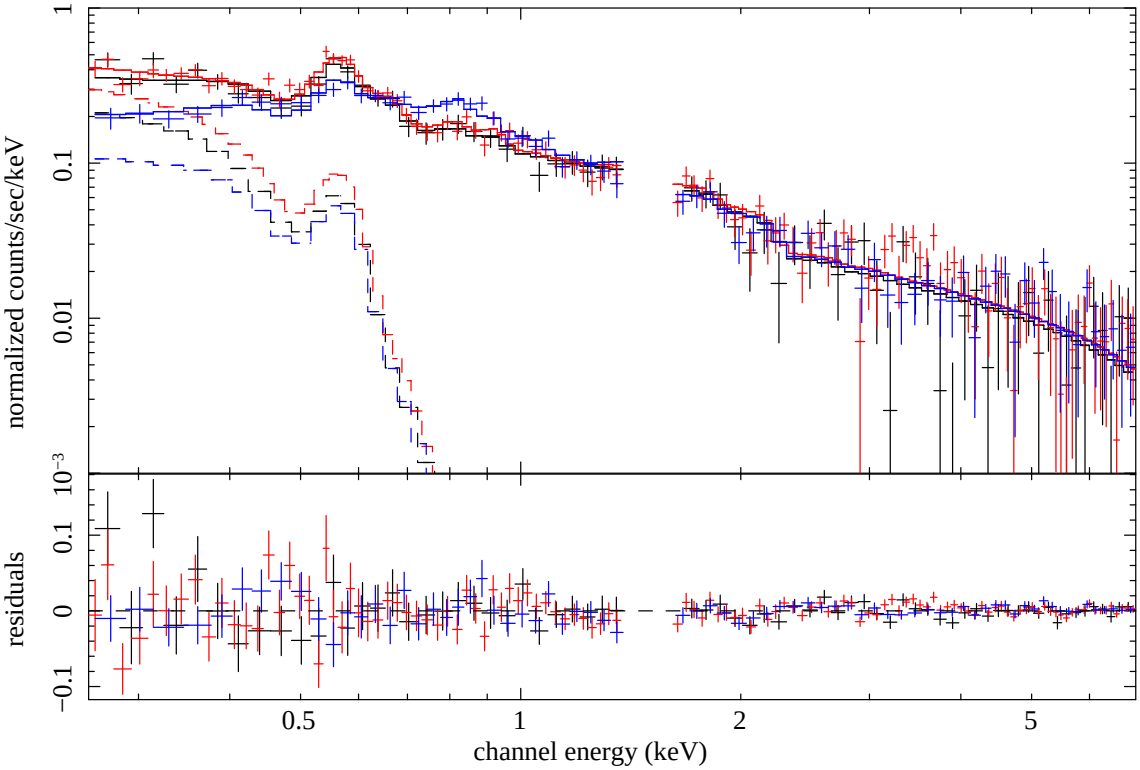

FIGURE 5.5: The soft x-ray spectra towards the Hyades and Taurus. In this figure is shown the plot, resulting from the simultaneous fit to the A (blue), B (red) and C (black) spectra. The model consists of one unabsorbed thermal plasma, representing the LB, plus two absorbed Galactic Halo plasmas and the extragalactic x-ray cosmic background component. The main results from the fit are shown in table 5.2. The LB temperature was found to be 8.6×10^5 K, with an average electron density $n_e \sim 0.016$ cm^{-3} .

5.4.3 The Second Model

A different model composed of two unabsorbed thermal plasmas plus two absorbed components, a thermal plasma and the extragalactic component, was also fitted to

the x-ray data. The model is,

$$I = I_{LB} + I_{Halo\ I} + e^{-\tau N_H}[I_{Halo\ II} + AE^{\Gamma}] \quad (5.2)$$

The simultaneous spectra fit gave a worse reduced χ^2 of 1.1. The LB thermal plasma temperature derived form the fit was $k_BT = 0.109$ keV (1.26×10^6 K). The emission measures (EMs) obtained from the fit were 0.009 0.010, and 0.011 cm^{-6} pc for fields A, B and C, respectively. For spectra from fields B and C no second unabsorbed thermal plasma was required, in contrast to field A, where a plasma with a temperature of $k_BT = 0.545$ keV (6.3×10^6 K) was needed. The best fit values of the column densities were $1.74{\times}10^{21}$ cm^{-2}, $2.64{\times}10^{21}$ cm^{-2} and $3.65{\times}10^{21}$ cm^{-2} for fields A, B and C, respectively. The column density for field C is, however, too high when compared to field B, where the highest column density should be observed due to the Taurus L1551 molecular cloud. The absorbed plasma temperature, corresponding to the galactic halo component, derived from this fit, was $k_BT = 0.238$ keV ($\sim 2.8 \times 10^6$ K), with EMs of 0.0045, 0.0065 and 0.0116 cm^{-6} pc for fields A, B, and C, respectively. This temperature also seems to be too high for a cold Galactic halo plasma in the Galactic anticenter direction. The EM of this plasma, derived from the fit in field C, also seems to be too large, compared with the other two EMs values, by a factor of 2.6 and 1.8. Also, the fact that in this model a very hot and non-absorbed plasma is required in field B, and not in the other two fields, is also physically unacceptable in these small degree scales, like in the present case. Because of the reasons above mentioned, this model was rejected.

5.5 The electron density and thermal pressure from the LB

The x-ray emissivity maps derived by Snowden et al. [116] allow us to estimate the extension of the LB in this direction to be 65 pc. If we assume, that the LB extension in each of these three observations is the same, then the following electron densities of $0.016^{+0.004}_{-0.004}$ cm^{-3}, $0.017^{+0.004}_{-0.005}$ cm^{-3} and $0.015^{+0.005}_{-0.004}$ cm^{-3} are obtained for the A, B, and C fields, respectively. It is interesting to note, that the average electron density for each observation decreases as |b| increases. As expected, this is an indication of an electron density gradient in the LB. However, given the errors associated to these measurements, it will be assumed that the representative electron density value in this sky direction is the average electron density of these three observations. Therefore, the average electron density in this general direction is set to $0.016^{+0.005}_{-0.005}$ cm^{-3}. The pressure of LB plasma derived, using the former values of temperature and electron density, is $p/2k_B = 1.38^{+0.20}_{-0.26} \times 10^4$ cm^{-3} K.

5.6 The O VI and O VII column densities

In a similar form, as performed for the Ophiuchus x-ray shadow experiment, we can estimate physical observables such as the column density of the O VI ion. We can estimate this value by using equation 4.9, given in chapter 4, § 4.13.

The column densities of the O VI ion derived for the LB model component from these observations are $8.6^{+3.0}_{-2.7} \times 10^{12}$ cm^{-2}, $9.1^{+3.2}_{-2.8} \times 10^{12}$ cm^{-2}, and $8.3^{+3.0}_{-2.6} \times 10^{12}$ cm^{-2} for the A, B and C fields, respectively. The average column density of these observations is $8.7^{+3.6}_{-3.0} \times 10^{12}$ cm^{-2}, see table 5.3. The space average density of O VI, obtained from the values above, is $4.3^{+1.8}_{-1.5} \times 10^{-8}$ cm^{-3}. In the study performed by Oegerle et al. [226] in the LISM, a column density of O VI of $\sim 7 \times 10^{12}$ cm^{-2} was attributed to the LB and an average space density of 2.45×10^{-8} cm^{-3} was derived, assuming a radius of 100 pc. The column and the average space densities, derived from the values obtained from this analysis, are higher than the ones from Oegerle et al. [226]. However, given the errors associated to these physical parameters, it must be concluded that the values of Oegerle et al. [226] are compatible with the ones derived from the x-ray spectra.

Besides, calculating the column densities for the O VI ion, the same exercise can be done for the O VII ion and for all three thermal plasmas: LB, HALO I and HALO II. In table 5.3 the estimated column densities for the O VII ion, for these model plasmas, are presented. When calculating these physical quantities, it was assumed a line of sight of 5.85 kpc for the Galactic halo plasmas. This was done in order to assume that at that distance, and for a Galactic latitude of $|20°|$, these observations were sampling hot gas at a scale height of 2.0 kpc. As it can be seen from table 5.3, column 5, the column density of the O VII ion, associated to the cold halo plasma, is ~ 4 times higher than the column density associated to the cold halo in direction of the Galactic center, see table 4.8 on § 4.13.

Several reasons can be put forward to explain this discrepancy. One of the reasons may be due to the assumption of a line of sight of 5.85 kpc, when calculating these values. Another reason may reside simply in the fact that these plasmas have different plasma temperatures, and therefore, different ionization fractions with the ionization peak for the O VII ion at $\sim 8 \times 10^5$ K. Besides the reasons above, theoretically, it would also be possible, that we are observing some x-ray emission from gas of the warm-hot intergalactic medium (WHIM), in particular of hot baryons predicted by Cen and Ostriker [254] and Davé et al. [255] in hydrodynamic cosmological simulations. However, with this kind of medium spectral resolution analysis it is not possible to disentangle any contribution of this hot baryons from the Galactic emission. In order to be able to disentangle that contribution, high spectral resolution absorption (emission) studies would be required. This is not possible with the EPIC-MOS and EPIC-pn cameras. It is interesting to note that, there is an on-going discussion about the location for such highly ionized gas [256, 257, 258]. For instance, Wang et al. [235] have concluded that the bulk of the highly ionized gas, like the O VII absorbers, is located near the Milky Way Galaxy, most likely in a thick hot gaseous disc.

5.7 The equivalent widths

The equivalent widths (EWs) associated to the column density from the O VII ion can also be estimated by using equation 4.13, on § 4.13, and the values of the column densities from table 5.3. The calculated EWs are given in table 5.4. The

TABLE 5.3: OVI and OVII column densities. In this table we present the expected values for the following physical quantities: The N(O VI) for the LB in column 2. Columns 3, 5 and 7 show the N(O VII) for the LB, HALO I and HALO II, respectively. In columns 4, 6 and 8 the expected thermal velocity dispersions for these different components of the oxygen ion are shown. For calculating the column densities of O VII of the halo components, a line of sight of 5.85 kpc was assumed. This line of sight was assumed in order to sample gas at a scale height of 2.0 kpc for a |b|=20°.

	LB	LB		HALO I		HALO II	
FIELD	N(O VI) 10^{12} cm^{-2}	N(O VII) 10^{15} cm^{-2}	v_{th} km/s	N(O VII) 10^{17} cm^{-2}	v_{th} km/s	N(O VII) 10^{15} cm^{-2}	v_{th} km/s
(1)	(2)	(3)	(4)	(5)	(6)	(7)	(8)
A	$8.6^{+3.0}_{-2.7}$	$1.5^{+0.5}_{-0.4}$	$29.8^{+2.6}_{-2.0}$	1.0	27.8	$0.8^{+0.7}_{-0.6}$	$60.3^{+4.3}_{-3.3}$
B	$9.1^{+3.2}_{-2.8}$	$1.6^{+0.5}_{-0.4}$		1.3		$2.1^{+0.3}_{-0.9}$	$53.3^{+2.6}_{-2.5}$
C	$8.3^{+3.0}_{-2.6}$	$1.5^{+0.6}_{-0.4}$		1.0		$1.7^{+0.3}_{-0.8}$	
Average	$8.7^{+3.6}_{-3.0}$	$1.5^{+0.6}_{-0.4}$	$29.8^{+2.6}_{-2.0}$	1.1	27.8		

EWs derived for the HALO I plasma also show very high values as expected from the column densities of O VII.

TABLE 5.4: The EWs associated to the OVI and OVII column densities. These values are obtained using the equation 4.9 and the values of the columnn densities given in table 5.3.

	LB	HALO I	HALO II
FIELD	EW (mÅ)	EW (mÅ)	EW (mÅ)
A	$5.1^{+1.5}_{-1.3}$	349	$2.6^{+2.4}_{-1.9}$
B	$5.4^{+1.6}_{-1.5}$	429	$7.1^{+0.7}_{-3.0}$
C	$4.9^{+1.5}_{-1.4}$	328	$5.8^{+0.9}_{-2.6}$
Average	$5.1^{+1.9}_{-1.6}$	369	$5.2^{+9.2}_{-4.3}$

5.8 Discussion

This analysis shows, that in this sky direction the LB temperature and electron density are very different from the values associated to the standard picture of the LB, see Snowden et al. [116]. The pressure of the LB in this case is also too high to allow the presence of cold and warm clouds within the LB boundaries.

In this general direction towards the Galactic anticenter there are a series of OB associations. In table 5.5 the general properties of these OB associations are given. This information is given, in order to infer possible sources for the hot plasmas,

TABLE 5.5: OB star associations in the Galactic anticenter and close to the XMM-Newton observations.

NAME	GALACTIC RANGE		DISTANCE	AGE
	LONGITUDE	LATITUDE	kpc	Myrs
α Persei	$140° — 165°$	$+3° — -17°$	$0.177^{(1)}$	~ 50
Aur OB 1	$168° — 178°$	$+4° — -7°$	$1.320^{(2,3)}$	$46 — 87^{(3)}$
Cas-Tau	$119° — 220°$	$+12° — -45°$	$0.140^{(1)}$	~ 50
Per OB 2	$145° — 170°$	$-13° — -27°$	$0.318^{(1)}$	$1 — 4$

(1) - de Zeeuw et al. [181] (2) - Humphreys [259] (3) - Kharchenko et al. [260]

resulting from SNe, in this general direction. In this anticenter direction there is the Perseus arm. Therefore, it is plausible, that the hotter plasma component may also be the result of gas associated to this arm, streaming from the stellar activity in the Galactic plane. In this general direction there are, at least, two well known examples of such stellar activity. They are the remnants of the Crab (l = 184.55°, b= −5.78°) and of Sim 147 (l = 180.33°, b= −1.68°), at a distance of 2 kpc and 1.47 kpc, respectively.

Chapter 6

Conclusions and Perspectives

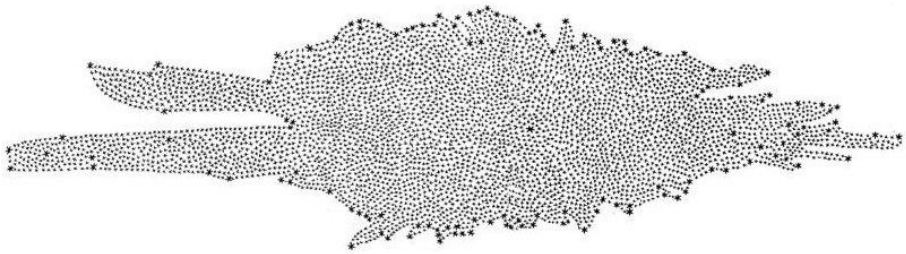

The Milky Way Galaxy structure deduced from star counts by William Herschel (1738-1822). In his 1785 paper "On the Construction of the Heavens" he presented a cross section of the Milky Way, composed of millions of stars. The Sun is located in the center of the map. By studying the soft x-ray emission in many lines of sight through the Galaxy, it would be possible to derive a 3D structure for the hot Galactic plasma pervading our Galaxy. However, in order to run into the problem that as Herschel, by not taking into account the dust extinction, one should be very careful and take into account the extinction and the intrinsic luminosity (as well as the unresolved point sources) of the diffuse X-ray emission.

6.1 Conclusions

The main purpose of the present work was, to investigate the Galactic soft x-ray emission towards the Ophiuchus molecular cloud, in particular the LB x-ray emission. This program was designed to use the high x-ray absorption, produced by the dark molecular filament from the Ophiuchus cloud complex, with column densities ranging from $\sim 10^{21}$ to $\sim 10^{22}$ cm^{-2}, to disentangle the LB emission from other Galactic x-ray emissions.

The results obtained from this analysis, shows that the physical parameters associated to the LB plasma are different from the work of Snowden et al. [116]. A temperature of $T_{LB} = 1.20^{+0.67}_{-0.61} \times 10^6$ K and an $n_e(\text{LB}) = 0.017^{+0.025}_{-0.007}$ cm^{-3} were derived, see § 4.11.

The temperature of 3×10^6 K, derived from the spectral fits from the Ophiuchus dark filament observations for the Loop I supperbubble, agrees with the values derived by Egger and Aschenbach [196].

Moreover, since the Ophiuchus molecular complex is approximately located in the direction of the Galactic center (GC), we could investigate the temperatures and EMs of the hot halo plasmas present in these line of sights, with a scale height of

2 kpc above the Galactic plane. The x-ray spectra model from the x-ray shadow experiment observations allows the presence of two other plasmas, representing other hot Galactic plasmas in the direction of the GC. The temperatures derived for these two plasmas were $T_{\text{Halo I}} = 1.5 \times 10^6$ K and $T_{\text{Halo II}} = 3.9 \times 10^6$ K, respectively.

Complementing the former study, another was performed to analyse the soft x-ray emission in the Galactic anticenter direction. Three XMM-Newton observations were used to study the LB and other Galactic x-ray emissions. These observations were performed in the Hyades star cluster and Taurus directions.

The simultaneous fit to these spectra reveals a $T_{\text{LB}} = 0.86^{+0.16}_{-0.11} \times 10^6$ K and an average $n_e(\text{LB}) = 0.016^{+0.005}_{-0.005}$ cm^{-3}, see § 5.4. In this analysis three different halo plasmas were required to reproduce the XMM-Newton spectra. This x-ray spectral fit reveals a cool Galactic plasma, with a temperature of $T_{\text{Halo I}} = 0.75 \times 10^6$ K, and two hotter plasmas of temperatures of $T_{\text{Halo II B,C}} = 2.8 \times 10^6$ K and $T_{\text{Halo II A}} = 3.5 \times 10^6$ K.

From these studies it is evident, that the colder component of the hot halo shows a temperature gradient from $T_{\text{Halo I}} = 1.5 \times 10^6$ K (in direction of the GC) to $T_{\text{Halo I}} = 0.75 \times 10^6$ K (in the opposite direction). This result was expected, because most of the star formation occurs, in our Galaxy, within the Galactic orbit of the Sun. Therefore, lower temperatures should be observed in the anticenter direction.

In regard to the hotter halo component, and in particular towards the GC, the higher temperature of this plasma is probably the result of the stream of hot gas from the GC region. In the Galactic anticenter direction this may be also the result of the stream of hot plasma from SNe in the galactic disc or from old SN remnants in these regions.

This work shows, that the physical parameters of the temperature and of the electron density assumed in the standard LB model, derived from fits of low resolution spectra —obtained by the ROSAT satellite— by Snowden et al. [116] are not observed in the present analysis. Even if it can be argued, that the temperature derived from the x-ray shadow experiment on the Ophiuchus dark filament is compatible with analyses supporting the LB paradigm, this is more likely to be due to the low statistics, resulting from the small exposures times and small spectral extraction areas.

The results from the analysis of the soft x-ray emission of the LB in the Galactic anticenter direction also show strongly, that the LB temperature does not match the one from the LB paradigm, and as well, the electron density. Interestingly, the electron densities derived from the Ophiuchus shadow and Hyades-Taurus XMM-Newton observations agree remarkably well with each other.

If it is assumed, that the temperatures derived from these independent XMM-Newton oppositional observations represent the LB plasma temperature in each direction, then this fact would imply that the LB plasma is in a non-CIE state, or in a NEI state, as suggested by Breitschwerdt and Schmutzler [92] and further developed in Breitschwerdt [128, 261]. Since, the temperature derived from these different observations should be the same. Moreover, an astrophysical overionized NEI plasma, with lower kinetic electron temperature, when fitted with CIE plasmas invariably leads to higher temperatures fits, see figure 2.3 on § 2.2.2.

Undoubtedly, the electron density derived in this analysis and from other independent studies, see the results from Henley et al. [224] and Smith et al. [225], gives support to the claim of a revision of the value of the temperature, of the electron density, and as well of the physical plasma state of the LB.

6.2 Perspectives for further work

The direction of future work should contemplate a new analysis on the x-ray shadow experiment on the Ophiuchus dark filament with deeper exposure times. The present XMM-Newton observations have very short exposure times. For instance, compared with the Hyades-Taurus observations, they have in average ~ 6 times less exposure time. Moreover, the spectra extraction regions of the Ophiuchus XMM-Newton observations have in average ~ 4.5 less extraction area than the Hyades-Taurus observations. These combined effects strongly contribute for the weak constraint on the LB temperature and electron density, derived from these observations. In order to improve these results, as achieved for the Hyades-Taurus observations, it would be required to have, at least, clean observations with exposure times of 50.0 ks for the new XMM-Newton on-cloud observations. Besides obtaining x-ray data with the EPIC-pn camera for the same three XMM-Newton pointings, the reflection grating spectrometer (RGS)—on-board of the XMM-Newton spacecraft with a bandpass from 5 Å to 35 Å—should also be used in the third pointing. This would allow us to obtain spectra of high resolution from the x-ray source 1RXS J164042.2-243513. As reported in the appendix C the 1RXS J164042.2-243513 x-ray source shows a featureless spectrum, and it may be at a distance of ~ 520 pc. Therefore, the high resolution spectrum would allow us to study the important ISM absorption lines, such as the O VII (18.627 Å and 21.60 Å) and O VIII (18.967 Å), along this line of sight. With this information of the absorption EWs, the contribution of the LB and Loop I supperbubble could be investigated. However, since the XMM-Newton performance is highly affected by periods of solar proton flares, with 40 to 50 per cent of the observing time being contaminated, a serious proposal has to take into consideration this effect, with a request for more exposure time, in order to compensate it.

As performed with the Hyades-Taurus observations, other XMM-Newton observations stored in the archive can also be used for further studies of the LB and other Galactic soft x-ray emissions.

From a more global perspective, it would also be desirable to do other x-ray shadow experiments to more distant Galactic molecular clouds, in many different directions. These studies would permit us to probe the different Galactic plasma temperatures and spatial extensions—therefore, making it possible to draw the 3D structure of these Galactic plasmas.

The extended ROentgen Survey with an Imaging Telescope Array (eROSITA) mission, under development at MPE and to be launch in 2012, design to produce x-ray all sky surveys, has the potential to resolve the question of the physical state of the LB plasma. The eROSITA CCD detectors, developed for spectroscopy and imaging of x-ray photons, will be able to operate efficiently in the energy band of 0.2–12 keV. In conjunction with the high collecting area, the new pn detectors will have an unprecedented spectral resolution and quantum efficiency. The best spectral resolution will be attainable, precisely, on the soft x-ray band, with FWHM of 54 eV at 0.277 keV, a FWHM of 74 eV at 1.5 keV, and a FWHM of 134 eV at 5.9 keV, reaching almost 100 per cent, in terms of quantum efficiency, in the energy band of 0.3–10 keV. These capabilities are of fundamental importance to resolve spectral emission lines and, therefore, to distinguish between CIE or NIE plasmas.

On the long term, other missions are being considered. The X-Ray Evolving Universe Spectrometer (XEUS), a future x-ray mission under study by ESA, given its projected high collecting area and high spectral resolution will surpass the capabilities of eROSITA. The Missing Baryon Explorer (MBE) and the Diffuse Intergalactic Oxygen Surveyor (DIOS) have been recently proposed to investigate the soft x-ray emission of the warm hot intergalactic medium (WHIM) will complement the eROSITA and XEUS missions. In orbit they will give an invaluable contribution for the study of the soft x-ray emission from our local galactic environment to the very distant Universe.

Appendix A

Physical Constants

Table A.1: Physical Constants

Symbol	Quantity	Value		Units
c	Speed of light in vacuum	299792458		m s^{-1}
e	Elementary charge	1.602176487	10^{-19}	C
m_n	Neutron rest mass	1.674927211	10^{-27}	kg
m_p	Proton rest mass	1.672621637	10^{-27}	kg
m_e	Electron rest mass	9.10938215	10^{-31}	kg
h	Planck's constant	6.62606896	10^{-34}	J s
$\hbar$	Dirac's constant ($= h/2\pi$)	1.05457163	10^{-34}	J s
k_B	Boltzmann's constant	1.3806504	10^{-23}	J K^{-1}
		1.3806504	10^{-23}	m^2 kg s^{-2} K^{-1}
		1.3806504	10^{-16}	erg K^{-1}
G	Gravitational constant	6.67428(67)	10^{-11}	N m^2 kg^{-2}
σ	Stefan-Boltzmann constant	5.670400	10^{-8}	J m^{-2} K^{-4} s^{-1}
ε_o	Permittivity of free space	8.854187817	10^{-12}	C^2 N^{-1} m^{-2}
μ_o	Permeability of free space	4π	10^{-7}	H m^{-1}
N_A	Avogadro constant	6.02214179	10^{23}	mol^{-1}
R	Gas constant	8.314		J K^{-1} mol^{-1}
a_0	Bohr radius	5.2917720859	10^{-11}	m
μ_B	Bohr magneton	9.27400915	10^{-24}	J T^{-1}
α	Fine structure constant	1/137.03599907		
$M_\odot$	Solar Mass	1.989	10^{30}	kg
$R_\odot$	Solar radius	6.96	10^8	m
$L_\odot$	Solar luminosity	3.827	10^{26}	J s^{-1}
$M_\oplus$	Earth Mass	5.976	10^{24}	kg
$R_\oplus$	Mean Earth radius	6.371	10^6	m
1 ly	Light Year	9.461	10^{15}	m
1 AU	Astronomical Unit	1.496	10^{11}	m
1 pc	Parsec	3.086	10^{16}	m
1 yr	Year	3.156	10^7	s

A.1 Solar Wind Charge Emission lines

Table A.2: The Solar Wind Charge Exchange X-ray Emission lines. Table showing the most important SWCE emission lines taken from Wargelin et al. [262].

Line	Energy (eV)	Wavelength Å	Line Yield
C V K_α	298.97^f, 304.41^i, 307.88^r	41.469 , 40.728, 40.269	0.899
C VI Ly_α	368	33.690	0.650
N VI K_α	419.86^f, 426.36^i, 430.65^r	29.529, 29.079, 28.789	0.872
N VII	500	4.796	
C VI Ly_β	436	28.436	0.108
C VI Ly_γ	459	27.011	0.165
O VII K_α	561.02^f, 568.74^i, 574.00^r	22.099, 21.799, 21.599	0.865
O VIII Ly_α	654	18.957	0.707
O VII K_β	665.59	18.627	0.121
O VIII Ly_β	775	15.997	0.091
O VIII Ly_γ	817	15.175	0.033
O VIII Ly_δ	836	14.830	0.103
O VIII Ly_ϵ	847	14.678	0.030
Fe XVII	725, 727, 739	17.101, 17.054, 16.777	
Fe XVII	826	15.001	
Ne IX K_α	905.00^f, 915.02^i, 921.82^r	13.699, 13.549, 13.449	0.887
Mg XI	1331.74^f, 1343.28^i, 1357.07^r	9.310, 9.230, 9.136	
Si XIII	1839.54^f, 1853.29^i, 1864.44^r	6.740, 6.690, 6.650	

^{f} - forbidden line. ^{i} - intercombination line. ^{r} - resonance line.

Appendix B

Spectral Signature of the Soft Proton Flares

B.1 Spectral Signature of the Soft Proton Flares

In this appendix we present the complete results from the spectral fits, to the Soft Proton Flares (SPFs) periods, discussed in chapter 3, for all observations studied in that chapter and in each detector region. The purpose of this analysis was to investigate, if x-ray emission lines could be associated to SPFs.

The x-ray data was fitted with an unfolded power-law function, having the following form:

$$\mathbf{P} = \text{Normalization} \; . \; \left(\frac{\mathbf{E}}{1 \text{ keV}}\right)^{-\Gamma}, \tag{B.1}$$

where Normalization (Nor) is the extrapolated normalization factor, at 1 keV, given in units of photons per keV, per cm^2, and per s, **E** is the energy in keV, and Γ is the spectral index of the power law. The x-ray spectral fit was done with the XSPEC package, version **11.0.3**. After converging to the best minimum (χ^2 minimization) , the associated errors to the model parameters were calculated within the 90 per cent confidence level, implying a $\Delta\chi^2 = 4.61$, for two interesting parameters. In the following tables the results of the fits are presented. In table B.1 the main observational properties of these XMM-Newton observations are presented again.

Table B.1: The main properties of the Hyades XMM-Newton observations. The values presented in this table correspond to the ones of the EPIC-pn camera.

Rev #	Observation ID	Filter	Observation Date	Time Total [ks]	Galactic Longitude	Galactic Latitude	Target Name
0049	0094810301	Thin	2000-03-16T00:12:12	10	179.7830°	−20.5840°	Obser. 1
0059	0122320701	Closed	2000-04-05T07:06:39	52	279.9951°	−19.8089°	—
0135	0101440501	Thick	2000-09-03T03:08:43	43	180.2301°	−21.9713°	Obser. 2
0138	0109060301	Medium	2000-09-10T10:18:12	55	178.8850°	−20.0110°	Obser. 3
0410	0101441501	Medium	2002-03-06T06:44:07	47	180.5870°	−23.5390°	Obser. 4
0462	0134521601	Closed	2000-04-05T07:06:39	23	275.3203°	−33.0685°	—

TABLE B.2: MBM 12. Results from the spectral fitting of the soft protons from period 2 using period 1 as the background. Comparison of the unfolded power-law fits between observation MBM 12 A and MBM 12 B.

Detector Regions	XMM-Newton Observations	
i	MBM 12 A	MBM 12 B
01	$\Gamma = 0.59 \pm 0.07$	$\Gamma = 0.69 \pm 0.07$
	$Nor = 0.20 \pm 0.02$	$Nor = 0.23 \pm 0.02$
02	$\Gamma = 0.56 \pm 0.06$	$\Gamma = 0.63 \pm 0.07$
	$Nor = 0.22 \pm 0.02$	$Nor = 0.23 \pm 0.02$
03	$\Gamma = 0.59 \pm 0.06$	$\Gamma = 0.64 \pm 0.07$
	$Nor = 0.22 \pm 0.02$	$Nor = 0.22 \pm 0.02$
04	$\Gamma = 0.61 \pm 0.06$	$\Gamma = 0.65 \pm 0.07$
	$Nor = 0.22 \pm 0.02$	$Nor = 0.23 \pm 0.02$
05	$\Gamma = 0.59 \pm 0.07$	$\Gamma = 0.63 \pm 0.08$
	$Nor = 0.21 \pm 0.02$	$Nor = 0.29 \pm 0.02$
06	$\Gamma = 0.59 \pm 0.07$	$\Gamma = 0.64 \pm 0.08$
	$Nor = 0.20 \pm 0.02$	$Nor = 0.22 \pm 0.02$
07	$\Gamma = 0.65 \pm 0.07$	$\Gamma = 0.66 \pm 0.08$
	$Nor = 0.22 \pm 0.02$	$Nor = 0.21 \pm 0.02$
08	$\Gamma = 0.61 \pm 0.07$	$\Gamma = 0.68 \pm 0.08$
	$Nor = 0.20 \pm 0.02$	$Nor = 0.20 \pm 0.02$
09	$\Gamma = 0.61 \pm 0.07$	$\Gamma = 0.69 \pm 0.07$
	$Nor = 0.20 \pm 0.02$	$Nor = 0.20 \pm 0.02$
10	$\Gamma = 0.60 \pm 0.03$	$\Gamma = 0.65 \pm 0.04$
	$Nor = 0.98 \pm 0.03$	$Nor = 0.96 \pm 0.04$

TABLE B.3: MBM 12. Results from the spectral fitting of the soft protons from period 3 using period 1 as the background. Comparison of the unfolded power-law fits between observation MBM 12 A and MBM 12 B.

Detector Regions	XMM-Newton Observations	
i	MBM 12 A	MBM 12 B
01	$\Gamma = 0.60 \pm 0.03$	$\Gamma = 0.69 \pm 0.03$
	$Nor = 0.56 \pm 0.02$	$Nor = 0.53 \pm 0.02$
02	$\Gamma = 0.59 \pm 0.03$	$\Gamma = 0.66 \pm 0.03$
	$Nor = 0.58 \pm 0.02$	$Nor = 0.56 \pm 0.02$
03	$\Gamma = 0.61 \pm 0.03$	$\Gamma = 0.65 \pm 0.03$
	$Nor = 0.60 \pm 0.02$	$Nor = 0.54 \pm 0.02$
04	$\Gamma = 0.59 \pm 0.03$	$\Gamma = 0.65 \pm 0.03$
	$Nor = 0.61 \pm 0.02$	$Nor = 0.56 \pm 0.02$
05	$\Gamma = 0.58 \pm 0.03$	$\Gamma = 0.63 \pm 0.03$
	$Nor = 0.57 \pm 0.02$	$Nor = 0.54 \pm 0.02$
06	$\Gamma = 0.58 \pm 0.03$	$\Gamma = 0.65 \pm 0.03$
	$Nor = 0.56 \pm 0.02$	$Nor = 0.54 \pm 0.02$
07	$\Gamma = 0.60 \pm 0.04$	$\Gamma = 0.65 \pm 0.03$
	$Nor = 0.56 \pm 0.02$	$Nor = 0.52 \pm 0.02$
08	$\Gamma = 0.61 \pm 0.03$	$\Gamma = 0.65 \pm 0.03$
	$Nor = 0.56 \pm 0.02$	$Nor = 0.48 \pm 0.02$
09	$\Gamma = 0.60 \pm 0.03$	$\Gamma = 0.68 \pm 0.03$
	$Nor = 0.58 \pm 0.02$	$Nor = 0.51 \pm 0.02$
10	$\Gamma = 0.60 \pm 0.02$	$\Gamma = 0.64 \pm 0.01$
	$Nor = 2.71 \pm 0.05$	$Nor = 2.43 \pm 0.03$

TABLE B.4: MBM 12. Results from the spectral fitting of the soft protons from period 3 using period 2 as background. Comparison of the unfolded power-law fits between observation MBM 12 A and MBM 12 B.

Detector Regions	XMM-Newton Observations	
i	MBM 12 A	MBM 12 B
01	$\Gamma = 0.60 \pm 0.06$	$\Gamma = 0.63 \pm 0.04$
	$Nor = 0.37 \pm 0.03$	$Nor = 0.32 \pm 0.02$
02	$\Gamma = 0.61 \pm 0.06$	$\Gamma = 0.63 \pm 0.04$
	$Nor = 0.37 \pm 0.03$	$Nor = 0.35 \pm 0.02$
03	$\Gamma = 0.62 \pm 0.06$	$\Gamma = 0.63 \pm 0.04$
	$Nor = 0.39 \pm 0.03$	$Nor = 0.34 \pm 0.02$
04	$\Gamma = 0.58 \pm 0.06$	$\Gamma = 0.61 \pm 0.04$
	$Nor = 0.39 \pm 0.03$	$Nor = 0.35 \pm 0.02$
05	$\Gamma = 0.58 \pm 0.06$	$\Gamma = 0.59 \pm 0.04$
	$Nor = 0.37 \pm 0.03$	$Nor = 0.33 \pm 0.02$
06	$\Gamma = 0.58 \pm 0.06$	$\Gamma = 0.60 \pm 0.04$
	$Nor = 0.37 \pm 0.03$	$Nor = 0.34 \pm 0.02$
07	$\Gamma = 0.57 \pm 0.07$	$\Gamma = 0.60 \pm 0.04$
	$Nor = 0.34 \pm 0.03$	$Nor = 0.33 \pm 0.02$
08	$\Gamma = 0.60 \pm 0.06$	$\Gamma = 0.59 \pm 0.04$
	$Nor = 0.37 \pm 0.03$	$Nor = 0.30 \pm 0.02$
09	$\Gamma = 0.60 \pm 0.06$	$\Gamma = 0.63 \pm 0.04$
	$Nor = 0.38 \pm 0.03$	$Nor = 0.32 \pm 0.02$
10	$\Gamma = 0.60 \pm 0.03$	$\Gamma = 0.62 \pm 0.02$
	$Nor = 1.74 \pm 0.06$	$Nor = 1.42 \pm 0.03$

TABLE B.5: V410 Tau. Results from the spectral fitting of the soft protons from period 2 using period 1 as background. Comparison of the unfolded power-law fits between observation V410 Tau A and V410 Tau B.

Detector Regions	XMM-Newton Observations	
i	V410 Tau A	V410 Tau B
01	$\Gamma = 0.81 \pm 0.08$	$\Gamma = 0.67 \pm 0.06$
	$Nor = 0.15 \pm 0.03$	$Nor = 0.10 \pm 0.01$
02	$\Gamma = 0.76 \pm 0.08$	$\Gamma = 0.68 \pm 0.07$
	$Nor = 0.13 \pm 0.03$	$Nor = 0.10 \pm 0.01$
03	$\Gamma = 0.77 \pm 0.08$	$\Gamma = 0.68 \pm 0.05$
	$Nor = 0.15 \pm 0.03$	$Nor = 0.12 \pm 0.01$
04	$\Gamma = 0.75 \pm 0.07$	$\Gamma = 0.63 \pm 0.05$
	$Nor = 0.17 \pm 0.03$	$Nor = 0.12 \pm 0.01$
05	$\Gamma = 0.73 \pm 0.08$	$\Gamma = 0.66 \pm 0.06$
	$Nor = 0.14 \pm 0.03$	$Nor = 0.11 \pm 0.01$
06	$\Gamma = 0.74 \pm 0.08$	$\Gamma = 0.64 \pm 0.06$
	$Nor = 0.15 \pm 0.03$	$Nor = 0.11 \pm 0.01$
07	$\Gamma = 0.78 \pm 0.08$	$\Gamma = 0.65 \pm 0.05$
	$Nor = 0.16 \pm 0.03$	$Nor = 0.12 \pm 0.01$
08	$\Gamma = 0.75 \pm 0.08$	$\Gamma = 0.59 \pm 0.06$
	$Nor = 0.15 \pm 0.03$	$Nor = 0.10 \pm 0.01$
09	$\Gamma = 0.77 \pm 0.08$	$\Gamma = 0.62 \pm 0.05$
	$Nor = 0.16 \pm 0.03$	$Nor = 0.11 \pm 0.01$
10	$\Gamma = 0.76 \pm 0.04$	$\Gamma = 0.64 \pm 0.02$
	$Nor = 0.70 \pm 0.07$	$Nor = 0.52 \pm 0.02$

TABLE B.6: V410 Tau. Results from the spectral fitting of the soft protons from period 3 using period 1 as background. Comparison of the unfolded power-law fits between observation V410 Tau A and V410 Tau B.

Detector Regions	XMM-Newton Observations	
i	V410 Tau A	V410 Tau B
01	$\Gamma = 0.71 \pm 0.01$	$\Gamma = 0.61 \pm 0.04$
	$Nor = 0.49 \pm 0.05$	$Nor = 0.43 \pm 0.02$
02	$\Gamma = 0.69 \pm 0.01$	$\Gamma = 0.58 \pm 0.04$
	$Nor = 0.46 \pm 0.05$	$Nor = 0.40 \pm 0.02$
03	$\Gamma = 0.71 \pm 0.01$	$\Gamma = 0.62 \pm 0.04$
	$Nor = 0.56 \pm 0.05$	$Nor = 0.48 \pm 0.02$
04	$\Gamma = 0.70 \pm 0.01$	$\Gamma = 0.58 \pm 0.04$
	$Nor = 0.59 \pm 0.06$	$Nor = 0.50 \pm 0.02$
05	$\Gamma = 0.65 \pm 0.01$	$\Gamma = 0.57 \pm 0.04$
	$Nor = 0.51 \pm 0.06$	$Nor = 0.45 \pm 0.02$
06	$\Gamma = 0.66 \pm 0.01$	$\Gamma = 0.60 \pm 0.04$
	$Nor = 0.52 \pm 0.05$	$Nor = 0.47 \pm 0.02$
07	$\Gamma = 0.69 \pm 0.01$	$\Gamma = 0.61 \pm 0.04$
	$Nor = 0.56 \pm 0.05$	$Nor = 0.48 \pm 0.02$
08	$\Gamma = 0.67 \pm 0.01$	$\Gamma = 0.56 \pm 0.04$
	$Nor = 0.51 \pm 0.05$	$Nor = 0.43 \pm 0.02$
09	$\Gamma = 0.71 \pm 0.01$	$\Gamma = 0.58 \pm 0.04$
	$Nor = 0.56 \pm 0.05$	$Nor = 0.45 \pm 0.02$
10	$\Gamma = 0.69 \pm 0.01$	$\Gamma = 0.59 \pm 0.02$
	$Nor = 2.49 \pm 0.01$	$Nor = 2.13 \pm 0.04$

TABLE B.7: V410 Tau. Results from the spectral fitting of the soft protons from period 3 using the spectra from period 2 as background. Comparison of the unfolded power-law fits between observation V410 Tau A and V410 Tau B.

Detector Regions	XMM-Newton Observations	
i	V410 Tau A	V410 Tau B
01	$\Gamma = 0.67 \pm 0.05$	$\Gamma = 0.59 \pm 0.05$
	$Nor = 0.35 \pm 0.03$	$Nor = 0.33 \pm 0.02$
02	$\Gamma = 0.66 \pm 0.05$	$\Gamma = 0.55 \pm 0.06$
	$Nor = 0.33 \pm 0.03$	$Nor = 0.30 \pm 0.02$
03	$\Gamma = 0.69 \pm 0.05$	$\Gamma = 0.60 \pm 0.05$
	$Nor = 0.40 \pm 0.03$	$Nor = 0.36 \pm 0.02$
04	$\Gamma = 0.68 \pm 0.06$	$\Gamma = 0.56 \pm 0.05$
	$Nor = 0.43 \pm 0.03$	$Nor = 0.37 \pm 0.02$
05	$\Gamma = 0.63 \pm 0.06$	$\Gamma = 0.54 \pm 0.05$
	$Nor = 0.37 \pm 0.03$	$Nor = 0.34 \pm 0.02$
06	$\Gamma = 0.63 \pm 0.05$	$\Gamma = 0.58 \pm 0.06$
	$Nor = 0.38 \pm 0.03$	$Nor = 0.35 \pm 0.02$
07	$\Gamma = 0.66 \pm 0.05$	$\Gamma = 0.60 \pm 0.05$
	$Nor = 0.40 \pm 0.03$	$Nor = 0.36 \pm 0.02$
08	$\Gamma = 0.64 \pm 0.06$	$\Gamma = 0.55 \pm 0.05$
	$Nor = 0.37 \pm 0.03$	$Nor = 0.32 \pm 0.02$
09	$\Gamma = 0.69 \pm 0.06$	$\Gamma = 0.56 \pm 0.05$
	$Nor = 0.40 \pm 0.03$	$Nor = 0.33 \pm 0.02$
10	$\Gamma = 0.67 \pm 0.04$	$\Gamma = 0.57 \pm 0.03$
	$Nor = 1.79 \pm 0.04$	$Nor = 1.61 \pm 0.05$

TABLE B.8: HDFN. Results from the spectral fitting of the soft protons from period 2 using period 1 as background. Spectral fit to an unfolded power-law for observation HDFN.

Detector Regions i	XMM-Newton Observation HDFN
01	$\Gamma = 0.70 \pm 0.06$
	$Nor = 0.12 \pm 0.01$
02	$\Gamma = 0.70 \pm 0.06$
	$Nor = 0.13 \pm 0.01$
03	$\Gamma = 0.75 \pm 0.06$
	$Nor = 0.13 \pm 0.01$
04	$\Gamma = 0.71 \pm 0.06$
	$Nor = 0.14 \pm 0.01$
05	$\Gamma = 0.64 \pm 0.06$
	$Nor = 0.13 \pm 0.01$
06	$\Gamma = 0.70 \pm 0.06$
	$Nor = 0.13 \pm 0.01$
07	$\Gamma = 0.72 \pm 0.06$
	$Nor = 0.13 \pm 0.01$
08	$\Gamma = 0.71 \pm 0.06$
	$Nor = 0.11 \pm 0.01$
09	$\Gamma = 0.73 \pm 0.06$
	$Nor = 0.13 \pm 0.01$
10	$\Gamma = 0.72 \pm 0.03$
	$Nor = 0.62 \pm 0.02$

TABLE B.9: HDFN. Results from the spectral fitting of the soft protons from period 3 using period 1 as background. Spectral fit to an unfolded power-law for observation HDFN.

Detector Regions i	XMM-Newton Observation HDFN
01	$\Gamma = 0.64 \pm 0.05$
	$Nor = 0.45 \pm 0.02$
02	$\Gamma = 0.65 \pm 0.04$
	$Nor = 0.46 \pm 0.02$
03	$\Gamma = 0.69 \pm 0.04$
	$Nor = 0.52 \pm 0.02$
04	$\Gamma = 0.64 \pm 0.04$
	$Nor = 0.51 \pm 0.02$
05	$\Gamma = 0.60 \pm 0.04$
	$Nor = 0.48 \pm 0.02$
06	$\Gamma = 0.61 \pm 0.04$
	$Nor = 0.48 \pm 0.02$
07	$\Gamma = 0.64 \pm 0.04$
	$Nor = 0.47 \pm 0.02$
08	$\Gamma = 0.63 \pm 0.05$
	$Nor = 0.41 \pm 0.02$
09	$\Gamma = 0.68 \pm 0.04$
	$Nor = 0.44 \pm 0.02$
10	$\Gamma = 0.65 \pm 0.02$
	$Nor = 2.22 \pm 0.05$

TABLE B.10: HDFN. Results from the spectral fitting of the soft protons from period 3 using period 2 as background. Spectral fit to an unfolded power-law for observation HDFN.

Detector Regions	XMM-Newton Observation
i	HDFN
01	$\Gamma = 0.64 \pm 0.07$
	$Nor = 0.32 \pm 0.03$
02	$\Gamma = 0.64 \pm 0.07$
	$Nor = 0.36 \pm 0.03$
03	$\Gamma = 0.68 \pm 0.06$
	$Nor = 0.38 \pm 0.03$
04	$\Gamma = 0.63 \pm 0.06$
	$Nor = 0.37 \pm 0.03$
05	$\Gamma = 0.59 \pm 0.07$
	$Nor = 0.35 \pm 0.03$
06	$\Gamma = 0.59 \pm 0.06$
	$Nor = 0.35 \pm 0.03$
07	$\Gamma = 0.62 \pm 0.06$
	$Nor = 0.34 \pm 0.03$
08	$\Gamma = 0.60 \pm 0.07$
	$Nor = 0.29 \pm 0.02$
09	$\Gamma = 0.66 \pm 0.07$
	$Nor = 0.31 \pm 0.02$
10	$\Gamma = 0.63 \pm 0.03$
	$Nor = 1.61 \pm 0.05$

TABLE B.11: Ophiuchus. Results from the spectral fitting of the soft protons from period 2 using period 1 as background. Comparison of the unfolded power-law fits between observation Oph 1 and Oph 3.

Detector Regions	XMM-Newton Observations	
i	Oph 1	Oph 3
01	$\Gamma = 0.91 \pm 0.10$	$\Gamma = 0.58 \pm 0.15$
	$Nor = 0.16 \pm 0.02$	$Nor = 0.07 \pm 0.01$
02	$\Gamma = 0.82 \pm 0.10$	$\Gamma = 0.51 \pm 0.17$
	$Nor = 0.17 \pm 0.02$	$Nor = 0.06 \pm 0.01$
03	$\Gamma = 0.83 \pm 0.10$	$\Gamma = 0.53 \pm 0.16$
	$Nor = 0.16 \pm 0.02$	$Nor = 0.06 \pm 0.01$
04	$\Gamma = 0.89 \pm 0.10$	$\Gamma = 0.54 \pm 0.15$
	$Nor = 0.16 \pm 0.02$	$Nor = 0.07 \pm 0.01$
05	$\Gamma = 0.90 \pm 0.10$	$\Gamma = 0.63 \pm 0.15$
	$Nor = 0.17 \pm 0.02$	$Nor = 0.08 \pm 0.01$
06	$\Gamma = 0.87 \pm 0.10$	$\Gamma = 0.62 \pm 0.15$
	$Nor = 0.17 \pm 0.02$	$Nor = 0.08 \pm 0.01$
07	$\Gamma = 0.89 \pm 0.10$	$\Gamma = 0.62 \pm 0.14$
	$Nor = 0.15 \pm 0.02$	$Nor = 0.08 \pm 0.01$
08	$\Gamma = 0.91 \pm 0.10$	$\Gamma = 0.63 \pm 0.15$
	$Nor = 0.15 \pm 0.02$	$Nor = 0.08 \pm 0.01$
09	$\Gamma = 0.92 \pm 0.09$	$\Gamma = 0.64 \pm 0.15$
	$Nor = 0.16 \pm 0.02$	$Nor = 0.07 \pm 0.01$
10	$\Gamma = 0.90 \pm 0.04$	$\Gamma = 0.58 \pm 0.07$
	$Nor = 0.75 \pm 0.04$	$Nor = 0.33 \pm 0.03$

TABLE B.12: Abell Cluster 478. Results from the spectral fitting of the soft protons from period 2 using period 1 as background. Fit performed on the spectra extracted on observation Abell Cluster 478. As it can be seen the soft protons from period 2 are well fitted by an unfolded power law.

Detector Regions i	XMM-Newton Observation Abell Cluster 478
01	$\Gamma = 0.67 \pm 0.04$
	$Nor = 0.17 \pm 0.01$
02	$\Gamma = 0.69 \pm 0.04$
	$Nor = 0.19 \pm 0.01$
03	$\Gamma = 0.70 \pm 0.02$
	$Nor = 0.18 \pm 0.01$
04	$\Gamma = 0.67 \pm 0.03$
	$Nor = 0.18 \pm 0.01$
05	$\Gamma = 0.65 \pm 0.05$
	$Nor = 0.19 \pm 0.01$
06	$\Gamma = 0.68 \pm 0.05$
	$Nor = 0.20 \pm 0.01$
07	$\Gamma = 0.71 \pm 0.03$
	$Nor = 0.17 \pm 0.01$
08	$\Gamma = 0.67 \pm 0.03$
	$Nor = 0.17 \pm 0.01$
09	$\Gamma = 0.69 \pm 0.02$
	$Nor = 0.16 \pm 0.01$
10	$\Gamma = 0.68 \pm 0.02$
	$Nor = 0.82 \pm 0.02$

TABLE B.13: Abell Cluster 478. Results from the spectral fitting of the soft protons from period 3 using period 1 as background. Fit performed on the spectra extracted on observation Abell Cluster 478. As it can be seen the soft protons from period 3 are well fitted by an unfolded power law.

Detector Regions i	XMM-Newton Observation Abell Cluster 478
01	$\Gamma = 0.61 \pm 0.03$
	$Nor = 0.47 \pm 0.02$
02	$\Gamma = 0.59 \pm 0.03$
	$Nor = 0.50 \pm 0.02$
03	$\Gamma = 0.62 \pm 0.02$
	$Nor = 0.49 \pm 0.01$
04	$\Gamma = 0.59 \pm 0.02$
	$Nor = 0.49 \pm 0.01$
05	$\Gamma = 0.60 \pm 0.04$
	$Nor = 0.52 \pm 0.03$
06	$\Gamma = 0.62 \pm 0.04$
	$Nor = 0.52 \pm 0.03$
07	$\Gamma = 0.62 \pm 0.02$
	$Nor = 0.47 \pm 0.01$
08	$\Gamma = 0.60 \pm 0.02$
	$Nor = 0.45 \pm 0.01$
09	$\Gamma = 0.63 \pm 0.02$
	$Nor = 0.44 \pm 0.01$
10	$\Gamma = 0.62 \pm 0.01$
	$Nor = 2.26 \pm 0.04$

TABLE B.14: Abell Cluster 478. Results from the spectral fitting of the soft protons from period 3 using period 2 as background. Fit performed on the spectra extracted on observation Abell Cluster 478. As it can be seen, the soft protons from period 3 are well fitted by an unfolded power law.

Detector Regions i	XMM-Newton Observation Abell Cluster 478
01	$\Gamma = 0.58 \pm 0.05$ $Nor = 0.29 \pm 0.02$
02	$\Gamma = 0.54 \pm 0.05$ $Nor = 0.31 \pm 0.02$
03	$\Gamma = 0.58 \pm 0.04$ $Nor = 0.31 \pm 0.01$
04	$\Gamma = 0.55 \pm 0.04$ $Nor = 0.31 \pm 0.01$
05	$\Gamma = 0.57 \pm 0.06$ $Nor = 0.32 \pm 0.03$
06	$\Gamma = 0.59 \pm 0.06$ $Nor = 0.32 \pm 0.03$
07	$\Gamma = 0.58 \pm 0.04$ $Nor = 0.30 \pm 0.01$
08	$\Gamma = 0.56 \pm 0.04$ $Nor = 0.28 \pm 0.01$
09	$\Gamma = 0.60 \pm 0.04$ $Nor = 0.28 \pm 0.01$
10	$\Gamma = 0.58 \pm 0.02$ $Nor = 1.43 \pm 0.04$

Appendix C

The main bright X-ray sources in the X-ray Shadow Experiment

In this appendix, and as promise in chapter 4, § 4.3, some information regarding these sources is reported.

A source detection was preformed on the data by using the SAS **edetect_chain** task. Images in five energy bands were produced by selecting events with (PATTERN <= 4). The five bands are 200 to 500, 500 to 2000, 2000 to 4500, 4500 to 7500 and from 7500 to 12000 eV. The conversion between the count rates and the implied fluxes were done, using the energy conversion factors (ECFs) given in table C.1.

Table C.1: Energy conversion factors (ECFs). The ECFs used in the SAS **edetect_chain** task to calculate the source flux, given the measured count rate. The ECFs values are given in units of 10^{11} counts cm^{-2} erg^{-1}.

Band [keV]	0.2-0.5	0.5-2.0	2.0-4.5	4.5-7.5	7.5-12.0
ECFs	10.596	6.7340	1.2473	0.94206	0.24273

In table C.2 the galactic positions of these X-ray sources are presented. The associated positional error obtained from the SAS **edetect_chain** task is also shown. The flux derived from this analysis is given in two cases twice, because the sources were also present in two different XMM-Newton observations. The optical and x-ray counterpart, when known, are also shown. When no x-ray counterparts exists, the XMM-Newton designation is adopted.

C.1 The first Ophiuchus dark filament XMM-Newton observation

On the first of the Ophiuchus dark filament XMM-Newton observations, a total of seventeen x-ray point sources were detected by the SAS **edetect_chain** task. Of these, only one is a relative bright source with $7.4 \pm 0.8 \times 10^{-13}$ cgs (erg cm^{-2}s^{-1}). It is seen in the top right border of the detector. The x-ray emission of this object

TABLE C.2: The main bright x-ray sources. The x-ray sources flux is given in units of 10^{-13} erg cm^{-2} s^{-1}.

Source	Galactic		Error	Optical Counterpart	Flux	Source
	Longitude	Latitude	arcsec			Designation
A	355.5986°	14.8266°	0.34	V 2307 Oph	7.4±0.8	1RXS J164018.3-235331
B	355.3651°	14.3032°	0.25	F5 V	5.1±0.5	1RXS J164126.8-242405
C	355.3360°	14.2339°	1.86	A7 III	0.3±0.5	
D	355.1018°	14.3179°	0.37	?	7.8±0.8	1RXS J164042.2-243513
	355.1022°	14.3179°	0.16	-	33.4±1.3	
E	355.1277°	14.2491°	1.12	?	1.2±0.9	XMM J164098.0-243649
	355.1549°	14.1483°	0.56	-	1.6±0.4	
F	355.1287°	14.2494°	0.65	?	1.2±0.6	XMM J164124.0-243909

seems to be associated with the ROSAT 1RXS J164018.3-235331 source, having as optical counterpart the variable star V2307 Oph (HD 150193A), with the galactic coordinates l = 355.5983° and b = +14.8266°, or its companion a T Tau-type star (HD 150193B) from the SIMBAD[1] database. This source is a pre-main sequence star of spectral type A1 Ve at a distance of 150^{+50}_{-30} pc. A radius of 72 arcsec was used to extract the area associated to this source.

C.2 The second Ophiuchus dark filament XMM-Newton observation

On the the second Ophiuchus dark filament XMM-Newton observation the SAS **edetect_chain** task has detected fourteen point sources.

The brightest x-ray source in this field is most likely associated with the faint ROSAT 1RXS J164042.2-243513 source. This source is also present on the third pointing, see the subsection C.3. The measured flux for this source during this observation was $7.8 \pm 0.8 \times 10^{-13}$ cgs (erg cm^{-2}s^{-1}). A radius of 1.10 arcmin was used to define the extracting area and centered at the source detected at a position of l = 355.1018° and b = +14.3179°. This x-ray source shows a continuum spectrum. This spectrum was well fitted with a model composed by a simple power-law and a Gaussian emission line subject to absorption. The absorption was fixed to the best fit value derived from the analysis of the spectrum from the third observation, due to the higher spectral quality, see § C.3. The derived value of the spectral index of the power-law was $\Gamma = 1.68^{+0.37}_{-0.28}$, with a normalization of $9.8^{+2.1}_{-2.0} \times 10^{-5}$ photons/keV/cm^2/s. The derived line centroid of the Gaussian was $3.77^{+0.37}_{-0.24}$ keV, with an equivalent width of $0.13^{+0.60}_{-0.13}$ keV and a normalization of $1.1^{+1.3}_{-0.9} \times 10^{-5}$ photons/cm^2/s. The former values are given within the 90 per cent confidence level for five free model parameters and a $\chi^2_{\rm red}$ of 1.14. The result from this fit is shown on the left plot of figure C.1.

The second strongest x-ray source with a flux of $5.1\pm0.5\times10^{-13}$ cgs (erg cm^{-2}s^{-1}) seem to be associated with the HD 150345 star. This source has been already detected by the ROSAT satellite and designated by 1RXS J164126.8-242405. This is the bright source located in the middle left part of the field of view. It is a star of

[1] http://simbad.u-strasbg.fr/

spectral type F5 V with the galactic coordinates l = 355.3355° and b = +14.2345° at a distance of 75^{+6}_{-5} pc (from SIMBAD). For extracting a circular area centered on the source, a radius of 1.42 arcmin was used.

The third stronger x-ray source (XMM J164098-243649) does not seem to be associated with any known object and is also present on the third XMM-Newton pointing, see subsection C.3. The measured flux of this source is $1.2 \pm 0.9 \times 10^{-13}$ cgs (erg $cm^{-2}s^{-1}$). This source has the galactic coordinates l = 355.1277° and b = +14.2491°. In this case a radius of 0.52 arcmin was used to extract a circle centered at the detected source position. This source is found on the border of the EPIC-pn field of view.

The very soft x-ray source (very red) seen in the field of view, is associated with the star HD 150366. This star Which is of spectral type A7 III, and with the galactic coordinates of l = 355.3355° and b = +14.2345°. This stellar object is located at a distance of 80^{+5}_{-4} pc (from SIMBAD). This source was removed using a cut-out radius of 0.45 arcmin.

C.3 The third Ophiuchus dark filament XMM-Newton observation

On the third XMM-Newton pointing, a total of sixteen point sources was detected by the SAS **edetect_chain** task. Two of them are also present in the second XMM-Newton observation, namely the first and third detections, see previous subsections.

The strongest source seems to be associated with the ROSAT 1RXS J164042.2-243513 source. The measured flux for this source was $3.3 \pm 0.1 \times 10^{-12}$ cgs which is more than four times higher than during the second observation. The detected source position is l = 355.1022° and b = +14.3179°. When one compares in detail the position, given by the SAS **edetect_chain** task, for this source on both observations, an angular separation of 1.4 arcsec is detected. In this case a cut-out radius of 1.74 arcmin was used to remove an area around the source. This x-ray source shows a featureless spectrum. This spectrum is well fitted with a model composed by a simple power-law and subjected to absorption. The derived column density was $N_H = 0.37^{+0.09}_{-0.08} \times 10^{21}$ cm^{-2}. The spectral index of the power-law has a value of $\Gamma = 1.77^{+0.20}_{-0.18}$, with a normalization of $4.7^{+1.0}_{-0.8} \times 10^{-4}$ photons/keV/cm^2/s. The former values are given within the 99 per cent confidence level, with a χ^2_{red} of 1.0 for three free model parameters. The fit plot is given on the right plot of figure C.1. The column density associated to the dark filament is 2.5×10^{21} cm^{-2}, which means that 1.2×10^{21} cm^{-2} is the column density in the background of the Ophiuchus filament. Assuming an hydrogen density of 1 cm^{-3} this would imply a line of path of $\sim$ 390 pc for the former column density, therefore requiring a distance of 515 pc to the source.

The second strongest source (XMM J164098-243649) in this pointing is the third strongest x-ray source of the second XMM-Newton observation. The flux, observed for this source was $1.6 \pm 0.4 \times 10^{-13}$ cgs. Given the errors, no variability can be inferred for this source. The detected source position was, in galactic coordinates,

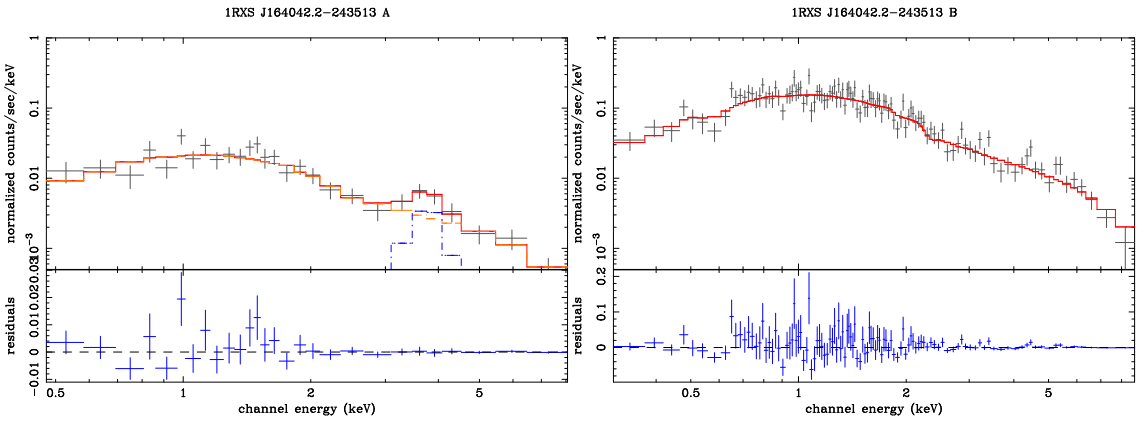

Figure C.1: Spectra from the 1RXS J164042.2-243513 source in two different periods, on the second (A) and third (B) XMM-Newton observations, respectively.

l = 355.1287° and b = +14.2494°. To remove the source and surrounding area, a radius of 0.77 arcmin was employed.

The third strongest source (XMM J164124-243909) in the filed was not previously detected by any other astrophysical observation. The registered flux for this source was $1.2 \pm 0.6 \times 10^{-13}$ cgs (erg $cm^{-2}s^{-1}$). The source position in galactic coordinates is l = 355.1549° and b = +14.1483°. In this case a radius of 0.74 arcmin was used to extract the source and neighbourhood.

C.4 Abundance Tables

Table C.3: Abundance tables used in XSPEC and the relative difference between the two tables in %. The Angr table has higher abundances.

Atomic Number	Atomic Mass	Element	Angr[a]	Wilms[b]	Δ%
1	1	H	1.0	1.0	0
2	4	He	9.77×10^{-2}	9.77×10^{-2}	0
6	12	C[c]	3.63×10^{-4}	2.40×10^{-4}	34.07
7	14	N[d]	1.12×10^{-4}	7.59×10^{-5}	32.23
8	16	O	8.51×10^{-4}	4.90×10^{-4}	42.43
10	20	Ne	1.23×10^{-4}	8.71×10^{-5}	29.19
11	22	Na	2.14×10^{-6}	1.45×10^{-6}	32.24
12	24	Mg	3.80×10^{-5}	2.51×10^{-5}	33.95
13	26	Al	2.95×10^{-6}	2.14×10^{-6}	27.46
14	28	Si	3.55×10^{-5}	1.86×10^{-5}	47.61
16	32	S	1.62×10^{-5}	1.23×10^{-5}	24.07
17	34	Cl	1.88×10^{-7}	1.32×10^{-7}	29.79
18	36	Ar	3.63×10^{-6}	2.57×10^{-6}	29.20
20	40	Ca	2.29×10^{-6}	1.58×10^{-6}	31.00
24	48	Cr	4.84×10^{-7}	3.23×10^{-7}	33.26
26	52	Fe	4.68×10^{-5}	2.69×10^{-5}	42.53
27	54	Co	8.60×10^{-8}	8.32×10^{-8}	03.26
28	56	Ni	1.78×10^{-6}	1.12×10^{-6}	37.08

[a] Anders & Grevesse (1989)
[b] Wilms, Allen & McCray (2000)
[c] Updated value is 3.93×10^{-4}, Grevesse et al. (1991).
[d] Updated value is 9.34×10^{-5}, Grevesse & Noels (1993).

Appendix D

Contour Plots Ophiuchus Results

In this appendix the contour levels derived from the best model fits to the x-ray data calculated with the XSPEC package are presented. As discussed in chapter 4, § 4.11 the number of free model parameters was reduced to four. The four parameters are the Local Bubble (LB) temperature and emission measure (EM), and the Loop I temperature and EM, respectively. The default contour levels produced by the XSPEC package for a plasma, are the temperature in keV and the normalization factor (K). These parameters where mapped into a temperature given in Kelvin, and into an EM given in units of cm^{-6} pc.

To map the normalization factor K into an EM, the following expression was used:

$$EM \equiv n_e^2 \, D_{pc} = 4.072 \times 10^{-4} \, K_{plasma} \, \Omega^{-1} \quad [cm^{-6} \text{ pc}] \tag{D.1}$$

where Ω is the solid angle. The definition given in the XSPEC manual for the plasma normalization K is,

$$K_{plasma} = \frac{1}{4\pi \ 10^{14}} \frac{\int n_e n_H dV}{(D(1+z))^2} = \frac{1}{4\pi \ 10^{14}} \frac{\int n_e^2 dV}{D^2} = \frac{1}{4\pi \ 10^{14}} \frac{n_e^2 AD}{D^2} \tag{D.2}$$

assuming that $n_H = n_e$[1] and for a local plasma means, that the redshift (z) is 0.

$$K_{plasma} = \frac{n_e^2 \ \Omega \ D}{4\pi \ 10^{14}} \tag{D.3}$$

where Ω is defined as $\Omega = \pi \ (r/D)^2 = A/D^2$. Transforming the distance units from cm to pc we get,

$$K_{plasma} = 2.456 \times 10^3 \ n_e^2 \ \Omega \ D_{pc} \tag{D.4}$$

So we arrive at the first expression:

$$n_e^2 \ D_{pc} = 4.072 \times 10^{-4} \ K_{plasma} \Omega^{-1} \tag{D.5}$$

[1] It is also frequently assumed that $n_e \approx 1.2 \ n_H$ or $n_H \approx n_e/1.2$.

To map these physical parameters, an algorithm was written in Interactive Data Language (IDL) using the CONTOUR routine to plot the contour levels obtained from the XSPEC **steppar** command.

The contour levels are calculated by finding the pair of temperature and EM values at which its χ^2 distance to the $\chi^2_{\rm min}$ equals 68.3%, 90% and 99% levels, also known as confidence levels, in the χ^2-space. More formally, we find the χ^2 using the following expression

$$\chi^2 = \chi^2_{\rm min} + \Delta\chi^2 \tag{D.6}$$

where $\Delta\chi^2$ is chosen, in order to attain the desired contour level. For a four parameters model the $\Delta\chi^2$s to be used are 4.7, 7.8 and 13.3, for a 68.3%, 90.0% and 99.0% confidence level, respectively. In table D.1 we present a list of the $\Delta\chi^2$, from 1 to 20 free model parameters, and given for a set of 5 confidence levels.

D.1 Confidence Levels from Set A

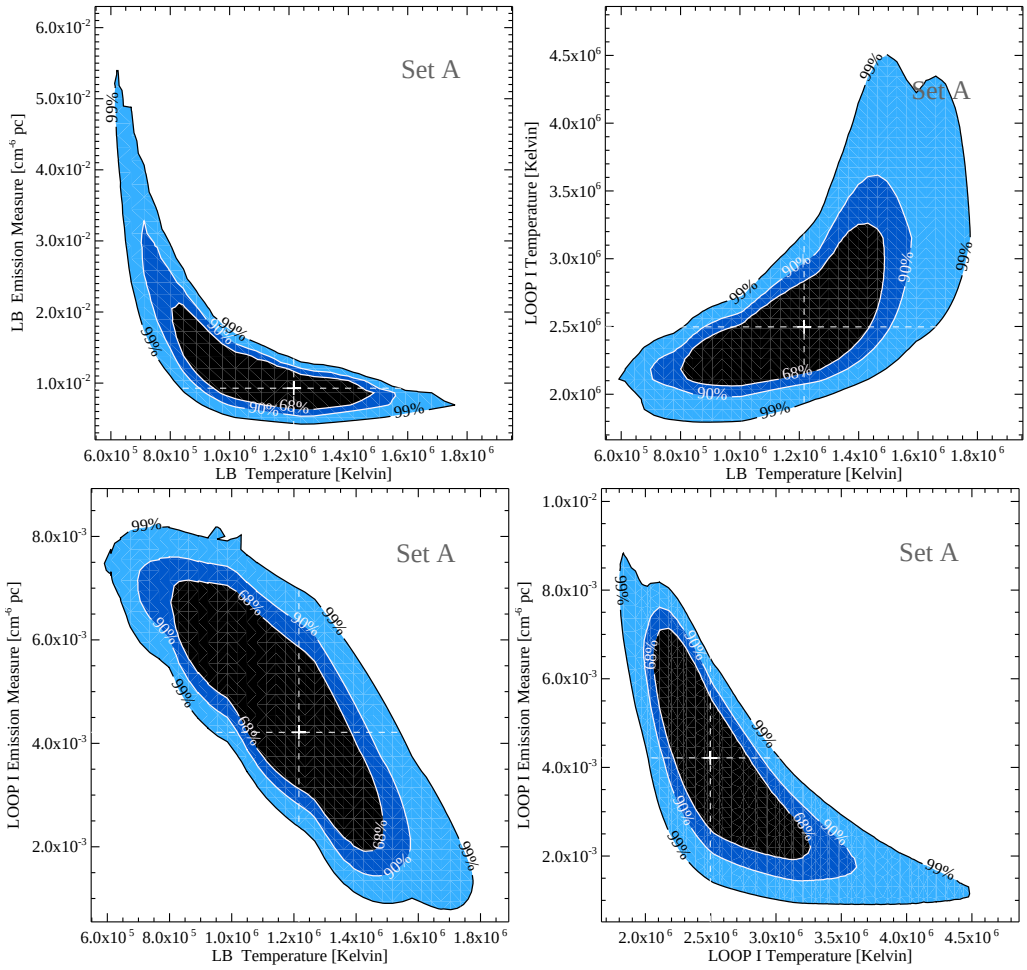

Figure D.1: Contour Levels from Set A.

D.2 Confidence Levels from Set B

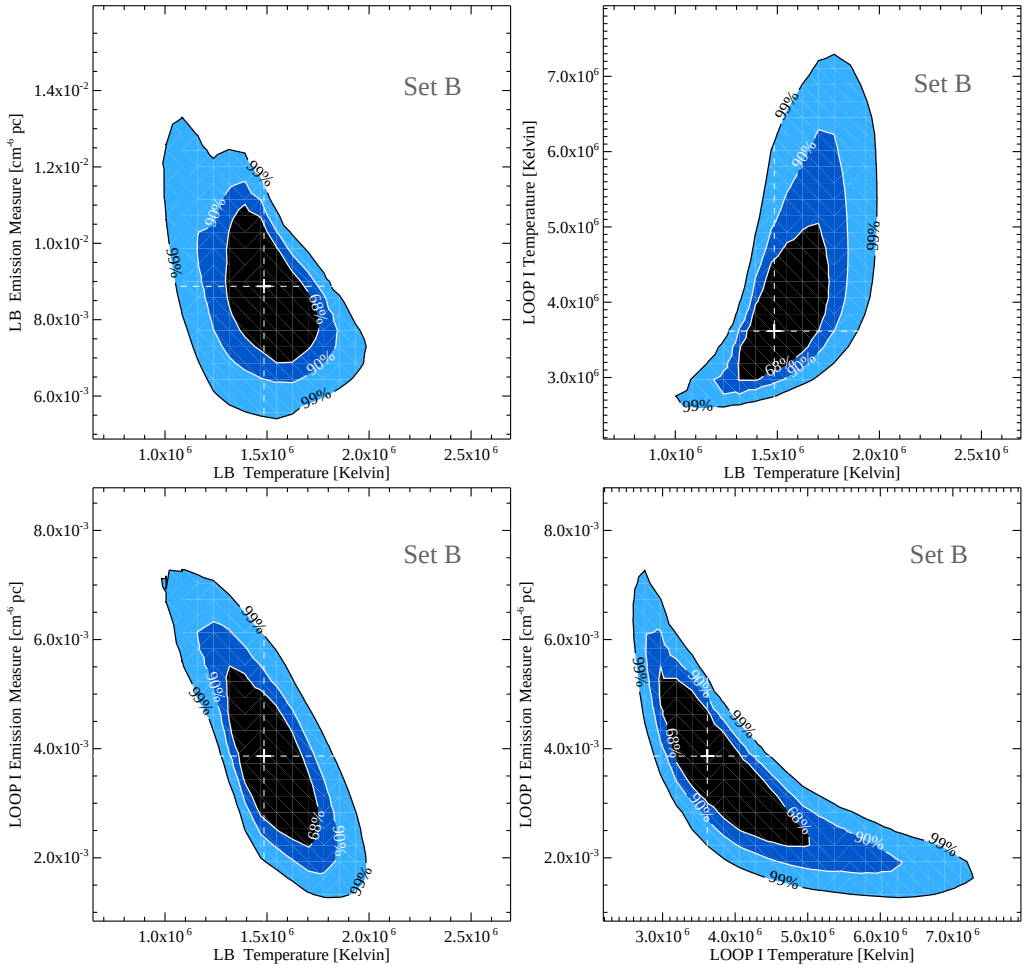

FIGURE D.2: Contour Levels from Set B.

D.3 Confidence Levels from Set C

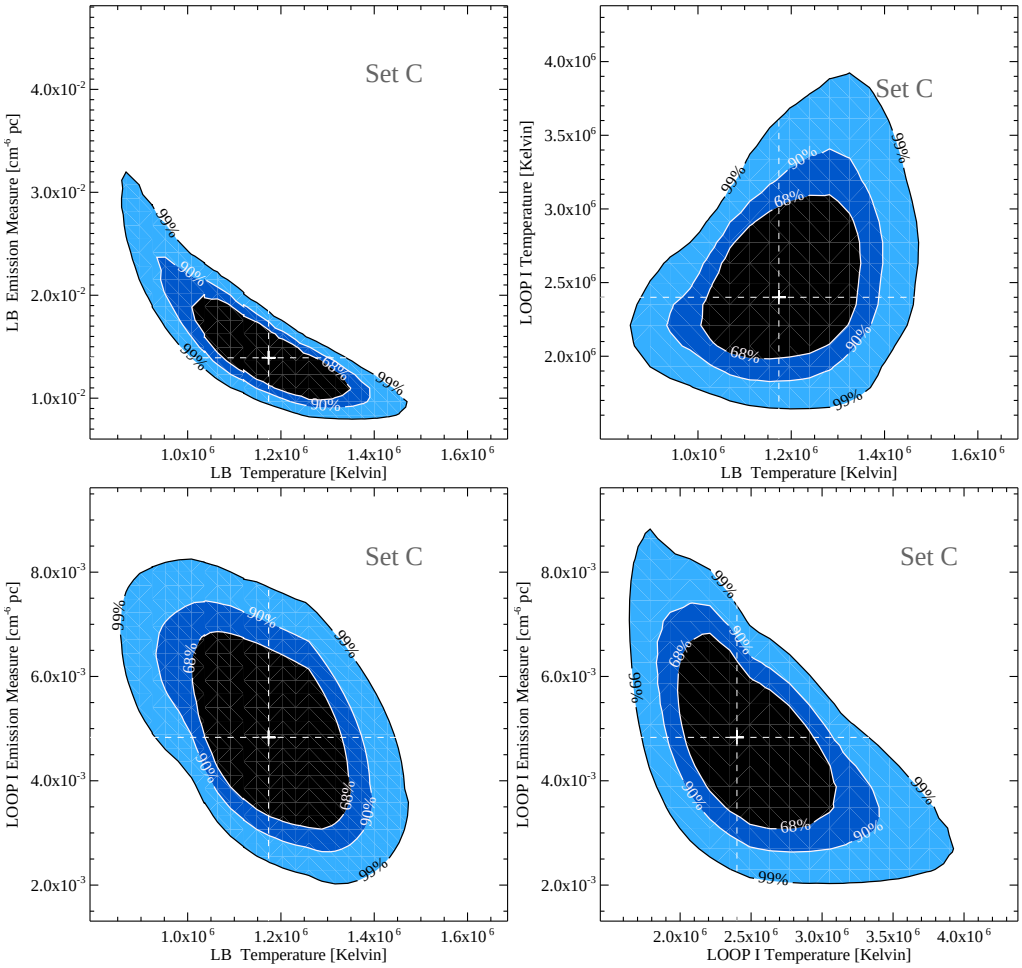

FIGURE D.3: Contour Levels from Set C.

D.4 Confidence Levels from Set D

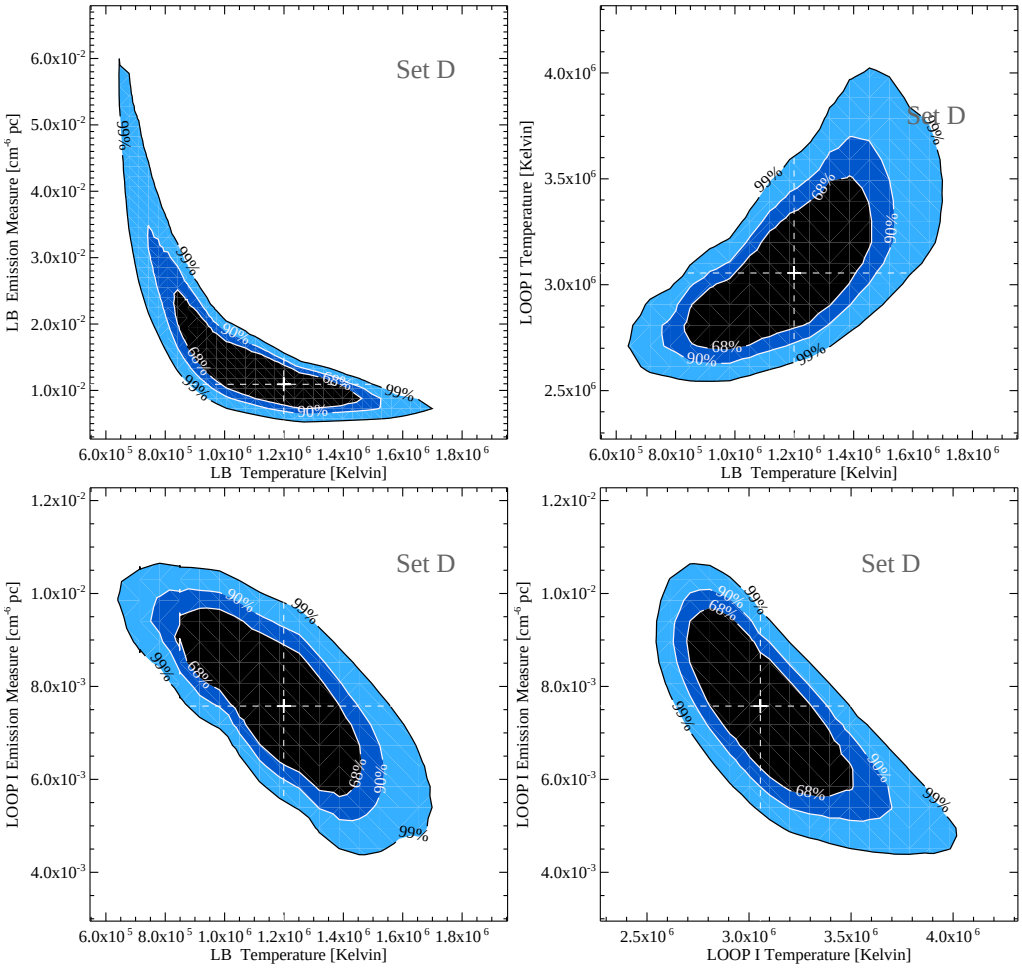

FIGURE D.4: Contour Levels from Set D.

D.5 Confidence Levels from Set E

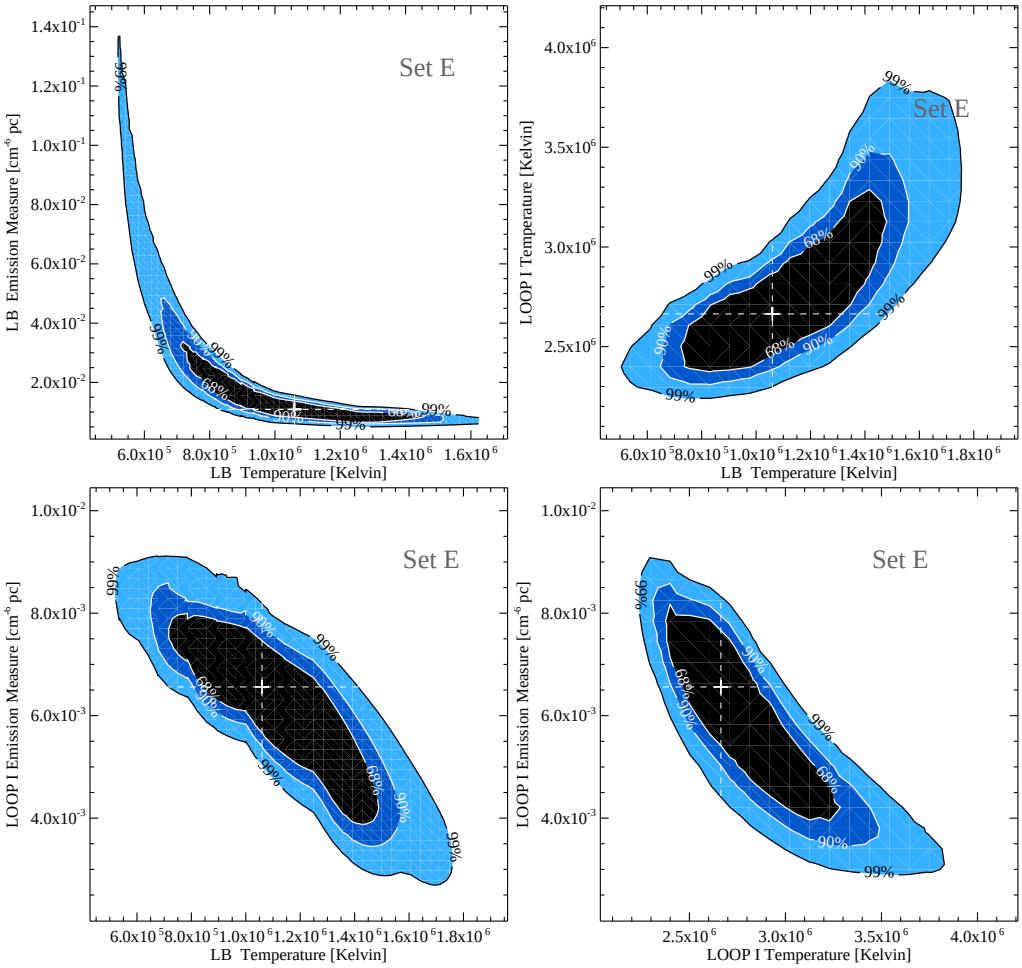

FIGURE D.5: Contour Levels from Set E.

D.6 Confidence Levels from Set F

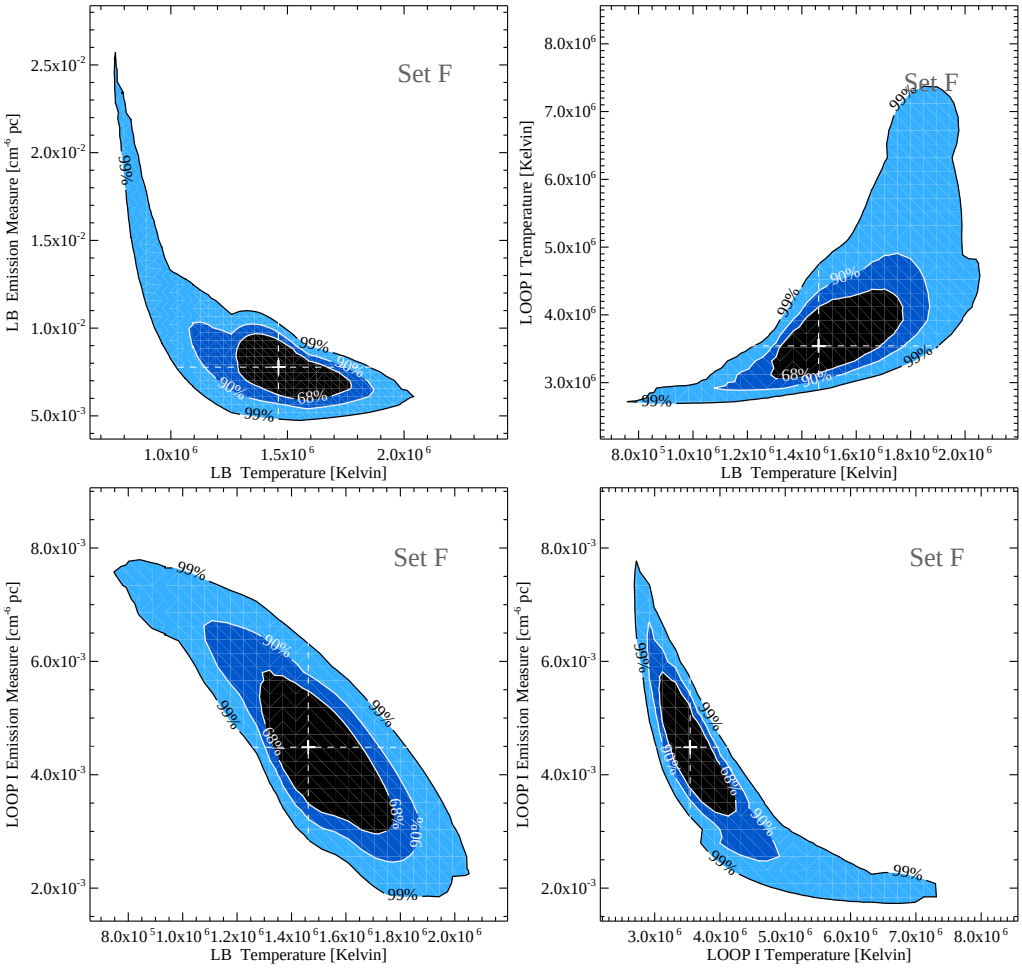

FIGURE D.6: Contour Levels from Set F.

D.7 Confidence Levels from Set G

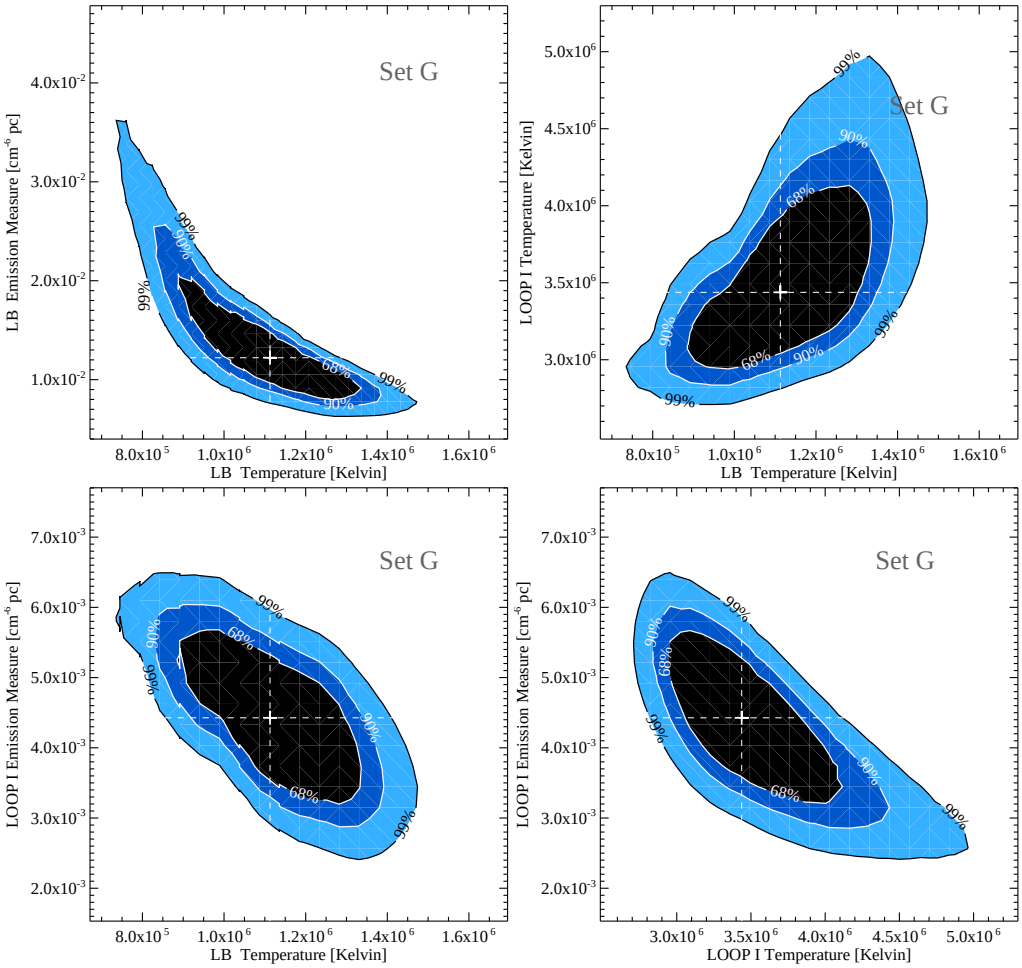

FIGURE D.7: Contour Levels from Set G.

D.8 Confidence Levels from Set H

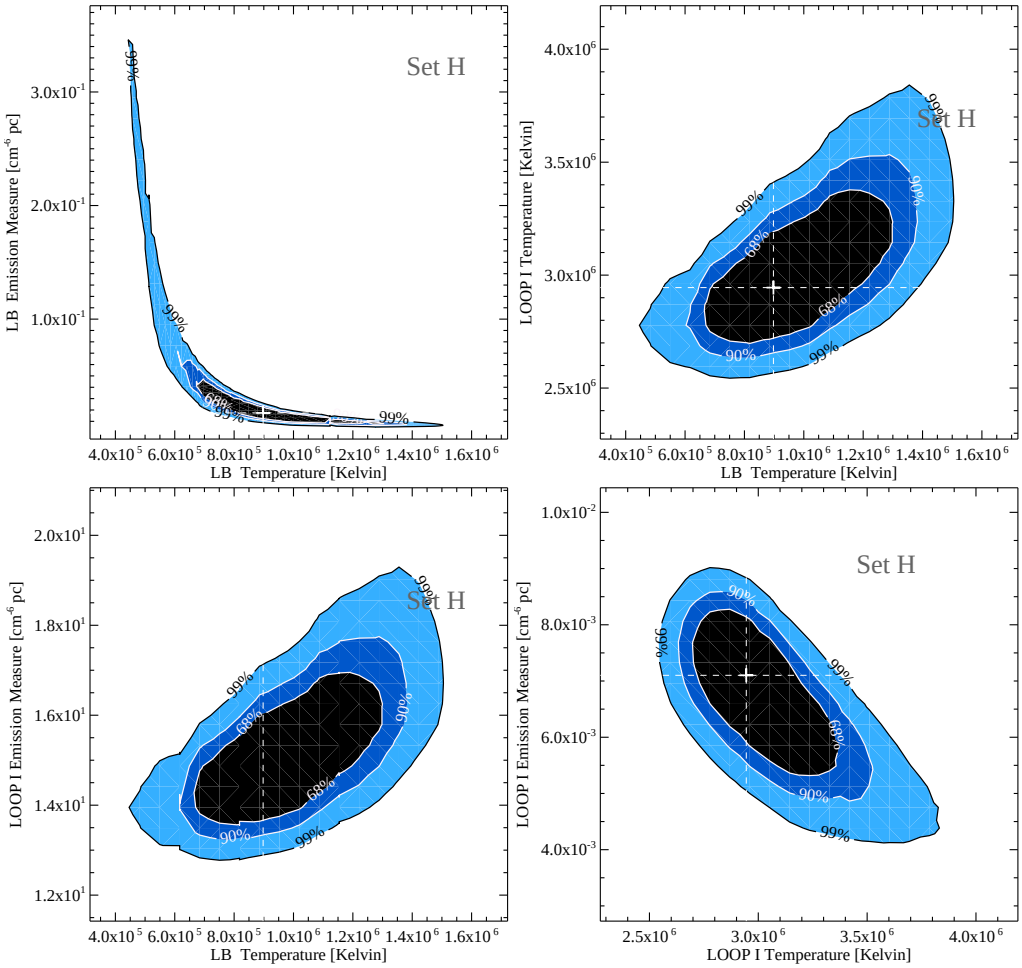

FIGURE D.8: Contour Levels from Set H.

D.9 Confidence Levels from Set I

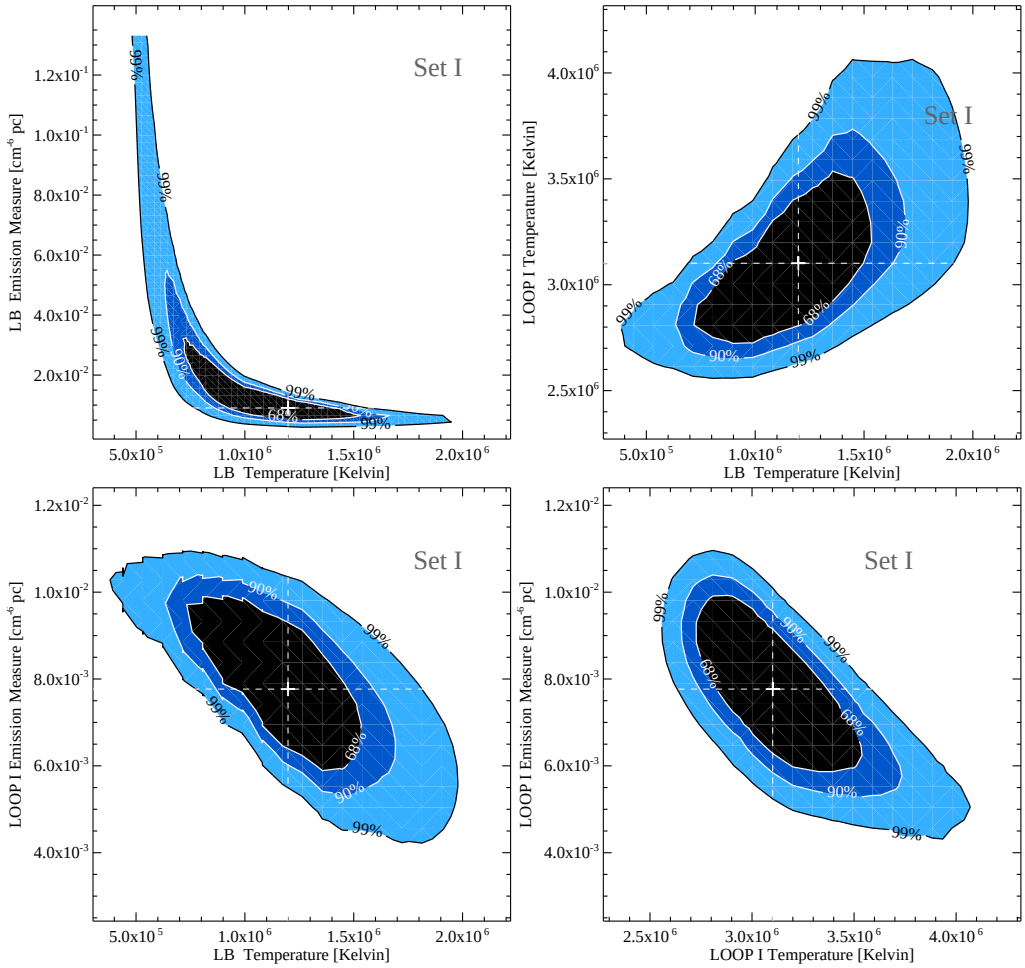

FIGURE D.9: Contour Levels from Set I.

D.10 The χ^2 Distribution

The tabulated function is the inverse cumulative distribution function of a Chi-squared distribution, having ν degrees of freedom.

TABLE D.1: The χ^2 Confidence Levels Table. The table shows the hypercontours which encloses the probability of simultaneously observing 1 to 20 free model parameters.

$\Delta\chi^2$ Confidence Levels Table					
d.o.f.	68.3% CL	90.0% CL	95.0% CL	99.0% CL	99.9% CL
1	1.000	2.706	3.841	6.635	10.828
2	2.279	4.605	5.991	9.210	13.816
3	3.506	6.251	7.815	11.340	16.266
4	4.695	7.779	9.488	13.280	18.467
5	5.861	9.236	11.070	15.090	20.515
6	7.009	10.640	12.592	16.810	22.458
7	8.145	12.020	14.067	18.480	24.322
8	9.270	13.360	15.507	20.090	26.124
9	10.390	14.680	16.919	21.670	27.877
10	11.500	15.990	18.307	23.210	29.588
11	12.600	17.280	19.675	24.720	31.264
12	13.700	18.550	21.026	26.220	32.909
13	14.800	19.810	22.362	27.690	34.528
14	15.890	21.060	23.685	29.140	36.123
15	16.980	22.310	24.996	30.580	37.697
16	18.070	23.540	26.296	32.000	39.252
17	19.150	24.770	27.587	33.410	40.790
18	20.230	25.990	28.869	34.810	42.312
19	21.310	27.200	30.144	36.190	43.820
20	22.380	28.410	31.410	37.570	45.315

Appendix E

Stars towards the Hyades cluster and Taurus fields

E.1 Stars towards the Hyades cluster and Taurus fields

Table E.1: Stars in directions of the Hyades cluster and Taurus fields. Shown in the table are the HD star number, the Galactic coordinates, the pre- and post-Hipparcos distances and the column densities. The column densities towards these stars were calculated using the information from the catalogue of Lallement et al. [118], Redfield and Linsky [250] and obtained from SIMBAD.

Star HD number	l_{II} deg	b_{II} deg	Pre-Hipparcos [pc]	log(NH) [cm^{-2}]
Hyades and Taurus star fields				
HD 29763	176.6450	−15.0720	123.0	19.95
HD 27236	184.1670	−27.9290	161.0	20.37
HD 26128	171.2140	−20.7480	245.0	21.17
HD 26571	172.4160	−20.5540	316.0	21.82
HD 26571	172.4200	−20.5500	316.5	21.82
λ Tau	178.3700	−29.3800	113.5	19.33
μ Tau	184.2100	−28.8500	133.3	20.87
HD 23763	166.6780	−23.1210	145.0	20.06
HD 23258	168.4740	−26.2640	75.0	18.96
HD 28929	170.7730	−12.5280	143.0	20.32
HD 35189	187.6810	−10.8160	137.0	20.31
HD 35909	190.9320	−11.4220	99.0	20.20
HD 23324	165.7050	−23.2640	113.0	20.29
HD 23432	166.0490	−23.3630	119.0	20.45
HD 23288	166.0390	−23.7290	103.0	20.43
HD 23441	166.0950	−23.3620	109.0	20.29
HD 23985	166.1040	−21.9340	59.0	17.72

continues on next page

continued from previous page

Star HD number	l_{II} deg	b_{II} deg	Pre-Hipparcos [pc]	log(NH) [cm^{-2}]
HD 23568	166.2730	−23.2240	150.0	20.64
HD 23642	166.5350	−23.3190	111.0	19.83
HD 24368	166.6090	−21.3590	147.0	21.31
HD 24118	166.6070	−22.0710	210.0	21.42
HD 23873	166.8090	−22.9630	125.0	20.57
HD 23632	166.8650	−23.6990	120.0	19.84
HD 23862	166.9570	−23.1690	119.0	20.31
HD 23850	167.0140	−23.2340	117.0	20.76
HD 23410	167.0650	−24.4210	103.0	20.62
HD 23964	167.3120	−23.2600	159.0	20.76
HD 23753	167.3320	−23.8260	104.0	20.63
HD 24076	167.3930	−23.0360	102.0	20.42
HD 23923	167.3690	−23.3980	117.0	20.83
HD 23913	168.2320	−24.2730	99.0	21.13
HD 23950	168.5020	−24.4390	99.0	20.99
HD 24899	168.6400	−21.7720	197.0	20.91
HD 23016	168.9960	−27.5080	125.0	21.13
HD 24769	169.0950	−22.6260	163.0	21.21
HD 25201	169.7620	−21.9800	332.0	21.21
HD 30836	192.8900	−23.5220	386.0	20.82
19 Tau	165.9800	−23.5500	114.3	20.73
20 Tau	166.1700	−23.5100	110.4	20.24
23 Tau	166.5700	−23.7500	110.1	19.92
17 Tau	166.1800	−23.8500	113.6	19.79
27 Tau	167.0100	−23.2300	116.7	20.41
eta Tau	166.6700	−23.4600	112.7	20.29
Taken from SIMBAD				
HD 28991	179.7456	−19.7087	101.3	21.35
HD 285844	178.9869	−19.8502	154.3	21.49
HD 29038	180.4166	−20.1259	124.1	21.89
CCDM J04335+1801AB	179.3408	−19.7551	129.7	20.64
CCDM J04298+1741AB	179.0238	−20.6619	206.2	21.02
HD 29023	179.2220	−19.2609	282.5	21.02
HD 27797	180.8048	−23.8121	235.3	21.94
* 73 Tau	180.9893	−23.1211	139.5	21.78
HD 28113	181.4161	−23.4205	126.3	21.53
HD 27789	181.2615	−24.2255	182.8	21.83
Hyades stars taken from Redfield and Linsky [250]				
HD 21847	156.2	−16.6	48.9	18.31
HD 26345	175.2	−23.6	43.1	18.23
HD 26784	182.4	−27.9	47.4	18.05
HD 27561	180.4	−24.3	51.4	18.14

continues on next page

continued from previous page

Star HD number	l_{II} deg	b_{II} deg	Pre-Hipparcos [pc]	log(NH) [cm^{-2}]
HD 27808	174.8	−19.1	40.9	18.23
HD 27848	178.6	−22.0	53.4	18.18
HD 28033	175.4	−18.9	46.4	18.23
HD 28205	180.4	−22.4	45.8	18.15
HD 28237	183.7	−24.7	47.2	18.07
HD 28406	178.8	−20.6	46.3	18.18
HD 28483	177.3	−19.2	50.2	18.21
HD 28568	180.5	−21.4	41.2	18.15
HD 28608	185.1	−24.7	43.6	18.06
HD 28736	190.2	−27.6	43.2	18.00
HD 29225	181.6	−20.5	43.5	18.14
HD 29419	176.0	−15.6	44.2	18.22
HD 30738	183.5	−17.6	51.8	18.13
HD 31845	185.1	−16.0	43.3	18.12

⋆

Appendix F

Contour Plots Hyades-Taurus Results

In this appendix the contour plots from the Hyades-Taurus x-ray spectral fit are presented. These contour plots were created using a grid of 50×50 points.

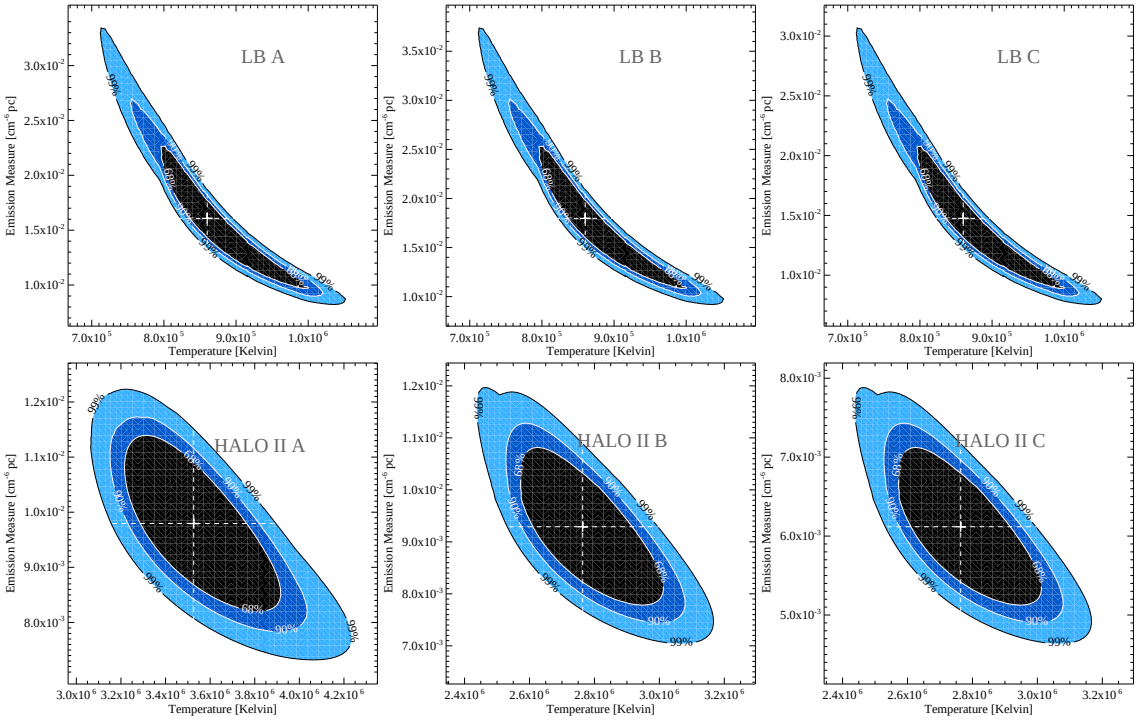

Figure F.1: Contour Levels from the Hyades-Taurus simultaneous fit.

Appendix G

The extinction map in the Galactic anticenter

In this appendix the extinction map in the Galactic anticenter direction, created by Froebrich et al. [251], is presented. These authors have produced an extinction map by using the (J-H) and (H-K) colour excess of stars in the Two-Micron All-Sky Survey (2MASS). This plate represents a sky field of 127°×63°, including the regions of Orion, Perseus, Taurus, Auriga, Monoceros, Camelopardalis and Cassiopeia.

The averaged extinctions (A_V) in each of these three XMM-Newton directions were determined to be 1.27, 4.22, and 1.07 mag in fields A, B and C, respectively. These A_V values can be converted into a column density (N_H) by using a conversion factor of 2.0×10^{21} mag^{-1} cm^{-2}. This conversion implies a N_H of 2.54×10^{21} cm^{-2}, 8.45×10^{21} cm^{-2}, and 2.15×10^{21} cm^{-2}.

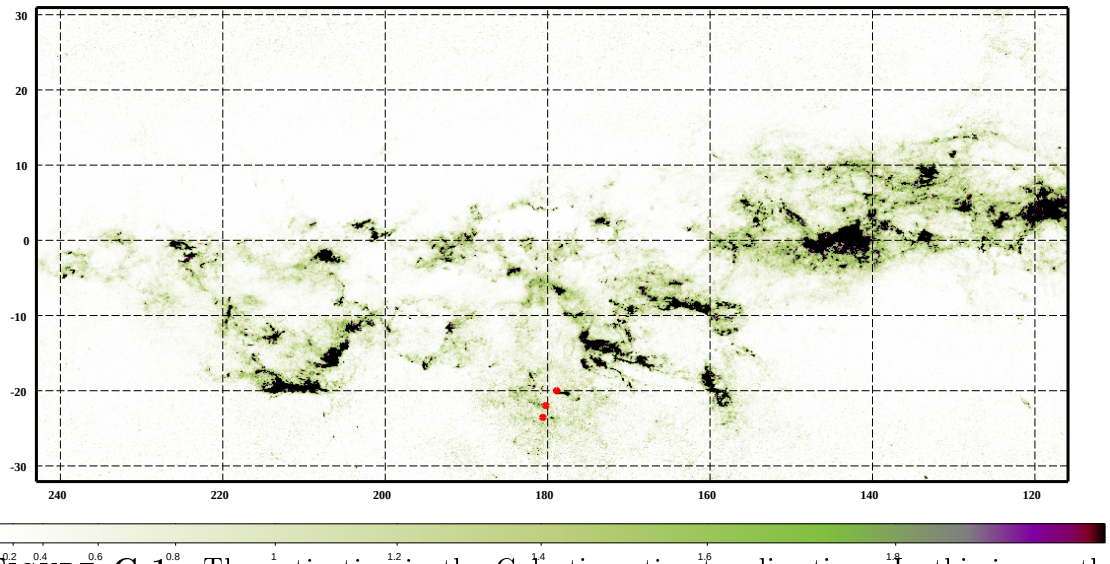

Figure G.1: The extinction in the Galactic anticenter direction. In this image the visual extinction A_V in the galactic anticenter due to Froebrich et al. [251] is presented. The plot was created using an inverted squared scale in the interval of 0 to 2 A_V. The red circles show the three XMM-Newton pointings used in this work.

If instead, the dust emissivity, most readily seen at 100 μm [263], had been used to estimate the N_H towards the three pointings, then an A_V of 0.994, 2.132 and 1.009 mag would have been found for A, B and C fields, respectively. The former values were calculated by first finding the average of the 100 μm emissivity, in each XMM-Newton observation, on a circle of radius of 12.5 arcmin, which were then converted into a column density using the extinction relation $A_V = 0.06\ I_{100\ \mu m}$ MJy^{-1} sr mag [264]. With a conversion factor of 2×10^{21} mag^{-1} cm^{-2}, the A_V are transformed into column densities of $1.99{\times}10^{21}$ cm^{-2}, $4.26{\times}10^{21}$ cm^{-2} and $2.02{\times}10^{21}$ cm^{-2}, respectively.

Bibliography

[1] W. B. Burton, B. G. Elmegreen, and R. Genzel, editors. *The galactic interstellar medium*, 1992. Springer-Verlag, 412 p.

[2] B. W. Carroll and D. A. Ostlie. *An Introduction to Modern Astrophysics*. Reading, Mass. : Addison-Wesley Pub., 1996.

[3] F. Zwicky. Die Rotverschiebung von extragalaktischen Nebeln. *Helvetica Physica Acta*, 6:110–127, 1933.

[4] D. Clowe, M. Bradač, A. H. Gonzalez, M. Markevitch, S. W. Randall, C. Jones, and D. Zaritsky. A Direct Empirical Proof of the Existence of Dark Matter. *ApJ*, 648:L109–L113, September 2006. doi: 10.1086/508162.

[5] J. R. Brownstein and J. W. Moffat. The Bullet Cluster 1E0657-558 evidence shows modified gravity in the absence of dark matter. *MNRAS*, 382:29–47, November 2007. doi: 10.1111/j.1365-2966.2007.12275.x.

[6] J. Hartmann. Investigations on the spectrum and orbit of delta Orionis. Translated from **Sitzb. Kgl. Akad. Wiss.** *(Translated from Sitzb. Kgl. Akad. Wiss.)*, *ApJ*, 19:268–286, May 1904. doi: 10.1086/141112.

[7] J. S. Plaskett and J. A. Pearce. The radial velocities of 523 O and B type stars obtained at Victoria, 1 923-1929. *Publications of the Dominion Astrophysical Observatory Victoria*, 5:1–98, 1931.

[8] M. A. Dopita and R. S. Sutherland. *Astrophysics of the diffuse universe*. Astrophysics of the diffuse universe, Berlin, New York: Springer, 2003. Astronomy and astrophysics library, ISBN 3540433627, 2003.

[9] K. M. Ferrière. The interstellar environment of our galaxy. *Reviews of Modern Physics*, 73:1031–1066, October 2001.

[10] J. Bland-Hawthorn, R. Reynolds, and P. Murdin. Gas in Galaxies. *Encyclopedia of Astronomy and Astrophysics*, November 2000. doi: 10.1888/0333750888/2636.

[11] H. Scheffler and H. Elsaesser. *Physics of the galaxy and interstellar matter*. Berlin and New York, Springer-Verlag, 1987, 503 pages. Translation., 1987.

[12] B. P. Wakker. A FUSE Survey of High-Latitude Galactic Molecular Hydrogen. *ApJS*, 163:282–305, April 2006. doi: 10.1086/500365.

[13] F. J. Lockman. The H I halo in the inner galaxy. *ApJ*, 283:90–97, August 1984. doi: 10.1086/162277.

[14] P. M. W. Kalberla, G. Westphalen, U. Mebold, D. Hartmann, and W. B. Burton. HI in the galactic halo. *A&A*, 332:L61–L64, April 1998.

[15] D. J. Hollenbach and A. G. G. M. Tielens. Dense Photodissociation Regions (PDRs). *ARA&A*, 35:179–216, 1997. doi: 10.1146/annurev.astro.35.1.179.

[16] B. Strömgren. The Physical State of Interstellar Hydrogen. *ApJ*, 89:526, May 1939.

[17] R. J. Reynolds. Ionized disk/halo gas - Insight from optical emission lines and pulsar dispersion measures. In H. Bloemen, editor, *The Interstellar Disk-Halo Connection in Galaxies*, volume 144 of *IAU Symposium*, pages 67–76, 1991.

[18] R. J. Reynolds. The Warm Ionized Medium. In S. S. Holt and F. Verter, editors, *Back to the Galaxy*, volume 278 of *American Institute of Physics Conference Series*, page 156, 1993.

[19] F. Hoyle and G. R. A. Ellis. On the Existence of an Ionized Layer about the Galactic Plane. *Australian Journal of Physics*, 16:1–+, March 1963.

[20] R. J. Reynolds. The optical emission-line background and accompanying emissions at ultraviolet, infrared, and millimeter wavelengths. *ApJ*, 392:L35–L38, June 1992. doi: 10.1086/186419.

[21] R. J. Reynolds. High spatial and spectral resolution pictures of the faint galactic H alpha background. *ApJ*, 236:153–159, February 1980. doi: 10.1086/157728.

[22] J. H. Dennison, B. Simonetti and G. A. Topasna. The Virginia Tech H-alpha and [SII] Imaging Survey of the Northern Sky. *Bulletin of the American Astronomical Society*, 31:1455–+, December 1999.

[23] J. E. Gaustad, P. R. McCullough, W. Rosing, and D. Van Buren. A Robotic Wide-Angle Hα Survey of the Southern Sky. *PASP*, 113:1326–1348, November 2001.

[24] R. J. Reynolds, L. M. Haffner, and G. J. Madsen. Three-Dimensional Studies of the Warm Ionized Medium in the Milky Way using WHAM (Invited Talk). In M. Rosada, L. Binette, and L. Arias, editors, *ASP Conf. Ser. 282: Galaxies: the Third Dimension*, pages 31–+, January 2002.

[25] D. P. Finkbeiner. A Full-Sky Hα Template for Microwave Foreground Prediction. *ApJS*, 146:407–415, June 2003. doi: 10.1086/374411.

[26] C. S. Bowyer, G. B. Field, and J. F. Mack. Detection of an Anisotropic Soft X-Ray Background Flux. *Nature*, 217:32–+, 1968.

[27] H. Inoue, K. Koyama, M. Matsuoka, T. Ohashi, Y. Tanaka, and H. Tsunemi. Evidence of O VII emission line in diffuse soft X-rays from the N_H minimum region in Hercules. *ApJ*, 227:L85–L88, January 1979. doi: 10.1086/182872.

[28] H. W. Schnopper, J. P. Delvaille, R. Rocchia, C. Blondel, C. Cheron, J. C. Christy, R. Ducros, L. Koch, and R. Rothenflug. Carbon and oxygen X-ray line emission from the interstellar medium. *ApJ*, 253: 131–135, February 1982. doi: 10.1086/159617.

[29] W. T. Sanders, R. J. Edgar, D. A. Liedahl, and J. P. Morgenthaler. The Soft X-ray Background Spectrum from DXS. *LNP Vol. 506: IAU Colloq. 166: The Local Bubble and Beyond*, 506:83–90, 1998.

[30] J. Trümper. The ROSAT mission. *Advances in Space Research*, 2:241–249, 1982. doi: 10.1016/0273-1177(82)90070-9.

[31] D. N. Burrows and J. A. Mendenhall. Soft X-ray shadowing by the Draco cloud. *Nature*, 351:629–631, June 1991.

[32] S. L. Snowden, U. Mebold, W. Hirth, U. Herbstmeier, and J. H. M. Schmitt. ROSAT detection of an X-ray shadow in the 1/4-keV diffuse background in the Draco nebula. *Science*, 252:1529–1532, June 1991.

[33] B. D. Savage, K. R. Sembach, E. B. Jenkins, J. M. Shull, D. G. York, G. Sonneborn, H. W. Moos, S. D. Friedman, J. C. Green, W. R. Oegerle, W. P. Blair, J. W. Kruk, and E. M. Murphy. Far Ultraviolet Spectroscopic Explorer Observations of O VI Absorption in the Galactic Halo. *ApJ*, 538:L27–L30, July 2000. doi: 10.1086/312792.

[34] B. D. Savage, B. P. Wakker, K. R. Sembach, P. Richter, and M. Meade. O VI in the Gaseous Galactic Halo. In R. Braun, editor, *Extra-Planar Gas*, volume 331 of *Astronomical Society of the Pacific Conference Series*, pages 3–+, June 2005.

[35] J. M. Shull and J. D. Slavin. Highly ionized gas in the Galactic halo. *ApJ*, 427: 784–792, June 1994. doi: 10.1086/174185.

[36] M. Ito and S. Ikeuchi. Ionization structure of the gaseous halo in our Galaxy. *PASJ*, 40:403–411, 1988.

[37] D. V. Bowen, E. B. Jenkins, T. M. Tripp, K. R. Sembach, and B. D. Savage. The FUSE Survey of O VI Absorption in the Galactic Disk. In G. Sonneborn, H. W. Moos, and B.-G. Andersson, editors, *Astrophysics in the Far Ultraviolet: Five*

Years of Discovery with FUSE, volume 348 of *Astronomical Society of the Pacific Conference Series*, pages 412–+, June 2006.

[38] B. D. Savage, K. R. Sembach, B. P. Wakker, P. Richter, M. Meade, E. B. Jenkins, J. M. Shull, H. W. Moos, and G. Sonneborn. Distribution and Kinematics of O VI in the Galactic Halo. *ApJS*, 146:125–164, May 2003. doi: 10.1086/346229.

[39] L. J. Spitzer. On a Possible Interstellar Galactic Corona. *ApJ*, 124:20–+, July 1956.

[40] G. B. Field, D. W. Goldsmith, and H. J. Habing. Cosmic-Ray Heating of the Interstellar Gas. *ApJ*, 155:L149+, March 1969.

[41] P. Burstein, R. J. Borken, W. L. Kraushaar, and W. T. Sanders. Three-band observations of the soft X-ray background and some implications of thermal emission models. *ApJ*, 213:405–407, April 1977.

[42] E. B. Jenkins and D. A. Meloy. A survey with Copernicus of interstellar O VI absorption. *ApJ*, 193:L121–L125, November 1974.

[43] D. G. York. Highly ionized atoms observed with Copernicus. *ApJ*, 193:L127–L131, November 1974.

[44] D. G. York. On the temperature and the interstellar nature of coronal gas observed by Copernicus. *ApJ*, 213:43–51, April 1977.

[45] B. E. Woodgate, H. S. Stockman, J. R. P. Angel, and R. P. Kirshner. Detection of the [Fe XIV] Coronal Line at 5303 Å in the Cygnus Loop. *ApJ*, 188:L79+, March 1974.

[46] C. F. McKee and J. P. Ostriker. A theory of the interstellar medium - Three components regulated by supernova explosions in an inhomogeneous substrate. *ApJ*, 218:148–169, November 1977.

[47] D. P. Cox and B. W. Smith. Large-Scale Effects of Supernova Remnants on the Galaxy: Generation and Maintenance of a Hot Network of Tunnels. *ApJ*, 189:L105+, May 1974.

[48] J. D. Slavin and D. P. Cox. Evolution of Supernova Remnant Bubbles in a Warm Diffuse Medium: Survey of Results from One-dimensional Models and Their Impact on Estimates of Interstellar Porosity. *ApJ*, 417:187–+, November 1993. doi: 10.1086/173302.

[49] M. A. de Avillez and D. Breitschwerdt. Volume filling factors of the ISM phases in star forming galaxies. I. The role of the disk-halo interaction. *A&A*, 425:899–911, October 2004. doi: 10.1051/0004-6361:200400025.

[50] M. A. de Avillez and D. Breitschwerdt. Global dynamical evolution of the ISM in star forming galaxies. I. High resolution 3D simulations: Effect of the magnetic field. *A&A*, 436:585–600, June 2005. doi: 10.1051/0004-6361:20042146.

[51] N. Panagia. Some Physical parameters of early-type stars. *AJ*, 78:929–934, November 1973.

[52] A. Sternberg, T. L. Hoffmann, and A. W. A. Pauldrach. Ionizing Photon Emission Rates from O- and Early B-Type Stars and Clusters. *ApJ*, 599:1333–1343, December 2003. doi: 10.1086/379506.

[53] N. Smith. A census of the Carina Nebula - I. Cumulative energy input from massive stars. *MNRAS*, 367:763–772, April 2006. doi: 10.1111/j.1365-2966.2006.10007.x.

[54] R. A. Chevalier. Supernova Remnants in Molecular Clouds. *ApJ*, 511:798–811, February 1999. doi: 10.1086/306710.

[55] D. C. Abbott. The return of mass and energy to the interstellar medium by winds from early-type stars. *ApJ*, 263:723–735, December 1982. doi: 10.1086/160544.

[56] R.-P. Kudritzki and J. Puls. Winds from Hot Stars. *ARA&A*, 38:613–666, 2000. doi: 10.1146/annurev.astro.38.1.613.

[57] J. E. Dyson and J. de Vries. The Dynamical Effects of Stellar Mass Loss on Diffuse Nebulae. *A&A*, 20:223–+, August 1972.

[58] J. Castor, R. McCray, and R. Weaver. Interstellar bubbles. *ApJ*, 200:L107–L110, September 1975.

[59] R. Weaver, R. McCray, J. Castor, P. Shapiro, and R. Moore. Interstellar bubbles. II - Structure and evolution. *ApJ*, 218:377–395, December 1977.

[60] L. L. Cowie, C. F. McKee, and J. P. Ostriker. Supernova remnant revolution in an inhomogeneous medium. I - Numerical models. *ApJ*, 247:908–924, August 1981. doi: 10.1086/159100.

[61] L. Woltjer. Supernova Remnants. *ARA&A*, 10:129–+, 1972. doi: 10.1146/annurev.aa.10.090172.001021.

[62] D. C. Ellison, D. J. Patnaude, P. Slane, P. Blasi, and S. Gabici. Particle Acceleration in Supernova Remnants and the Production of Thermal and Nonthermal Radiation. *ApJ*, 661:879–891, June 2007. doi: 10.1086/517518.

[63] L. I. Sedov. *Similarity and Dimensional Methods in Mechanics*. Similarity and Dimensional Methods in Mechanics, New York: Academic Press, 1959.

[64] D. P. Cox. Cooling and Evolution of a Supernova Remnant. *ApJ*, 178:159–168, November 1972.

[65] R. A. Chevalier. The Evolution of Supernova Remnants. Spherically Symmetric Models. *ApJ*, 188:501–516, March 1974.

[66] S. A. E. G. Falle. Catastrophic cooling in supernova remnants. *MNRAS*, 195:1011–1028, June 1981.

[67] L. J. Spitzer. Theories of the hot interstellar gas. *ARA&A*, 28:71–101, 1990. doi: 10.1146/annurev.aa.28.090190.000443.

[68] D. P. Cox. The Three-Phase Interstellar Medium Revisited. *ARA&A*, 43:337–385, September 2005.

[69] J. C. Houck and J. N. Bregman. Low-temperature Galactic fountains. *ApJ*, 352:506–521, April 1990. doi: 10.1086/168554.

[70] J. Lequeux. *The interstellar medium*. The interstellar medium, Translation from the French language edition of: Le Milieu Interstellaire by James Lequeux, EDP Sciences, 2003 Edited by J. Lequeux. Astronomy and astrophysics library, Berlin: Springer, 2005.

[71] C. Heiles. H I shells and supershells. *ApJ*, 229:533–537, April 1979. doi: 10.1086/156986.

[72] R. McCray and T. P. Snow. The violent interstellar medium. *ARA&A*, 17:213–240, 1979. doi: 10.1146/annurev.aa.17.090179.001241.

[73] K. Tomisaka, A. Habe, and S. Ikeuchi. Sequential explosions of supernovae in an OB association and formation of a superbubble. *Ap&SS*, 78:273–285, August 1981.

[74] R. McCray and M. Kafatos. Supershells and propagating star formation. *ApJ*, 317:190–196, June 1987. doi: 10.1086/165267.

[75] S. Ikeuchi. Fundamental Processes in the Interstellar Medium and Evolution of Galaxies. *Fundamentals of Cosmic Physics*, 12:255–327, 1988.

[76] C. A. Norman and S. Ikeuchi. The disk-halo interaction - Superbubbles and the structure of the interstellar medium. *ApJ*, 345:372–383, October 1989. doi: 10.1086/167912.

[77] K. Tomisaka. Fragmentation, contraction, and accretion in magnetized clouds. In B. Reipurth and C. Bertout, editors, *IAU Symp. 182: Herbig-Haro Flows and the Birth of Stars*, page 250, 1997.

[78] M. A. de Avillez and D. L. Berry. Three-dimensional evolution of worms and chimneys in the Galactic disc. *MNRAS*, 328:708–718, December 2001. doi: 10.1046/j.1365-8711.2001.04865.x.

[79] M. A. de Avillez and M.-M. Mac Low. Mushroom-shaped Structures as Tracers of Buoyant Flow in the Galactic Disk. *ApJ*, 551:L57–L61, April 2001. doi: 10.1086/319842.

[80] P. R. Shapiro and G. B. Field. Consequences of a New Hot Component of the Interstellar Medium. *ApJ*, 205:762–765, May 1976. doi: 10.1086/154332.

[81] F. O. Williamson, W. T. Sanders, W. L. Kraushaar, D. McCammon, R. Borken, and A. N. Bunner. Observation of features in the soft X-ray background flux. *ApJ*, 193:L133–L137, November 1974.

[82] C. A. Muller, J. H. Oort, and E. Raymond. Hydrogène neutre dans la couronne galactique? *Academie des Sciences Paris Comptes Rendus, Paris*, 257:1661–1662, 1963.

[83] J. N. Bregman. The galactic fountain of high-velocity clouds. *ApJ*, 236:577–591, March 1980. doi: 10.1086/157776.

[84] F. D. Kahn. *Dynamics of the galactic fountain*, pages 1–28. ASSL Vol. 91: Investigating the Universe, 1981.

[85] D. Breitschwerdt and S. Komossa. Galactic Fountains and Galactic Winds. *Ap&SS*, 272:3–13, 2000.

[86] A. Rosen, J. N. Bregman, and M. L. Norman. Hydrodynamical simulations of star-gas interactions in the interstellar medium with an external gravitational potential. *ApJ*, 413:137–149, August 1993. doi: 10.1086/172983.

[87] A. Rosen and J. N. Bregman. Global Models of the Interstellar Medium in Disk Galaxies. *ApJ*, 440:634–+, February 1995. doi: 10.1086/175303.

[88] M. A. de Avillez. The Evolution of Galactic Fountains. *Ph.D. Thesis, University of Évora, Portugal*, July 1997.

[89] S. Veilleux, G. Cecil, and J. Bland-Hawthorn. Galactic Winds. *ARA&A*, 43:769–826, September 2005.

[90] A. Habe and S. Ikeuchi. Dynamical Behavior of Gaseous Halo in a Disk Galaxy. *Progress of Theoretical Physics*, 64:1995–2008, December 1980.

[91] D. Breitschwerdt, H. J. Völk, and J. F. McKenzie. Galactic winds. I - Cosmic ray and wave-driven winds from the Galaxy. *A&A*, 245:79–98, May 1991.

[92] D. Breitschwerdt and T. Schmutzler. Delayed Recombination as a Major Source of the Soft X-Ray Background. *Nature*, 371:774–+, October 1994.

[93] D. Breitschwerdt and T. Schmutzler. The dynamical signature of the ISM in soft X-rays. I. Diffuse soft X-rays from galaxies. *A&A*, 347:650–668, July 1999.

[94] B.-C. Koo and C. F. McKee. Dynamics of Wind Bubbles and Superbubbles. II. Analytic Theory. *ApJ*, 388:103–+, March 1992. doi: 10.1086/171133.

[95] B.-C. Koo and C. F. McKee. Dynamics of wind bubbles and superbubbles. I - Slow winds and fast winds. II - Analytic theory. *ApJ*, 388:93–126, March 1992. doi: 10.1086/171132.

[96] H. Friedman, S. W. Lichtman, and E. T. Byram. Photon Counter Measurements of Solar X-Rays and Extreme Ultraviolet Light. *Physical Review*, 83:1025–1030, September 1951. doi: 10.1103/PhysRev.83.1025.

[97] R. Giacconi, H. Gursky, F. R. Paolini, and B. B. Rossi. Evidence for x Rays From Sources Outside the Solar System. *Physical Review Letters*, 9:439–443, December 1962. doi: 10.1103/PhysRevLett.9.439.

[98] R. J. Gould and G. R. Burbidge. X-Rays from the Galactic Center, External Galaxies, and the Intergalactic Medium. *ApJ*, 138:969–+, November 1963.

[99] R. C. Henry, G. Fritz, J. F. Meekins, H. Friedman, and E. T. Byram. Possible Detection of a Dense Intergalactic Plasma. *ApJ*, 153:L11+, July 1968.

[100] B. D. Savage and E. B. Jenkins. A Survey of Local Interstellar Hydrogen from OAO-2 Observations of Lyman Alpha Absorption. *ApJ*, 172:491–+, March 1972.

[101] E. B. Jenkins and B. D. Savage. Ultraviolet photometry from the orbiting astronomical observatory. XIV. an extension of the survey of Lyman-alf absorption from interstellar hydrogen. *ApJ*, 187:243–255, January 1974.

[102] Y. Tanaka and J. A. M. Bleeker. The diffuse soft X-ray sky - Astrophysics related to cosmic soft X-rays in the energy range 0.1-2.0 keV. *Space Science Reviews*, 20: 815–888, September 1977.

[103] W. T. Sanders, W. L. Kraushaar, J. A. Nousek, and P. M. Fried. Soft diffuse X-rays in the southern galactic hemisphere. *ApJ*, 217:L87–L91, October 1977.

[104] P. C. Frisch and D. G. York. Synthesis maps of ultraviolet observations of neutral interstellar gas. *ApJ*, 271:L59–L63, August 1983.

[105] F. Paresce. On the distribution of interstellar matter around the sun. *AJ*, 89:1022–1037, July 1984. doi: 10.1086/113598.

[106] J. J. Bloch, K. Jahoda, M. Juda, D. McCammon, W. T. Sanders, and S. L. Snowden. Observations of the soft X-ray diffuse background at 0.1 keV. *ApJ*, 308:L59–L62, September 1986. doi: 10.1086/184744.

[107] D. McCammon, D. N. Burrows, W. T. Sanders, and W. L. Kraushaar. The soft X-ray diffuse background. *ApJ*, 269:107–135, June 1983. doi: 10.1086/161024.

[108] D. P. Cox and R. J. Reynolds. The local interstellar medium. *ARA&A*, 25:303–344, 1987. doi: 10.1146/annurev.aa.25.090187.001511.

[109] D. McCammon and W. T. Sanders. The soft X-ray background and its origins. *ARA&A*, 28:657–688, 1990. doi: 10.1146/annurev.aa.28.090190.003301.

[110] S. L. Snowden, D. P. Cox, D. McCammon, and W. T. Sanders. A model for the distribution of material generating the soft X-ray background. *ApJ*, 354:211–219, May 1990.

[111] J. C. Raymond and B. W. Smith. Soft X-ray spectrum of a hot plasma. *ApJS*, 35: 419–439, December 1977.

[112] S. L. Snowden, G. Hasinger, K. Jahoda, F. J. Lockman, D. McCammon, and W. T. Sanders. Soft X-ray and H I surveys of the low N_H region in Ursa Major. *ApJ*, 430:601–609, August 1994. doi: 10.1086/174434.

[113] S. L. Snowden, M. J. Freyberg, P. P. Plucinsky, J. H. M. M. Schmitt, J. Trümper, W. Voges, R. J. Edgar, D. McCammon, and W. T. Sanders. First Maps of the Soft X-Ray Diffuse Background from the ROSAT XRT/PSPC All-Sky Survey. *ApJ*, 454:643–+, December 1995. doi: 10.1086/176517.

[114] A. Fruscione, I. Hawkins, P. Jelinsky, and A. Wiercigroch. The distribution of neutral hydrogen in the interstellar medium. 1: The data. *ApJS*, 94:127–146, August 1994. doi: 10.1086/192075.

[115] D. Breitschwerdt, R. Egger, M. J. Freyberg, P. C. Frisch, and J. V. Vallerga. The Local Bubble Origin and Evolution. *Space Science Reviews*, 78:183–198, October 1996.

[116] S. L. Snowden, R. Egger, D. P. Finkbeiner, M. J. Freyberg, and P. P. Plucinsky. Progress on Establishing the Spatial Distribution of Material Responsible for the 1/4 keV Soft X-Ray Diffuse Background Local and Halo Components. *ApJ*, 493: 715–+, January 1998. doi: 10.1086/305135.

[117] D. M. Sfeir, R. Lallement, F. Crifo, and B. Y. Welsh. Mapping the contours of the Local bubble: preliminary results. *A&A*, 346:785–797, June 1999.

[118] R. Lallement, B. Y. Welsh, J. L. Vergely, F. Crifo, and D. Sfeir. 3D mapping of the dense interstellar gas around the Local Bubble. *A&A*, 411:447–464, December 2003. doi: 10.1051/0004-6361:20031214.

[119] R. L. Branham, Jr. The Sun's Distance from the Galactic Plane. *Ap&SS*, 288: 417–419, December 2003. doi: 10.1023/B:ASTR.0000005097.18183.64.

[120] D. P. Cox and P. R. Anderson. Extended adiabatic blast waves and a model of the soft X-ray background. *ApJ*, 253:268–289, February 1982. doi: 10.1086/159632.

[121] H. Böhringer. Equilibrium Ionization and Non-Equilibrium Ionization Plasma Models. *LNP Vol. 506: IAU Colloq. 166:*

The Local Bubble and Beyond, 506:341–352, 1998.

[122] R. Mewe. Atomic Physics of Hot Plasmas. *LNP Vol. 520: X-Ray Spectroscopy in Astrophysics*, 520:109–+, 1999.

[123] T. R. Kallman and P. Palmeri. Atomic data for x-ray astrophysics. *Reviews of Modern Physics*, 79:79–133, January 2007. doi: 10.1103/RevModPhys.79.79.

[124] J. S. Kaastra. X-Ray Spectroscopic Observations with ASCA and BeppoSAX. In J. van Paradijs and J. A. M. Bleeker, editors, *X-Ray Spectroscopy in Astrophysics*, volume 520 of *Lecture Notes in Physics, Berlin Springer Verlag*, pages 269–+, 1999.

[125] S. Hayakawa. Galactic Latitude Dependence of the Diffuse Soft X-Ray Intensity. In *Bulletin of the American Astronomical Society*, volume 8 of *Bulletin of the American Astronomical Society*, pages 447–+, June 1976.

[126] D. E. Innes and T. W. Hartquist. Are we in an old superbubble? *MNRAS*, 209:7–13, July 1984.

[127] R. J. Edgar and D. P. Cox. Hot bubbles in a magnetic interstellar medium - Another look at the soft X-ray background. *ApJ*, 413:190–197, August 1993. doi: 10.1086/172987.

[128] D. Breitschwerdt. The Local Bubble Current state of observations and models. *Space Science Reviews*, 78:173–182, October 1996.

[129] S. Redfield. The Local Interstellar Medium. In S. J. Kannappan, S. Redfield, J. E. Kessler-Silacci, M. Landriau, and N. Drory, editors, *New Horizons in Astronomy: Frank N. Bash Symposium*, volume 352 of *Astronomical Society of the Pacific Conference Series*, pages 79–+, September 2006.

[130] D. Breitschwerdt. Self-consistent Modelling of the interstellar medium. *Ap&SS*, 289:489–498, February 2004. doi: 10.1023/B:ASTR.0000014982.31688.bf.

[131] M. Kafatos. Time-Dependent Radiative Cooling of a Hot Low-Density Cosmic Gas. *ApJ*, 182:433–448, June 1973.

[132] P. R. Shapiro and R. T. Moore. Time-dependent radiative cooling of a hot, diffuse cosmic gas, and the emergent X-ray spectrum. *ApJ*, 207:460–483, July 1976.

[133] T. Schmutzler and W. M. Tscharnuter. Effective radiative cooling in optically thin plasmas. *A&A*, 273:318–+, June 1993.

[134] S. N. Nahar. Electron-Ion Recombination Rate Coefficients, Photoionization Cross Sections, and Ionization Fractions for Astrophysically Abundant Elements. II. Oxygen Ions. *ApJS*, 120:131–145, January 1999. doi: 10.1086/313173.

[135] S. N. Nahar and A. K. Pradhan. Electron-Ion Recombination Rate Coefficients, Photoionization Cross Sections, and Ionization Fractions for Astrophysically Abundant Elements. I. Carbon and Nitrogen. *ApJS*, 111:339–+, July 1997. doi: 10.1086/313013.

[136] R. Mewe, E. H. B. M. Gronenschild, and G. H. J. van den Oord. Calculated X-radiation from optically thin plasmas. V. *A&AS*, 62:197–254, November 1985.

[137] J. S. Kaastra and R. Mewe. X-ray emission from thin plasmas. I - Multiple Auger ionisation and fluorescence processes for Be to Zn. *A&AS*, 97:443–482, January 1993.

[138] R. K. Smith, N. S. Brickhouse, D. A. Liedahl, and J. C. Raymond. Collisional Plasma Models with APEC/APED: Emission-Line Diagnostics of Hydrogen-like and Helium-like Ions. *ApJ*, 556:L91–L95, August 2001. doi: 10.1086/322992.

[139] B. D. Savage. UV absorption and emission lines from highly ionized gas in the Galactic halo. In H. Bloemen, editor, *The Interstellar Disk-Halo Connection in Galaxies*, volume 144 of *IAU Symposium*, pages 131–142, 1991.

[140] D. P. Cox. Hot gas in the disk, halo, and disk-halo interaction. In H. Bloemen, editor, *The Interstellar Disk-Halo Connec-*

tion in Galaxies, volume 144 of *IAU Symposium*, pages 143–148, 1991.

[141] D. Breitschwerdt and M. A. de Avillez. The history and future of the Local and Loop I bubbles. *A&A*, 452:L1–L5, June 2006. doi: 10.1051/0004-6361:20064989.

[142] E. Anders and N. Grevesse. Abundances of the elements - Meteoritic and solar. *Geochim. Cosmochim. Acta*, 53: 197–214, January 1989. doi: 10.1016/0016-7037(89)90286-X.

[143] R. Morrison and D. McCammon. Interstellar photoelectric absorption cross sections, 0.03-10 keV. *ApJ*, 270:119–122, July 1983. doi: 10.1086/161102.

[144] R. Lallement. On the contribution of charge-exchange induced X-ray emission in the ISM and ICM. *A&A*, 422:391–400, August 2004. doi: 10.1051/0004-6361:20035625.

[145] R. Lallement. The heliospheric soft X-ray emission pattern during the ROSAT survey: Inferences on Local Bubble hot gas. *A&A*, 418:143–150, April 2004. doi: 10.1051/0004-6361:20040059.

[146] C. M. Lisse, K. Dennerl, J. Englhauser, M. Harden, F. E. Marshall, M. J. Mumma, R. Petre, J. P. Pye, M. J. Ricketts, J. Schmitt, J. Trumper, and R. G. West. Discovery of X-ray and Extreme Ultraviolet Emission from Comet C/Hyakutake 1996 B2. *Science*, 274:205–209, October 1996.

[147] T. E. Cravens. Comet Hyakutake x-ray source: Charge transfer of solar wind heavy ions. *Geophys. Res. Lett.*, 24:105–108, 1997. doi: 10.1029/96GL03780.

[148] M. J. Freyberg. . *Ph.D. Thesis, Ludwig-Maximilians Universität München, Munich, Germany*, December 1994.

[149] S. L. Snowden, M. R. Collier, and K. D. Kuntz. XMM-Newton Observation of Solar Wind Charge Exchange Emission. *ApJ*, 610:1182–1190, August 2004. doi: 10.1086/421841.

[150] F. Jansen, D. Lumb, B. Altieri, J. Clavel, M. Ehle, C. Erd, C. Gabriel, M. Guainazzi, P. Gondoin, R. Much, R. Munoz, M. Santos, N. Schartel, D. Texier, and G. Vacanti. XMM-Newton observatory. I. The spacecraft and operations. *A&A*, 365:L1–L6, January 2001.

[151] B. Aschenbach, O. Citterio, J. M. Ellwood, P. Jensen, P. Dekorte, A. Peacock, and R. Willingale. *The high throughput X-ray Spectroscopy Mission. Report of the Telescope Working Group.* ESA, Report SP-1084, February 1987.

[152] J. W. den Herder, A. C. Brinkman, S. M. Kahn, G. Branduardi-Raymont, K. Thomsen, H. Aarts, M. Audard, J. V. Bixler, A. J. den Boggende, J. Cottam, T. Decker, L. Dubbeldam, C. Erd, H. Goulooze, M. Güdel, P. Guttridge, C. J. Hailey, K. A. Janabi, J. S. Kaastra, P. A. J. de Korte, B. J. van Leeuwen, C. Mauche, A. J. McCalden, R. Mewe, A. Naber, F. B. Paerels, J. R. Peterson, A. P. Rasmussen, K. Rees, I. Sakelliou, M. Sako, J. Spodek, M. Stern, T. Tamura, J. Tandy, C. P. de Vries, S. Welch, and A. Zehnder. The Reflection Grating Spectrometer on board XMM-Newton. *A&A*, 365:L7–L17, January 2001. doi: 10.1051/0004-6361:20000058.

[153] K. O. Mason, A. Breeveld, R. Much, M. Carter, F. A. Cordova, M. S. Cropper, J. Fordham, H. Huckle, C. Ho, H. Kawakami, J. Kennea, T. Kennedy, J. Mittaz, D. Pandel, W. C. Priedhorsky, T. Sasseen, R. Shirey, P. Smith, and J.-M. Vreux. The XMM-Newton optical/UV monitor telescope. *A&A*, 365:L36–L44, January 2001. doi: 10.1051/0004-6361:20000044.

[154] M. J. L. Turner, A. Abbey, M. Arnaud, M. Balasini, M. Barbera, E. Belsole, P. J. Bennie, J. P. Bernard, G. F. Bignami, M. Boer, U. Briel, I. Butler, C. Cara, C. Chabaud, R. Cole, A. Collura, M. Conte, A. Cros, M. Denby, P. Dhez, G. Di Coco, J. Dowson, P. Ferrando, S. Ghizzardi, F. Gianotti, C. V. Goodall, L. Gretton, R. G. Griffiths, O. Hainaut, J. F. Hochedez, A. D. Holland,

E. Jourdain, E. Kendziorra, A. Lagostina, R. Laine, N. La Palombara, M. Lortholary, D. Lumb, P. Marty, S. Molendi, C. Pigot, E. Poindron, K. A. Pounds, J. N. Reeves, C. Reppin, R. Rothenflug, P. Salvetat, J. L. Sauvageot, D. Schmitt, S. Sembay, A. D. T. Short, J. Spragg, J. Stephen, L. Strüder, A. Tiengo, M. Trifoglio, J. Trümper, S. Vercellone, L. Vigroux, G. Villa, M. J. Ward, S. Whitehead, and E. Zonca. The European Photon Imaging Camera on XMM-Newton: The MOS cameras : The MOS cameras. *A&A*, 365:L27–L35, January 2001. doi: 10.1051/0004-6361:20000038.

[155] L. Strüder, U. Briel, K. Dennerl, R. Hartmann, E. Kendziorra, N. Meidinger, E. Pfeffermann, C. Reppin, B. Aschenbach, W. Bornemann, H. Bräuninger, W. Burkert, M. Elender, M. Freyberg, F. Haberl, G. Hartner, F. Heuschmann, H. Hippmann, E. Kastelic, S. Kemmer, G. Kettenring, W. Kink, N. Krause, S. Müller, A. Oppitz, W. Pietsch, M. Popp, P. Predehl, A. Read, K. H. Stephan, D. Stötter, J. Trümper, P. Holl, J. Kemmer, H. Soltau, R. Stötter, U. Weber, U. Weichert, C. von Zanthier, D. Carathanassis, G. Lutz, R. H. Richter, P. Solc, H. Böttcher, M. Kuster, R. Staubert, A. Abbey, A. Holland, M. Turner, M. Balasini, G. F. Bignami, N. La Palombara, G. Villa, W. Buttler, F. Gianini, R. Lainé, D. Lumb, and P. Dhez. The European Photon Imaging Camera on XMM-Newton: The pn-CCD camera. *A&A*, 365:L18–L26, January 2001.

[156] M. J. Freyberg, E. Pfeffermann, and U. G. Briel. The XMM-Newton EPIC PN Camera: Spatial Distribution of the Internal Background Fluorescence Lines. In J. Jansen and TBD, editors, *New Visions of the X-ray Universe in the XMM-Newton and Chandra Era, ESA SP*, volume 488, August 2002.

[157] D. H. Lumb. EPIC Background Files . *XMM-SOC-CAL-TN-0016, issue 2.0*, 2:1–15, January 2002.

[158] D. H. Lumb, R. S. Warwick, M. Page, and A. De Luca. X-ray background measurements with XMM-Newton EPIC. *A&A*, 389:93–105, July 2002.

[159] M. J. Freyberg, U. G. Briel, K. Dernnerl, F. Haberl, G. Hartner, E. Kendziorra, and M. Kirsch. The XMM-Newton EPIC PN Camera: Spectral and Temporal Properties of the Internal Background. In J. Jansen and TBD, editors, *New Visions of the X-ray Universe in the XMM-Newton and Chandra Era, ESA SP*, volume 488, August 2002.

[160] D. H. Lumb and A. D. Holland. X-ray imaging spectroscopy with EEV CCDs. In L. Golub, editor, *X-ray instrumentation in astronomy II; Proceedings of the Meeting, San Diego, CA, Aug. 15-17, 1988 (A89-40276 17-35). Bellingham, WA, Society of Photo-Optical Instrumentation Engineers, 1988, p. 116-122. Sponsorship: European Space Research and Technology Centre.*, pages 116–122, January 1988.

[161] K. C. Gendreau, R. Mushotzky, A. C. Fabian, S. S. Holt, T. Kii, P. J. Serlemitsos, Y. Ogasaka, Y. Tanaka, M. W. Bautz, Y. Fukazawa, Y. Ishisaki, Y. Kohmura, K. Makishima, M. Tashiro, Y. Tsusaka, H. Kunieda, G. R. Ricker, and R. K. Vanderspek. ASCA Observations of the Spectrum of the X-Ray Background. *PASJ*, 47: L5–L9, April 1995.

[162] J. de Plaa, J. S. Kaastra, T. Tamura, E. Pointecouteau, M. Mendez, and J. R. Peterson. X-ray spectroscopy on Abell 478 with XMM-Newton. *A&A*, 423:49–56, August 2004. doi: 10.1051/0004-6361:20047170.

[163] M. A. C. Perryman, A. G. A. Brown, Y. Lebreton, A. Gomez, C. Turon, G. C. de Strobel, J. C. Mermilliod, N. Robichon, J. Kovalevsky, and F. Crifo. The Hyades: distance, structure, dynamics, and age. *A&A*, 331:81–120, March 1998.

[164] M. J. Freyberg, U. G. Briel, K. Dennerl, F. Haberl, G. D. Hartner, E. Pfeffermann, E. Kendziorra, M. G. F. Kirsch, and D. H. Lumb. EPIC pn-CCD detector aboard XMM-Newton: status of the background calibration. In K. A. Flanagan and O. H. W. Siegmund, editors,

X-Ray and Gamma-Ray Instrumentation for Astronomy XIII. Edited by Flanagan, Kathryn A.; Siegmund, Oswald H. W. Proceedings of the SPIE, Volume 5165, pp. 112-122 (2004)., volume 5165 of *Presented at the Society of Photo-Optical Instrumentation Engineers (SPIE) Conference*, pages 112–122, February 2004. doi: 10.1117/12.506277.

[165] F. C. Bertiau. Absolute Magnitudes of Stars in the Scorpo-Centaurus Association. *ApJ*, 128:533–+, November 1958.

[166] K. Imanishi, K. Koyama, and Y. Tsuboi. Chandra Observation of the ρ Ophiuchi Cloud. *ApJ*, 557:747–760, August 2001. doi: 10.1086/321691.

[167] K. L. Luhman and G. H. Rieke. Low-Mass Star Formation and the Initial Mass Function in the ρ Ophiuchi Cloud Core. *ApJ*, 525:440–465, November 1999. doi: 10.1086/307891.

[168] E. J. de Geus, P. T. de Zeeuw, and J. Lub. Physical parameters of stars in the Scorpio-Centaurus OB association. *A&A*, 216:44–61, June 1989.

[169] J. Knude and E. Høg. Interstellar reddening from the HIPPARCOS and TYCHO catalogues. I. Distances to nearby molecular clouds and star forming regions. *A&A*, 338:897–904, October 1998.

[170] N. V. Sujatha, P. Shalima, J. Murthy, and R. C. Henry. Dust Properties in the Far-Ultraviolet in Ophiuchus. *ApJ*, 633: 257–261, November 2005. doi: 10.1086/444532.

[171] B. A. Wilking. *Star Formation in the Ophiuchus Molecular Cloud Complex*, pages 159–+. in: ESO Sci. Rep. 11: Low Mass Star Formation in Southern Molecular Clouds, 1992.

[172] E. J. de Geus, L. Bronfman, and P. Thaddeus. A CO survey of the dark clouds in Ophiuchus. *A&A*, 231:137–150, May 1990.

[173] F. Boulanger, W. T. Reach, A. Abergel, J. P. Bernard, C. J. Cesarsky, D. Cesarsky, F. X. Desert, E. Falgarone, J. Lequeux, L. Metcalfe, M. Perault, J. L. Puget, D. Rouan, M. Sauvage, D. Tran, and L. Vigroux. Mid-Infrared Imaging Spectroscopy in Ophiuchus. *A&A*, 315:L325–L328, November 1996.

[174] T. P. Greene and E. T. Young. Near-infrared observations of young stellar objects in the Rho Ophiuchi dark cloud. *ApJ*, 395:516–528, August 1992. doi: 10.1086/171672.

[175] J. M. Dickey and F. J. Lockman. H I in the Galaxy. *ARA&A*, 28:215–261, 1990.

[176] T. M. Dame, D. Hartmann, and P. Thaddeus. The Milky Way in Molecular Clouds: A New Complete CO Survey. *ApJ*, 547:792–813, February 2001.

[177] M. Lombardi and J. Alves. Mapping the interstellar dust with near-infrared observations: An optimized multi-band technique. *A&A*, 377:1023–1034, October 2001. doi: 10.1051/0004-6361:20011099.

[178] N. A. Ridge, J. Di Francesco, H. Kirk, D. Li, A. A. Goodman, J. F. Alves, H. G. Arce, M. A. Borkin, P. Caselli, J. B. Foster, M. H. Heyer, D. Johnstone, D. A. Kosslyn, M. Lombardi, J. E. Pineda, S. L. Schnee, and M. Tafalla. The COMPLETE Survey of Star-Forming Regions: Phase I Data. *AJ*, 131:2921–2933, June 2006. doi: 10.1086/503704.

[179] M. D. Gladders, T. E. Clarke, C. R. Burns, A. Attard, M. P. Casey, D. Hamilton, G. Mallén-Ornelas, J. L. Karr, S. M. Poirier, M. Sawicki, L. F. Barrientos, and S. W. Mochnacki. The Distance to the Draco Intermediate-Velocity Cloud. *ApJ*, 507:L161–L164, November 1998. doi: 10.1086/311697.

[180] I. A. Crawford. High resolution observations of interstellar NA I and CA II towards the Scorpio-Centaurus association. *A&A*, 247:183–201, July 1991.

[181] P. T. de Zeeuw, R. Hoogerwerf, J. H. J. de Bruijne, A. G. A. Brown, and A. Blaauw. A HIPPARCOS Census of the Nearby OB Associations. *AJ*, 117:354–399, January 1999. doi: 10.1086/300682.

[182] R. Egger. Interaction of the Local Bubble with its environment. *LNP Vol. 506: IAU Colloq. 166: The Local Bubble and Beyond*, 506:287–296, 1998.

[183] F. J. Vrba. Role of magnetic fields in the evolution of five dark cloud complexes. *AJ*, 82:198–208, March 1977.

[184] E. J. de Geus. Interactions of stars and interstellar matter in Scorpio Centaurus. *A&A*, 262:258–270, August 1992.

[185] M. C. Moreira and J. L. Yun. Gas and dust emission in the Lupus globular filaments GF 17 and GF 20. *A&A*, 381: 628–652, January 2002. doi: 10.1051/0004-6361:20011558.

[186] J. A. Combi, J. C. Testori, G. E. Romero, and F. R. Colomb. 1435MHz continuum observations of Upper-Scorpius. *A&A*, 296:514–+, April 1995.

[187] J. L. Jonas. The 2336 MHz Radio Continuum Emission of the Milky Way. *Ph.D. Thesis, Rhodes University, South Africa*, October 1998.

[188] K. Koyama, R. Petre, E. V. Gotthelf, U. Hwang, M. Matsuura, M. Ozaki, and S. S. Holt. Evidence for Shock Acceleration of High-Energy Electrons in the Supernova Remnant SN:1006. *Nature*, 378: 255–+, November 1995. doi: 10.1038/378255a0.

[189] K. Koyama, K. Kinugasa, K. Matsuzaki, M. Nishiuchi, M. Sugizaki, K. Torii, S. Yamauchi, and B. Aschenbach. Discovery of Non-Thermal X-Rays from the Northwest Shell of the New SNR RX J1713.7-3946: The Second SN 1006? *PASJ*, 49:L7–L11, June 1997.

[190] J. W. Keohane, R. Petre, E. V. Gotthelf, M. Ozaki, and K. Koyama. A Possible Site of Cosmic Ray Acceleration in the Supernova Remnant IC 443. *ApJ*, 484:350–+, July 1997. doi: 10.1086/304329.

[191] P. Gulliford. A Simple Shock Wave Model of Supernova Remnant IC 443. *Ap&SS*, 31:241–+, November 1974.

[192] C. M. Olbert, C. R. Clearfield, N. E. Williams, J. W. Keohane, and D. A. Frail. A Bow Shock Nebula around a Compact X-Ray Source in the Supernova Remnant IC 443. *ApJ*, 554:L205–L208, June 2001. doi: 10.1086/321708.

[193] E. M. Berkhuijsen, C. G. T. Haslam, and C. J. Salter. Are the galactic loops supernova remnants ? *A&A*, 14:252–+, September 1971.

[194] Y. Sofue, K. Hamajima, and M. Fujimoto. Radio Spurs and Spiral Structure of the Galaxy, II. On the Supernova Remnant Hypothesis for Spurs. *PASJ*, 26:399–+, 1974.

[195] R. Egger. *Der Supernova-Ueberrest North Polar Spur in der ROSAT-Himmelsdurchmusterung*. MPE Report, Garching: Max Planck Institut für Extraterrestrische Physik, 1993.

[196] R. J. Egger and B. Aschenbach. Interaction of the Loop I supershell with the Local Hot Bubble. *A&A*, 294:L25–L28, February 1995.

[197] R. Génova, J. E. Beckman, S. Bowyer, and T. Spicer. Kinematical Structure of the Local Interstellar Medium: The Galactic Center Hemisphere. *ApJ*, 484:761–+, July 1997. doi: 10.1086/304348.

[198] B. Y. Welsh, N. Craig, P. W. Vedder, and J. V. Vallerga. The local distribution of NA I interstellar gas. *ApJ*, 437:638–657, December 1994. doi: 10.1086/175028.

[199] J.-L. Vergely, R. Freire Ferrero, A. Siebert, and B. Valette. NaI and HI 3-D density distribution in the solar neighbourhood. *A&A*, 366:1016–1034, February 2001. doi: 10.1051/0004-6361:20010006.

[200] M. P. Muno, F. K. Baganoff, M. W. Bautz, E. D. Feigelson, G. P. Garmire, M. R. Morris, S. Park, G. R. Ricker, and L. K. Townsley. Diffuse X-Ray Emission in a Deep Chandra Image of the Galactic Center. *ApJ*, 613:326–342, September 2004. doi: 10.1086/422865.

[201] E. Quataert. A Dynamical Model for Hot Gas in the Galactic Center. *ApJ*, 613: 322–325, September 2004. doi: 10.1086/422973.

[202] M. P. Muno, J. S. Arabadjis, F. K. Baganoff, M. W. Bautz, W. N. Brandt, P. S. Broos, E. D. Feigelson, G. P. Garmire, M. R. Morris, and G. R. Ricker. The Spectra and Variability of X-Ray Sources in a Deep Chandra Observation of the Galactic Center. *ApJ*, 613:1179–1201, October 2004. doi: 10.1086/423164.

[203] M. Revnivtsev, S. Sazonov, M. Gilfanov, E. Churazov, and R. Sunyaev. Origin of the Galactic ridge X-ray emission. *A&A*, 452:169–178, June 2006. doi: 10.1051/0004-6361:20054268.

[204] S. Sazonov, M. Revnivtsev, M. Gilfanov, E. Churazov, and R. Sunyaev. X-ray luminosity function of faint point sources in the Milky Way. *A&A*, 450:117–128, April 2006. doi: 10.1051/0004-6361:20054297.

[205] A. Senda, K. Koyama, K. Ebisawa, J. Kataoka, and Y. Sofue. Detection of Nonthermal X-ray structures near the Galactic Center with Chandra. In E. J. A. Meurs and G. Fabbiano, editors, *Populations of High Energy Sources in Galaxies*, volume 230 of *IAU Symposium*, pages 24–28, 2006. doi: 10.1017/S174392130600771X.

[206] F. Matteucci. *The Chemical Evolution of the Galaxy.* The Chemical Evolution of the Galaxy. By Francesca Matteucci, Department of Astronomy, University of Trieste, Italy. Astrophysics and Space Science Library Volume 253 reprint Kluwer Academic Publishers, Dordrecht, October 2003.

[207] J. H. Taylor and J. M. Cordes. Pulsar distances and the galactic distribution of free electrons. *ApJ*, 411:674–684, July 1993. doi: 10.1086/172870.

[208] N. M. McClure-Griffiths, J. M. Dickey, B. M. Gaensler, and A. J. Green. The Galactic Distribution of Large H I Shells. *ApJ*, 578:176–193, October 2002. doi: 10.1086/342470.

[209] F. Eisenhauer, R. Genzel, T. Alexander, R. Abuter, T. Paumard, T. Ott, A. Gilbert, S. Gillessen, M. Horrobin, S. Trippe, H. Bonnet, C. Dumas, N. Hubin, A. Kaufer, M. Kissler-Patig, G. Monnet, S. Ströbele, T. Szeifert, A. Eckart, R. Schödel, and S. Zucker. SINFONI in the Galactic Center: Young Stars and Infrared Flares in the Central Light-Month. *ApJ*, 628:246–259, July 2005. doi: 10.1086/430667.

[210] F. E. Marshall, E. A. Boldt, S. S. Holt, R. B. Miller, R. F. Mushotzky, L. A. Rose, R. E. Rothschild, and P. J. Serlemitsos. The diffuse X-ray background spectrum from 3 to 50 keV. *ApJ*, 235:4–10, January 1980. doi: 10.1086/157601.

[211] R. Giacconi, J. Bechtold, G. Branduardi, W. Forman, J. P. Henry, C. Jones, E. Kellogg, H. van der Laan, W. Liller, H. Marshall, S. S. Murray, J. Pye, E. Schreier, W. L. W. Sargent, F. Seward, and H. Tananbaum. A high-sensitivity X-ray survey using the Einstein Observatory and the discrete source contribution to the extragalactic X-ray background. *ApJ*, 234: L1–L7, November 1979. doi: 10.1086/183099.

[212] H. Tananbaum, Y. Avni, G. Branduardi, M. Elvis, G. Fabbiano, E. Feigelson, R. Giacconi, J. P. Henry, J. P. Pye, A. Soltan, and G. Zamorani. X-ray studies of quasars with the Einstein Observatory. *ApJ*, 234:L9–L13, November 1979. doi: 10.1086/183100.

[213] G. Hasinger, R. Burg, R. Giacconi, G. Hartner, M. Schmidt, J. Trumper, and G. Zamorani. A Deep X-Ray Survey in the Lockman-Hole and the Soft X-Ray N-Log. *A&A*, 275:1, August 1993.

[214] G. Hasinger, R. Burg, R. Giacconi, M. Schmidt, J. Trumper, and G. Zamorani. The ROSAT Deep Survey. I. X-ray sources in the Lockman Field. *A&A*, 329:482–494, January 1998.

[215] W. N. Brandt and G. Hasinger. Deep Extragalactic X-Ray Surveys. *ARA&A*, 43: 827–859, September 2005.

[216] S. Redfield and J. L. Linsky. The Three-dimensional Structure of the Warm Local Interstellar Medium. II. The Colorado Model of the Local Interstellar Cloud. *ApJ*, 534:825–837, May 2000. doi: 10.1086/308769.

[217] A. Diplas and B. D. Savage. An IUE survey of interstellar H I LY alpha absorption. 1: Column densities. *ApJS*, 93:211–228, July 1994. doi: 10.1086/192052.

[218] E. Churazov, M. Gilfanov, W. Forman, and C. Jones. Mapping the Gas Temperature Distribution in Extended X-Ray Sources and Spectral Analysis in the Case of Low Statistics: Application to ASCA Observations of Clusters of Galaxies. *ApJ*, 471:673–+, November 1996. doi: 10.1086/177997.

[219] J. Wilms, A. Allen, and R. McCray. On the Absorption of X-Rays in the Interstellar Medium. *ApJ*, 542:914–924, October 2000. doi: 10.1086/317016.

[220] F. Haberl, S. Sembay, B. Altieri, and W. Brinkmann. EPIC observations of bright BL Lac objects: what can we learn from the X-ray spectra about the ISM. In A. Wilson, editor, *ESA Special Publication*, volume 604 of *ESA Special Publication*, pages 353–358, January 2006.

[221] M. Balucinska-Church and D. McCammon. Photoelectric absorption cross sections with variable abundances. *ApJ*, 400:699–+, December 1992. doi: 10.1086/172032.

[222] P. R. Bevington and D. K. Robinson. *Data reduction and error analysis for the physical sciences*. New York: McGraw-Hill, 3rd ed., August 2002.

[223] D. Breitschwerdt, M. J. Freyberg, and R. Egger. Origin of H I clouds in the Local Bubble. I. A hydromagnetic Rayleigh-Taylor instability caused by the interaction between the Loop I and the Local Bubble. *A&A*, 361:303–320, September 2000.

[224] D. B. Henley, R. L. Shelton, and K. D. Kuntz. An XMM-Newton Observation of the Local Bubble Using a Shadowing Filament in the Southern Galactic Hemisphere. *ApJ*, 661:304–319, May 2007. doi: 10.1086/513590.

[225] R. K. Smith, M. W. Bautz, R. J. Edgar, R. Fujimoto, K. Hamaguchi, J. P. Hughes, M. Ishida, R. Kelley, C. A. Kilbourne, K. D. Kuntz, D. McCammon, E. Miller, K. Mitsuda, K. Mukai, P. P. Plucinsky, F. S. Porter, S. L. Snowden, Y. Takei, Y. Terada, Y. Tsuboi, and N. Y. Yamasaki. Suzaku Observations of the Local and Distant Hot ISM. *PASJ*, 59:141–150, January 2007.

[226] W. R. Oegerle, E. B. Jenkins, R. L. Shelton, D. V. Bowen, and P. Chayer. A Survey of O VI Absorption in the Local Interstellar Medium. *ApJ*, 622:377–389, March 2005. doi: 10.1086/427792.

[227] R. S. Sutherland and M. A. Dopita. Cooling functions for low-density astrophysical plasmas. *ApJS*, 88:253–327, September 1993. doi: 10.1086/191823.

[228] U. J. Sofia and D. M. Meyer. Interstellar Abundance Standards Revisited. *ApJ*, 554:L221–L224, June 2001. doi: 10.1086/321715.

[229] U. J. Sofia and D. M. Meyer. Erratum: Interstellar Abundance Standards Revisited. *ApJ*, 558:L147–L147, September 2001. doi: 10.1086/323609.

[230] D. A. Verner, E. M. Verner, and G. J. Ferland. Atomic Data for Permitted Resonance Lines of Atoms and Ions from H to Si, and S, Ar, Ca, and Fe. *Atomic Data and Nuclear Data Tables*, 64:1–+, 1996.

[231] T. Fang, H. L. Marshall, J. C. Lee, D. S. Davis, and C. R. Canizares. Chandra Detection of O VIII Lyα Absorption from an Overdense Region in the Intergalactic Medium. *ApJ*, 572:L127–L130, June 2002. doi: 10.1086/341665.

[232] F. Nicastro, A. Zezas, J. Drake, M. Elvis, F. Fiore, A. Fruscione, M. Marengo, S. Mathur, and S. Bianchi. Chandra Discovery of a Tree in the X-Ray Forest toward PKS 2155-304: The Local Filament? *ApJ*, 573:157–167, July 2002. doi: 10.1086/340489.

[233] T. Fang, K. R. Sembach, and C. R. Canizares. Chandra Detection of Local O VII Heα Absorption along the Sight Line toward 3C 273. *ApJ*, 586:L49–L52, March 2003. doi: 10.1086/374680.

[234] A. Rasmussen, S. M. Kahn, and F. Paerels. X-ray IGM in the Local Group. In J. L. Rosenberg and M. E. Putman, editors, *The IGM/Galaxy Connection. The Distribution of Baryons at z=0*, volume 281 of *Astrophysics and Space Science Library*, pages 109–+, April 2003.

[235] Q. D. Wang, Y. Yao, T. M. Tripp, T.-T. Fang, W. Cui, F. Nicastro, S. Mathur, R. J. Williams, L. Song, and R. Croft. Warm-Hot Gas in and around the Milky Way: Detection and Implications of O VII Absorption toward LMC X-3. *ApJ*, 635: 386–395, December 2005. doi: 10.1086/497584.

[236] P. Mendes, M. J. Freyberg, and D. Breitschwerdt. The soft X-ray emission in direction of Hyades. In A. Wilson, editor, *ESA Special Publication*, volume 604 of *ESA Special Publication*, pages 371–372, January 2006.

[237] E. Franciosini, J. Sanz-Forcada, A. Maggio, and R. Pallavicini. XMM-Newton Spectroscopy of Two Hyades Stars. In G. Branduardi-Raymont, editor, *High Resolution X-ray Spectroscopy with XMM-Newton and Chandra*, December 2002.

[238] M. A. C. Perryman, L. Lindegren, J. Kovalevsky, E. Hoeg, U. Bastian, P. L. Bernacca, M. Crézé, F. Donati, M. Grenon, F. van Leeuwen, H. van der Marel, F. Mignard, C. A. Murray, R. S. Le Poole, H. Schrijver, C. Turon, F. Arenou, M. Froeschlé, and C. S. Petersen. The HIPPARCOS Catalogue. *A&A*, 323:L49–L52, July 1997.

[239] B. T. Lynds. Catalogue of Dark Nebulae. *ApJS*, 7:1–+, May 1962.

[240] F. Favata, G. Giardino, G. Micela, S. Sciortino, and F. Damiani. An XMM-Newton-based X-ray survey of pre-main sequence stellar emission in the L1551 star-forming complex. *A&A*, 403:187–203, May 2003. doi: 10.1051/0004-6361:20030305.

[241] S. J. Kenyon, D. Dobrzycka, and L. Hartmann. A new optical extinction law and distance estimate for the Taurus-Auriga molecular cloud. *AJ*, 108:1872–1880, November 1994. doi: 10.1086/117200.

[242] C. Briceño, L. Hartmann, J. Stauffer, and E. Martín. A Search for Very Low Mass Pre-Main-Sequence Stars in Taurus. *AJ*, 115:2074–2091, May 1998. doi: 10.1086/300338.

[243] D. Devine, B. Reipurth, and J. Bally. L1551 NE or L1551 IRS 5: Which Source Drives HH 28/29? *AJ*, 118:972–982, August 1999. doi: 10.1086/300992.

[244] R. L. Snell, R. B. Loren, and R. L. Plambeck. Observations of CO in L1551 - Evidence for stellar wind driven shocks. *ApJ*, 239:L17–L22, July 1980. doi: 10.1086/183283.

[245] R. Rainey, G. J. White, K. J. Richardson, M. J. Griffin, N. J. Cronin, T. S. Monteiro, and J. Hilton. Millimetre and submillimetre molecular line observations of the southwest lobe of L 1551 - Evidence of a shell structure. *A&A*, 179:237–248, June 1987.

[246] N. D. Parker, G. J. White, P. G. Williams, and S. S. Hayashi. High resolution CO J = 3-2 observations of L 1551 - Fragmentary structure in the outflowing shell. *A&A*, 250:134–142, October 1991.

[247] L. Carkner, E. D. Feigelson, K. Koyama, T. Montmerle, and I. N. Reid. X-Ray-emitting T Tauri Stars in the L1551 Cloud. *ApJ*, 464:286–+, June 1996. doi: 10.1086/177320.

[248] M. Gomez, B. F. Jones, L. Hartmann, S. J. Kenyon, J. R. Stauffer, R. Hewett, and I. N. Reid. On the ages of pre-main-sequence stars in Taurus. *AJ*, 104:762–773, August 1992. doi: 10.1086/116272.

[249] P. M. Garnavich, A. Noriega-Crespo, and P. J. Green. Wide field imaging of the

star forming region Lynds 1551. *Revista Mexicana de Astronomia y Astrofisica*, 24: 99–107, April 1992.

[250] S. Redfield and J. L. Linsky. Microstructure of the Local Interstellar Cloud and the Identification of the Hyades Cloud. *ApJ*, 551:413–428, April 2001. doi: 10.1086/320096.

[251] D. Froebrich, G. C. Murphy, M. D. Smith, J. Walsh, and C. Del Burgo. A large-scale extinction map of the Galactic Anticentre from 2MASS. *MNRAS*, 378:1447–1460, July 2007. doi: 10.1111/j.1365-2966.2007.11886.x.

[252] E. M. Berkhuijsen. Galactic continuum loops and the diameter-surface brightness relation for supernova remnants. *A&A*, 24: 143–147, April 1973.

[253] V. Borka. Spectral indices of Galactic radio loops between 1420, 820 and 408 MHz. *MNRAS*, 376:634–644, April 2007. doi: 10.1111/j.1365-2966.2007.11499.x.

[254] R. Cen and J. P. Ostriker. Where Are the Baryons? *ApJ*, 514:1–6, March 1999.

[255] R. Davé, R. Cen, J. P. Ostriker, G. L. Bryan, L. Hernquist, N. Katz, D. H. Weinberg, M. L. Norman, and B. O'Shea. Baryons in the Warm-Hot Intergalactic Medium. *ApJ*, 552:473–483, May 2001.

[256] F. Nicastro, S. Mathur, M. Elvis, J. Drake, T. Fang, A. Fruscione, Y. Krongold, H. Marshall, R. Williams, and A. Zezas. The mass of the missing baryons in the X-ray forest of the warm-hot intergalactic medium. *Nature*, 433:495–498, February 2005. doi: 10.1038/nature03245.

[257] R. J. Williams, S. Mathur, and F. Nicastro. Galactic Corona or Local Group Intergalactic Medium? In A. Wilson, editor, *The X-ray Universe 2005*, volume 604 of *ESA Special Publication*, January 2006.

[258] S. Mathur, F. Nicastro, and R. Willimas. Lost Baryons at Low Redshift. In J. Davies & M. Disney, editor, *IAU Symposium*, volume 244 of *IAU Symposium*, pages 35–43, May 2008. doi: 10.1017/S1743921307013816.

[259] R. M. Humphreys. Studies of luminous stars in nearby galaxies. I. Supergiants and O stars in the Milky Way. *ApJS*, 38: 309–350, December 1978.

[260] N. V. Kharchenko, A. E. Piskunov, S. Röser, E. Schilbach, and R.-D. Scholz. Astrophysical parameters of Galactic open clusters. *A&A*, 438:1163–1173, August 2005. doi: 10.1051/0004-6361:20042523.

[261] D. Breitschwerdt. Modeling the Local Interstellar Medium. *Ap&SS*, 276:163–176, 2001.

[262] B. J. Wargelin, M. Markevitch, M. Juda, V. Kharchenko, R. Edgar, and A. Dalgarno. Chandra Observations of the "Dark" Moon and Geocoronal Solar Wind Charge Transfer. *ApJ*, 607:596–610, June 2004. doi: 10.1086/383410.

[263] M.-A. Miville-Deschênes and G. Lagache. IRIS: A New Generation of IRAS Maps. *ApJS*, 157:302–323, April 2005. doi: 10.1086/427938.

[264] M. Rowan-Robinson, M. Jones, K. Leech, K. Vedi, and J. Hughes. IRAS maps of galactic emission and the zodiacal bands. *MNRAS*, 249:729–741, April 1991.

Index